

KINEMATICS AND DYNAMICS OF BARRED SPIRAL GALAXIES

BY

MARTIN NICHOLAS ENGLAND

A DISSERTATION PRESENTED TO THE GRADUATE SCHOOL  
OF THE UNIVERSITY OF FLORIDA IN  
PARTIAL FULFILLMENT OF THE REQUIREMENTS  
FOR THE DEGREE OF DOCTOR OF PHILOSOPHY

UNIVERSITY OF FLORIDA

1986

"To the Reader Concerning the Hypothesis of this Work"

Andrew Osiander c1543 in

"De Revolutionibus Orbium Caelestium"

N. Copernicus

It is the job of the astronomer to use painstaking and skilled observation in gathering together the history of the celestial movements, and then, since he cannot by any line of reasoning reach the true cause of these movements to think up or construct whatever causes or hypotheses he pleases such that, by the assumption of these causes, those same movements can be calculated from the principles of geometry for the past and for the future, too. And if [mathematical astronomy] constructs and thinks up causes-- and it has certainly thought up a good many--nevertheless it does not think them up in order to persuade anyone of their truth but only in order that they may provide a correct basis for calculation. And as far as hypotheses go, let no one expect anything in the way of certainty from astronomy, since astronomy can offer us nothing certain.

Plato: Timaeus

As being is to becoming, so is truth to belief. If then, Socrates, amid the many opinions about the gods and the generation of the universe, we are not able to give notions which are altogether and in every respect exact and consistent with one another, do not be surprised.

## ACKNOWLEDGEMENTS

It is rather difficult to acknowledge all the people who in one way or another have contributed to this document without using the standard oft-repeated phrases so common in these sections of dissertations.

Dr. Stephen Gottesman led me through the intricacies of the VLA and extragalactic radio astronomy. This was no trivial achievement as he was dealing with someone who was initially a confirmed optical stellar spectroscopist. His success in this can be measured by the results contained in the next few hundred pages. Not only was he my dissertation chairman but a person who was always willing to help in other matters of general well-being, and above all, a friend.

Dr. James Hunter, who continually challenged me with his seemingly "straightforward" problems, acted as cochairman for the dissertation. He is also responsible for showing an observational astronomer that theoretical astronomy is not the great insurmountable barrier that it was first considered to be. He, probably more than anyone else, taught me the virtue of sitting down with something, as with his course work problems (generally unpleasant) and persevering until it was done. The satisfaction of completing the problem was worth the effort.

The rest of my committee, Drs. Thomas Carr, Haywood Smith and Gary Ihas, performed their duties competently and allowed me the freedom, within guidelines, to do as I pleased.

The 21cm observations utilized in this dissertation were obtained at the Very Large Array of the National Radio Astronomy Observatory. The National Radio Astronomy Observatory is operated by Associated Universities, Inc., under contract with the National Science Foundation. My thanks to all the staff, especially Drs. Jacqueline van Gorkom and Patrick Palmer. They not only helped make a competent spectral line observer out of me but introduced me to the mountains of southwest New Mexico.

My thanks go also to Drs. Bruce and Debra Elmegreen who made their surface photometry available and to Drs. C. Telesco and I. Gatley who allowed me to use their 2.2um data.

The diagrams and photographs were produced by Paul Gombola and Hans Schrader.

Computing was done using the facilities of the Astronomy Department and the Northeast Regional Data Center (NERDC). I thank the numerous people who provided free consultation in the hallways and helped with problems as diverse as image processing and dissertation printing. Thanks especially to Virginia Hetrick and Jim Parkes. This dissertation was produced using UFTHESES on NERDC.

Irma Smith typed the equations and the "fiddle bits", and provided typing services throughout my stay in Florida.

Finally, my heartfelt thanks must go to my parents, Michael and Maureen England, who supported and actively encouraged their "professional student." Without their support none of the next few hundred pages would have been written. I hope that I can repay them someday for their sacrifices and dedication.

My wife, Sheila, has been a veritable "Rock of Gibraltar" and has put up with more and had less than any wife and woman should reasonably be expected to endure. It is all over now and it is to her and my parents that this volume is dedicated.

# TABLE OF CONTENTS

	PAGE
ACKNOWLEDGEMENTS . . . . .	iv
LIST OF TABLES . . . . .	ix
LIST OF FIGURES . . . . .	x
ABSTRACT . . . . .	xiv
CHAPTER	
I. INTRODUCTION . . . . .	1
Selection Criteria . . . . .	6
Survey Galaxies . . . . .	8
NGC 1073 . . . . .	8
NGC 1300 . . . . .	15
NGC 3359 . . . . .	15
NGC 3992 . . . . .	16
II. RADIO OBSERVATIONS . . . . .	18
HI As A Kinematic Tracer . . . . .	18
Aperture Synthesis Theory . . . . .	23
Observing Strategy and Calibration . . . . .	27
Map-Making and Image Processing . . . . .	37
III. DETERMINATION OF THE NEUTRAL HYDROGEN PROPERTIES . . . . .	79
Spectrum Integration Techniques . . . . .	79
Neutral Hydrogen Distribution . . . . .	86
Continuum . . . . .	113
Kinematics of the Neutral Hydrogen . . . . .	115
Mass Models . . . . .	132
IV. SURFACE PHOTOMETRY . . . . .	140
Calculation of the Volume Mass Distribution . . . . .	142
Surface Photometry of NGC 1300 . . . . .	146
Modeling the I Passband Features . . . . .	146
Comparisons Between Different Passbands . . . . .	165
Triaxial Ellipsoid . . . . .	175

V. MODELING . . . . .	185
The Beam Scheme . . . . .	185
Hydrodynamical Modeling of NGC 1300 . . . . .	200
Triaxial Bar Models . . . . .	200
Oval Distortion Models . . . . .	207
Composite Models . . . . .	210
Bulge Models . . . . .	234
VI. RESULTS FROM OTHER GALAXIES . . . . .	247
NGC 3359 . . . . .	247
Observational Results . . . . .	247
Hydrodynamical Models . . . . .	252
NGC 3992 . . . . .	255
Observational Results . . . . .	256
Hydrodynamical Models . . . . .	261
NGC 1073 . . . . .	263
Observational Results . . . . .	264
Hydrodynamical Models . . . . .	269
VII. PROPERTIES OF BARRED SPIRAL GALAXIES . . . . .	272
Observational Comparisons . . . . .	272
Dynamical Properties . . . . .	275
VIII. SUMMARY . . . . .	282
Neutral Hydrogen Results for NGC 1300 . . . . .	282
Hydrodynamical Results . . . . .	283
Dynamical Properties . . . . .	285
APPENDIX	
A.    DERIVATION OF VOLUME BRIGHTNESS DISTRIBUTIONS . . . . .	287
B.    OVAL DISTORTIONS FOR N=1 TYPE TOOMRE DISKS . . . . .	291
BIBLIOGRAPHY . . . . .	299
BIOGRAPHICAL SKETCH . . . . .	305



# LIST OF TABLES

TABLE	PAGE
1.1. Global Properties of Survey Galaxies . . . . .	14
2.1. Properties of Survey Calibrators . . . . .	38
2.2. Image Signal and Noise Characteristics . . . . .	53
3.1. Signal Characteristics for Spectrum Integration . .	85
3.2. Summary of Neutral Hydrogen Observations for NGC 1300 . . . . .	139
4.1. Bar Projection Parameters for NGC 1300 . . . . .	183
6.1. Summary of Integrated Properties of NGC 3359 . .	254
6.2. Summary of Integrated Properties of NGC 3992 . .	262
6.3. Summary of Integrated Properties of NGC 1073 . .	270
8.1. Summary of Results for NGC 1300 . . . . .	284

## LIST OF FIGURES

FIGURE	PAGE
1.1. Survey Galaxies . . . . .	9
2.1. Spheroidal Convolving Function . . . . .	43
2.2. (u,v) Coverage . . . . .	45
2.3. Spectral Line Channel Maps . . . . .	55
2.4. Wide Field Map . . . . .	76
2.5. Channel Zero . . . . .	77
3.1. Neutral Hydrogen Distribution Contour Plot . . . . .	88
3.2. Neutral Hydrogen Distribution with the Optical Image . . . . .	89
3.3. Neutral Hydrogen Distribution Gray Scale Image . . . . .	91
3.4. Neutral Hydrogen Distribution False Color Image . . . . .	92
3.5. Logarithmic Fit to Spiral Arms . . . . .	96
3.6. Deprojected Azimuthal Profiles . . . . .	97
3.7. HII Regions in NGC 1300 . . . . .	98
3.8. Deprojected HI Surface Density . . . . .	104
3.9. Profiles Through HI Surface Density Distribution . . . . .	107
3.10. Continuum Emission . . . . .	114
3.11. Velocity Contours . . . . .	116
3.12. False Color Representation of Velocities . . . . .	117
3.13. Velocity Field Superimposed on Optical Object . . . . .	119

3.14.	Angle-Averaged Rotation Curve . . . . .	125
3.15.	Wedge Rotation Curve . . . . .	126
3.16.	Optical and HI Rotation Curves . . . . .	129
3.17.	Rotation Curve to 6.4 arcmin . . . . .	131
3.18.	Mass Models for NGC 1300 . . . . .	134
3.19.	HI Observed Global Profile . . . . .	138
4.1.	NGC 1300 Gray Scale I Passband . . . . .	147
4.2.	Contour Plot of I Plate . . . . .	148
4.3.	Convolved I Passband Image NGC 1300 . . . . .	151
4.4.	Bar Brightness Profiles . . . . .	153
4.5.	Disk Surface Brightness . . . . .	155
4.6.	Bulge Component Model . . . . .	158
4.7.	Bulge Subtracted Disk Profile . . . . .	159
4.8.	Bulge Subtracted Contour Plot . . . . .	160
4.9.	I Band Model Isophotes . . . . .	163
4.10.	I Band Model Profiles . . . . .	164
4.11.	Gray Scale of Blue Passband . . . . .	166
4.12.	Contour Plot Blue Passband . . . . .	167
4.13.	Minor-axis Profiles Blue and I Passbands . . . . .	169
4.14.	Profile Comparison . . . . .	171
4.15.	Comparison of Blue and I Profiles . . . . .	172
4.16.	Contour Plot 2.2um . . . . .	176
4.17.	False Color Plot 2.2um . . . . .	177
4.18.	Flux Profile 2.2um . . . . .	179
4.19.	Comparison Between Different Wavelengths . . . . .	180
5.1.	Dependence of Rotation Curve on Projection Parameters . . . . .	198

5.2.	Gas Response for Disk and Triaxial . . . . .	202
5.3.	Velocity Field for Bar and Triaxial . . . . .	204
5.4.	Model Rotation Curve . . . . .	205
5.5.	Supermassive Bar Rotation Curve . . . . .	206
5.6.	Oval Distortion Model Gas Response . . . . .	211
5.7.	Oval Distortion Model Velocity Field . . . . .	212
5.8.	Composite Model Gray Scale . . . . .	215
5.9.	Composite Model Contour Plot . . . . .	216
5.10.	Composite Model Velocity Field . . . . .	217
5.11.	Composite Model Rotation Curve . . . . .	218
5.12.	Slow Pattern Speed Model Gray Scale . . . . .	225
5.13.	Velocity Field Vectors . . . . .	229
5.14.	Velocity Field in Perturbation Frame . . . . .	230
5.15.	Noncircular Velocities . . . . .	231
5.16.	Gas Response for Bulge Model . . . . .	236
5.17.	Density Compared with Observations . . . . .	237
5.18.	Bulge Model Velocity Field . . . . .	238
5.19.	Velocity Compared with Observations . . . . .	239
5.20.	Comparison of Rotation Curves . . . . .	241
5.21.	Velocity Vectors for Bulge Model . . . . .	242
5.22.	Velocity Field in Perturbation Frame . . . . .	243
5.23.	Noncircular Velocities . . . . .	244
6.1.	HI Distribution NGC 3359 . . . . .	249
6.2.	Velocity Field NGC 3359 . . . . .	250
6.3.	Rotation Curve NGC 3359 . . . . .	253
6.4.	HI Distribution NGC 3992 . . . . .	257
6.5.	Velocity Field NGC 3992 . . . . .	258

6.6.	Rotation Curve NGC 3992 . . . . .	260
6.7.	HI Distribution NGC 1073 . . . . .	265
6.8.	Velocity Field NGC 1073 . . . . .	266
6.9.	Rotation Curve NGC 1073 . . . . .	268

Abstract of Dissertation Presented to the Graduate School  
of the University of Florida in Partial Fulfillment of the  
Requirements for the Degree of Doctor of Philosophy

KINEMATICS AND DYNAMICS OF BARRED SPIRAL GALAXIES

By

Martin Nicholas England

December 1986

Chairman: S. T. Gottesman  
Cochairman: J. H. Hunter, Jr.  
Major Department: Astronomy

The kinematics and dynamics of a group of barred spiral galaxies are analysed. Hydrodynamical models using the "beam scheme" are calculated and provide a set of dynamical properties for barred spiral galaxies.

Neutral hydrogen radio observations of NGC 1300 show the galaxy to be an excellent example of a grand design spiral system. The HI gas is confined almost entirely to the spiral arms with very little interarm gas. These HI arms correlate very well with the position of the optical arms. The HI arms can be traced through about 310 degrees in azimuth. The central region, the region occupied by the bar, is deficient in gas.

The velocity field shows that circular motion is the dominant component but that large non-circular motions, mainly in the arms, are present. The rotation curve rises to a maximum of 185km/sec at  $r=2.5'$  and then remains essentially flat out to about  $r=3.2'$ .

Near infrared surface photometry is used to calculate a triaxial ellipsoidal figure for the bar. Blue and 2.2um photometry is analysed and compared with the I band and 21cm observations.

Hydrodynamical models for NGC 1300 are partially successful in reproducing the observed morphology and kinematics of NGC 1300. Various combinations of parameters are investigated and a composite "best model" presented. This model consists of an  $n=1$  Toomre disk, a triaxial bar, an  $l=2$  oval distortion and a halo. The pattern speed of 19.3km/sec/kpc places corotation just outside the end of the bar.

Hydrodynamical models for NGC 1073, NGC 3359 and NGC 3992 are examined and compared with that for NGC 1300. This results in a set of dynamical properties for barred spiral galaxies.

## CHAPTER I INTRODUCTION

Barred spiral galaxies present a very interesting but very difficult problem for astronomers. De Vaucouleurs (1963) in his sample of 994 spiral galaxies found that about 37% are pure barred galaxies, while another 28% are mixed spirals. The remaining galaxies are pure spirals, and are thus in the minority. Therefore, barred systems are common, and a good understanding of the physical processes occurring in them would give insight into the formation and maintenance of the observed spiral structure.

Until recently the comparison of theoretical models and observations of barred spiral galaxies has not been very fruitful for a number of reasons. Hydrodynamical calculations have indicated that the gas distribution and kinematics in barred spiral galaxies are very sensitive tracers of the underlying gravitational potential (Roberts, Huntley and van Albada, 1979). This is due to the fact that the gas may respond in a highly non-linear way to even small deviations from axial symmetry (Sanders and Huntley, 1976). Theory is capable of producing high resolution models of gas kinematics and structure. However, the observations have either not had sufficient spatial resolution for a good



comparison to be made, or their spatial coverage has been poor. Traditionally, optical measurements of the kinematics of spiral galaxies have provided high spatial resolution but very poor spatial coverage as they have relied upon HII regions. The distribution of these regions is patchy; Hodge (1969) has distributions of HII regions in spiral galaxies. These regions are not a good tracer of the kinematics of the gas in barred spiral galaxies. These HII regions are mainly in the inner regions and spiral arms. However, they would provide an excellent complement for some other, more global, gas tracer.

Neutral hydrogen is known to be distributed over large regions in spiral galaxies and could provide the global kinematic tracer needed to test the theoretical model results. However, until recently, observations of the neutral hydrogen in barred spiral galaxies have been made using single dish radio telescopes. These observations do not have the required spatial resolution needed to compare with the theories, and even have difficulty in isolating the bar from the underlying disk. The National Radio Astronomy Observatory Very Large Array (NRAO VLA) is a sensitive instrument of high resolution, on the order of 20" for the HI emission from barred spiral systems. The VLA is sensitive enough that a complete two-dimensional map of the velocity field can be completed in a reasonable amount of observing time, even though there are no bright, nearby, easily-

observed large barred spirals. Thus, observations of the gas kinematics and structure can now be made that can confront theoretical models in a quantitative fashion.

High resolution mapping of the gas kinematics in barred systems, combined with two-dimensional hydrodynamical modeling, could address the following questions (Teuben et al., 1986):

1. What is the radial mass distribution in barred systems?
2. Are principal resonances present in barred spiral galaxies? Sanders and Huntley (1976) have shown that the gas flow changes character at the resonances, consistent with the dominant periodic orbits. Within the inner Lindblad resonance, gas flow is on elliptical streamlines oriented perpendicular to the bar major-axis. Determining the location of the resonances, combined with the radial mass distribution, would allow an estimation of the pattern speed of the bar.
3. What is the character of the gas motions? Elliptical streaming is recognizable as a skewing of the velocity contours along the major-axis (Bosma, 1981). The degree of skewing is related to the bar strength (Sanders and Tubbs, 1980).
4. What is the nature of the parallel, straight dust lanes in barred spiral galaxies of type SBb? In

hydrodynamical calculations, such structures arise naturally as shocks. These dust lanes often lie along the leading edge of the rotating bar, for example NGC 1300 and NGC 1365, and as yet there have been no unambiguous, kinematic verifications that they are actually associated with shocks. Ondrechen and van der Hulst (1983) have shown that for NGC 1097 the radio continuum emission is enhanced along the dust lanes, which is to be expected from compression in shock regions.

Asymmetries in the mass distribution, such as barlike configurations or oval distortions, play an important role in the dynamics of galaxies. Various numerical simulations have indicated that barlike configurations are robust and long-lived and may be a preferred configuration for gravitationally interacting particles (Miller, 1971, 1976, 1978; Ostriker and Peebles, 1973; Hohl, 1978; Miller and Smith, 1979). Evidence, both theoretical (Sanders and Huntley, 1976) and experimental (Sanders and Huntley, 1976; Huntley, Sanders and Roberts, 1978; Sanders and Tubbs, 1980) has been presented that supports the origin of spiral arms as being the dynamical response of a gaseous disk to a rotating stellar bar. On the other hand, it may be the case that spiral arms could result from either the dynamical response of the gas to a rotating barred-spiral potential (Liebovitch, 1978; Roberts, Huntley and van Albada, 1979) or

from the effects of self-gravity in a bar-driven disk of gas (Huntley, 1980). Evidence that the gas in barred galaxies does "sense" the presence of a stellar bar is concluded from a morphological study of barred systems (Kormendy, 1979).

Other observational features which may have significant implications for the modeling process are

1. The sharp bending of the bar into spiral arms.
2. The presence of luminous, giant HII regions which often distinguish the spiral arms from the bar in the region where the arms break from the bar.

The basic aim of this study is to observe a variety of barred spiral galaxies and to calculate theoretical models for each galaxy, using some of the observational parameters as input quantities for the modeling procedure. The VLA was used to provide detailed, high resolution observations of the properties of the atomic hydrogen in each of the galaxies at the highest possible signal-to-noise ratio. These observations provide an estimate of the rotation curve for each galaxy and allow the mapping of the galaxian velocity field and neutral hydrogen gas distribution. Observations in the near infrared region ( $\lambda_0 = 8250\text{\AA}$ ) are reduced to provide data for an "observed" bar, after some M/L assumptions. This bar is used as an input parameter for the modeling procedure. Optical observations of the gas kinematics, where available, are used to complement the neutral hydrogen kinematical information.

The modeling procedure consists of a hydrodynamical computer code, the "beam scheme" of Sanders and Prendergast (1974), kindly provided by Dr. J. M. Huntley. This code calculates the response of a gaseous disk to an imposed perturbation, for example a bar figure or an oval distortion. The results from these models are compared with the observations of the kinematics and distribution of the neutral hydrogen gas.

### Selection Criteria

The sample of barred spiral galaxies used for this study was selected using several criteria;

1. The galaxy should be large, with an optical diameter of at least 5'.
2. The bar should be prominent and large in comparison with the 15"-30" beam synthesized at the VLA.
3. The HI surface brightness should be reasonably high to allow observations with good signal-to-noise ratio.
4. The object should not be too far south.
5. The system should be symmetrical.
6. The inclination of the disk of the galaxy, with respect to the sky plane, should not be too high.
7. Surface photometry, especially in the near infrared, I passband ( $\lambda=8250\text{\AA}$ ), should be available.

8. A variety of types of barred spiral galaxy should be obtained.

The first four criteria are used to ensure that the observations are feasible in a reasonable amount of observing time, and that the signal-to-noise ratio is optimal. The size of the object and the bar allow good, high resolution observations to be made and the declination requirement is imposed to obtain as circular a synthesized beam as possible. Criterion 5 is used to facilitate the modeling procedure. If the galaxies are not symmetrical, the complexity of the modeling procedure is increased greatly. Criterion 6 avoids the problems associated with observing a galaxy with a line-of-sight through a disk of finite thickness. The availability of surface photometry, especially near infrared (Criterion 7) allows an approximate determination of the underlying distribution of non-gaseous luminous matter (stars) in the galaxy. Near infrared photometry gives valuable information on the distribution of the bar mass as it can penetrate, to some extent, the dust lanes. This in turn provides constraints on the non-axisymmetric bar component of the gravitational potential which is required as input data for the modeling procedure. Lastly, a variety of galaxies is needed, spanning a range of galaxy types. This will allow some general conclusions to be drawn about barred spiral galaxies as a class of object.

The galaxies NGC 1073, NGC 1300, NGC 3359, NGC 3992 satisfy most of the selection criteria.

### Survey Galaxies

The four galaxies used in this study are shown in Figure 1-1 (a-d). These photographs are taken from various sources. Other photographs of these galaxies which may be of interest are near infrared exposures in Elmegreen (1981), yellow and hydrogen alpha images in Hodge (1969), and for NGC 1073, NGC 1300 and NGC 3359 blue exposures from the Palomar 200" in Sandage (1961). Table 1-1 lists some global properties of these galaxies compiled from a variety of sources. No independent effort has been made to verify these parameters. As can be seen from Figure 1-1 these galaxies all have rather different morphologies and each should present different problems for the modeling procedure. Thus, a wide range of morphological types is represented by this sample and should allow some general conclusions to be drawn.

#### NGC 1073

This galaxy, shown in Figure 1-1 (a), is classified as an SBT5 by de Vaucouleurs, de Vaucouleurs and Corwin (1976) and as an SBc(sr) by Sandage (1961). The two prominent spiral arms do not begin at the ends of the bar, but at  $30^\circ$  from the ends. The bar has a bright, central, elliptical

Figure 1-1. Survey Galaxies. Optical photographs of the four galaxies used in this survey.

- A. NGC 1073 (Arp and Sulentic, 1979).
- B. NGC 1300 (National Geographic--Palomar Sky Survey).
- C. NGC 3359 (National Geographic--Palomar Sky Survey).
- D. NGC 3992 (National Geographic--Palomar Sky Survey).

In all photographs north is to the top and east is to the left except for NGC 3359 where north is to the top and west is to the left.



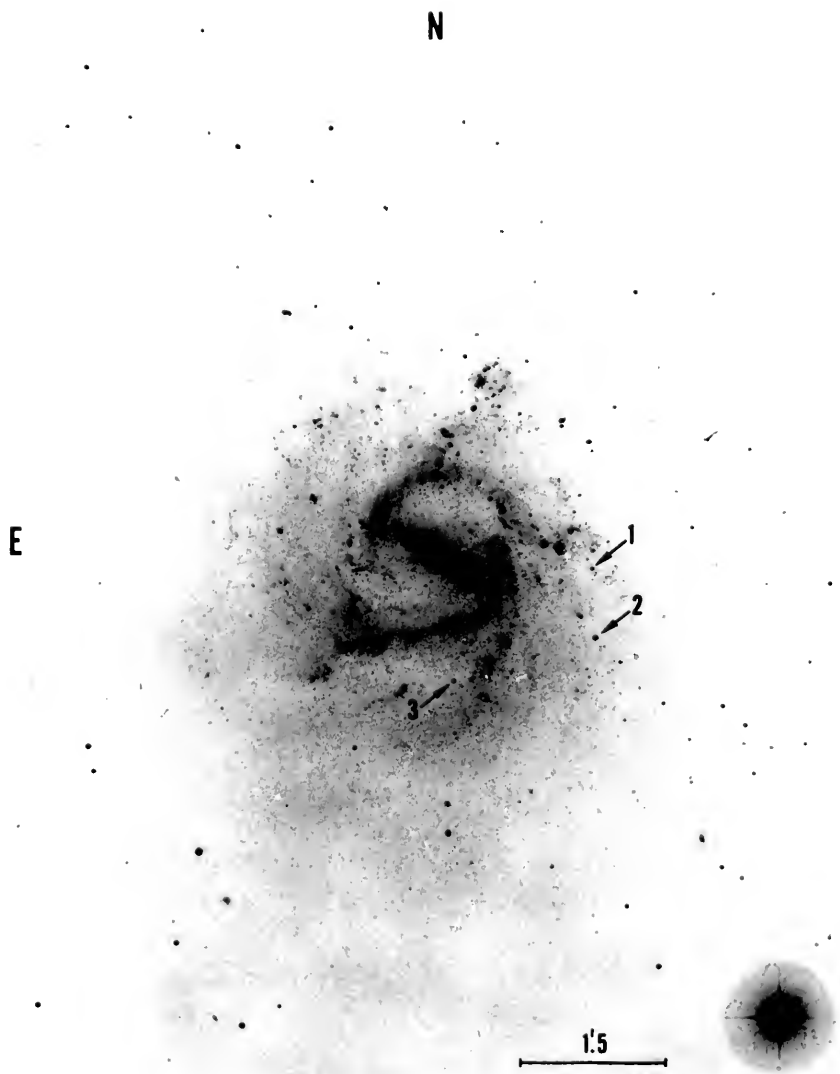


Figure 1-1 cont. (Part A).

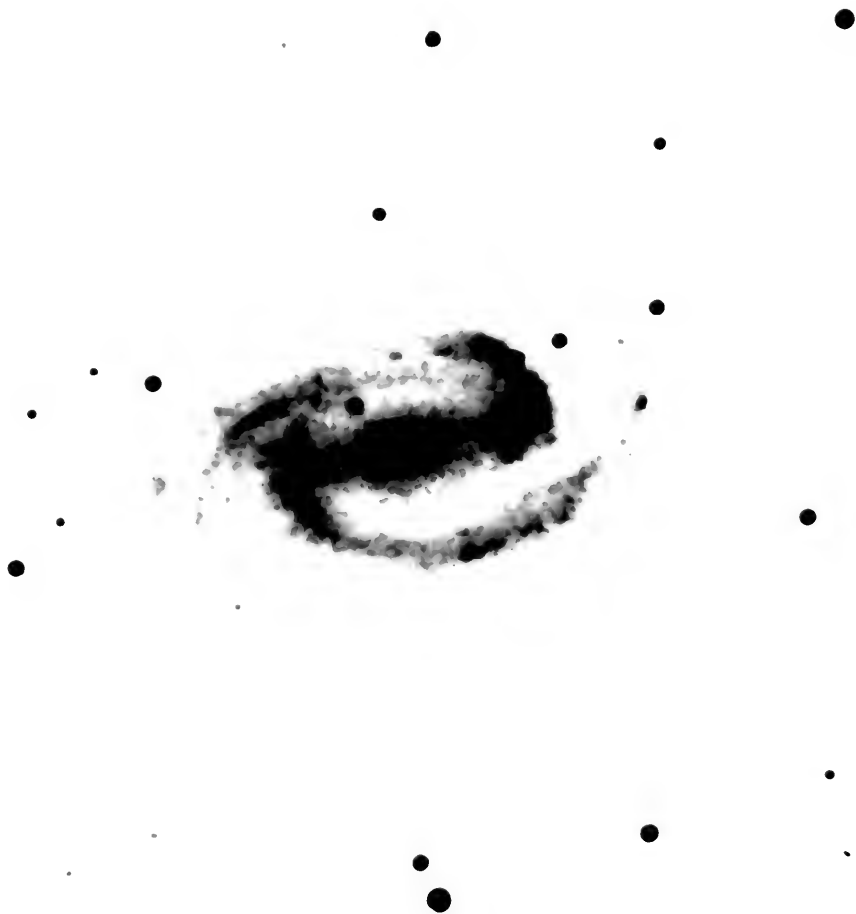


Figure 1-1 cont. (Part B).

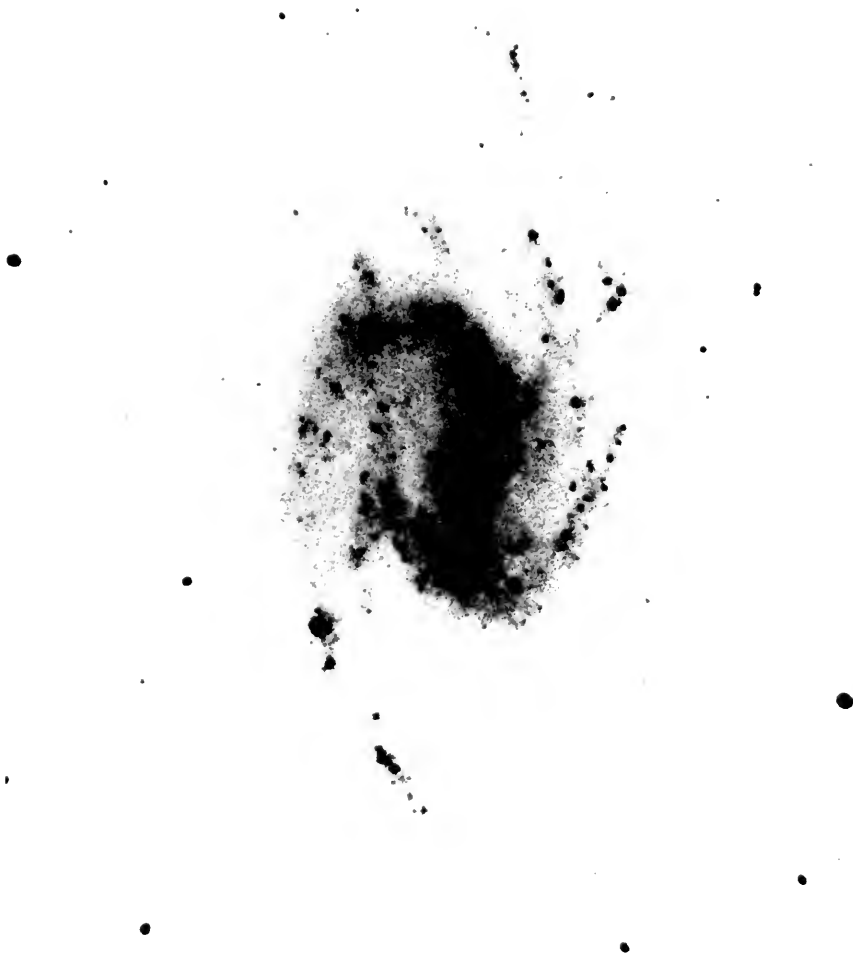


Figure 1-1 cont. (Part C).

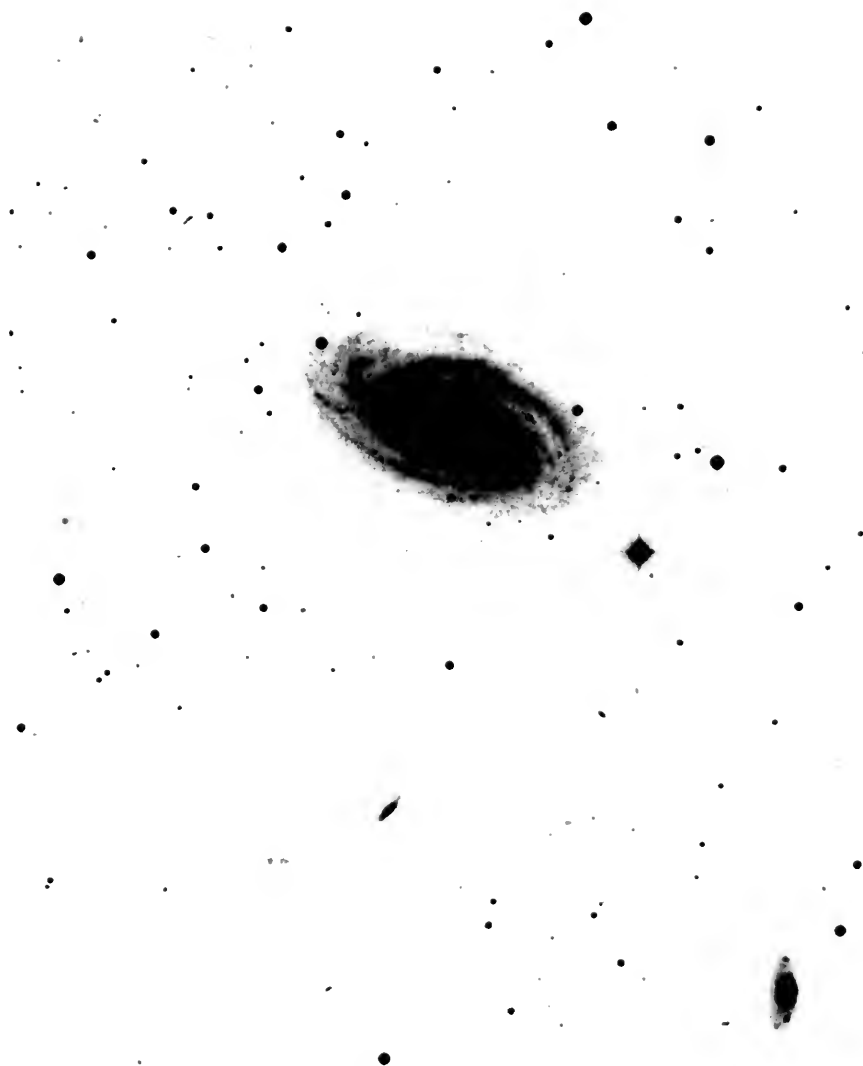


Figure 1-1 cont. (Part D).

TABLE 1.1  
Global Properties of Survey Galaxies

Parameter	NGC 1300	NGC 1073
Right Ascension <sup>a</sup>	3 17 25.2	2 41 09.0
Declination <sup>a</sup>	-19 35 29.0	1 09 54.0
Morphological Type <sup>b</sup>	SBT4	SBT5
Distance (Mpc) <sup>c</sup>	17.1	13.6
Photometric Diameter <sup>b</sup> D <sub>25</sub> (arcmin)	6.5	4.9
Photometric Diameter (kpc)	32.3	19.4
Dimensions of Optical Bar (arcmin)	2.3x0.5	1.2x0.2
Corrected Blue Luminosity <sup>d</sup> (10 <sup>10</sup> Lo)	2.39	0.93
Corrected Blue Magnitude	10.7	11.2
Parameter	NGC 3359	NGC 3992
Right Ascension <sup>a</sup>	10 43 20.7	11 55 01.0
Declination <sup>a</sup>	63 29 12.0	53 39 13.0
Morphological Type <sup>b</sup>	SBT5	SBT4
Distance (Mpc) <sup>c</sup>	11.0	14.2
Photometric Diameter <sup>b</sup> D <sub>25</sub> (arcmin)	6.3	7.6
Photometric Diameter (kpc)	20.2	31.4
Dimensions of Optical Bar (arcmin)	1.7x0.6	1.7x0.5
Corrected Blue Luminosity <sup>d</sup> (10 <sup>10</sup> Lo)	1.08	2.40
Corrected Blue Magnitude	10.6	10.22

a Gallouet, Heidmann and Dampierre (1973).

b De Vaucouleurs, de Vaucouleurs and Corwin (1976).

c De Vaucouleurs and Peters (1981).

d Calculated using above values of distance and magnitude,  
and using  $M_B(0)=+5.48$  (Allen, 1973).

region, decreasing in brightness noticeably before meeting the arms. The ring is not complete and there are no straight absorption lanes. Both the arms and the bar can be resolved into many knots. The west arm appears to bifurcate at about the end of the bar. Arp and Sulentic (1979) identified three quasars in the field of NGC 1073, namely objects 1, 2 and 3 in Figure 1-1 (a).

#### NGC 1300

NGC 1300, Figure 1-1 (b), is described by Sandage (1961) as the prototype of the pure SBb(s) system. It is classified as an SBT4 by de Vaucouleurs, de Vaucouleurs and Corwin (1976). The bar is very prominent, distinct and smooth in texture, with two straight dust lanes emerging at an angle from the nucleus and following the bar to its ends and turning sharply and following the inside of the spiral arms. The two arms start abruptly at the ends of the bar each forming almost complete ellipses with the nucleus and the other end of the bar being the approximate foci. They can be traced through almost  $340^\circ$ .

#### NGC 3359

This galaxy, Figure 1-1 (c), described by Sandage (1961) as being a broken ring galaxy, is classified an SBc(rs), and as an SBT5 by de Vaucouleurs, de Vaucouleurs and Corwin (1976). A fairly prominent two-armed pattern

emerges from a strong central bar. The arms are asymmetric, with the arm beginning at the southern end of the bar being far less structured than the other. This arm appears to break up into two or more segments whereas the other arm more closely follows a "grand design" spiral pattern. There is a high degree of resolution of both bar and arms into knots.

#### NGC 3992

Significant spiral structure (two bifurcated arms or possibly even a three-arm pattern) emerges from an incomplete ring surrounding the bar in NGC 3992 (Figure 1-1 (d)). De Vaucouleurs, de Vaucouleurs and Corwin (1976) classify this galaxy as an SBT4. Two absorption lanes are visible emerging from a bright, central nuclear region. The bar is smooth in texture but the arms can be resolved easily into knots.

This dissertation will describe in detail, the observations, reduction and analysis, and hydrodynamical modeling of NGC 1300. Data for NGC 1073, NGC 3359 (Ball, 1984, 1986) and NGC 3992 (Hunter et al., 1986) are published elsewhere and only the conclusions are utilized here. The neutral hydrogen data collection, reduction and analysis are described in Chapters 2 and 3. Surface photometry in the blue, near infrared and 2.2um passbands is discussed in Chapter 4, with the results from Chapters 3 and 4 being used

in the hydrodynamical modeling in Chapter 5. The observational and modeling results for NGC 1073, NGC 3359 and NGC 3992 are summarized in Chapter 6 and comparisons between these galaxies are made in Chapter 7. A summary of all the results is presented in Chapter 8.



## CHAPTER II RADIO OBSERVATIONS

### HI As A Kinematic Tracer

To successfully model and understand the dynamics of a barred spiral galaxy, some sort of tracer of the dynamics of the system is needed. Any tracer which is closely associated with the gas may be used. Several components are available for use as this tracer. Observations of the optical Hydrogen alpha line provide velocities for HII regions, which are associated with hot young stars which have recently formed from the gas. Observations of the other Population I component, molecular gas clouds, also could provide the kinematical information needed. However, both these measurements have serious drawbacks. The HII observations have high spatial resolution but generally very incomplete coverage. This is due to the clumpiness of these regions which means that only velocities near the hottest stars can be measured. Molecular hydrogen, which presumably makes up a significant portion of the molecular clouds, is difficult to detect. Carbon monoxide, CO, the second most abundant interstellar molecule, coexists with molecular hydrogen and can be used to map the molecular regions in galaxies and elucidate the varying rates of star formation (Black, 1985;

Dalgano, 1985). CO is usually far more concentrated in the inner disk (Morris and Rickard, 1982), although it does appear to follow the intensity distribution of the blue light (Young et al., 1984; Young, 1985). The CO transitions are fairly easy to excite and lie in the millimeter wavelength region.

A dominant component of the gas of the interstellar medium consists of neutral hydrogen, HI, in its ground state. It is well-distributed spatially and is relatively easy to detect. This gas has a spin temperature,  $T_S$ , of approximately 100K (Mihalas and Binney, 1981 p485). The ground state is split into two hyperfine levels separated by  $6 \times 10^{-6}$  eV. This energy difference is extremely small; it corresponds to a temperature  $T=0.07$ K (through  $E=kT$ ), well below the ambient temperature of the surrounding medium, and, consequently, much of the gas is in the upper level. The upper level, or ortho-state, has the dipole moments of the electron and nucleus parallel and the lower level, the para-state, has the dipole moments anti-parallel. The probability of the forbidden ortho-para radiative transition, the  $F=1$  to  $F=0$  spin-flip transition, is so low that the mean lifetime of the excited level is  $1.1 \times 10^7$  yrs. In contrast, the collisional de-excitation timescale is much shorter, 400 yrs at  $N = 20 \text{ atoms/cm}^3$ , than the radiative de-excitation timescale, even in the low densities typical of the interstellar medium. This implies that collisions can

establish equilibrium populations in the two levels, which means that there will be nearly three atoms in the upper level (which is threefold degenerate) to every one in the lower level.

Because the collisional excitation and de-excitation rates are so much faster than the rate of radiative decay, the atomic populations  $n_1$  and  $n_2$  in the two levels will be essentially the same as those expected in thermodynamic equilibrium. Thus,

$$n_2/n_1 = (g_2/g_1) \exp (-h\nu/kT_S) \quad (2-1)$$

where  $g_2/g_1=3$  is the ratio of the degeneracies of the two levels. In a typical cloud  $T_S=100\text{K}$ , so  $(h\nu/kT_S)=6.8\times 10^{-4}$  and  $\exp (-h\nu/kT_S)=0.9993$ , giving,

$$n_2/n_1 \approx g_2/g_1 = 3. \quad (2-2)$$

In terms of probability coefficients,

$$n_1 C_{12} = n_2 (C_{21} + A_{21}) = n_2 C_{21} (1 + A_{21}/C_{21}) \quad (2-3)$$

where  $C_{12}$  and  $C_{21}$  are collisional probabilities and  $A_{21}$  is the Einstein probability coefficient for spontaneous radiative decay from level 2 to level 1. As  $A_{21}$  is small,

$$n_1 C_{12} \approx n_2 C_{21} \quad (2-4)$$

and approximate equilibrium is established. Although  $A_{21}$  is small  $\sim 2.868 \times 10^{-15} \text{ sec}^{-1}$ , radiative decay is the observable transition mechanism. The large column densities along a typical line-of-sight in a galaxy make this radiative

transition detectable. This transition is observable at a frequency of 1420.40575MHz ( $\lambda_0=21.105\text{cm}$ ). Its observation was predicted by van de Hulst (1945) and first measured by Ewen and Purcell (1951). Muller and Oort (1951) and Christiansen and Hindman (1952) confirmed the measurement.

Neutral hydrogen generally covers a region larger than the observed optical object and thus provides good coverage of the whole disk of the galaxy and not just selected regions, as do Hydrogen alpha observations. If the outermost regions are excluded, then HI is among the flattest and thinnest of the disk components of ours and other galaxies (Jackson and Kellerman, 1974). This allows the determination, with a resonable degree of confidence, of the two-dimensional location of any observed emission. This gas is pervasive enough that the emission recorded by radio telescopes appears to be continuously distributed.

If the neutral hydrogen gas is assumed to be optically thin, a simple integration of the brightness temperature,  $T_B$ , over velocity,  $V$ , determines the column density,  $N_h$ , of the gas at that point (Mihalas and Binney, 1981 p489):

$$N_h(x,y) = 1.8226 \times 10^{18} \int_{-\infty}^{\infty} T_B(x,y) dv, \quad (2-5)$$

where  $V$  is in km/s,  $T_B$  is in Kelvin, and,  $N_h$  in atoms/cm<sup>2</sup>.

The mean temperature-weighted velocity at a point is given by the first moment with respect to velocity,

$$\langle V(x,y) \rangle = \frac{\int_{-\infty}^{\infty} T_B(x,y) V(x,y) dV}{\int_{-\infty}^{\infty} T_B(x,y) dV} . \quad (2-6)$$

If the neutral hydrogen gas is not optically thin this will lead to an underestimate of the surface density. In this case the observed brightness temperature,  $T_B$ , would approach the physical, spin temperature of the gas,  $T_S$ .

In general,

$$T_B = T_S (1 - e^{-\tau}) , \quad (2-7)$$

and, for an optically thin gas,  $\tau \ll 1$ ,  $T_B \approx T_S$ , while for an optically thick gas,  $T_B = T_S$  (Mihalas and Binney, 1981 p487).

The highest observed brightness temperature for NGC 1300, averaged over the beam, was 16.95K. Assuming a mean temperature for the gas of 100K (McKee and Ostriker, 1977; Spitzer, 1978) gives an approximate optical depth of  $\tau=0.19$ , thereby justifying the optically thin assumption. Although this leads to an underestimate of the column density the effect is <15% at the peak emission and will be less at other points. As the "optical depth structure" of the medium is not known, the assumption of an optically thin medium will be retained.

Thus, in summary, neutral hydrogen provides a good tracer for the kinematics of the gas in a galaxy;

1. It is well distributed spatially.
2. It is relatively easy to observe.
3. Assuming it is optically thin, the above simple expressions hold for the column density of the gas and the mean velocity of the gas at an observed location, equations 2-5 and 2-6.

### Aperture Synthesis Theory

The neutral hydrogen content of NGC 1300 was observed using the Very Large Array (VLA) of the National Radio Astronomy Observatory (NRAO). The VLA is the largest and most sensitive radio telescope which exploits the principle of earth-rotation aperture synthesis. The array is a multiple-interferometer instrument using a maximum of 27 antennae. As the basic theory of interferometry and earth-rotation aperture synthesis is well covered in Fomalont and Wright (1974), Hjellming and Basart (1982), Thompson (1985), D'Addario (1985), Clark (1985) and, from an electrical engineer's perspective in Swenson and Mathur (1968), only a brief discussion will be given here and some fundamental results quoted.

The basic process of interferometry is the cross-correlation of signals from two antennae observing the same source. The resulting signal is analogous to the

interference pattern in the classical optical double slit experiment. The cross-correlation of these two signals produces information on both the intensities of sources in the beam of the antennae and on their positions relative to the pointing position of the antennae. Any distribution of radio emission in the beam of an antenna can be considered as a superposition of a large number of components of different sizes, locations and orientations. As the relationship between intensity distributions and the components can be described in terms of a Fourier integral, it follows that an interferometer pair, at any instant, measures a single Fourier component of the angular distribution of sources in the beam pattern. The essential goal in radio aperture synthesis observations is to measure a large number of these Fourier components. This procedure allows the reconstruction of an image of the spatial intensity distribution of sources in the beam. The VLA achieves the measurement of a large number of Fourier components by using multiple interferometer pairs and allowing their geometric relationships with the sources in the sky to change by utilizing the rotation of the earth, hence the term earth-rotation aperture synthesis. For multiple interferometer pairs,  $N$  antennae, there are  $N(N-1)/2$  different baselines, or samples of the Fourier components, at any one instant. The VLA has a maximum of 27 antennae or 351 samples of the Fourier components. These

samples are not all unique as there is redundancy in the baselines.

The output from a two element interferometer can be shown to be

$$V'(u,v) = \iint_{-\infty}^{\infty} I'(x,y) \exp[-i2\pi(ux+vy)] dx dy \quad (2-8)$$

where  $I'(x,y)$  is the observed brightness distribution,  $V'(u,v)$  is the observed complex visibility, and  $u,v$  are projected spacings in east and north directions respectively, sometimes called spatial frequencies (Hjellming and Basart, 1982).

This shows that a single measurement of the complex visibility,  $V'$ , corresponding to a particular projected baseline, or particular  $(u,v)$  point, gives a single Fourier component of  $I'$ , the observed brightness distribution. The similarity theorem of Fourier transforms (Bracewell, 1965) shows that large extent in the  $(x,y)$  plane means small extent in the  $(u,v)$  plane and vice versa. Thus, achievement of high spatial resolution requires large spacings between the antennae in an interferometer pair, and conversely, large scale structure requires low spatial frequencies, short spacings.

Equation 2-8 can be inverted to give the observed brightness distribution  $I'$  as a function of the measured complex visibilities,  $V'$ ,



$$I'(x,y) = \iint V'(u,v) \exp[i2\pi(ux+vy)] du dv \quad (2-9)$$

where  $I'$  is the product of the true brightness distribution  $I_O$  and the single antenna power pattern  $A$ ,

$$I'(x,y) = A(x,y) I_O(x,y) \quad (2-10)$$

These results have been calculated in the absence of noise. Since all observations measure only a finite number of  $(u,v)$  points and all contain noise,  $I'$  cannot be determined uniquely or without error. A later section deals with the problem of missing complex visibilities and the non-uniqueness of the solution of equation 2-9.

The extension of these results to spectral line observations introduces several complications. The signal has to be divided into a number of independent, narrow-band spectral channels. At the VLA this is achieved by introducing an additional delay,  $t_j$ , into the signal path. This delay destroys the coherence of the received signals except for those in a narrow frequency range centered on some frequency  $\nu_j$ . Changing this delay changes the frequency  $\nu_j$  and allows the signal to be divided into a number of independent, narrow-band channels. The integration of equation 2-8 over bandwidth gives

$$V'(u,v,t) = \iiint I'(x,y) F(\nu) \exp[-i(\nu t_j + 2\pi(ux+vy))] dx dy dt \quad (2-11)$$

where  $F(v)$  is the frequency bandpass function.

Due to the symmetry of the delays introduced, only the real part needs to be Fourier transformed, giving (Hjellming and Basart, 1982)

$$\int_{-\infty}^{\infty} \text{Re}[V'(u,v,t)] \exp(i2\pi vt) dt = \int_{-\infty}^{\infty} \int_{-\infty}^{\infty} I'(x,y) F(v) \exp[i2\pi v(ux+vy)] dx dy. \quad (2-12)$$

This is the Fourier transform at one of the frequencies and contains all the visibility information necessary to map the source at that frequency. Equivalently, as the number of delays  $t_j$  is finite, this procedure allows the mapping of the narrow-band channels. The right hand side of equation 2-11 contains the bandpass function,  $F(v)$ , which must be calibrated. This is done by observing a strong continuum source, which is assumed to exhibit no spectral variation over the quite narrow total bandpass normally used for spectral line work.

### Observing Strategy and Calibration

In an interferometer, such as the VLA, high resolution is achieved by using large separations of the antennae. Conversely, broad structure requires relatively small spacings; thus, both long and short spacings are required to

measure both the small scale and the extended structure in a galaxy. However, the higher the resolution, the poorer the brightness sensitivity. This conflict demands that a compromise be made between sensitivity and resolution.

The minimum detectable flux density,  $\Delta S_{\min}$ , depends only upon system temperature, bandwidth, integration time and effective collecting area, viz.,

$$\Delta S_{\min} \propto T_{\text{SYS}} / A_e \sqrt{\Delta \nu t} \quad (2-13)$$

where  $T_{\text{SYS}}$  is the system temperature in Kelvin,  $A_e$  is the effective collecting area,  $\Delta \nu$  is the bandwidth in Hz, and,  $t$  is the integration time in hours.

The effective collecting area  $A_e = \eta A_T$ , where  $A_T$  is the total area and  $\eta$  is the aperture efficiency.

However, for resolved sources the detectable brightness temperature is the important quantity, and

$$\Delta T_B = \Delta S_{\min} / \Omega_{\text{BEAM}} \quad (2-14)$$

where  $\Omega_{\text{BEAM}}$  is the synthesized beam solid angle.

The synthesized beam is the power pattern of the array as a whole, rather than the power pattern of an individual antenna. Thus, for a point source, the synthesized beam is the observed normalised brightness distribution. Consequently, as resolution is improved the brightness sensitivity is degraded, and vice versa.

If observing time were unlimited, the choice of arrays would be an easy undertaking. The resolution required would dictate the largest separation of the antennae, and the required signal-to-noise ratio would dictate the amount of integration time needed. However, as observing time is limited, in order to determine which array configurations were practical to use for this project required consideration of both the resolution needed to observe the structure and the sensitivity needed to ensure that the majority of the gas was observed. Another factor which had to be considered was that, as the VLA was used as a spectrometer, the sensitivity in each narrow line channel is relatively poor. With these considerations in mind, it soon became evident that the two lowest resolution configurations, the D and C arrays, would be the only two practical configurations to use for a reasonable amount of observing time. The D array would ensure that no low amplitude large scale structure emission was missed, whereas the C array would resolve the smaller scale structure. Using only these two arrays means that some small scale structure below the resolution limit of the C array will be missed, but will ensure that the majority of the emission was observed. As the best peak signal-to-noise ratio observed in any of the channels was 13.4 this would mean that the best detection achievable with the next largest array, the B array, would be, for the same amount of observing time, a less than "two sigma" detection.

In spectral line observations the correlator must multiply the signals from  $2n$  delay lines for each of  $N(N-1)/2$  baselines, where  $n$  is the number of spectral channels and  $N$  is the number of antennae used. The correlator thus has an upper limit for the product  $nN$  which necessitates a compromise when choosing  $n$  and  $N$ . The larger the value of  $n$ , the greater the spectral, and hence velocity, resolution but the poorer the sensitivity. The larger  $N$  is, the better the sensitivity as more antennae contribute to the signal. Ideally the largest values possible for  $n$  and  $N$  are required. However, as  $n$  has to be an integer power of two to allow the Fourier transform of the lag spectrum to be calculated using Fast Fourier Transform techniques (FFT), this also places some restrictions on  $n$ .

The choice of  $n$  depends upon the velocity range of the global profile of the galaxy under study and the velocity resolution desired. Also, a few "line-free" channels on each end of the spectrum are desirable to allow the continuum emission to be mapped. Previous studies and single dish results (Bottinelli et al., 1970) indicate that the global profile for NGC 1300 has a velocity width (full width at a level of 25% of the peak level) of 290km/sec. These observations, coupled with the other considerations above, lead to a choice of  $n=32$  with a single channel separation of 20.63km/sec, 97.656kHz. This choice of  $n$  allowed a maximum

of 25 antennae to be used. The discarded antennae were chosen simply on the basis of their recent malfunction performance.

During the observing run the central channel, channel 16, was centered on 1540km/sec, a value equal to the approximate mean of other previous determinations of the systemic velocity; Sandage and Tammann (1975) find  $1535 \pm 9$  km/sec; de Vaucouleurs, de Vaucouleurs and Corwin (1976) find  $1502 \pm 10$  km/sec; and Botinelli et al. (1970) find  $1573 \pm 7$  km/sec. Channel 32 was chosen as the central channel in order to avoid using the end channels in the 64 channel spectrometer. Due to Gibbs phenomenon (oscillations in the bandpass function at the edges of the bandpass) a few channels at either end of the spectrometer are severely degraded, and it was considered prudent to avoid these channels. The mean velocity is a heliocentric velocity calculated using the definition

$$v = c \left( \frac{\Delta \lambda}{\lambda_0} \right) \quad (2-15)$$

Thirty-one of the channels are narrow line channels separated by 20.63km/sec, 97.656kHz, with a full width at half maximum (FWHM) of 25.2km/sec; the thirty-second is a pseudo-continuum channel with a total width of 1000km/sec, 4.7MHz. This channel, designated channel zero, contains the true continuum emission plus the line signal, utilizes ~75%

of the intermediate 6.25MHz broad band filter, and was used primarily to calibrate the line channels. As this is a broad band channel, the sensitivity to the calibration is much greater (~7x) than that for the line channels. Consequently, the calibration procedure was carried out using channel zero and then applied to the single line channels once a satisfactory solution was found. This procedure is summarized below.

The flux density for the primary calibrator, 3C48, is forced to assume some "known" value at the frequency of the observations (VLA calibration manual based on Baars et al., 1977). Using the flux densities of the secondary calibrators as free parameters, a solution for amplitude and phase for each antenna in the array is computed as a function of time. All the scans of the secondary calibrators are utilized for this solution. Baselines with closure errors greater than some specified limits in amplitude and phase (~10% in amplitude and  $10^\circ$  in phase) can then be identified and rejected. If the assumption is made that the complex gain for the antenna pair  $jk$ ,  $G_{jkp}(t)$ , can be represented by amplitudes  $g_{jp}(t)$  and  $g_{kp}(t)$  and phases  $\phi_{jp}(t)$  and  $\phi_{kp}(t)$  then,

$$G_{jkp}(t) = g_{jp}(t) \exp[i(\phi_{jp} + \phi_{kp})] g_{kp}(t) + \epsilon_{jkp} \quad (2-16)$$

where  $\epsilon_{jkp}$  are the closure errors. Thus, the smaller these closure errors the better the approximation becomes for the actual complex gain. For the mode of observing employed for

these observations, few baselines had closure errors as large as 10% and  $10^\circ$ , and most were below the 7% and  $5^\circ$  range. After rejecting the baselines with unacceptable closure errors, the antenna solution is repeated. This iterative procedure is continued until acceptable solutions have been found for the complex gains.

This procedure utilizes one antenna as a reference antenna for the array. It is thus worthwhile repeating the calibration using a different reference antenna to improve the solution. The reference antenna should be particularly stable compared with the rest of the array and should have variations which are as slow as possible and not be monotonic functions of either space or time. A good stable antenna usually can be found by repeating the calibration procedure for a few different antennae.

Once acceptable solutions for the complex gains have been found using the primary calibration source, fluxes for the secondary calibrators can be determined. These fluxes are generally called "bootstrapped" fluxes and their errors give a good indication of the stability of the atmosphere during the observing run.

The bootstrapped fluxes can be applied to the entire dataset, including the program object observations, by a simple running mean, or "boxcar" interpolation of the amplitude and phase gains of the individual antennae. At every step of the process the database is inspected and



suspect signal data are flagged, hopefully leading to a better solution from the next iteration and not seriously degrading the overall quality of the dataset. The quality of the dataset is usually not degraded very much as there is a large duplication of baselines and rejecting a few data points does not have a large overall effect on the database. The final step in the calibration procedure is to calibrate the bandpass by assuming a flat spectrum for the primary calibrator over the total spectral-line bandwidth. The purpose of the bandpass calibration is to correct for the complex gain variations across the spectral channels. The bandpass usually varies only slowly with time and usually has to be measured only once during an observing run. The data are now ready for Fourier inversion and image processing.

Generally, the data for this project were unaffected by any serious problems, and few baselines or scans had to be flagged in the calibration procedures. However, the data from Summer 1984, for the second half of the observing run, exhibited some anomalous records at the beginning of each scan. The source of these anomalous records was not discovered and the records were simply deleted from the dataset. This improved the antenna solution noticeably and allowed an acceptable solution to be calculated quickly. Another problem with the more compact arrays when observing a source with a low southerly declination, such as NGC 1300

( $\delta = -19^{\circ}35'$ ) is "shadowing." This occurs when the projected separation of two antennae is smaller than the physical diameter of the antennae, 25m. This means that one antenna is partially blocking the other's view of the source. A correction for this effect can be applied, or the offending antenna can simply be removed from the database for the appropriate timerange. This "shadowing" also causes a more subtle problem for the calibration procedure. When one antenna is "shadowing" another, even slightly, the data collected during that time range by the "shadowed" antenna has a noticeable deterioration in quality. This "crosstalk" arises when the shadowed antenna detects signals from the electronics of its neighbour. As this effect can be difficult to detect, the safest method to avoid "crosstalk" is to flag all data from "shadowed" antennae. For NGC 1300 this amounted to approximately 2% of the data, the majority being at the beginning and the end of the run, at large hour angles, or low elevation angles. The amount of data flagged did not degrade seriously the overall quality of the database and allowed a good antenna solution to be calculated. Apart from these two problems, which were easily corrected, NGC 1300 showed no unpleasant surprises and a good solution was arrived at in a few iterations of the calibration procedure.

The galaxy NGC 1300 was observed using the D/C hybrid configuration on the 9th and 12th July 1984. A total of 25

antennae, evenly distributed over the three arms, was used. The north arm was in the C array configuration and the southwest and southeast arms were in the more compact D array configuration. This hybrid configuration allowed a nearly circular beam to be synthesized and gave a maximum unprojected separation of 2106.6m ( $9982\lambda$ ) and a minimum unprojected separation of 44.6m ( $213\lambda$ ). Seven hours of observing time were used on the 9th of July, 1984 and seven hours on the 12th of July, 1984.

Calibration sources were observed at the beginning of the session, every 40 minutes during the run, and again at the end of the session. More frequent observations of the calibrators were not deemed necessary as the timescale for phase stability of the atmosphere at 21cm (1420MHz) is considered to be a good deal longer than the intervals chosen here. The bandpass calibrator source, 3C48, was observed three times during the session: at the beginning, in the middle, and at the end. This also provided a check on the overall stability of the system as it allowed a comparison of the phase and amplitude response over the whole session.

The primary calibrator, 3C48, was used to calibrate the receiver bandpass and the flux densities of the secondary calibrators. Two secondary calibrators, 0237-233 and 0420-014, were needed for NGC 1300 due to the relative positions of available calibrators and the galaxy itself.

0237-233 was used for the first 4 hours of the observing run and 0420-014 for the remaining 3 hours of the run. The transition from one secondary calibrator to the other was accomplished by using the primary calibrator as an intermediate step between the two.

The 1985 observations employed 25 antennae in the C/B hybrid configuration. The north arm was once again in the higher resolution configuration and the antennae were evenly distributed over the three arms. The configuration gave a maximum unprojected separation of 6920m ( $32953\lambda$ ) and a minimum unprojected separation of 78m ( $372\lambda$ ). A total of 6 hours of observing were obtained using this hybrid array on the 28th of June, 1985 and 7.5 hours on the 1st of July, 1985. The phase and amplitude calibration of the data were done by using the same sources as for the D/C hybrid array; the observing strategy was the same for both seasons. The flux densities of these sources and the receiver bandpass were once again calibrated using 3C48. Table 2-1 lists calibrator positions and fluxes.

### Map-Making and Image Processing

The fundamental result of the aperture synthesis description is the existence of a Fourier transform relationship between the modified sky brightness and the visibility observed with an interferometer,

$$I'(x,y) = \iint_{-\infty}^{\infty} V'(u,v) \exp[i2\pi(ux+vy)] du dv \quad (2-17)$$

TABLE 2.1  
Properties of Survey Calibrators

Calibrator (1)	P/S (2)	Frequency (3)	Epoch (4)	Array (5)	Flux Density (6)
3C48	P	1413.251	Jul 84	C/D	15.82
	P	1413.240	Jun 85	B/C	15.82
0237-233	S	1413.251	Jul 84	C/D	6.25
	S	1413.240	Jun 85	B/C	6.12
0420-014	S	1413.251	Jul 84	C/D	2.03
	S	1413.240	Jun 85	B/C	2.22
3C48	01	34 49.8	(1950)		
	32	54 20.5			
0237-233	02	37 52.7	(1950)		
	-23	22 06.4			
0420-014	04	20 43.5	(1950)		
	-01	27 28.6			

- 
- (1) Calibrator identification.  
 (2) Primary (P) or Secondary (S) calibrator.  
 (3) Frequency of observation (MHz).  
 (4) Epoch of observation.  
 (5) Array configuration employed for observations.  
 (6) Flux adopted for primary or determined for  
       secondary calibrators.

where  $I'$  is the product of the true brightness distribution,  $I_0$ , and the single dish power pattern,  $A$ , equation (2-10).

This result can be used to derive the source brightness distribution from the observed interferometer visibilities. These visibilities are observed at a number of discrete  $(u,v)$  points. With a small number of points, model-fitting of the points is feasible, but as a VLA spectral-line database typically consists of ~500,000 points the most practical way of constructing the brightness distribution is to use Fourier inversion techniques.

There are two common ways of evaluating the Fourier transform:

1. By direct evaluation of equation (2-17) at the individual sample points, Direct Fourier Transform, DFT.
2. By using a Fast Fourier algorithm, FFT.

The advantages of the DFT are that aliasing and convolution introduced by the gridding procedure for the FFT are avoided, but the disadvantage is that the number of multiplications for an  $N \times N$  grid of  $M$  data points  $\propto 2MN^2$ , which can be substantial for the large datasets usually considered in spectral line observations. The use of the FFT reduces the number of multiplications to  $N^2 \log N^2$ , which can save a considerable amount of computing time. However, for the FFT the data points must be on a rectangular grid,  $mxp$ ,

where  $m$  and  $p$  are integer powers of two. The use of FFT algorithms can lead to the introduction of aliasing in the maps. This aliasing results from the gridding process. The gridded visibilities may be represented as

$$V(u,v) = III(u,v) \cdot [C(u,v) * S(u,v) \cdot V'(u,v)] \quad (2-18)$$

where  $III$  is a two-dimensional Shah function,  $S$  is a sampling function, and  $C$  is a convolving function.

Due to the presence of the Shah function and the fact that the Fourier Transform of  $C$  is not exactly zero beyond the map limits, parts of the brightness distribution that lie outside the primary map field will be aliased into the primary field. The simplest way to tell if an image is aliased is to remap the field with a different cell size. The aliased source will appear to move while a primary source will stay the same angular distance from the field center.

The most common grid for the FFT is a square grid ( $m=p$ ) with the  $(u,v)$  spacings comparable with the cell size; as the observed data seldom lie on these grid points, some interpolation method must be used to specify the visibilities at the grid points. If a scheme which resembles a convolution in the  $(u,v)$  plane is used, then the image will have predictable distortions which can be corrected at later stages of the reduction procedure. A convolution also smoothes the data, providing a good estimate of the gridded visibility from noisy input data.

The best way to avoid, or at least reduce, aliasing problems is to use a convolving function,  $C$ , that results in a fast drop-off beyond the edge of the image. This requires that  $C$  be calculated over a large region in the  $(u,v)$  plane, requiring a large amount of computing time. Thus, in practice, a compromise between alias rejection and computing time must be reached. The function  $C$  should ideally be flat out to some distance and then drop off sharply without having sidelobes beyond the edges of the map. The lack of high sidelobes helps suppress the aliasing of sources lying outside the map into the map. Aliasing of sources that lie off the primary image back into the map is only part of the problem. A primary image source will have sidelobes extending beyond the edge of the image. These sidelobes will be aliased back in, effectively raising the background and resulting in a beam shape that is position invariant (Sramek, 1985). Thus, the convolving function suppresses aliasing due to replication of the image in the gridding process. It suppresses aliasing but not sidelobe or ringlobe responses from sources outside the area of the map. With alias suppression of  $10^2$  or  $10^3$  at two or three map radii, it is these sidelobe responses which may cause the dominant spurious map features. As  $C$  is usually separable

$$C(u,v) = C'(u) C'(v) \quad (2-19)$$

where



$$C'(x) = |1 - \eta^2(x)|^{\alpha} \psi_{\alpha,0}(C, \eta(x)),$$

$$\eta(x) = x/m\Delta x$$

and

$$\psi_{\alpha,0}(C, \eta) = (1 - \eta^2)^{-\alpha/2} S_{\alpha,\alpha}(C, \eta). \quad (2-20)$$

The function  $S_{\alpha,\alpha}(C, \eta)$  is a prolate spheroidal wave function (Schwab, 1980). At the VLA the parameters used are generally  $m=6$ ,  $\alpha=1$ ,  $n=0$ . Figure 2-1 shows the form of this function.

It is desirable not to have the product  $N\Delta u$  so large that the outer cells are all empty and the inner ones heavily undersampled, nor so small that many points at large spacings are rejected. For the VLA spectral-line observing mode an empirical relationship which produces good sampling is that the synthesized beam be about three to four times the cell size of the intensity images,  $\Delta\theta$ .

Once the data have been convolved, the map must be sampled to produce the gridded values. The sampling function is a two dimensional Shah function (Bracewell, 1965),

$$III(u,v) = \Delta u \Delta v \sum_{-\infty}^{\infty} \sum_{-\infty}^{\infty} \delta[(u-j\Delta u), (v-k\Delta v)] \quad (2-21)$$

where  $\Delta u, \Delta v$  are the separations between grid points.

Unfortunately, the sampling in baseline space by a rotation synthesis array, such as the VLA, is non-uniform. The projections  $(u,v)$  of sample points, with respect to a reference direction, are therefore non-uniformly distributed

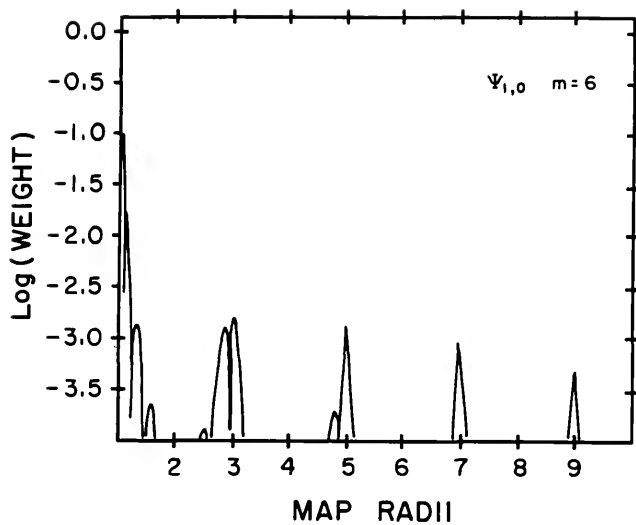


Figure 2-1. Spheroidal Convolving Function. Side-lobe responses for the gridding function used in this study.

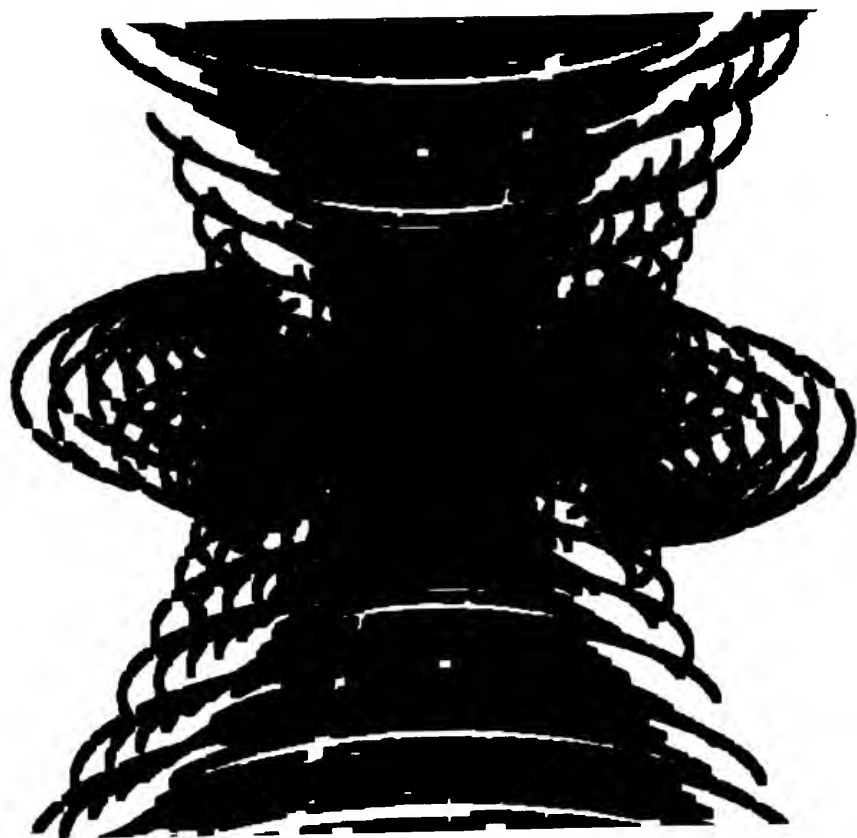
with varying density inside an irregular boundary, all of which depend upon the source declination, see Figure 2-2 for (u,v) coverage. Therefore some sort of weighting function, W, is necessary to correct for this effect and to control the synthesized beam shape. The sampling function can then be written

$$III(u,v) = \Delta u \Delta v \sum_{-\infty}^{\infty} \sum_{-\infty}^{\infty} W \delta[(u-j\Delta u), (v-k\Delta v)]. \quad (2-22)$$

The weighting function is usually expressed as the product  $W=dt$  where  $d$  corrects for the varying number of observed samples in each gridded cell, and  $t$  introduces a taper to reduce the sidelobes. The beam usually consists of a Gaussian core with broad sidelobes at a one to ten percent level. The shape of the sidelobes is simply the Fourier transform of the unsampled spacings in the (u,v) plane out to infinity. The taper,  $t$ , weights down the sparsely-sampled outer region of the (u,v) plane and helps suppress the small scale sidelobes at the expense of a broader beam. The tapering function is usually a truncated Gaussian function (Sramek, 1985).

The other weighting function,  $d$ , is generally chosen from one of two extremes, natural or uniform weighting. Natural weighting weights all observed samples equally:  $d=1$ . Thus, the weight of each gridded visibility is proportional to the number of observed visibilities contributing to that sample. Since the density of observed samples is always

Figure 2-2. (u,v) Coverage. Schematic representation of the (u,v) coverage obtained by the observations of NGC 1300.



higher for the shorter baselines, this tends to produce a beam with a broad low-level plateau (Sramek, 1982). However, this type of weighting gives the best signal-to-noise ratio for detecting weak emission. Natural weighting is undesirable for imaging sources with both large and small scale structure, such as extended emission from galaxies. Although the sensitivity is increased, the broad beam degrades the resolution and the small scale structure will become dependent on the beam shape. To remove the broad plateau each gridded cell is weighted by the inverse of the number of observed visibilities contributing to that cell:  $d=1/N$ . This weighting is called uniform weighting and, since not all visibilities are equally weighted, there will be a degradation in signal-to-noise ratio. Uniform weighting gives the same weight to each cell in the gridded (u,v) plane and the beam characteristics are controlled largely by the tapering,  $t$  (Sramek, 1985).

In principle the procedure for producing the gridded visibilities for the application of the FFT is

1. Convolve the observed visibility data points to produce a continuous function.
2. Resample this continuous function at the grid points.
3. Apply the weighting and taper to the resampled data.

These gridded visibilities can now be Fourier inverted, using equation 2-17, to produce an estimate of the source brightness distribution. For NGC 1300 the Fourier inversion

was performed using a 6" cell size with a  $7k\lambda$  taper (1484m) and uniform weighting producing 32 single channel "dirty maps" and their associated "dirty beams." These dirty maps are given by the true brightness distribution convolved with the dirty beam.

Direct Fourier inversion of the observed visibilities, with all unsampled visibilities set to zero, gives the principal solution, or dirty image. Thus, the quality of the image depends entirely upon the sampling in baseline space. In general this sampling is non-uniform. It is obvious that the true image cannot be as complex as this dirty image, where the visibility vanishes at all positions not sampled by the observation. There must be image components invisible to the instrument with non-zero visibilities at the unsampled positions. The unsampled points in the  $(u,v)$  plane give rise to the sidelobes of the dirty beam and reflect an unavoidable confusion over the true brightness distribution. Some estimate of these unsampled or invisible image components is necessary to augment the principal solution in order to obtain an astronomically plausible image. The scheme most widely used is the CLEAN algorithm introduced by Hogbom (1974). CLEAN performs a function resembling interpolation in the  $(u,v)$  plane.

The CLEAN algorithm uses the knowledge that radio sources can be considered as the sum of a number of point sources in an otherwise empty field of view. A simple

iterative procedure is employed to find the positions and strengths of these point sources. The final image, or "clean" image, is the sum of these point components convolved with a "clean" beam, usually a Gaussian, to de-emphasize the higher spatial frequencies which are usually spuriously extrapolated.

The original Hogbom algorithm proceeds as follows:

1. Find the strength,  $M$ , and position of the point brightest in absolute strength in the dirty image.
2. Convolve the dirty beam with a point source, at this location, of amplitude  $\gamma M$ , where  $\gamma$  is the loop gain, and  $\gamma < 1$ .
3. Subtract the result of this convolution from the dirty map.
4. Repeat until the residual is below some predetermined level.
5. Convolve the point sources with an idealized clean beam, usually an elliptical Gaussian fitted to the core of the dirty beam.
6. Add the residuals of the dirty image to the clean image. Keeping the residuals avoids having an amplitude cut-off in the structure corresponding to the lowest subtracted component and also it provides an indication of the level of uncertainty in the brightness values.



Since the basis of this method is to interpolate unobserved visibilities, the final image is the consequence of preconceived astrophysical plausibility. Interpretation of fine detail in clean maps should recognise this non-uniqueness of the solution.

Clark (1980) developed a variant of the Hogbom algorithm. The basic idea is to separate the operation of peak locating from that of convolution-subtract and perform the convolution-subtract step on a large number of point sources simultaneously. The algorithm has a minor cycle in approximate point source location using a truncated beam patch, which includes the highest exterior sidelobe, and a major cycle in proper subtraction of a set of point sources (Clark, 1985; Cornwell, 1985).

It should be clear that CLEAN provides some sort of estimate for unsampled  $(u,v)$  points. In most cases it does this reasonably well. However, quite often it underestimates the "zero-spacing" flux, the integral of the flux over the clean image. This results in the source appearing to rest in a "bowl" of negative surface brightness. Providing an estimate of this flux (from single dish measurements for example) can sometimes help (Cornwell, 1985).

In using CLEAN a decision has to be made concerning various parameters:

1. Is the addition of the zero-spacing flux necessary?

2. Over what region of the image should the CLEAN be done?
3. How deep should the CLEANing go, i.e. at what level should the cutoff be?

The solution to these questions for NGC 1300 was arrived at by considering the following:

1. The galaxy was observed using the D array. This array contains short spacings and thus, the unsampled region in the (u,v) plane is small. Owing to this, no zero-spacing flux was added. The decision was justified as no evidence for a negative brightness bowl was seen, meaning that CLEAN had provided a good estimate for this flux. The total flux measured at the VLA was 36.53Jy(km/sec) compared with 30.3Jy(km/sec) found by Reif et al. (1982).
2. All the line channels were examined and limits set on the spatial extent of the signal in each channel. This allowed only regions containing signal to be used in CLEANing, thus avoiding the time-consuming CLEANing of regions containing only random noise.
3. When CLEAN is applied to maps correctly the resultant "blank" sky should show only random noise and no sidelobe structure. The rms noise level should be approximately the same from channel to channel and should also be approximately equal to the expected rms noise level for spectral-line maps with natural weighting (Rots, 1982);

$$\sigma = \alpha [N(N-1) T_i \Delta \nu]^{-1/2} \quad (2-23)$$

where  $N$  is the number of antennae used,  $\alpha$  is a constant,  $\alpha=620$  for 21cm,  $T_i$  is the total on-source integration time in hours, and  $\Delta \nu$  is the bandwidth in kHz.

For NGC 1300 using 25 antennae,  $N=25$ ,  $T_i=20.58\text{hr}$ ,  $\Delta \nu=97.656\text{kHz}$  gave an expected rms noise level of 0.6mJy/beam. The rms noise level for the dirty maps is ~0.8mJy/beam and for the clean maps ~0.7mJy/beam and thus indicates that the CLEAN was acceptable. Table 2-2 shows the rms noise level for the dirty maps and the rms noise level for the clean maps. Once the expected rms value has been reached the CLEANing is stopped; proceeding beyond this point is tantamount to shuffling the noise around. For NGC 1300 this limit was generally reached after 1000 iterations, as the loop gain was small,  $\gamma=0.15$ .

Before the spectral-line channels are CLEANed some method of subtracting the continuum emission must be utilized. Continuum emission usually consists of unresolved point sources as well as some emission from the central region of the nucleus. The method used for NGC 1300 was to average a few "line-free" channels from both ends of the line spectrum producing a continuum emission map. This continuum map was then subtracted from the dirty spectral-line channel maps, producing a set of 18 dirty, continuum-free, spectral-line maps. It is important to note that, due

TABLE 2.2

## Image Signal and Noise Characteristics

Image	Velocity (km/sec)	rms Noise Dirty Map (mJ/beam)	rms Noise Clean Map (mJ/beam)	rms Noise Clean Map (K)	Peak Brightness Clean Map (K)
6	1746.10	0.84	0.82	1.28	5.40
7	1725.49	0.75	0.73	1.14	7.44
8	1704.88	0.86	0.83	1.30	16.95
9	1684.27	0.81	0.78	1.22	14.93
10	1663.66	0.84	0.81	1.27	12.59
11	1643.05	0.79	0.75	1.17	13.60
12	1622.44	0.83	0.83	1.30	9.72
13	1601.83	0.82	0.79	1.24	11.21
14	1581.22	0.91	0.91	1.42	9.52
15	1560.61	0.85	0.85	1.33	9.18
16	1540.00	0.84	0.83	1.30	8.87
17	1519.39	0.83	0.83	1.30	9.11
18	1498.78	0.78	0.77	1.20	11.08
19	1478.17	0.83	0.80	1.25	12.73
20	1457.56	0.83	0.80	1.25	15.82
21	1436.95	0.78	0.78	1.22	10.17
22	1416.34	0.80	0.78	1.22	5.51
23	1395.73	0.82	0.81	1.27	5.32
Continuum		0.30	0.27	0.43	12.63
Channel 0		0.18	0.17	0.19	-
Large Field		0.77	-	-	-

to the non-linearities of the CLEAN algorithm, this continuum subtraction must be performed before the maps are CLEANed. Subtracting CLEAN maps can introduce noise at the positions of continuum sources (van Gorkom, 1982). Table 2-2 has the noise levels for these continuum free line channels. The dirty, continuum-free line channels and the continuum map are now ready for the CLEANing procedure.

Figure 2-3 (a-s) shows the final CLEANed spectral line channels and the continuum map. The effective resolution is  $20.05'' \times 19.53''$  (FWHM). The beam is indicated on the continuum map, Figure 2-3 (s). As the astronomical significance of these observations will be considered in a later section, the CLEANed line channel maps are just presented here. The emission from the galaxy appears to be clumpy and is not very widespread. This hints at the structure found in the integrated density map, well-defined arms with an extremely low level disk component. The rms noise levels for the these maps can be converted from mJy/beam to brightness temperature using

$$\Delta T_B = \frac{\Delta S \times 10^{-26} c^2}{\nu^2 2k\Omega}$$

where  $\Delta T_B$  is in Kelvin,  $\Delta S$  is the rms noise level in mJy/beam,  $c$  is the speed of light,  $\nu$  is the frequency of observation in MHz,  $k$  is the Boltzman constant, and  $\Omega$  is the beam solid angle in radians.

Figure 2-3. Spectral Line Channel Maps. CLEAN, continuum-free spectral line channels for NGC 1300. The + mark the positions of fiducial stars and x the center of the galaxy. The velocity is indicated in the top right corner. All maps are plotted in intervals of twice the rms noise level.

A-R. Spectral line channels 6 through 23.

S. CLEAN continuum map showing the center of the galaxy (x), fiducial stars (+), H II regions (\*) and the beamsize.

## NGC 1300

NGC1300

1746.

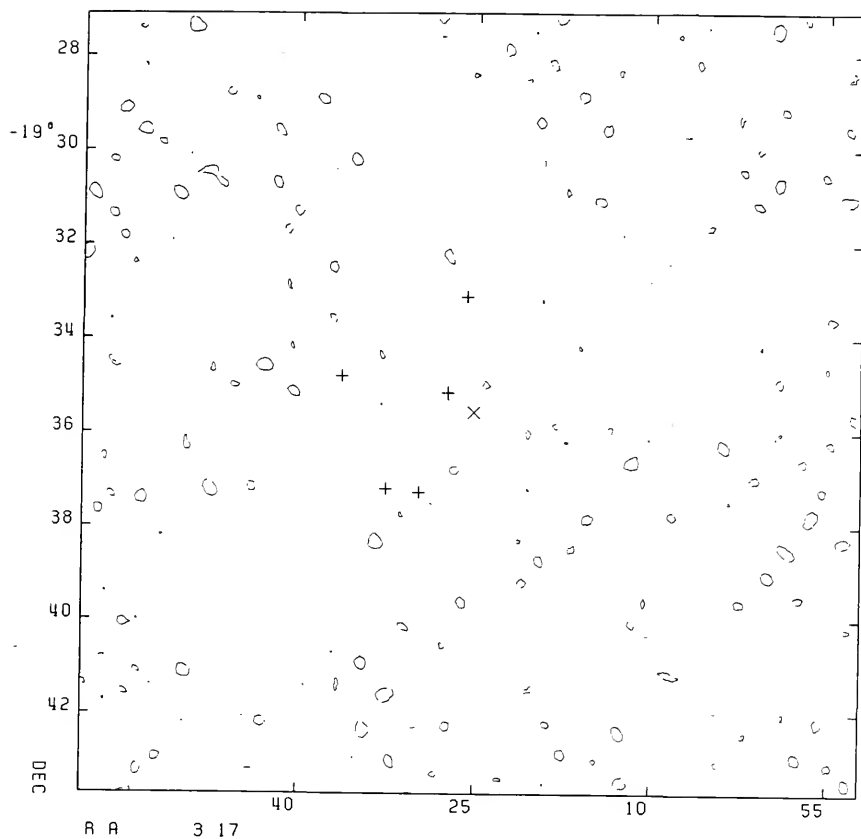


Figure 2-3 cont. (Part A).

## NGC 1300

NGC1300

1725.

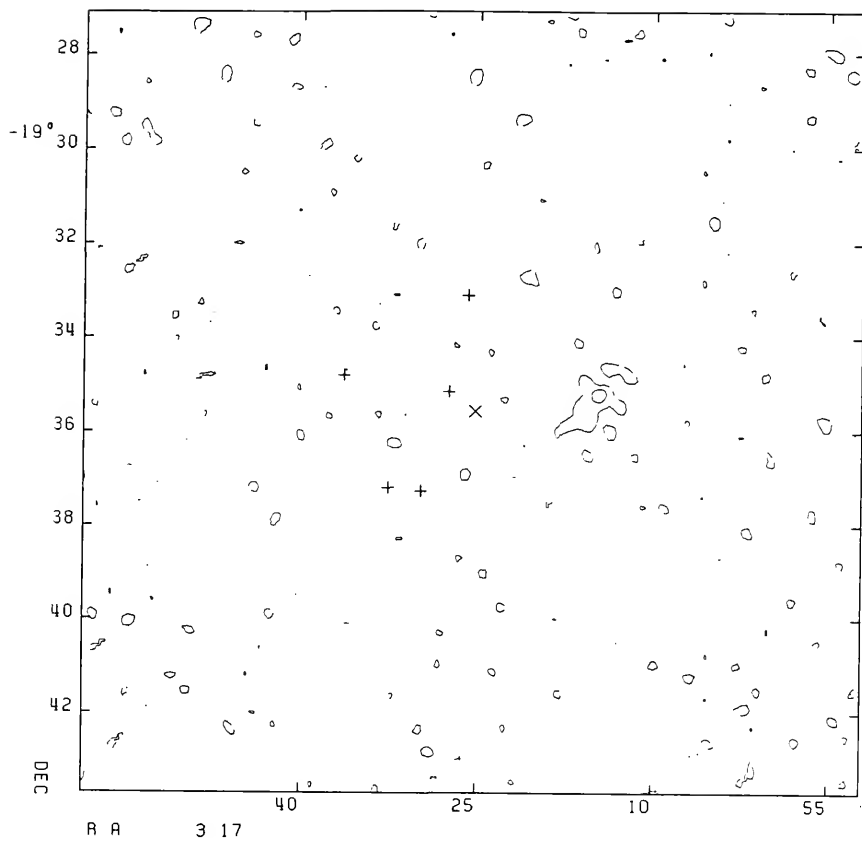


Figure 2-3 cont. (Part B).



## NGC 1300

NGC1300

1705.

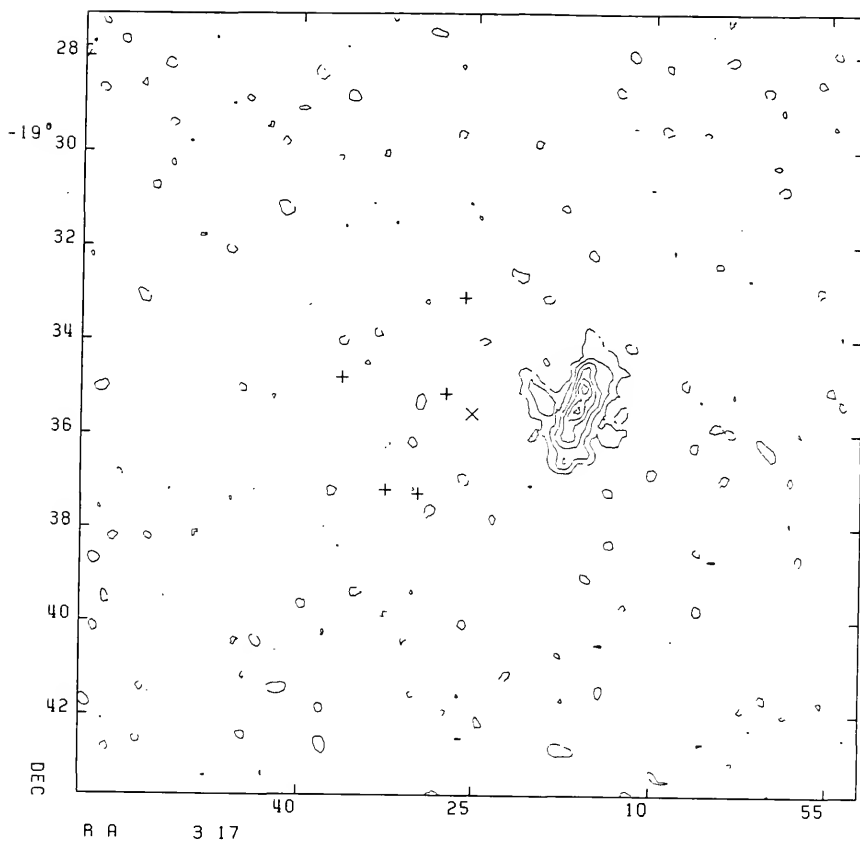


Figure 2-3 cont. (Part C).

## NGC 1300

NGC1300

1684.

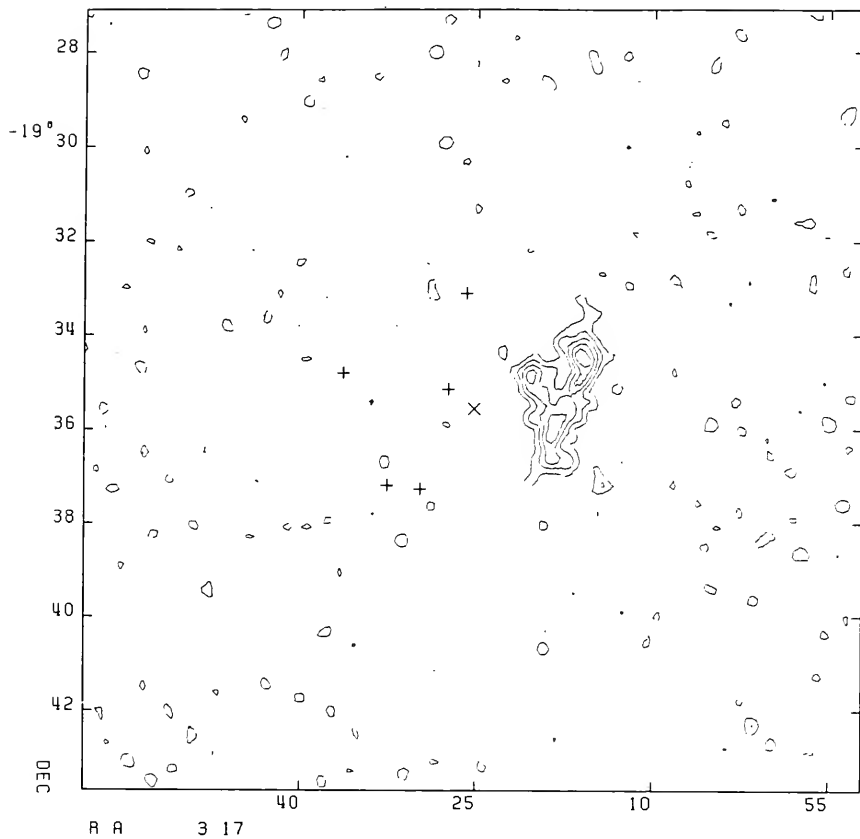


Figure 2-3 cont. (Part D).

## NGC 1300

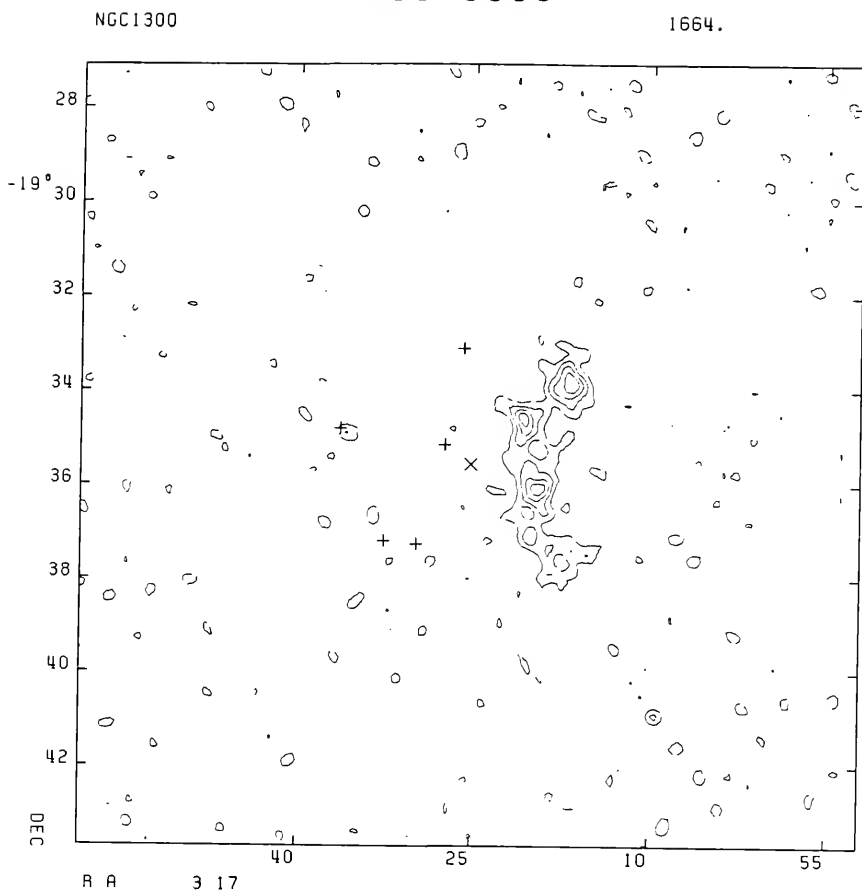


Figure 2-3 cont. (Part E).

## NGC 1300

NGC1300

1643.

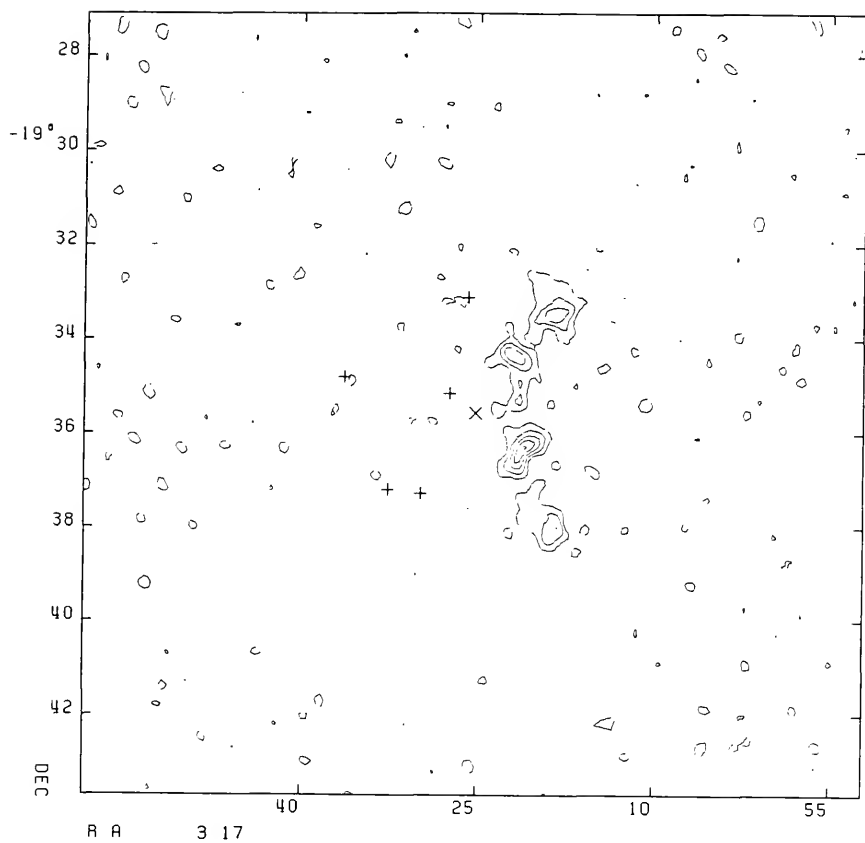


Figure 2-3 cont. (Part F).

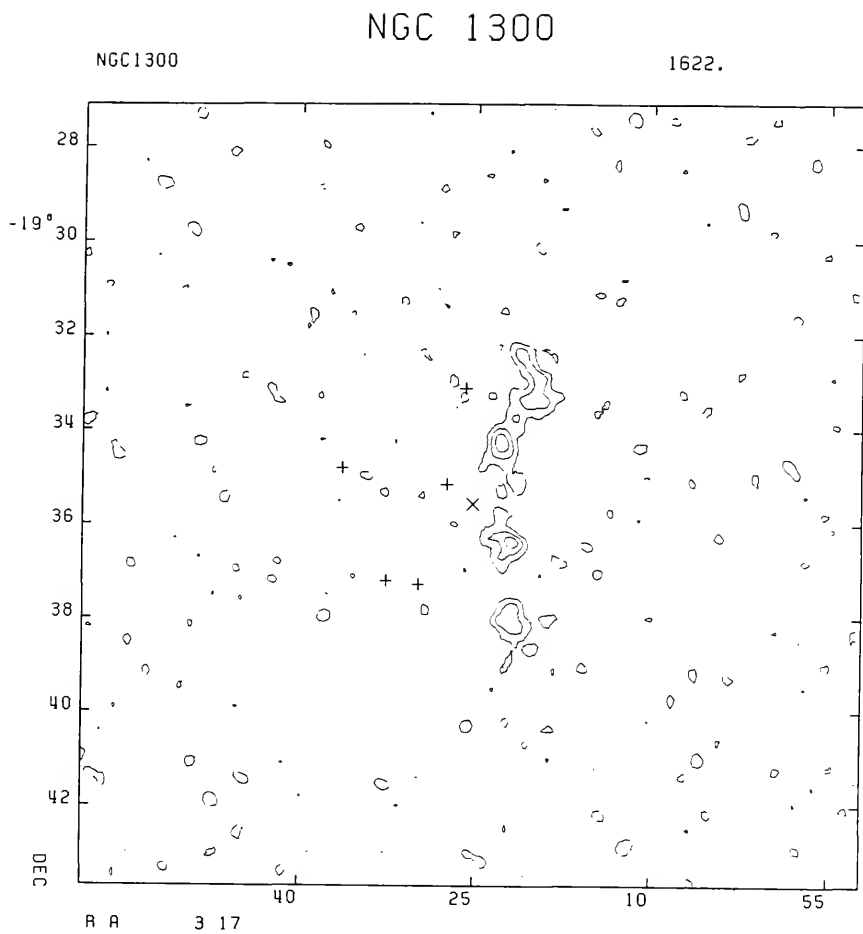


Figure 2-3 cont. (Part G).

## NGC 1300

NGC1300

1602.

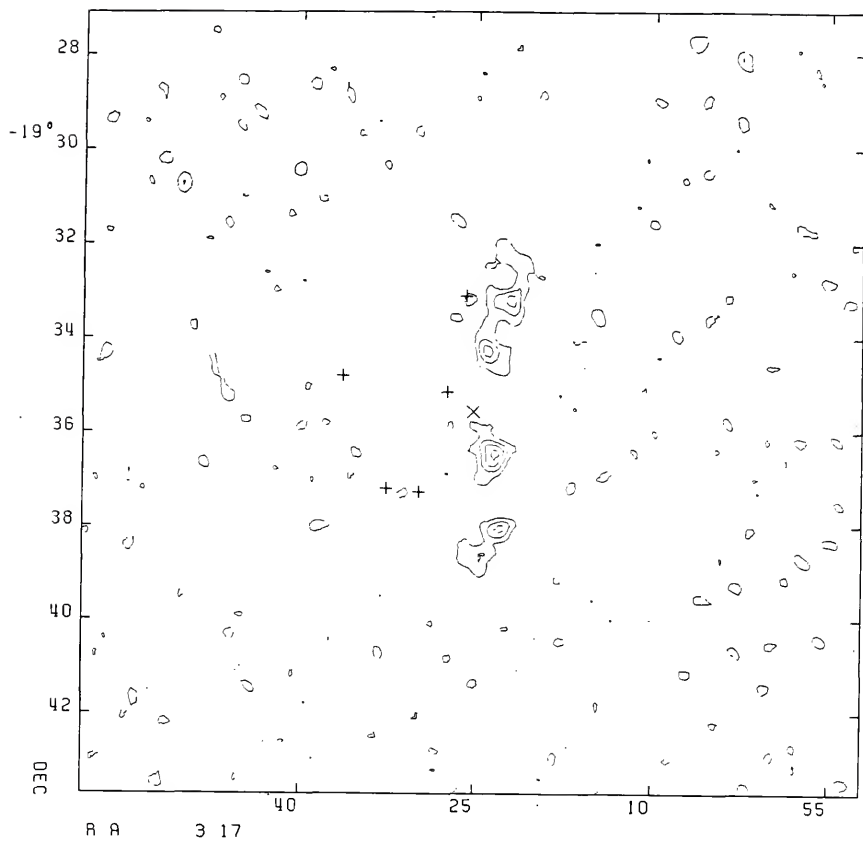


Figure 2-3 cont. (Part H).

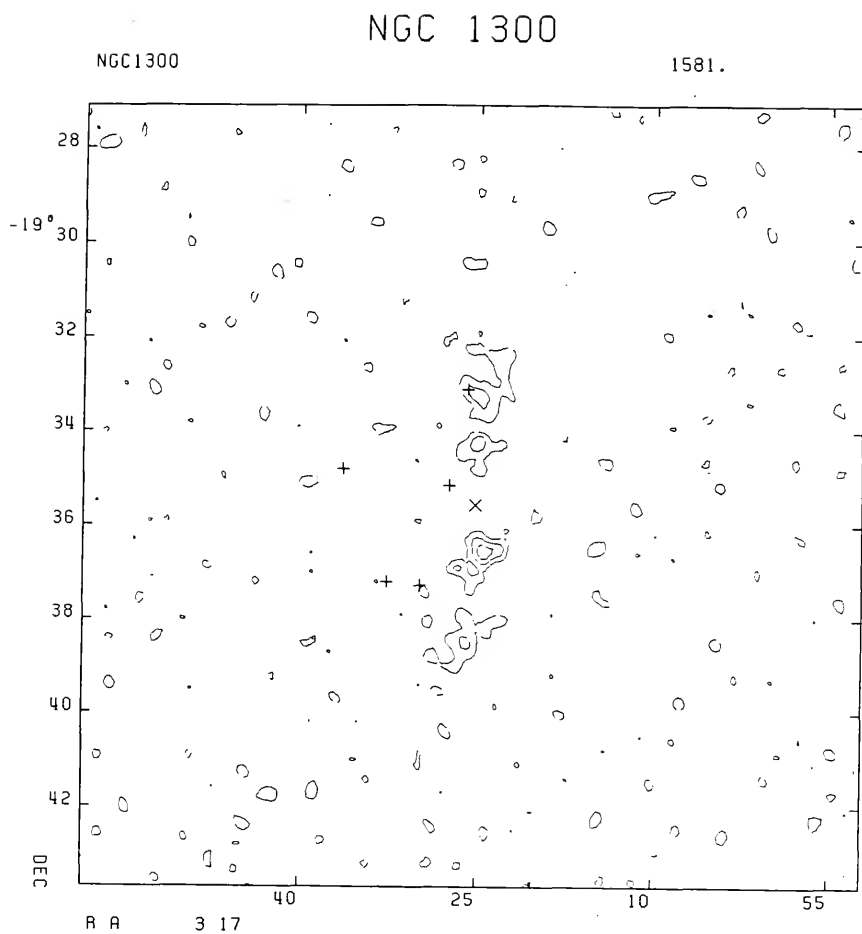


Figure 2-3 cont. (Part I).

## NGC 1300

NGC1300

1561.

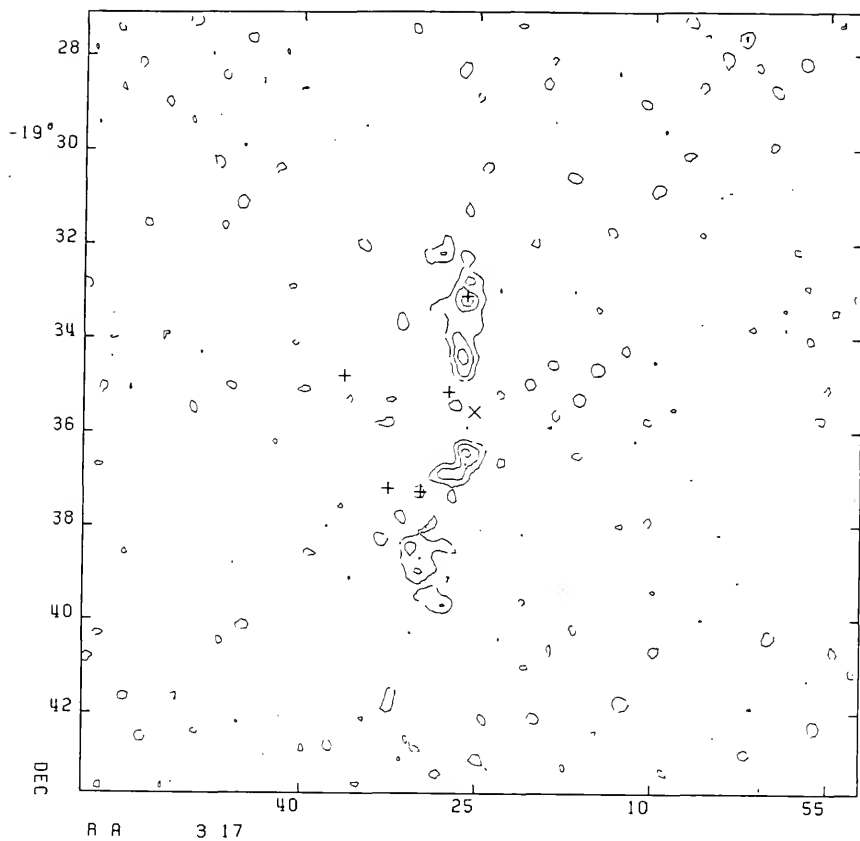


Figure 2-3 cont. (Part J).



## NGC 1300

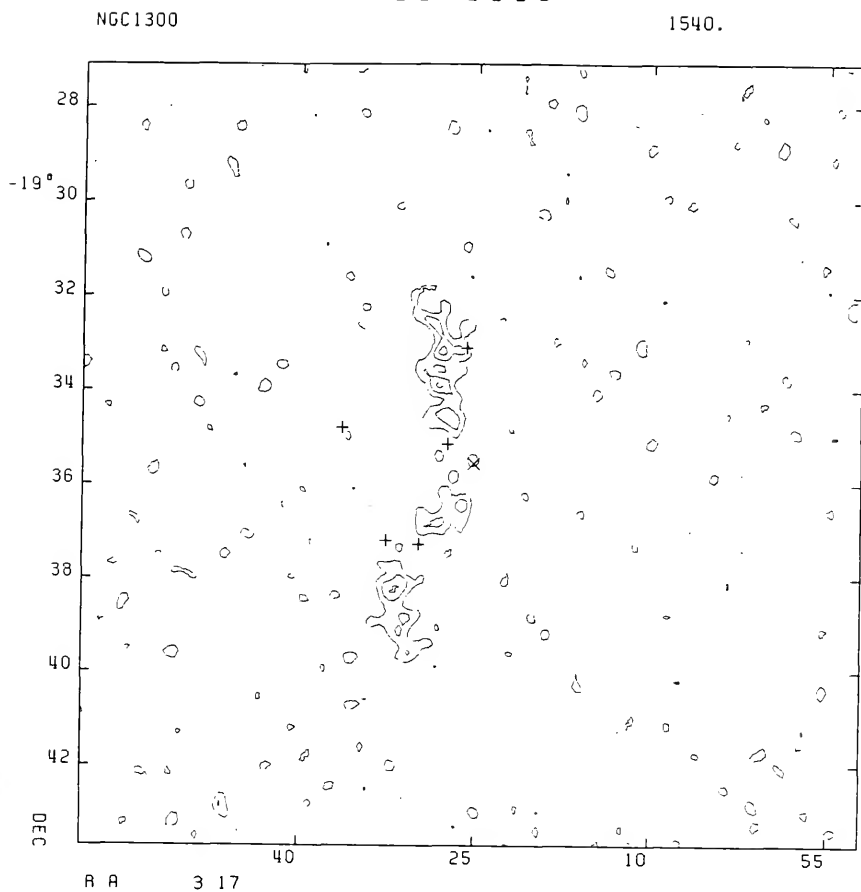


Figure 2-3 cont. (Part K).

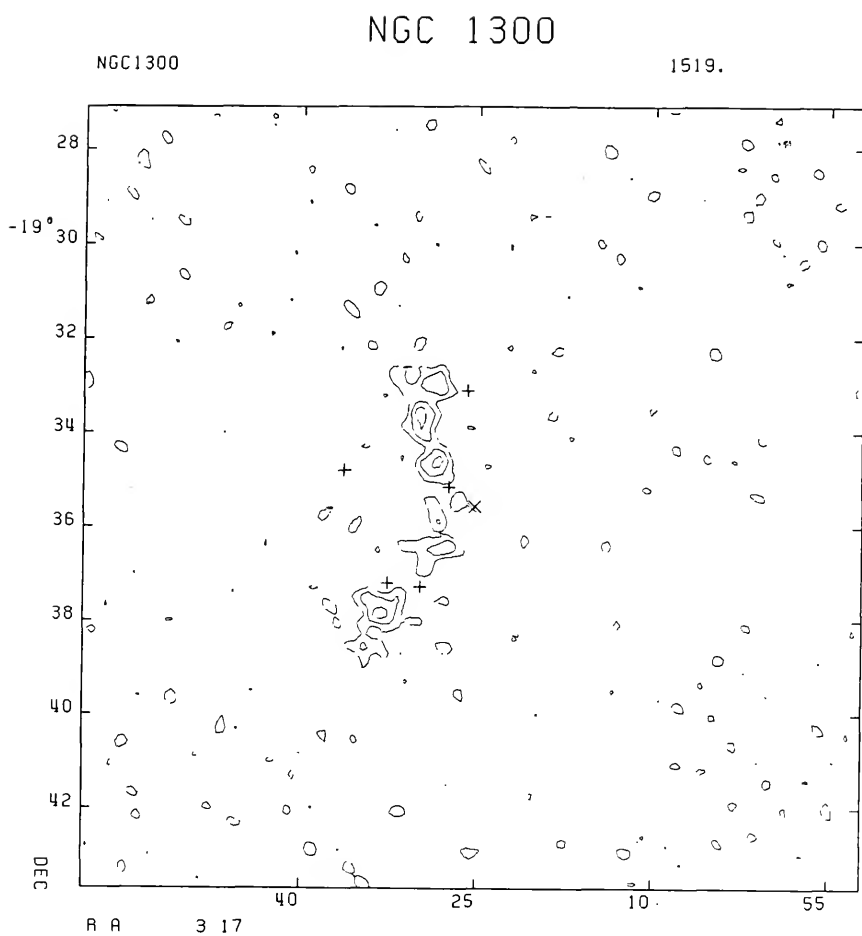


Figure 2-3 cont. (Part L).

## NGC 1300

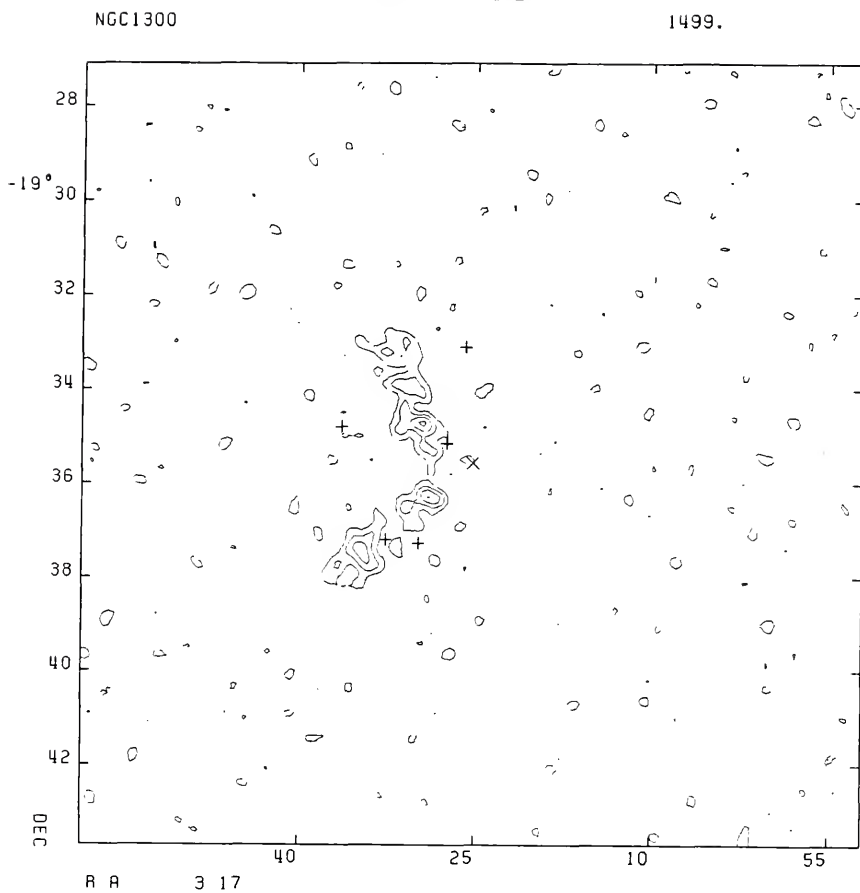


Figure 2-3 cont. (Part M).

## NGC 1300

NGC1300

1478.

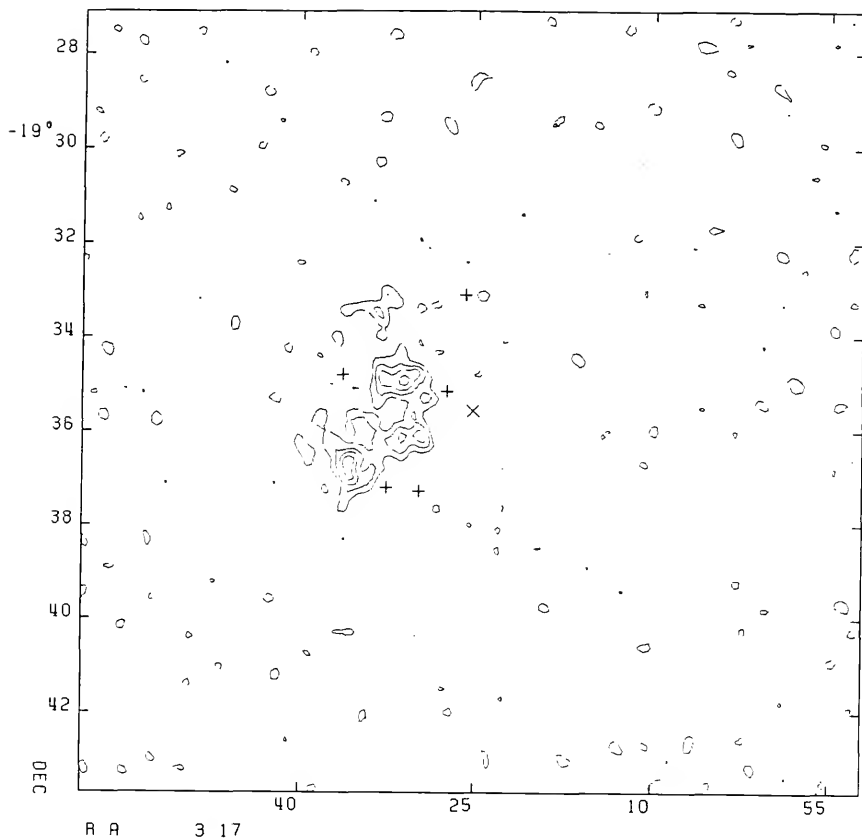


Figure 2-3 cont. (Part N).

## NGC 1300

NGC1300

1458.

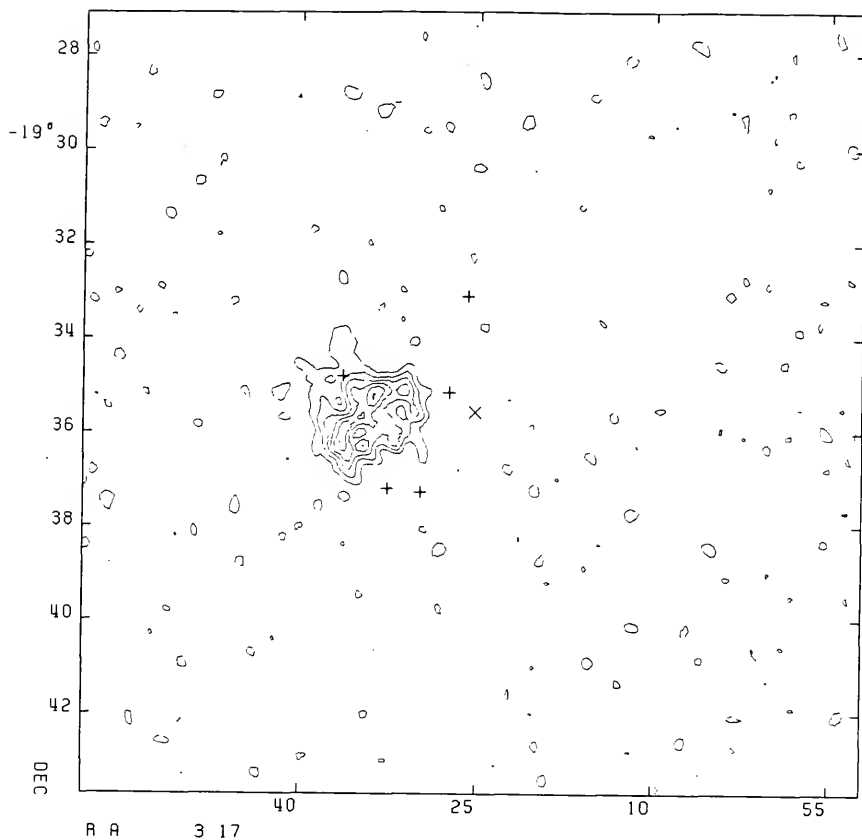


Figure 2-3 cont. (Part O).

## NGC 1300

NGC1300

1437.

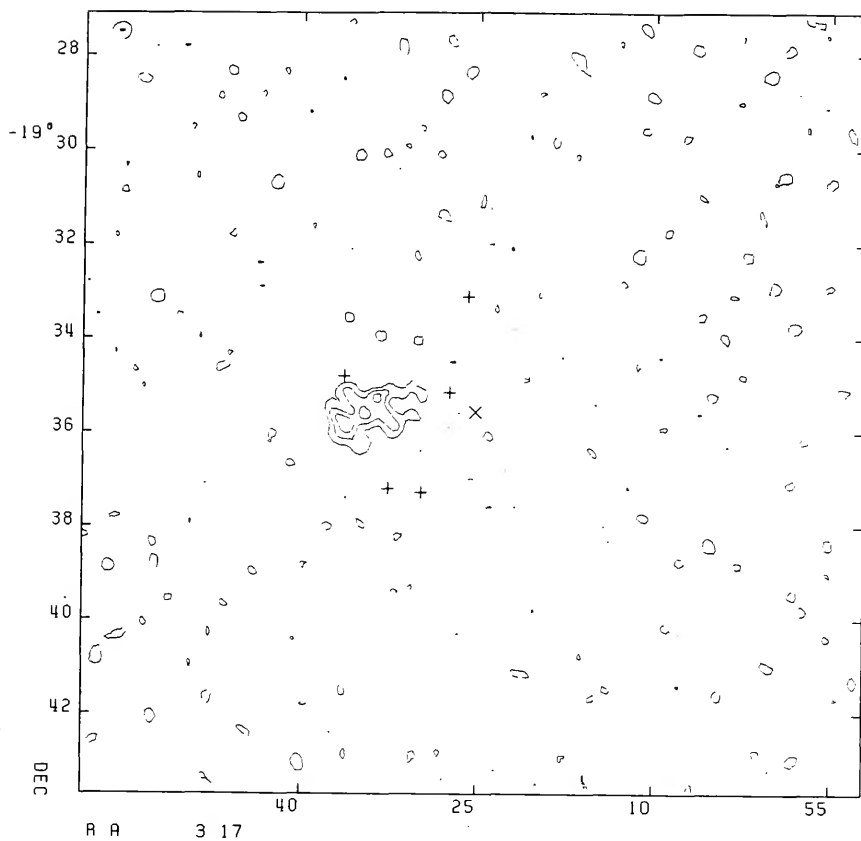


Figure 2-3 cont. (Part P).

## NGC 1300

NGC1300

1416.

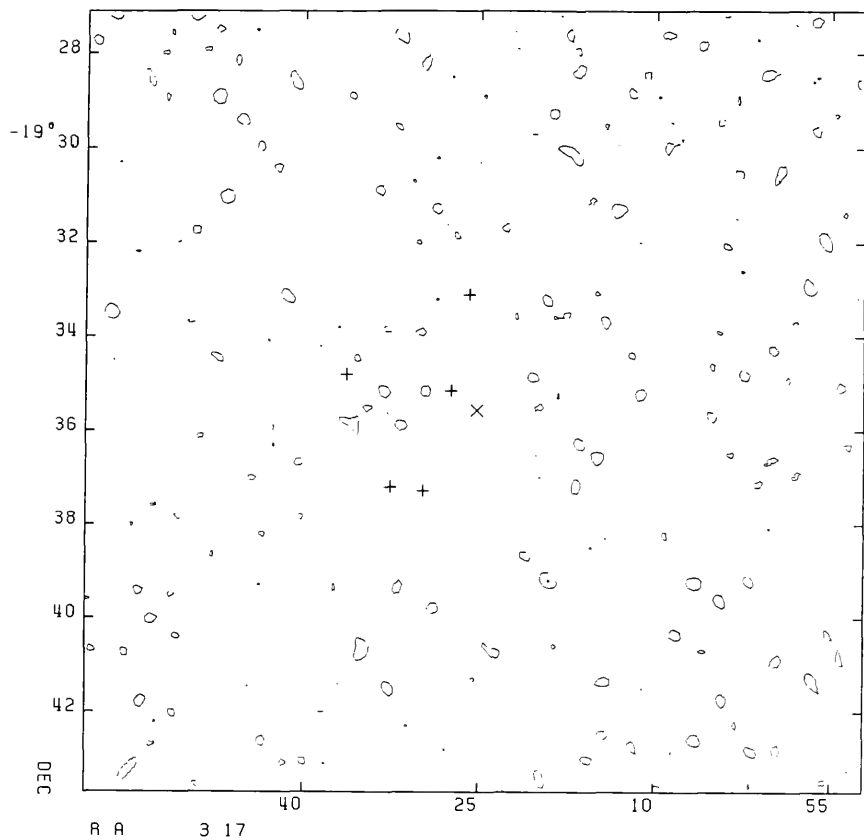


Figure 2-3 cont. (Part Q).

## NGC 1300

NGC1300

1396.

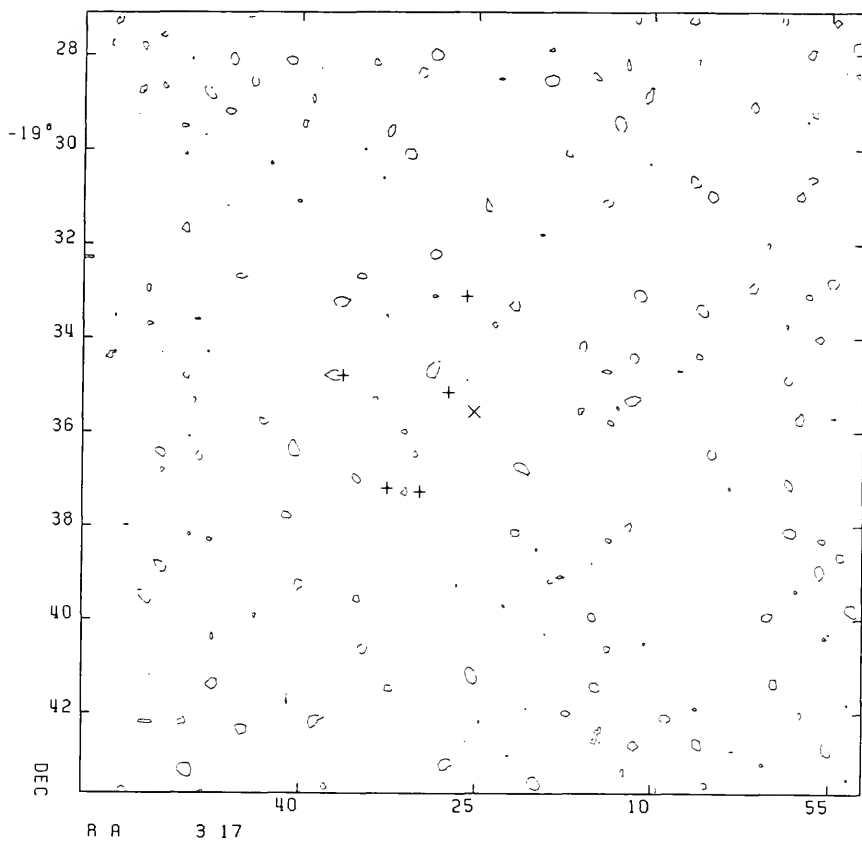


Figure 2-3 cont. (Part R).



## NGC 1300

NGC1300

1575.

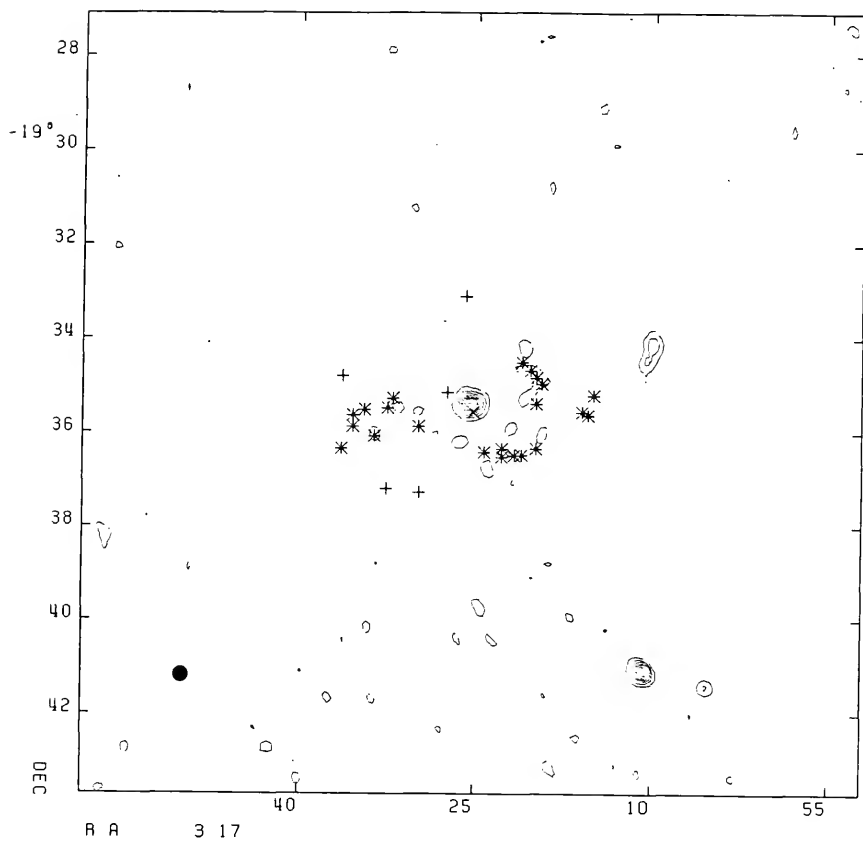


Figure 2-3 cont. (Part S).

Table 2-2 lists the rms noise levels for the CLEANed maps in mJy/beam and in Kelvin. As can be seen these values correspond very closely with the expected rms noise level from equation 2-23.

In addition to the narrow band line channel maps in Figure 2-3, several channels spaced over the whole velocity range were mapped over a large field of view,  $1.5^{\circ} \times 1.5^{\circ}$ . The effective resolution for these large field maps is  $24.25'' \times 22.59''$  (FWHM). These maps were used to search for any detections of satellite galaxies of NGC 1300 or any other objects. An example of the inner portion of one of these wide field maps is shown in Figure 2-4. This is a map of channel 16 and is a typical result. The continuum emission has not been subtracted from this map. No evidence was found for any 21cm line emission from any source other than NGC 1300 in this or any other wide field map. Figure 2-5 shows a wide field map of "channel zero" with the continuum emission still present. This, again, is only the inner portion of the total field mapped. As no evidence was found for any satellites or other objects, except unresolved continuum point sources, only the inner portion is shown as an example of the type of result obtained. The rms noise levels for these maps are tabulated in Table 2-2.

In summary the map making and CLEANing parameters used for NGC 1300 are

1. Map making (Channel and Continuum Maps)

## NGC 1300

NGC1300

1540.

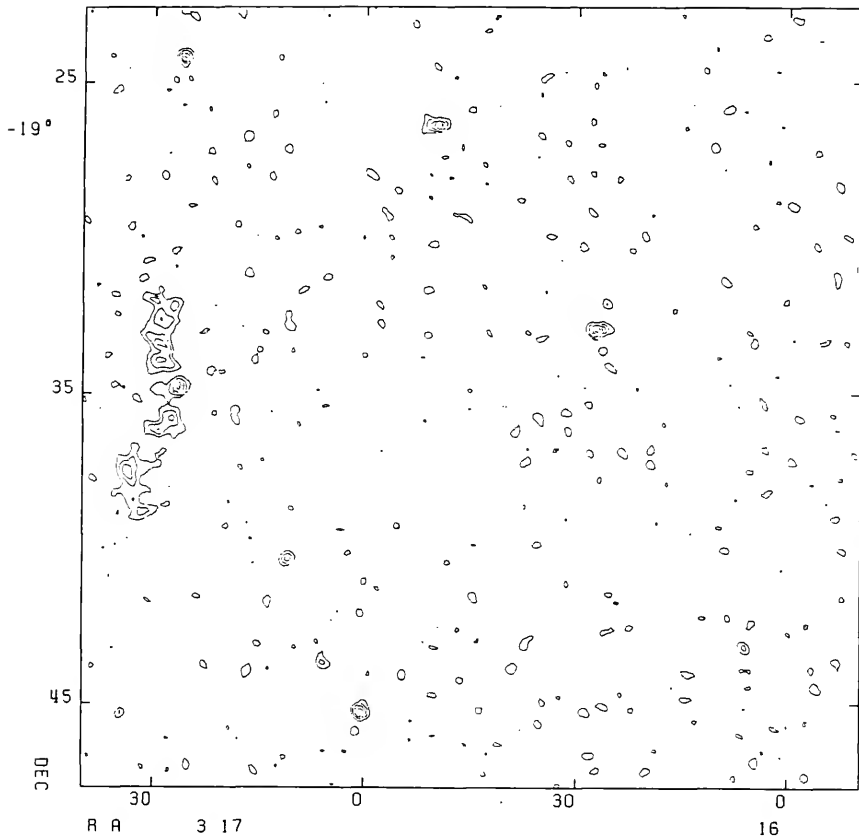


Figure 2-4. Wide Field Map. Inner portion of wide field image of channel 16. The continuum emission is still present. Contours are at intervals of twice the rms noise level.

## NGC 1300

NGC1300

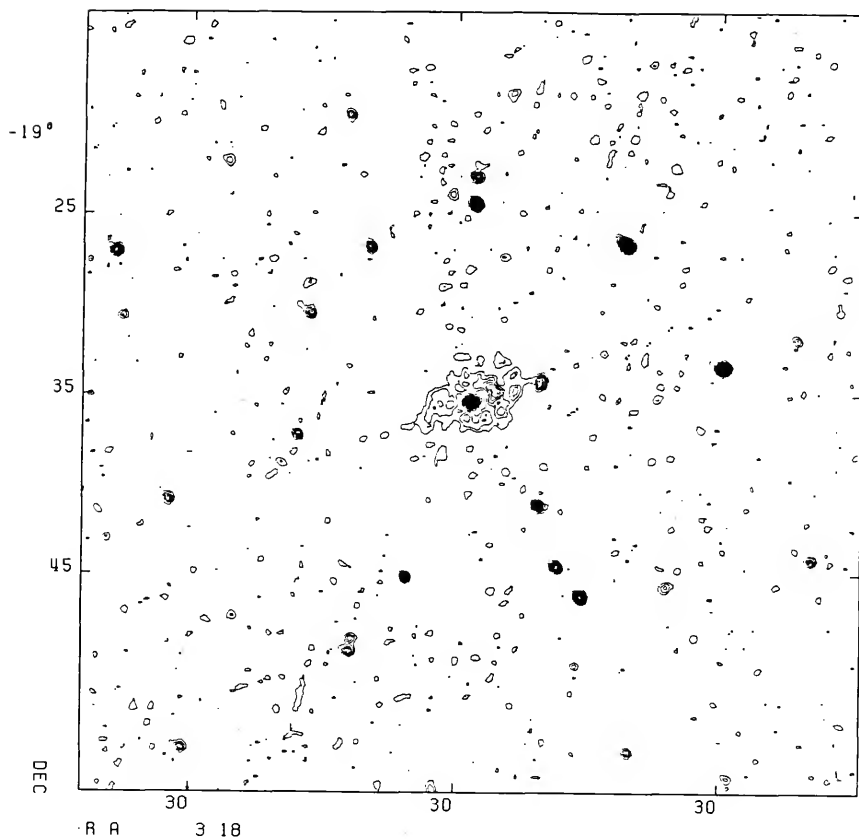


Figure 2-5. Channel Zero. Wide field map of channel zero. Contour levels are at approximately twice rms noise level.

- a) Weighting: Uniform
- b) Taper:  $7k \lambda (1484m)$  30% level of Gaussian.
- c) Convolving: Spheroidal with  $m=6$ ,  $n=0$ ,  $\alpha=1$ .
- d) Cell size:  $6'' \times 6''$
- e) Image size:  $256 \times 256$

## 2. Map Making (Wide Field Maps)

- a) Weighting: Uniform
- b) Taper:  $7k \lambda (1484m)$  30% level of Gaussian.
- c) Convolving: Spheroidal with  $m=6$ ,  $n=0$ ,  $\alpha=1$ .
- d) Cell size:  $10'' \times 10''$
- e) Image size:  $512 \times 512$

## 3. Clean

- a) Flux cutoff:  $0.5 \text{ mJy/beam}$
- b) Gain: 0.15

CHAPTER III  
DETERMINATION OF THE NEUTRAL HYDROGEN PROPERTIES

Spectrum Integration Techniques

The final product of the acquisition, calibration and processing of the 21cm VLA visibilities is a set of 18 continuum-free narrow spectral-line channels for NGC 1300. The set consists of signal-free channels at either end of the spectrum and a series of signal-rich spectral-line channels. The channel separation is 20.63km/sec and each channel has a width (FWHM) of 25.2km/sec. These continuum-free channel maps can be used to infer the neutral hydrogen distribution and its associated velocity field.

If we assume that the atomic hydrogen is optically thin, then the column density  $N_h$  at some point (x,y) is given by (Mihalas and Binney, 1981 p489)

$$N_h(x,y) = 1.8226 \times 10^{18} \int_{-\infty}^{\infty} T_B(x,y) dV \quad (3-1)$$

where the velocity,  $V$ , is in km/sec, and  $T_B$ , the brightness temperature, is in degrees Kelvin.

The mean temperature-weighted velocity at that point is given by

$$\langle V(x,y) \rangle = \frac{\int_{-\infty}^{\infty} T_B(x,y) V(x,y) dV}{\int_{-\infty}^{\infty} T_B(x,y) dV} . \quad (3-2)$$

These will be easily recognised as the zeroeth and first moments of the brightness temperature with respect to velocity.

In the absence of observational noise the evaluation of these quantities would be straightforward, being a straight summation over velocity at each (x,y) point. However, as noise is always present, a method is required which is capable of discriminating quickly between noise and line signal, and rejecting the noise before integration. As the channels cover only a limited spectral range the noise may not average to zero and will give a definite contribution to the summation, if the summation was naively carried out over the full spectral range. The problem is then to define a range, or window, in velocity space which contains only line signal. Various methods have been proposed to define this window (Bosma, 1978, 1981). Bosma considered four methods:

1. Study each spectrum visually and define limits in velocity.
2. Fit each spectrum with a preconceived shape.
3. Apply an acceptance level in intensity (the cut-off method).

4. Apply an acceptance level in velocity (the "window" method).

Bosma (1978) studied these various methods and concluded that the optimum method is the "window" technique.

The method used here is a variation of the "window" method. Bosma's procedure is followed with some additional discriminating features. A narrow window in velocity is initially defined and gradually expanded with the value outside the window being compared with the value outside the window calculated in the previous step. When these two values agree to within a specified tolerance level then all the signal is considered to have been found and the procedure is stopped for that pixel. Using this procedure implies that the real signal is going to be present in a single range of contiguous channels and any large spike at a very discrepant velocity is considered to be noise. Also, any large spike occurring in only one channel will be rejected. The tolerance level depends upon the rms noise of the single channel maps and on the number of points remaining in the empirically defined continuum. This continuum is the mean level of points outside the window.

Two additional criteria are added to improve the signal detection and noise rejection capabilities of the procedure. The procedure requires at least  $n$  points in the spectrum to be above a specified brightness temperature. If this criterion is not satisfied then no further effort is spent



on that pixel and it is rejected from all further consideration. However, if this criterion is satisfied then a further test is applied to reject pixels which have the required number of points above the specified brightness temperature but do not actually contain line signal. The total value at each pixel (equation 3-1) must be above a specified cut-off level, e.g. three times the rms noise level. If the integrated value is below this cut-off level then that pixel is considered not to contain line signal and is rejected. Usually the procedure tests for at least two points in the spectrum being above twice the rms noise level in the single channel maps. The integrated value usually must lie above three times the rms noise level of the single channel maps or be discarded.

In an effort to ensure that all the low brightness gas was used in the integrations, various tests were carried out utilizing different combinations of smoothed single channel maps for signal discrimination and integration. Combinations tested included testing for integrable signal on convolved maps and integrating using Hanning smoothed maps, and testing for signal on convolved maps and integrating the same convolved image. Various-sized convolving functions were tried, all two-dimensional Gaussian functions, in order to determine the optimum convolving method. The tests also were carried out using different cut-off values for the integrated spectrum and different-size boxes surrounding the region of HI emission.

The smoothing function used was a running, three-point Hanning function

$$X_n = 0.25 X_{n-1} + 0.5 X_n + 0.25 X_{n+1}. \quad (3-3)$$

This function was applied in velocity space to each pixel position. The convolving function is designed to bring out the low brightness features and to suppress the noise. Various beam solid angles were tested and the convolution was applied to each single channel map. Values ranging from half the synthesized beamwidth (FWHM) to two and a half times the synthesized beamwidth were tried. Below half the synthesized beamwidth the convolution had essentially no effect; whereas, above two and a half times the synthesized beamwidth, the convolution became so broad as to render the maps unusable. With this size convolving function, the resolution was so severely degraded that essentially no fine structure was visible; all that remained was a broad, beam-smearred, disk-like feature.

The criteria used to determine which combinations of smoothing and convolving functions, and cut-off values gave the optimum results were

1. The number of spectra used in the integration.
2. The signal-to-noise ratio in the convolved and integrated maps.
3. The HI mass-integral.

4. The ratio of mass-integral to rms noise level in the integrated maps.

The mass-integral is defined as (Mihalas and Binney, 1981 p490)

$$HI_{\text{mass}} = 2.35 \times 10^5 D^2 / S \Delta v \quad (3-4)$$

where S is the flux in Jy, and D is the distance in Mpc. The integral is calculated for all pixel points deemed to belong to the galaxy. The region in which this integral is calculated is chosen by inspection of the HI density distribution map produced by the "window" procedure. The ratio of mass-integral to rms noise level is calculated using the value found by evaluating equation 3-4 inside the box surrounding the galaxy, and the rms noise level calculated outside the box. This ratio should be maximized for the optimum combination of smoothing, convolving and cutoff values. Table 3-1 shows some typical values from two runs during this testing procedure. This shows quite clearly that for these tests:

1. The rms noise level clearly goes through a minimum.
2. The mass-integral goes through a maximum.
3. The ratio of mass-integral to rms noise goes through a maximum.

As a result of these tests the following procedures were adopted:

1. Hanning smooth, in velocity space, the original single channel maps with a running three-point function.

TABLE 3.1

## Signal Characteristics for Spectrum Integration

Npoint (1)	Beamwidth (2)	rms Noise (3)	Mass-integral (4)	Ratio (5)
1	0.5	24.29	1.1430	0.0471
	1.0	30.78	1.1781	0.0383
	1.5	22.07	1.1777	0.0534
	2.0	20.38	1.1788	0.0578
	2.5	20.41	1.1784	0.0577
2	0.5	17.68	1.1248	0.0636
	1.0	24.75	1.1700	0.0473
	1.5	14.92	1.1742	0.0787
	2.0	14.67	1.1739	0.0800
	2.5	15.00	1.1727	0.0782

- (1) Minimum number of points in each spectrum required to be above the cut-off value.
- (2) Convolution beamsize, in units of synthesized beamwidth.
- (3) Rms noise level outside a box surrounding the galaxy in arbitrary units.
- (4) Mass-integral for all points deemed to belong to the galaxy in arbitrary units.
- (5) Ratio of mass-integral to rms noise level.

2. Convolve the smoothed channel maps using a Gaussian with a beamwidth (FWHM) twice the synthesized beam.
3. Test for line signal on the convolved maps using a two point test and a cut-off of twice the rms noise level.
4. Integrate the smoothed maps using three times the rms noise level as a cut-off.

This procedure produces maps of the beam-smoothed column density of the HI gas distribution and temperature-weighted mean velocities of the gas.

#### Neutral Hydrogen Distribution

The spectrum integration procedure described above was used to produce the beam-smoothed column density of the observed HI gas, assuming a small optical depth, shown in Figures 3-1 to 3-4. The maximum observed density is  $1.59 \times 10^{21}$  atoms/cm<sup>2</sup>. Generally, the signals are not spread over more than 4 or 5 channels. This gives an rms noise level of about  $5 \times 10^{19}$  atoms/cm<sup>2</sup> or approximately 3% of the peak density. Various methods of presenting these data are shown in these diagrams in an attempt to get a clear understanding of the neutral hydrogen distribution. Figure 3-1 shows a contour plot of the data for NGC 1300. This diagram is rather confused and difficult to interpret. By superimposing the contour plot on an optical photograph of the galaxy, Figure 3-2, the structure of the hydrogen

distribution can be discerned. A gray scale of the distribution, Figure 3-3, shows the regions of high density gas and low density gas; but a better method to display the structural detail of the neutral hydrogen gas distribution is to use a false color display where each color represents a range of values. Figure 3-4 is a false color image of the gas distribution in NGC 1300. This diagram vividly illustrates the structural detail of the galaxy.

Before interpretation of the observed column density, all pixels had their spectra examined for any anomalous effects, a beam-smoothed noise spike at an unlikely velocity, for example. Any such anomalous spectra were discarded and corrections applied by hand to the dataset. If a pixel obviously had a weak signal but had been discarded by the automated routine as the integrated value was not three times the rms noise level, it was added into the dataset. Very few, <1%, of the spectra examined required corrections; a few pixels in the center of the galaxy and some at the outer edges of the arms were all that required corrections.

The most noticeable features in the HI distribution are

1. The very prominent and strong spiral arms.
2. The lack of gas in the central bar region.

The contrast between the spiral arms and the background region is high as there is essentially no gas in the interarm regions. The observed gas is confined almost exclusively to the spiral arms, making NGC 1300 an excellent

## NGC 1300

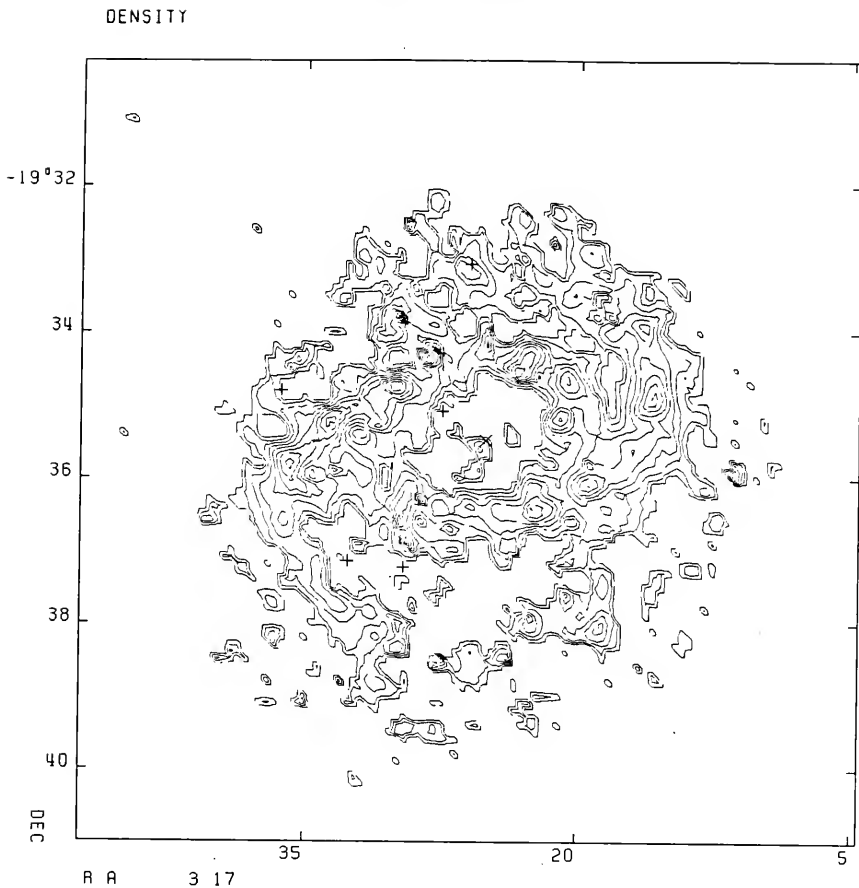
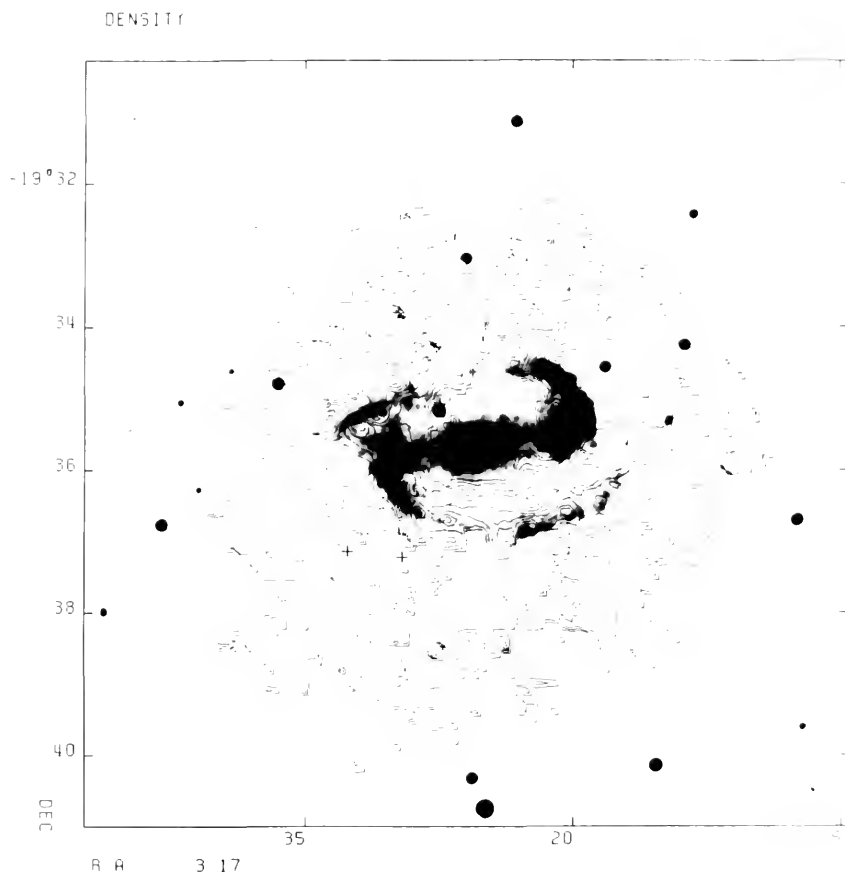


Figure 3-1. Neutral Hydrogen Distribution Contour Plot. The center of the galaxy (x) and fiducial stars (+) are marked. The contour levels are in intervals of 10% of the peak observed density. Peak observed density is  $1.59 \times 10^{21} \text{ cm}^{-2}$ .

Figure 3-2. Neutral Hydrogen Distribution with the Optical Image. HI gas distribution superimposed upon an image of NGC 1300 from the National Geographic-Palomar Sky Survey.



## NGC 1300



NGC 1300 HI DENSITY

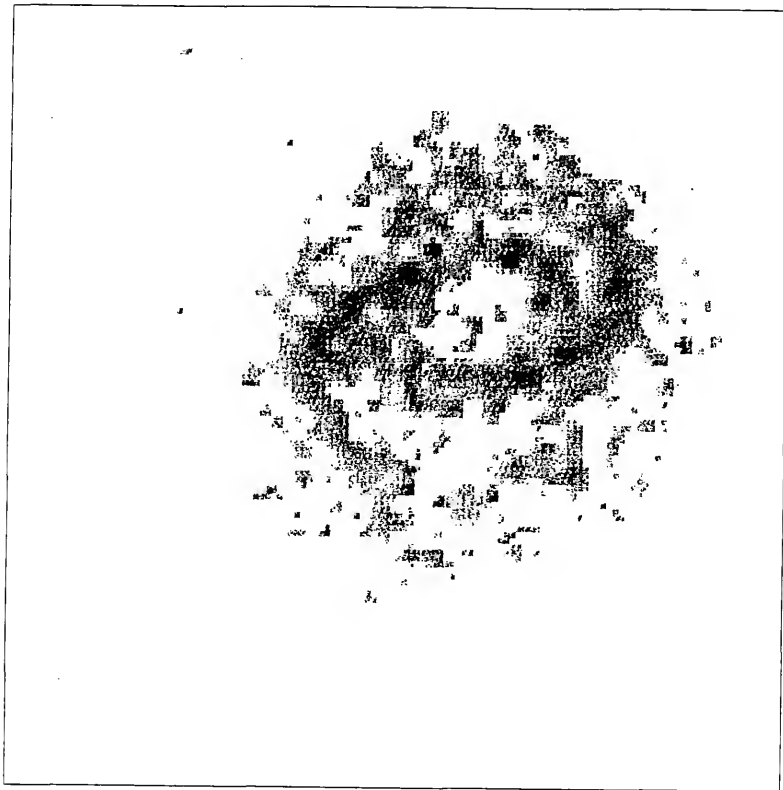
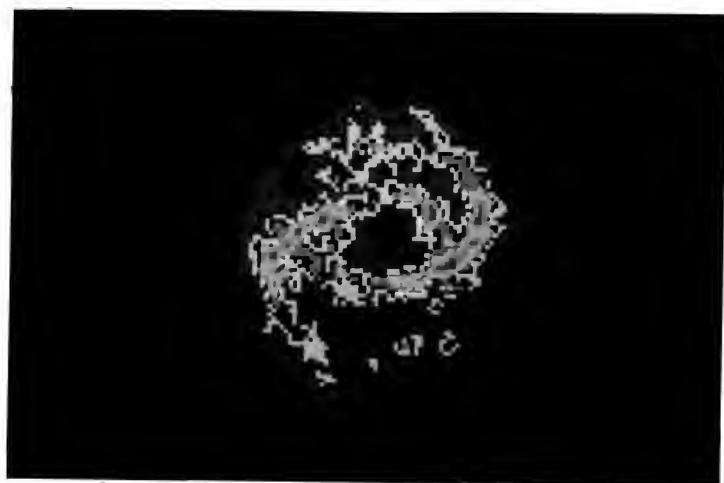


Figure 3-3. Neutral Hydrogen Distribution Gray Scale Image.

Figure 3-4. Neutral Hydrogen Distribution False Color Image. Blue represents low density gas and red high density gas.



example of a grand design spiral. There is some evidence for gas in the nuclear region of the galaxy but this is very low density gas and confined to a few pixels. The inner region of the galaxy was convolved in an attempt to enhance the low level gas in the nuclear region. No extra, low density gas was found, thus indicating that the gas is probably hidden in the noise, if it exists.

Comparing the observed HI spiral structure with the optical spiral arms shows that the two features correspond very well. The optical arms can be reliably traced through approximately  $200^\circ$  in azimuth whereas the HI arms can be traced through about  $310^\circ$  in azimuth. Noticeable features in the optical image of the system are also evident in the HI gas distribution image. The breaks in the optical arms at position angles  $0^\circ$  and  $175^\circ$  are also prominent in the HI gas distribution. Also, at position angles  $0^\circ$  and  $175^\circ$ , breaks in the outer regions of the gas arms may be evident. However, the gas density in these regions is low, and these breaks may only be the result of the low density and not actually physical breaks, as in the inner regions. These breaks may be manifestations of stellar orbital resonances. The region of maximum brightness in the northern section of the western arm, in the optical image, shows a definite shift in position before and after the break in the arm. The HI gas arm does not show this shift in position, with the gas maximum being slightly closer to the nucleus than

the optical maximum before the break, and slightly farther from the nucleus than the optical maximum after the break. Thus, the optical arm lies slightly outside the gas arm, whereas after the break the optical arm lies inside the gas arm. The situation is not as pronounced in the southern section of the east arm where the gas and optical arms are more nearly coincident.

The arms may be described by a simple logarithmic form

$$\theta(R) = \ln(R/R_0)/\tan \alpha \quad (3-5)$$

where  $R$ ,  $R_0$  and  $\theta$  are measured in the plane of the galaxy. The pitch angle of the spiral and  $R_0$  are constants. However, the values for  $\alpha$  and  $R$  do not remain constant along the arms. The east arm shows a change in  $\alpha$  and  $R_0$  at an azimuthal angle of  $\sim 195^\circ$ , changing from  $\alpha=5^\circ$  and  $R_0=1.73'$  to  $\alpha=25^\circ$  and  $R_0=0.46'$ ; thus it becomes less tightly wound in the outer regions than in the inner regions. The west arm shows the same pattern;  $\alpha=5^\circ$  and  $R_0=1.5'$  and changes to  $\alpha=25^\circ$  and  $R_0=0.6'$  at an azimuthal angle of  $\sim 145^\circ$ . These logarithmic spirals are shown in Figure 3-5, along with the deprojected observations. The observed spiral pattern is calculated using the peak observed densities in a small region at each azimuthal angle. Profiles along the arms are shown in Figure 3-6. The overall appearance of the gas distribution in NGC 1300 shows this to be an excellent grand design spiral system.

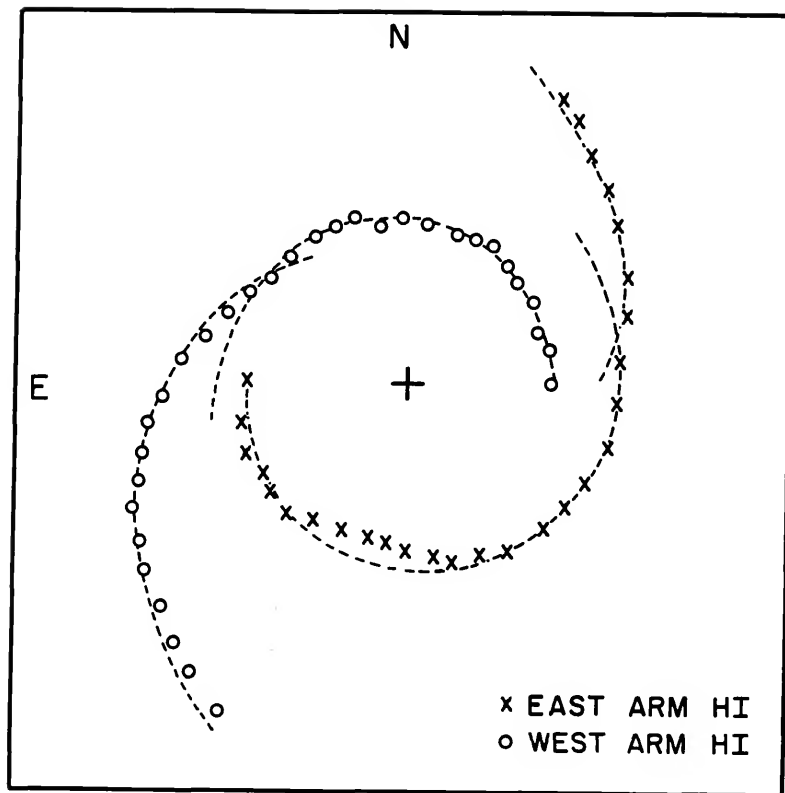


Figure 3-5. Logarithmic Fit to Spiral Arms. Two component logarithmic spiral representation of the deprojected, observed HI arms. The observations are (x) for the east arm and (o) for the west arm. The inner components have  $\alpha=5^\circ$  and the outer components have  $\alpha=25^\circ$ .

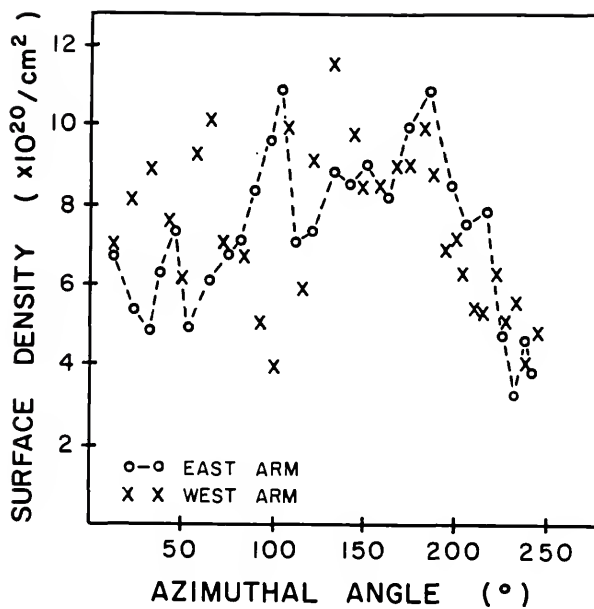


Figure 3-6. Deprojected Azimuthal Profiles. Surface density of the HI gas along the spiral arms.



## NGC 1300

DENSITY

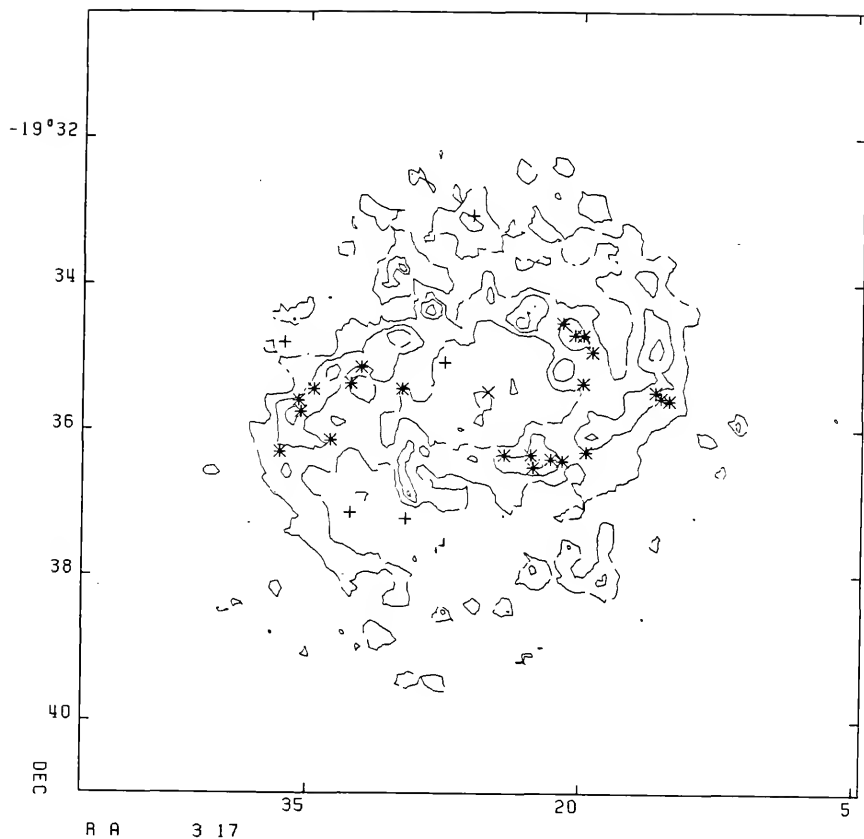


Figure 3-7. HII Regions in NGC 1300. Positions of the HII regions compared with the contour levels of 25%, 50% and 75% of the peak density. HII regions from Hodge (1969).

Hodge (1969) observed HII regions in NGC 1300. These regions are plotted in Figure 3-7. Also plotted are contours of the gas density at levels of 25%, 50% and 75% of the peak density. The positions of the HII regions correspond with the positions of regions of high HI gas density and are concentrated in regions of high brightness in the optical image. The regions in the west arm are clumped at the beginning of the spiral arm and in the region immediately following the break. Both these regions also show evidence for dust lanes and could possibly indicate shock regions in the galaxy. The HII emission in the east arm is located after the break in the arm. Again, the optical image shows some bright knots and some evidence for dust lanes. This, again, could be evidence for shock fronts.

Also very noticeable in the gas distribution is the HI gas poor region in the center of the galaxy. This region corresponds closely to the bar region and is possibly caused by dynamical effects of the rotating bar. There is some evidence for gas at the center of the galaxy, but as mentioned earlier, this is very low density gas. There is also some evidence for gas at the positions of the dust lanes in the bar region, but again, this is low density gas and cannot be regarded as conclusive evidence for shock regions; however, the suggestion is certainly strong. Low resolution observations indicated that there may be gas in this depleted region, but in the combined C/D array dataset

this gas, if it exists, probably lies below the rms noise level. In an attempt to recover any low level gas, the full resolution dataset was convolved to a resolution comparable to that of the D array and the integrations repeated. Some extra low level gas was brought out in the interarm regions but no significant enhancement of the gas was found in the depleted bar region. This depletion in the bar region has been observed in other barred spiral galaxies. The galaxy NGC 3992 (Gottesman et al., 1984) shows a similar depletion in the bar region whereas NGC 3359 (Ball, 1984) and NGC 1073 show a little depletion but not as markedly as do NGC 1300 and NGC 3992.

The extent of the depleted region, although somewhat irregular, can be approximated by an ellipse of semi-major axis  $a=1.1'$  and position angle  $-80^\circ$ . When deprojected into a circle this ellipse gives an inclination angle  $i=51^\circ$ . This is the same as the inclination angle for the galaxy deduced using 21cm radial velocities (see next section for details). The size of the semi-major axis of this ellipse,  $1.1'$ , corresponds well with the semi-major axis of the bar,  $1.28'$ , and thus possibly indicates that the region is depleted due to dynamical effects of the bar. Inside the bar region the bar has an angular velocity less than the angular velocity of the gas. Any interaction between the bar and the gas is likely to result in a loss of angular momentum of the gas. This will cause the gas to migrate towards the center of the

galaxy and cause a gas buildup. However, this gas enhancement is not seen in the HI, although, as will be seen in the modeling, section there is a gas buildup in the models.

Alternatively, molecular gas may be the dominant component in this region. Carbon monoxide has been shown to be a good tracer of  $H_2$  in molecular cloud complexes (see for example Thaddeus, 1977; Bloemen et al., 1986) and thus, detection of CO in the central region of NGC 1300 would give some estimate for the amount of molecular gas present. As no CO observations have been made of NGC 1300 some other method is needed to estimate the amount of molecular gas in the central region. Various studies have indicated that the CO emission is almost always enhanced in regions of suspected star formation (Thaddeus, 1977; Rieke et al., 1980; Telesco and Harper, 1980). Thus, if an estimate for the amount of star formation in the central region of NGC 1300 can be made, this will give some indication of the amount of molecular gas present in this region. Examination of IRAS fluxes for the inner 1.5' of the system will give an indication of the star-formation activity in the nuclear region and thus, an estimate for the amount of gas in the center. Following the discussion of Hawarden et al. (1985), the ratios of the 100 $\mu$ m flux to the 25 $\mu$ m flux, and of the 25 $\mu$ m flux to the 12 $\mu$ m flux give an indication of the star-forming activity in the center. If  $R(100\mu m/25\mu m) < 20$  and

$R(25\mu\text{m}/12\mu\text{m}) > 2$ , then there is very likely vigorous star formation in the center, and consequently, there may be large amounts of gas present, but unseen by the 21cm observations. The IRAS point source fluxes for NGC 1300 are

12 $\mu\text{m}$       < 0.25 Jy.

25 $\mu\text{m}$       < 0.31 Jy.

60 $\mu\text{m}$       2.39 Jy.

100 $\mu\text{m}$      10.78 Jy.

Thus, as there is no indication of vigorous star formation in the center, it seems unlikely that massive amounts of either ionized gas or molecular gas exist in the inner 1.5' of the galaxy. A dilemma therefore exists. On one hand we have the possible loss of angular momentum of the gas causing a gas buildup in the center, and on the other hand, all available data on gas tracers, at present, show no large amounts of gas in the center. What has happened to the gas? Perhaps it will show up in the CO observations but the present evidence indicates that this is unlikely. Another possible explanation is that this gas has become associated with the nuclear non-thermal continuum source. Further observations of molecular components might help resolve this problem.

The HI gas has a fairly-well defined extent with a major-axis diameter of about 7.6' at a level of  $2 \times 10^{20}$  atoms/cm<sup>2</sup>. The optical major-axis diameter, at a level of 25.0 mag/arcsec<sup>2</sup>, is 6.5' (de Vaucouleurs, de Vaucouleurs

and Corwin, 1976). The radial extent of the galaxy is determined by the outer sections of the spiral arms. Very little gas is seen as a broad disk-like feature. In fact the observed gas seems to be almost entirely confined to the spiral arm region. Any disk gas is below the rms noise level for this map. The rms noise level is  $5 \times 10^{19}$  atoms/cm<sup>2</sup>. Figure 3-8 shows the radial dependence of the deprojected HI surface density.

The depletion of the gas in the center is evident from the low surface densities for the inner 1.0' of the galaxy. The tail of the distribution has very low surface densities from about  $r=3.8'$  outwards. The line joining the two points plotted for each position indicates the upper and lower bounds for the surface density. Thus, this tail indicates that at  $r>3.8'$  the values are very uncertain due to low signal-to-noise ratio. Points in this region are determined from a few lumpy patches. All values for the surface density have upper and lower bounds indicated. In the inner 1.0' of the galaxy this is mainly due to the lack of gas whereas, for the regions encompassing the arms, this range is due to the lack of interarm gas. The HI distribution is patchy, being confined largely to the arm region, and thus, as each point in Figure 3-8 represents the annulus-averaged value at a particular deprojected radius, there will be some regions in the annulus which contain only very low surface density gas, the interarm regions for example. The nature of the

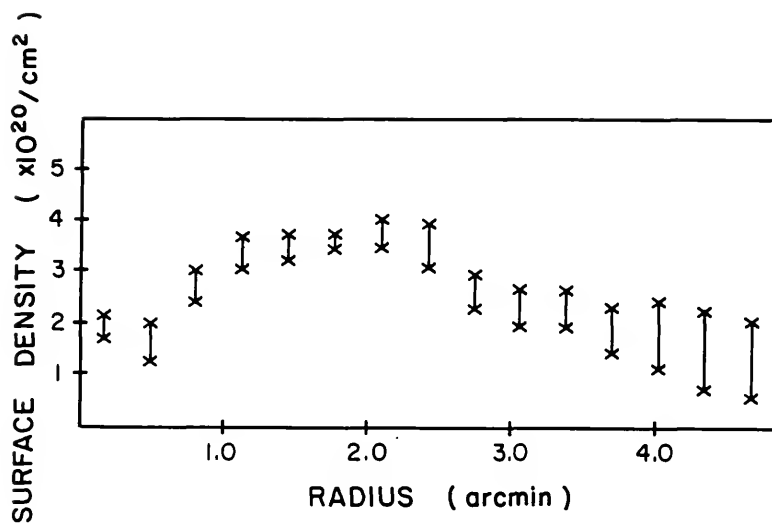


Figure 3-8. Deprojected HI Surface Density.  
Annulus-averaged surface density of HI gas in NGC 1300.

surface density distribution is well-illustrated by considering Figure 3-9 (a-e) which shows profiles at various positions of constant right ascension and declination. Figure 3-9 (a) shows the positions of these profiles and Figure 3-9 (b-e) shows the profiles. Very noticeable in Figure 3-9 (b) are the four peaks in the profile. In order of decreasing declination these peaks correspond to the outer region of the west arm, the inner region of the east arm, the inner region of the west arm and the outer region of the east arm. This profile crosses the inner and outer regions of the west arm at the breaks in the arm. This explains the relatively low level of the peaks when compared with the peaks for the east arm. The profile in Figure 3-9 (c) passes through the west arm at approximately the position of the "kink" in the arm. This profile gives a qualitative picture of the general decrease in flux level as the position along the arm is changed. A better representation of the levels along the arm can be obtained by plotting HI density as a function of azimuthal angle. Figure 3-6 is a plot of this, in the plane of the galaxy, for both the east and west arms. Noticeable is the decrease in density levels at the positions of the breaks in the arms. The profile in Figure 3-9 (d) passes through the "kink" in the east arm and shows three distinct peaks. These peaks correspond to the end of the west arm and two crossings of the east arm. Figure 3-9 (e) shows the profile



which crosses the center of the galaxy at constant declination. Very obvious is the lack of flux in the center region of the galaxy. These profiles illustrate well the very distinct and well-defined structural nature of the HI distribution in NGC 1300.

The total HI mass can be obtained by integrating the density distribution in Figure 3-1 in  $(x,y)$ , or solid angle. Integrating gives  $M_H/M_O = 8.7 \times 10^6 D^2 \text{Mpc}$ . Correcting to an adopted distance of 17.1 Mpc de Vaucouleurs and Peters (1981) give a total HI mass is  $2.54 \times 10^9 \text{Mo}$ . The value given by Bottinelli et al. (1970) becomes  $1.95 \times 10^9 \text{Mo}$ , and that from Reif et al. (1982) becomes  $3.60 \times 10^9 \text{Mo}$ . These determinations were made using single dish profiles. Thus, apart from the possibly low level gas in the center of the galaxy and the interarm regions mentioned earlier, the interferometric observations have not missed any significant HI emission. Comparing the HI mass from the combined B/C and C/D array dataset with the HI mass from the low resolution C/D array dataset shows that no extra hydrogen was detected in the low resolution dataset. The resolution limits for the arrays used in this project are approximately  $8''$  to  $17'$  and, as no structure in the maps is greater than about  $7'$ , no HI was lost due to angular limits imposed by the array configurations used in the observations.

Figure 3-9. Profiles Through HI Surface Density Distribution.

- A. Positions of the various profiles.
- B. Profile at position 1.
- C. Profile at position 2.
- D. Profile at position 3.
- E. Profile at position 4.

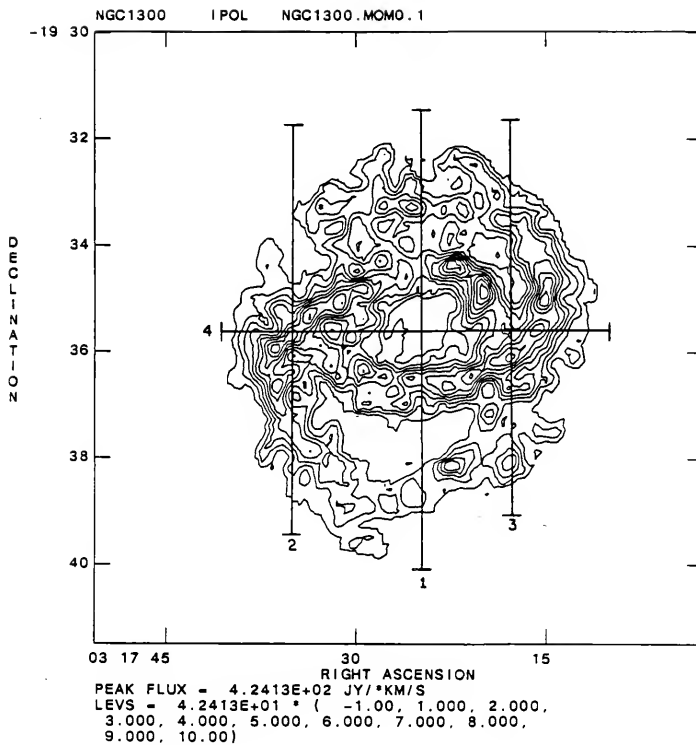


Figure 3-9 cont. (Part A).

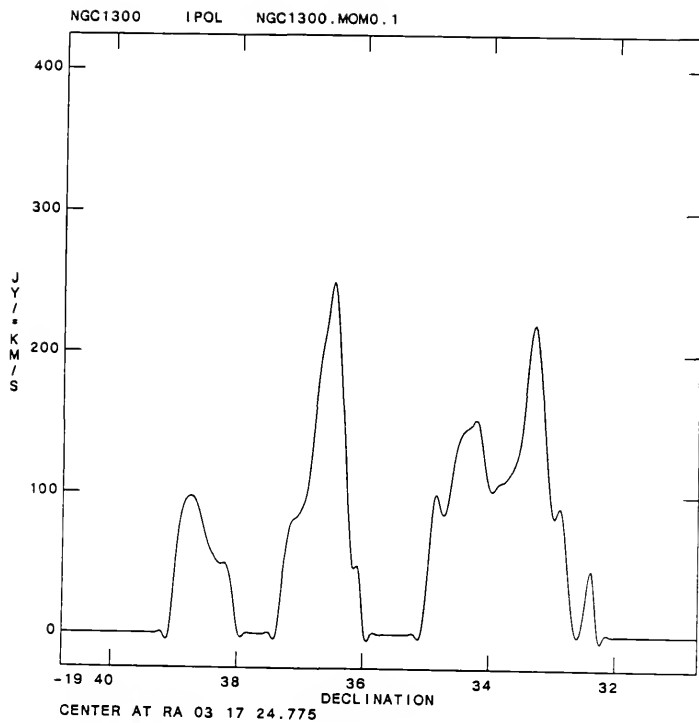


Figure 3-9 cont. (Part B).

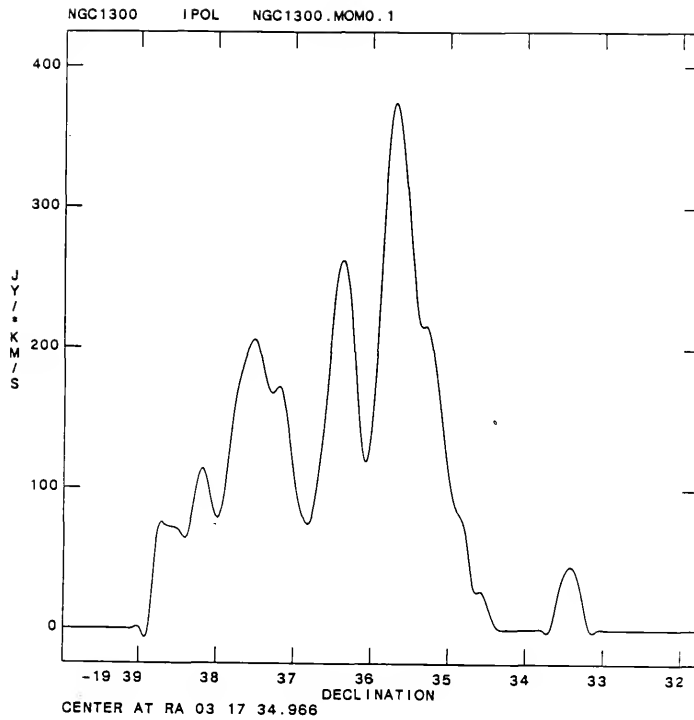


Figure 3-9 cont. (Part C).

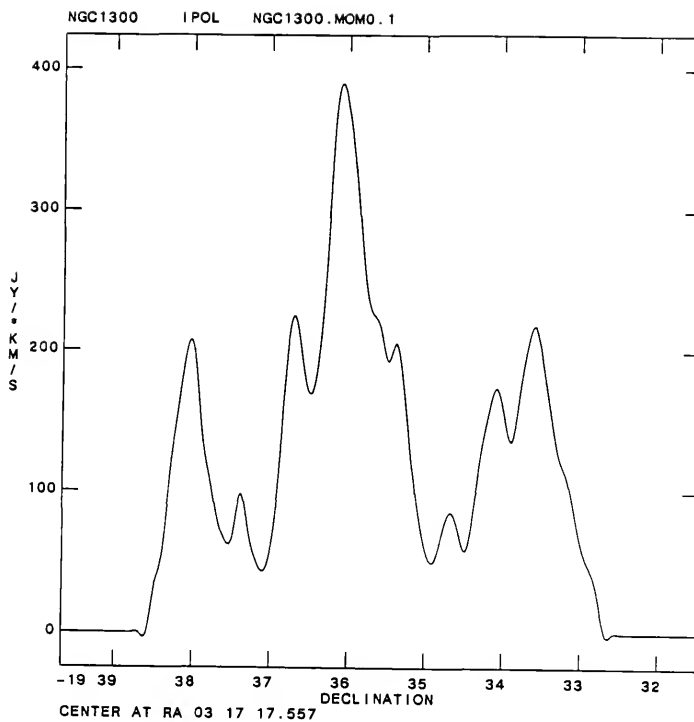


Figure 3-9 cont. (Part D).

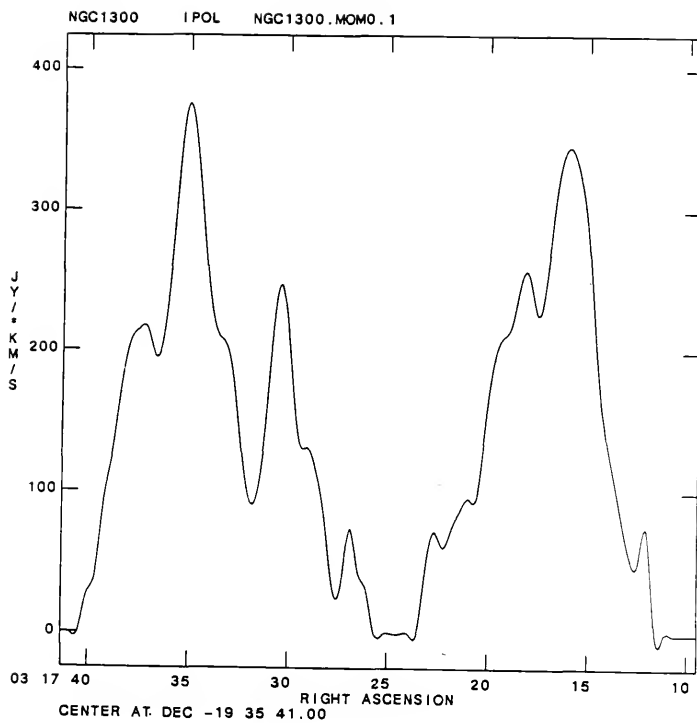


Figure 3-9 cont. (Part E).

### Continuum

Continuum emission was calculated by averaging several line-free channels at both ends of the spectral range. The resulting distribution is shown in Figure 3-10. The region covered by this map is just the region surrounding the galaxy and does not include most of the point sources in the large field map, Figure 2-5. Continuum emission in the region immediately surrounding NGC 1300 is confined to two strong point sources and some weak extended emission. One of the point sources coincides with the position of the nucleus of the galaxy. This strong source and the weak emission surrounding it continue the trend observed in the surface photometry. The surface photometry indicates that as the wavelength increases, the dominance of the central source over its surroundings also increases (see Chapter 4 for details). In an attempt to determine the extent of the low level emission, specifically from the disk and the arms, the central source was removed and the resultant image convolved with a two beamwidth (FWHM), two-dimensional Gaussian convolving function. This did not reveal any low level emission from either the disk or the arms. The full continuum emission is shown in Figure 3-10.

The low level continuum emission comes from the western end of the bar and from the confused region at the eastern end of the bar, between the bar and the extension of the western arm. Some emission is also seen from the eastern arm



## NGC 1300

NGC1300

1575.

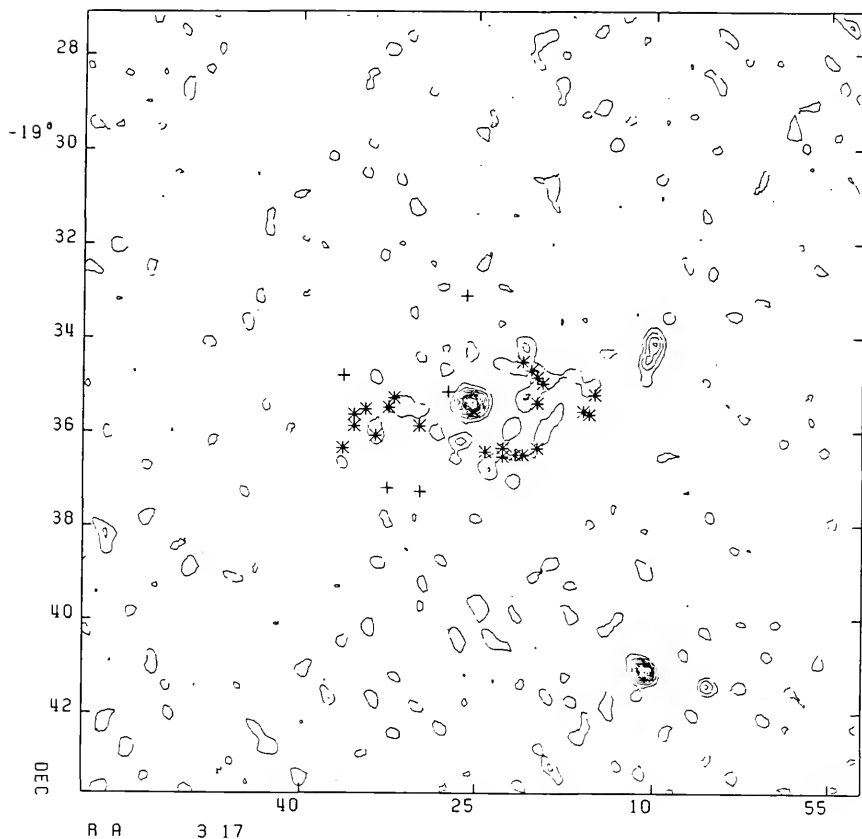


Figure 3-10. Continuum Emission. The contour levels are plotted at intervals of the rms noise level. (\*) represent the positions of HII regions and (+) the positions of fiducial stars. HII regions from Hodge (1969).

after the break. Also indicated in Figure 3-10 are the positions of Hodge's (1969) HII regions. There is a good correlation between these positions and the continuum emission. Continuum emission is also seen from a point source 6.8' south-west of the galaxy center and some extended emission 4' north-west of the center.

### Kinematics of the Neutral Hydrogen

The temperature-weighted mean velocity at a point (x,y) is given by equation 3-2. Before integrating, the spectra are Hanning-smoothed in velocity space as indicated by equation 3-3. The original sampling rate of the data, 20.62km/sec, is close to the filter bandwidth, 25.2km/sec. Therefore, after the smoothing, the data are sampled at the Nyquist rate. The smoothing also increased the signal-to-noise ratio. Figure 3-11 is the resultant velocity field plotted as a contour diagram. Figure 3-12 is the same velocity field shown as a false color image, and Figure 3-13 shows the velocity field superimposed on an optical photograph.

Figures 3-11 to 3-13 clearly indicate that reliable velocities are difficult to obtain in regions of low atomic gas density. The central region and the regions between the spiral arms have no velocities indicated due to the lack of gas. Irregularities can be seen in the velocity contours where the optical arms cross the contours. These irregularities are indicative of gas streaming motions

## NGC 1300

VELOCITY

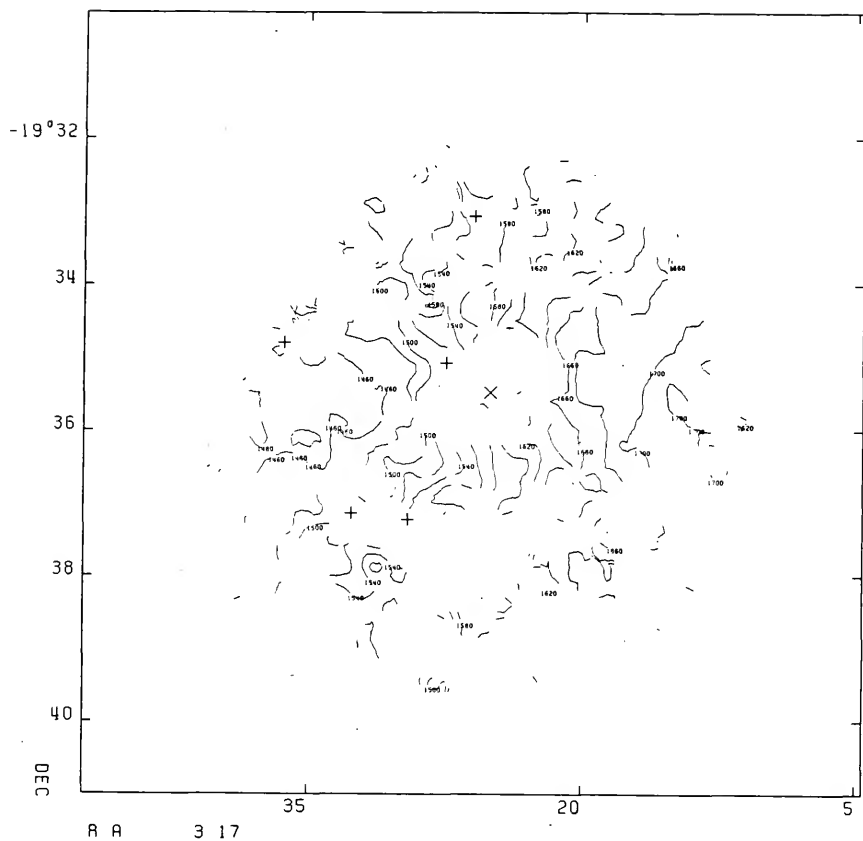


Figure 3-11. Velocity Contours. Velocity field for NGC 1300. The contour interval is 20 km/sec and the contours are labeled in km/sec. Fiducial star positions (+) and the galaxy center (x) are marked.

Figure 3-12. False Color Representation of Velocities. Blue represents low velocities and red represents high velocities.

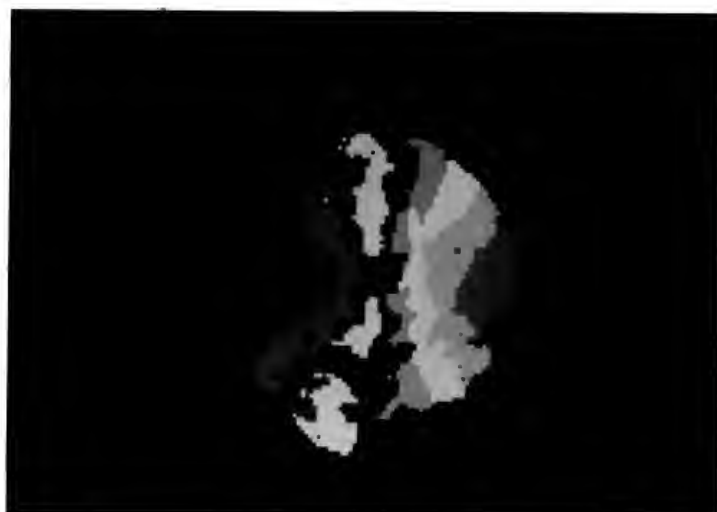
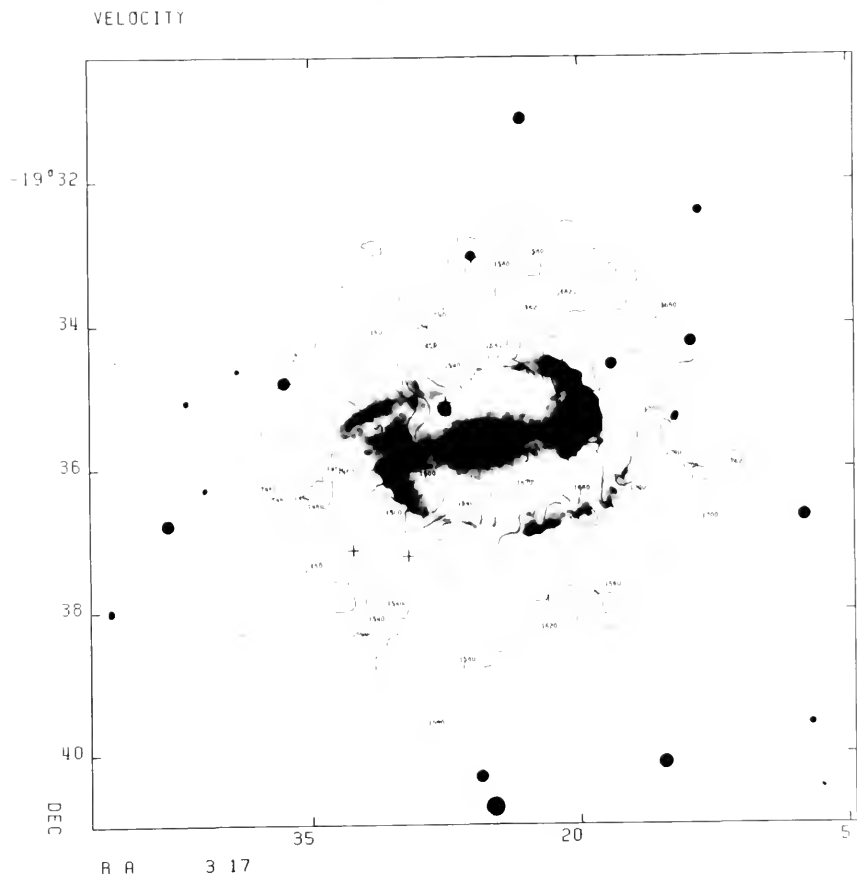


Figure 3-13. Velocity Field Superimposed on Optical Object. The optical image of NGC 1300 is from the National Geographic-Palomar Sky Survey.

## NGC 1300



associated with the spiral structure of the galaxy. The northern half of the galaxy, where there is more interarm gas than in the southern half, shows these irregularities for both the western arm and the end of the eastern arm. In the southern half these effects are emphasized by the lack of gas in the interarm region and the fact that velocities are only shown for the spiral arm regions. There does not appear to be any offset in the velocity contours as they are traced across the bar region. NGC 3992, which also shows a "hole" in the center of the galaxy, displays an offset in the velocity contours from one side of the bar to the other (Gottesman et al., 1984). Although the velocity field displays irregularities, the dominant component in the velocity field is circular rotation.

To quantify the velocity field and to investigate abnormalities, certain global properties of the system must be defined. Defining two components for the velocity field as  $V_{\text{ROT}}(R)$ , the rotation velocity, and  $V_{\text{NC}}(R, \theta)$ , the noncircular motions, the velocity at each point in the galaxy,  $V_{\text{OBS}}(R, \theta)$ , can be written

$$V_{\text{OBS}}(R, \theta) = V_{\text{ROT}}(R) \cos \theta \sin i + V_{\text{NC}}(R, \theta) + V_{\text{SYS}} \quad (3-6)$$

where  $V_{\text{SYS}}$  is the systemic velocity,  $i$  is the inclination of the galaxy, and  $R, \theta$  are the polar coordinates of the position in the galaxy. The inclination is the angle between the sky plane and the galaxy plane, and  $R, \theta$  are measured in the galaxy plane, where the origin for  $\theta$  is the line of nodes.



The noncircular effects,  $V_{NC}(R, \theta)$  can be written (Mihalas and Binney, 1981 pg. 499)

$$V_{NC}(R, \theta) = V_R(R, \theta) \sin \theta \sin i + V_P(R, \theta) \cos i \quad (3-7)$$

where  $V_R(R, \theta)$  is the radial velocity in the plane of the galaxy and  $V_P(R, \theta)$  is the velocity perpendicular to the plane. These noncircular effects can be seen as deviations, in the velocity contours of Figure 3-11, from what would be expected from pure circular rotation. However, it is apparent that the overall dominant component in the velocity field is circular rotation and therefore, for the purposes of the immediate discussion, the noncircular effects will be ignored. This leads to a solution for  $V_{SYS}$ ,  $i$  and the position angle of the line of nodes,  $\phi$ , by minimizing the residuals about equation 3-5 in a least squares fashion (Warner, Wright and Baldwin, 1973). To minimize the effects of radial streaming motions the data points used were constrained to lie within  $\pm 15^\circ$  of the major-axis. To reduce the effects due to regions of low signal-to-noise ratio the data were also constrained to lie between radii of 0.9' and 3.3'. The least squares procedure gave a position angle for the line of nodes of  $\phi = -85.5 \pm 0.5^\circ$ , a systemic velocity of  $V = 1575.0 \pm 0.5 \text{ km/sec}$  and an inclination angle of  $i = 50.2 \pm 0.8^\circ$ . The quoted errors are the standard deviations and are estimates of internal uncertainties; they do not imply that the actual values have been measured to this accuracy. As a point of interest, the major-axis of the bar, measured from the infrared image, is  $\phi = -79^\circ$ .

The value for the systemic velocity is within the range of previous determinations. Sandage and Tammann (1975) quote  $V=1535 \pm 9 \text{ km/sec}$ ; Bottinelli et al. (1970) give  $V=1573 \pm 7 \text{ km/sec}$  and de Vaucouleurs, de Vaucouleurs and Corwin (1976) give  $V=1502 \pm 10 \text{ km/sec}$ . The inclination,  $i=50.2^\circ$ , agrees well with that from de Vaucouleurs, de Vaucouleurs and Corwin (1976),  $i=49^\circ$ , but differs significantly from that suggested by Burkhead and Burgess (1973), who indicate that the galaxy is seen nearly face on. The least squares procedure was run having the inclination fixed and only solving for  $\phi_{\text{LON}}$  and  $V_{\text{SYS}}$ . The only acceptable solutions were found when the inclination was nearly  $50^\circ$ . All solutions with  $i=10\text{--}20^\circ$  gave unacceptable results for  $\phi$  and  $V_{\text{SYS}}$ . Thus, the value found originally,  $i=50.2^\circ$ , was adopted for the inclination of the galaxy.

Using these parameters an estimate for the rotation curve can be derived. The scheme introduced by Warner, Wright and Baldwin (1973) was utilized. This procedure corrects the data for the inclination of the galaxy and averages data in elliptical annuli, circular rings in the galaxy plane. Each point is weighted by the cosine of its azimuthal angle,  $\theta$ , to minimize the effects of systematic radial noncircular motions. Thus, points near the minor-axis will have lower weight than those near the major-axis. The rotation curve was calculated using two different methods:

1. All the data in each annulus were used (angle-averaged method).
2. Only points within  $15^\circ$  of the major-axis, in the plane of the sky, were used to calculate the rotation curve (wedge method).

The rotation curves from these methods are shown in Figures 3-14 and 3-15. The error bars represent plus or minus one standard deviation and are due to a combination of systematic noncircular motions and the sparse distribution of data in that annulus.

The angle-averaged rotation curve, Figure 3-14, shows a curve rising and reaching a maximum of  $V=185\text{km/sec}$ , corrected for inclination, at around  $2.5'$  and then dropping slowly. No data are plotted for the inner  $1.0'$  as there is no reliable information in this region. This is the region of the "hole" in the HI density distribution (see Figures 3-1 to 3-4). At radii greater than  $2.8'$  the errors are very large. However, in this region the value for the rotation curve is determined by only a few data points. The error bars for the rest of the curve are of the order of  $10\text{-}15\text{km/sec}$  and are this large due to the very well defined structure of the hydrogen distribution; each annulus crosses both spiral arms and the interarm region. The interarm region has a sparse data distribution and the errors will consequently be larger than those for the spiral arm region where the data are better distributed. The noncircular

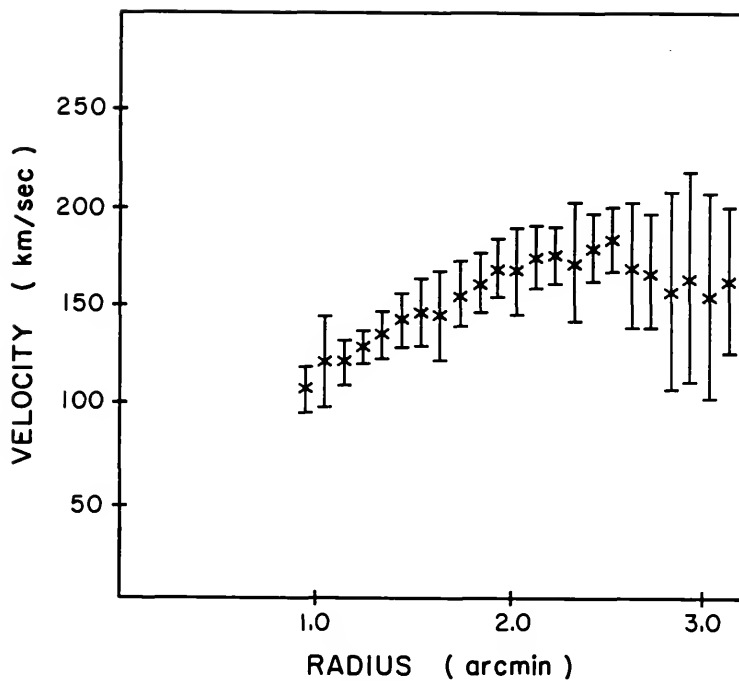


Figure 3-14. Angle-Averaged Rotation Curve. The error bars represent one standard deviation.

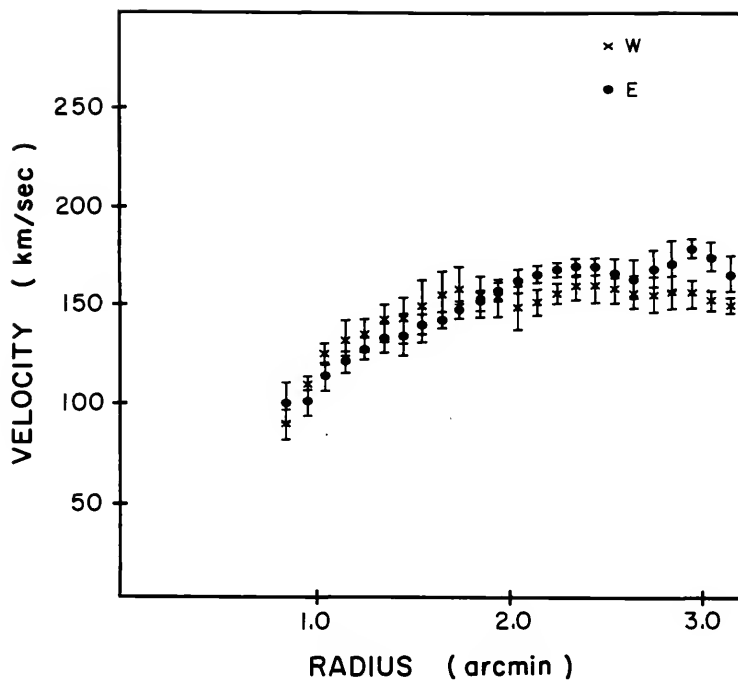


Figure 3-15. Wedge Rotation Curve. Values for the east and west halves of the major-axis are shown. The error bars represent one standard deviation.

effects which were ignored in calculating  $V_{\text{SYS}}$ ,  $i$  and  $\phi$ , also contribute to the error bars shown in the rotation curve. As can be seen from Figure 3-11, these non-circular effects are non-zero and will make a large contribution to the error bars in the rotation curve.

The rotation curve, calculated using the  $30^\circ$  wedge about the major-axis is shown in Figure 3-15. The shape of this curve is the same as the angle-averaged curve. The curve is plotted for two halves of the major-axis. As the data used for this curve are constrained to lie within  $15^\circ$  of the major-axis, the errors are smaller than those in Figure 3-14. This results from the fact that within  $15^\circ$  of the major-axis HI emission is strong and not patchy. In this case the errors are then mainly representative of systematic noncircular motions. Once again, at radii greater than about  $2.8'$ , the errors become large due to the lack of reliable information. From now on, "the rotation curve" will refer to the wedge rotation curve shown in Figure 3-15. The most significant difference between the angle-averaged rotation curve( Figure 3-14) and the wedge rotation curve (Figure 3-15) is that the error bars are significantly larger for the angle-averaged curve. In the region between  $r=1.9'$  and  $r=2.5'$ , the angle-averaged curve lies approximately 20km/sec above that determined by using the  $\pm 15^\circ$  wedge.

The inner portion,  $r < 1.2'$ , of the rotation curve is a fairly good approximation to solid-body rotation. This is

also the region occupied by the bar. Comparing this region with the optical velocities of Peterson and Huntley (1980) shows that the optical velocities and the HI velocities are in good agreement with each other, with the optical velocities rising just a little faster than the HI velocities in the inner 30" of the galaxy, thereafter corresponding well with the HI velocities. This is expected as the optical velocity measurements have higher resolution, 3"-5", than do the HI measurements (resolution 20"). The lower the resolution, the more the effects of beamsmeearing on the rotation curve. In the steeply-rising part of the rotation curve the lower resolution HI measurements will tend to underestimate the rotation curve (Burbidge and Burbidge, 1975). Bosma (1978) suggests that the ratio  $R/B$  should be greater than about 7 to avoid serious degradation of the rotation curve.  $R$  is the Holmberg radius and  $B$  is the halfpower beamwidth. The HI observations of NGC 1300 have  $R/B=4.03'/0.33'$  or  $R/B=12.2$ . Thus the difference between the optical and HI rotation curves should be small, as is seen from Figure 3-16.

The optical velocities only extend to 1.6' and are calculated from the emission lines of [NII] and [SII] and from the stellar H and K CaII absorption lines. Figure 3-16 shows a comparison of the rotation curves from HI, the emission lines and the absorption lines for the inner 1.6'. The HI rotation curve provides an estimate for the angular

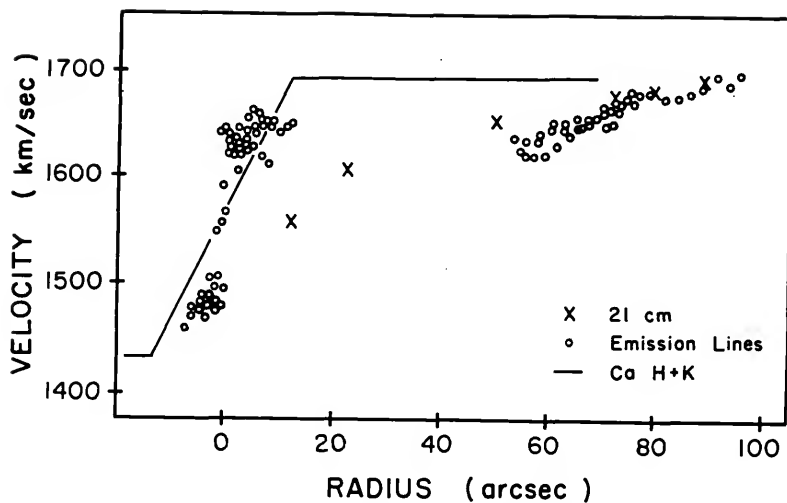


Figure 3-16. Optical and HI Rotation Curves. Comparison of rotation curves determined from optical measurements and from 21cm radio measurements. Optical measurements from Peterson and Huntley (1980).



velocity of the solid-body portion of the rotation curve. A least squares analysis for the inner 1.3' gives 108 10km/sec/arcmin, or at a distance of 17.1Mpc, 22km/sec/kpc. This region is the region inhabited by the bar. Outside this region the rotation curve rises less quickly, being nearly flat, reaching a maximum at approximately  $r=2.5'$ . In the above analysis of the 21cm rotation curve it must be remembered that these values are very dependent on only one or two data points. As can be seen in Figures 3-4 and 3-12, the density and velocity maps, the region covered by the optical velocities is the region occupied by the bar and this region has almost no reliable information at 21cm. Thus any analysis in the inner 1.3' must be considered to be very crude and be used only as an indication of general trends and not a definitive statement.

Casertano (1983) and Hunter, Ball and Gottesman (1984) described the effects of truncating a disk on its associated rotation curve. The rotation curve for a truncated disk exhibits a sharp drop just beyond the truncation edge of the disk. These truncation signatures may have been observed in NGC 5907 (see Casertano, 1983), NGC 3992 (Gottesman et al., 1984) and NGC 1073. As NGC 1300 has a well-defined hydrogen distribution it would seem a likely candidate to display a truncation signature in its rotation curve. However, Figure 3-17, which plots the rotation curve out to  $r=6.4'$ , shows that it is difficult to determine whether or not a truncation signature exists.

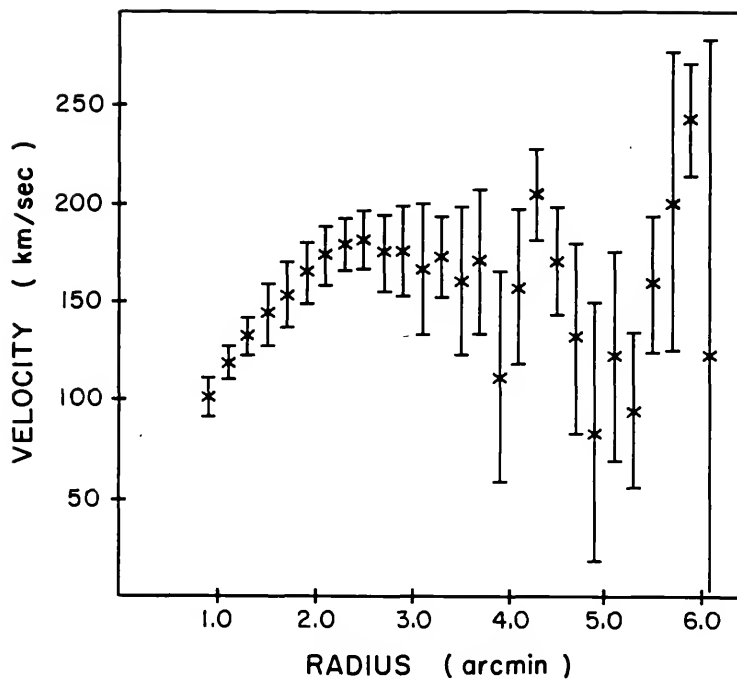


Figure 3-17. Rotation Curve to 6.4 arcmin. Annulus-averaged rotation curve for NGC 1300 out to  $r=6.4'$ . Error bars represent one standard deviation.

The lack of reliable data beyond about  $r=3.2'$  makes the determination of the rotation curve very unreliable. The apparent drop in the rotation curve is almost certainly only due to the poor signal-to-noise ratio and not to any real truncation signature. Comparing Figure 3-7, which is the radial dependence of the deprojected, angle-averaged surface density, with Figure 3-17, shows that the surface density is extremely low and the signal-to-noise ratio is small. The joined points in Figure 3-7 represent the upper and lower limits for a value, and, as can be seen, beyond  $r=3.2'$  this range is rather large. Thus, the conclusion is that the rotation curve for NGC 1300 does not show any evidence for a truncation signature at the sensitivity of this survey.

#### Mass Models

An estimate for the mass of NGC 1300 can be obtained by fitting simple models to the rotation curve of Figure 3-15. As more detailed models will be constructed in a later section, these mass models will be utilized as the initial input parameters for the hydrodynamical code. No attempt was made to fit the perturbations evident in the rotation curve; only the broad overall shape was modeled as the aim was to get an estimate for the mass interior to the last reliably measured point on the rotation curve and to get an estimate for the type of disk and its parameters.

Various types of disks were used in attempting to model the rotation curve. The first model considered was the Generalized Mestel Disk, or GMD, of Hunter, Ball and Gottesman (1984). The GMD is also a member of Toomre's (1963) family of infinitely flattened disks, specifically an  $n=0$  disk. The circular velocity in the GMD at  $r$  is given by

$$v_o(b,r) = C[1+b^2/r^2 + b/r(1+b^2/r^2)^{1/2}]^{-1/2} \quad (3-8)$$

and the disk mass interior to  $r$  by

$$M_o(b,r) = (C^2 r/G) [(1+b^2/r^2)^{1/2} - b/r]. \quad (3-9)$$

The length scale,  $b$ , and the amplitude,  $C$ , for the model shown in Figure 3-18 are  $b=0.95'$  and  $C=210.0\text{ km/sec}$ . The mass interior to the last measured point at  $r=3.2'$ ,  $15.9\text{ kpc}$ , is therefore  $7.8 \times 10^{10} \text{ Mo}$ . However, as can be seen from Figure 3-18, for  $r > 2.4'$  the model and the observations deviate significantly. In the bar region,  $r < 1.3'$ , the GMD curve lies above the observed HI curve but matches the optical velocities reasonably well.

A better model would have a more centrally condensed disk than the GMD. This type of disk has a rotation curve which drops in the outer regions of the disk, unlike the GMD. Figure 3-18 also shows the rotation curve for the  $n=1$  disk of Toomre (1963). For this disk the circular velocity at  $r$  is given by

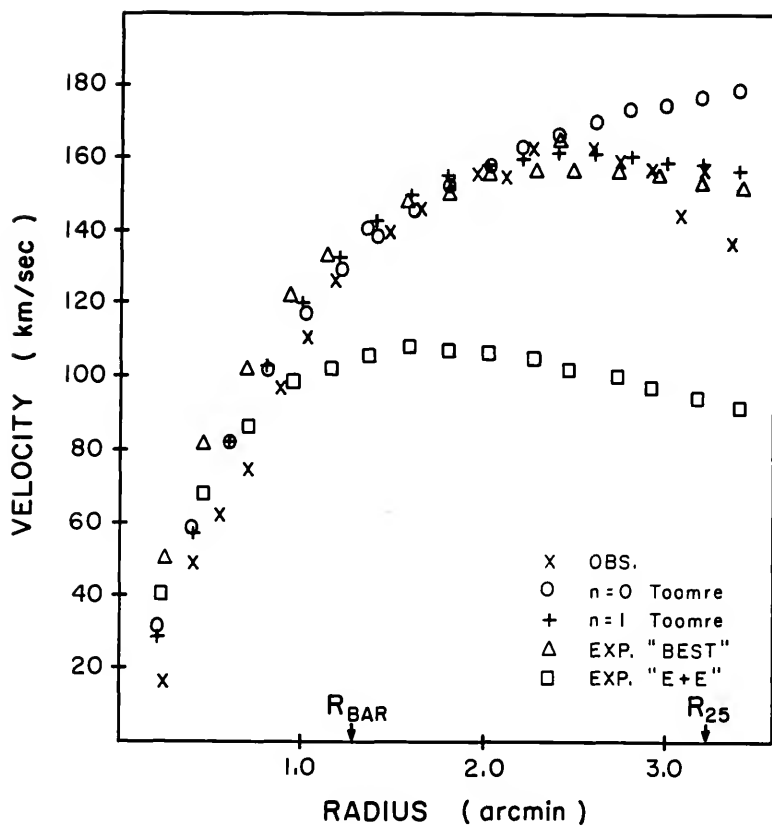


Figure 3-18. Mass Models for NGC 1300. Rotation curves for various mass models for NGC 1300 compared with the observations. The radius of the bar and the radius at 25 mag/arcsec<sup>2</sup> are shown.

$$v_1(b, r) = Cr[b(r^2 + b^2)^{3/2}]^{-1/2} \quad (3-10)$$

and the disk mass interior to  $r$  by

$$M_1(b, r) = (C^2 r / G) [1 - b(r^2 + b^2)^{-1/2}]. \quad (3-11)$$

The length scale,  $b$ , and the amplitude parameter,  $C$ , for the model shown in Figure 3-18 are  $b=1.75'$  and  $C=455.0(\text{km/sec})\text{arcmin}$ . The maximum value for this rotation curve occurs at  $r = \sqrt{2b} = 2.47'$  and is given by

$$v_{\max} = \left( \frac{4}{27} \right)^{1/4} \frac{C}{b}. \quad (3-12)$$

This model is a good fit to the observations, especially in the region of most interest and most reliable velocity data. The disk mass for this model interior to  $r=3.2'$  is  $4.9 \times 10^{10} M_{\odot}$ .

Higher order,  $n > 1$ , Toomre disks decline too rapidly, after reaching their maxima, to provide a good fit to the observed rotation curve. An exponential disk was also calculated in an attempt to match the observations. The form of the exponential disk is (Freeman, 1970)

$$v^2 = \pi G \mu_0 \alpha R^2 \left[ I_0 \left( \frac{\alpha R}{2} \right) K_0 \left( \frac{\alpha R}{2} \right) - I_1 \left( \frac{\alpha R}{2} \right) K_1 \left( \frac{\alpha R}{2} \right) \right] \quad (3-13)$$

where  $\mu_0$  is the surface density,  $\alpha^{-1}$  is the scale length and  $I_0$ ,  $I_1$ ,  $K_0$ ,  $K_1$  are modified Bessel functions. Using the

scale length  $\alpha^{-1}=6.96\text{kpc}$  from Elmegreen and Elmegreen (1985) gave the rotation curve shown in Figure 3-18. This curve does not reach the velocities observed in the HI. However, if a halo is added to this disk the rotation curve can be made to fit the observations far more closely. This case implies that the mass-to-luminosity ratio for the disk is constant. However, the HI rotation curve can be fit well by using an exponential disk with a different scale length. This model does not have a halo. The rotation curve resulting from this disk, with  $\alpha^{-1}=10\text{kpc}$ , is shown in Figure 3-18. This curve and the  $n=1$  Toomre curve are very similar, the main difference being that the exponential curve rises faster than the Toomre curve in the inner  $1.2'$ . In the region near the ends of the bar,  $r=1.0'$  to  $1.7'$ , the exponential rotation law lies above the observed HI rotation curve, whereas between  $r=2.2'$  and  $r=2.9'$ , the exponential lies below the observed HI curve. As this exponential rotation law has a scale length greater than the scale length for the luminosity distribution (Elmegreen and Elmegreen, 1985), this implies that the mass-to-luminosity ratio for this disk increases as the radius increases. The total mass, out to  $r=\infty$ , for this disk is  $4 \times 10^{11} \text{Mo}$ . As neither the exponential disk nor the  $n=1$  Toomre disk provide significantly better fits to the HI rotation curve than the other, an  $n=1$  Toomre disk is used initially in the hydrodynamical modeling procedure.

The observed global profile of the neutral hydrogen in NGC 1300 is shown in Figure 3-19. This spectrum has been formed by integrating the Hanning-smoothed pixel spectra over all pixels assumed to contain line signal. No correction has been made for the effect of bandwidth smoothing.

Table 3-2 presents a summary of the neutral hydrogen observations.



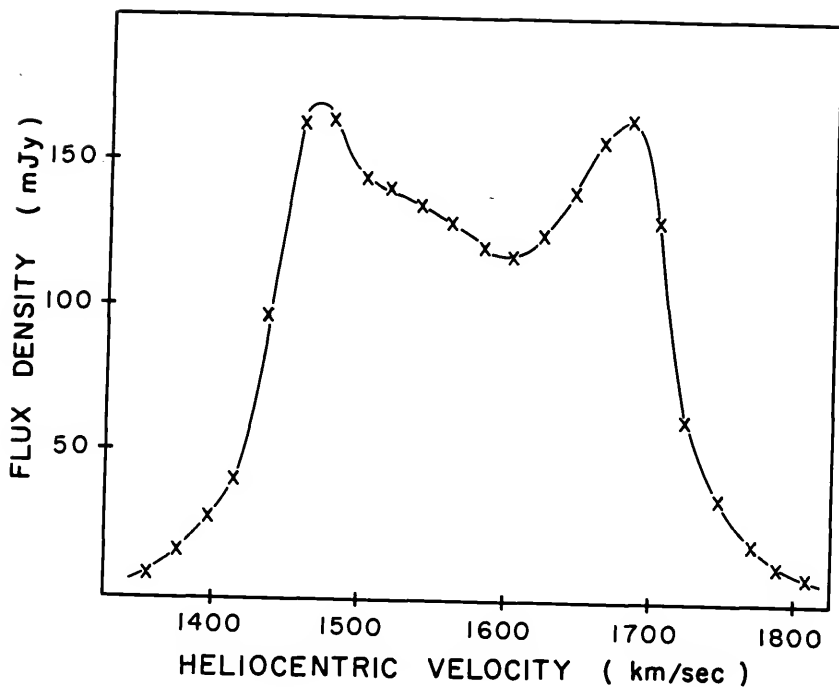


Figure 3-19. HI Observed Global Profile. This profile calculated from the interferometric observations of NGC 1300.

TABLE 3.2

Summary of Neutral Hydrogen Observations for NGC 1300

Parameter	NGC 1300
Synthesized beam (FWHM) (arcsec)	20.05x19.53
Position angle of beam ( $^{\circ}$ )	64.5
Channel separation (km/sec)	20.6
Filter width (km/sec)	25.2
Channel rms noise (K)	1.26
Total HI map rms noise ( $10^{19}\text{cm}^{-2}$ )	5.00
Peak HI density ( $10^{21}\text{cm}^{-2}$ )	1.59
Observed systemic velocity (km/sec)	$1575.2 \pm 0.5$
Adopted distance (Mpc) <sup>a</sup>	17.1
Diameter of HI disk (arcmin) <sup>b</sup>	6.40
Peak continuum brightness (K)	12.6
Position angle, line of nodes ( $^{\circ}$ )	$-85.5 \pm 0.5$
Inclination angle ( $^{\circ}$ )	$50.2 \pm 0.8$
Observed width, Global profile (km/sec) <sup>c</sup>	345
Maximum rotation velocity (km/sec)	185
Radius of maximum velocity (arcmin)	2.47
Atomic hydrogen mass, $M_{\text{HI}}$ , ( $10^9\text{Mo}$ )	2.54
$M_{\text{HI}}/L_{\text{B}}$ (solar units)	0.11

a De Vaucouleurs and Peters (1981).

b Measured at an observed surface density,  $N = 1.59 \times 10^{20}\text{cm}^{-2}$ .

c Full width at 0.2 of peak.

#### CHAPTER IV SURFACE PHOTOMETRY

Theoretical modeling of galaxies in recent years has shown a tendency for the stellar disks to develop long-lasting bar-like structures of global extent (see references in Baumgart and Peterson, 1986). N-body experiments by Miller and Smith (1979, 1980, 1981) and Hohl and Zang (1979) suggest that prolate or triaxial bars are the natural form to which a dynamical system may evolve. The conclusion is that bar-like stellar structures are a preferred dynamical form in the process of galaxy formation and evolution. In a previous attempt to model NGC 1300, Peterson and Huntley (1980) used a bar potential of the form given by Miller and Smith (1979) as the non-axisymmetric perturbation. However, Baumgart and Peterson (1986) show that the form of stellar bars in barred spirals is not consistent with the predictions of the three-dimensional N-body models of Miller and Smith (1979). They conclude, in fact, that the agreement is very poor. It would thus seem warranted that, in attempting to model the response of the gaseous disk to an imposed gravitational potential, some sort of "observed" bar potential be used, rather than a "nice, convenient" theoretical model which does not fit the observations very

well. With this objective set, surface photometry of NGC 1300 will be used to provide an "observed" bar potential to use in the numerical modeling of the galaxy. As the modeling procedure involves a search through a multi-parameter space, any observational constraints that are available will help to reduce the volume of the space that needs to be searched. By providing the bar potential the number of possible solutions is reduced and will hopefully lead to astronomically plausible solutions as well as providing some observational constraints for the non-axisymmetric mass distribution.

The stellar population of the bar in a barred spiral galaxy is expected to be well-mixed (Contopoulos, 1983). For the modeling procedure used here the assumption can be made that the imposed gravitational potential is due largely to the stellar distribution and that the gas is responding to this. Therefore for the "observed" bar potential some sort of measure of the stellar distribution is needed. Near infrared surface photometry is well-suited for this purpose. Often the bar regions in barred spiral galaxies contain dust lanes; NGC 1300 has two very prominent dust lanes in the bar region (see Figure 1-1). Surface photometry is needed that will penetrate these dust lanes and give the best possible information on the unobscured brightness distribution of the stellar population and contain as little contamination as possible from the dust in the galaxy. The surface photometry

used for this purpose, as well as photometry in the blue wavelength region, has been kindly provided by Drs. B. Elmegreen and D. Elmegreen. Photometry at 2.2  $\mu\text{m}$  has been provided by Drs C. Telesco and I. Gatley. For modeling the bar, only the near infrared region will be used. However, comparisons between colors and surface brightness distributions will be analysed using all the wavelength regions. Unfortunately, due to the lack of photoelectric photometry, only relative intensity calibrations are available. As the important quantities needed in the procedure to calculate an "observed" bar potential are the two-dimensional shape of the bar and the form of the brightness distribution, having only relative intensities will not hinder the determination of the "observed" bar.

#### Calculation of the Volume Mass Distribution

Surface photometry can only provide two-dimensional information on the bar shape and the brightness distribution. Some method is required to relate these two-dimensional quantities to the three-dimensional quantities needed in the modeling procedure. The modeling requires a triaxial figure and a volume mass distribution. There is no unique solution to this problem, which means that some astronomically plausible assumptions have to be made so that a three-dimensional figure can be calculated from the two-dimensional information available. The assumptions used for this conversion are

1. The mass-to-light ratio,  $M/L$ , within the bar is constant.
2. The three-dimensional shape of the bar can be described as a triaxial ellipsoid.

The assumption of constant  $M/L$  within the bar means that the form of the mass distribution is the same as the form for the surface brightness distribution. This assumption also means that only having relative intensities for the surface photometry will not preclude the extraction of the form of the mass distribution from the surface brightness distribution.

The assumption of a triaxial ellipsoid for the three-dimensional shape of the bar is made for the following reasons:

1. It is the most general form for a three-dimensional, elongated object that is analytically tractable.
2. It is the form most often speculated to be the three-dimensional shape of bars in barred spiral galaxies and of elliptical galaxies as well.

Projection effects in triaxial figures have been considered most recently by Stark (1977). He considered the specific case in which the volume brightness distribution is constant on similar concentric, nested ellipsoids. He shows that irrespective of viewing angle the projection of these surfaces will be similar concentric ellipses. The converse is also true. Thus, in principle, a triaxial figure can be

calculated from a set of observed isophotes, if the isophotes are assumed to be concentric ellipses. Ball (1984, 1986) applied this method to model the near infrared isophotes of NGC 3359; Hunter et al. (1986) have also used the technique to model the bar of NGC 3992.

The geometric parameters which describe the shape and orientation of the triaxial figure are the axial ratio,  $\beta$ , of the isophotes and the three Euler angles,  $\theta$ ,  $\phi$ , and  $\psi$ , which relate the observer's coordinates to those in which the equations of the ellipsoidal surfaces have the form

$$(tx)^2 + (ty)^2 + z^2 = -a_v \quad (4-1)$$

where  $a_v$  is a parameter describing the volume brightness distribution.

For a barred spiral galaxy where one axis is assumed to be normal to the disk, the Euler angles become:  $\theta$ , the complement of the inclination angle  $i$ ;  $\psi$ , the angle in the sky between the major-axis of the isophotes of the bar and the line of nodes of the disk; and  $\phi$ , which is the angle in the sky plane between the line of nodes and the projected direction of the shorter of the two axes which lie in the disk plane. The angle  $\phi$  is an unknown and has a finite range of values allowed by the observations (Ball, 1984).

The volume brightness distribution can be calculated from the surface brightness distribution and, assuming constant M/L within the bar, the form of the volume mass density can be found. The relationship between volume

brightness distribution,  $F_V(a_V)$  , and surface brightness distribution,  $F_S(a_S)$ , is given by (Stark, 1977)

$$F_V(a_V) = \frac{-f^{1/2}}{\pi} \int_{a_V}^{\infty} \left[ \frac{d}{da_S} F_S(a_S) \right] (a_S^2 - a_V^2)^{-1/2} da_S \quad (4-2)$$

where  $f$  is a constant for a given bar (Stark, 1977; Ball, 1984).

The function  $F_S$ , the surface brightness distribution, is obtained by describing the observed surface brightness as an analytical function. This function should be as good a fit to the observed surface brightness distribution as possible and must go to zero at infinity. For reasons of convenience it is helpful if the type of function chosen for  $F_S$  is one that allows equation 4-2 to be evaluated analytically.

Thus, in summary, the quantities needed from the surface photometry to describe the bar are

1. The functional form of the surface brightness distribution,  $F_S(a_S)$ , gives , via equation 4-2, the volume brightness distribution,  $F_V(a_V)$  , and, assuming constant  $M/L$  within the bar, the form of the volume mass density.
2. The axial ratio of the isophotes and their orientation gives the axial ratio and semi-major axis of the triaxial figure.



## Surface Photometry of NGC 1300

### Modeling the I Passband Features

The surface photometry used to model the bar for NGC 1300 is near infrared (I passband) having an effective wavelength of  $8250\text{\AA}$  and a short wavelength cut-off of  $7300\text{\AA}$ , which thus excludes the Hydrogen alpha line emission. The reduction procedures have been described previously by Elmegreen and Elmegreen (1985). Figure 4-1 shows a gray scale representation of the galaxy in this passband; Figure 4-2 is a contour plot of the I plate. The galaxy image in this passband is clearly dominated by the bar, as expected at this wavelength, although spiral arms can be traced through almost  $180^\circ$  in azimuth. Clearly evident at the center of the galaxy is a strong peak of emission, a nuclear bulge component. The west arm shows a break at a position angle of  $0^\circ$ . A similar but not as sharply delineated break is evident in the east arm at position angle  $170^\circ$ . These features correspond to the breaks evident in the optical photograph.

The prominence of the bar in this passband and the lack of evidence for major dust obscuration, although some will be present, bodes well for the extraction of a triaxial figure from this photometry for the hydrodynamical calculations. Some evidence for the dust lanes, clearly visible in the optical photograph (Figure 1-1), can be seen near the ends of the bar. Here the isophotes are pinched

NGC 1300 IR 8250A

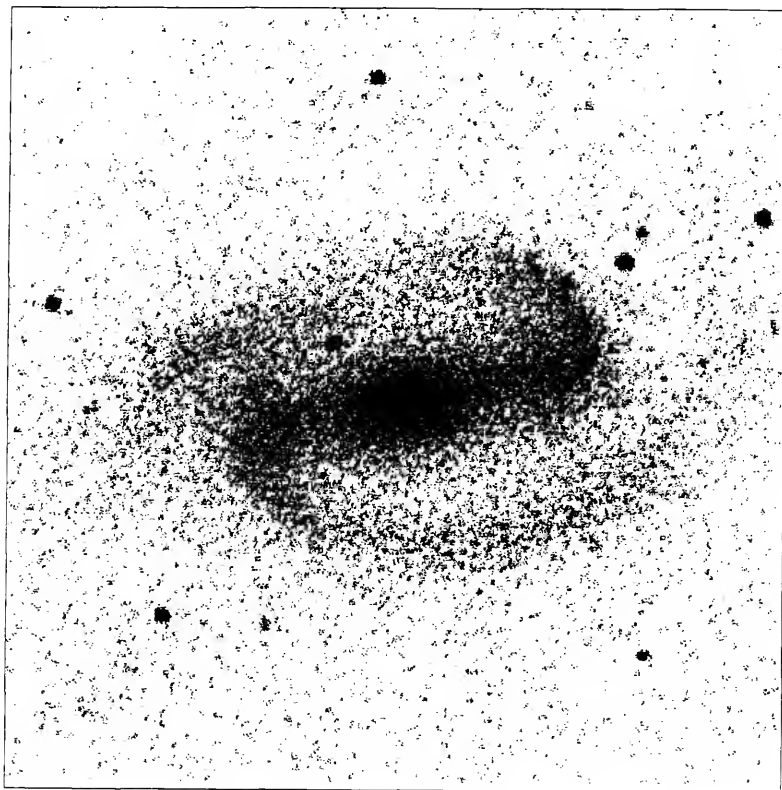


Figure 4-1. NGC 1300 Gray Scale I Passband.

## NGC 1300

N1300.1R

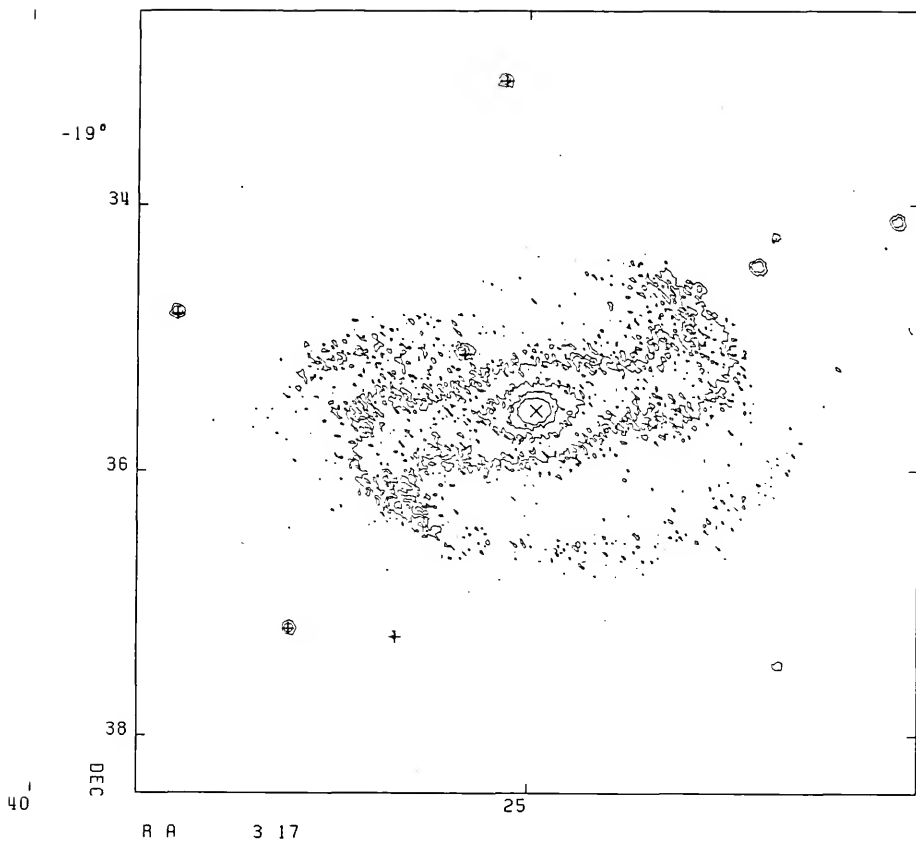


Figure 4-2. Contour Plot of I Plate. The contour interval is 10% of arbitrary peak value. Fiducial star positions are marked (+).

together. In following the isophotes from the center outwards, the general trend is for an elliptical shape. The dust lane region tends to pinch the isophotes together and beyond this region they again broaden out. This contamination of the isophotes will not be serious in the attempt to extract a triaxial figure, as long as it is recognized and compensated for in the modeling of the brightness distribution. The relative lack of importance of the dust obscuration at this wavelength can be estimated by comparing profiles from the I passband with profiles from other passbands, such as the blue. This will be done in a later section.

The first step in modeling the bar as a triaxial figure based on the observations is to remove some of these small scale fluctuations in the isophotes. Some method is needed to "average out" these fluctuations while leaving the overall shape of the isophotes largely unaltered and not too broadened. The data from Figure 4-2 were convolved with a two-dimensional Gaussian function with  $\sigma=0.045'$ , or 2 pixels (FWHM), and truncating the Gaussian at the 1% level. The resulting image is shown in Figure 4-3. A good deal of the small scale fluctuations have been smoothed-out but some are still present. A convolution of the original data with a two-dimensional Gaussian with  $\sigma=0.09'$ , or 4 pixels (FWHM), showed a significant decrease in the small scale fluctuations, but also showed a distinct broadening of the

isophotes. This convolution was therefore discarded and the 2 pixel convolution was used. Four components are clearly present in this image:

1. A central bulge.
2. A broad elongated bar.
3. Spiral arms.
4. A low brightness disk component.

Using this passband to provide constraints for the triaxial figure to be used in the hydrodynamical modeling procedure requires that only the bar component be used. Thus, estimates for the shapes and brightness contributions to the overall brightness distribution of the bulge and disk components must be made. The arms can, in actual fact, be ignored as their contribution starts at the end of the bar and does not affect the bar region itself. However, the bulge and the disk effects must be allowed for and corrections applied.

As an aid in isolating the various components, profiles were constructed at various positions in the galaxy. The bar major- and minor-axis profiles are plotted in Figure 4-4; cross profiles at 20" intervals along the bar are also shown. Some features of note in these profiles are the central bulge and the rise at  $r=76''$  of the major-axis brightness when compared with the other profiles. The latter is the beginning of the spiral structure. The disk component is seen at  $r=40''$  on the minor-axis and cross profiles. The

## NGC 1300

CNVLED

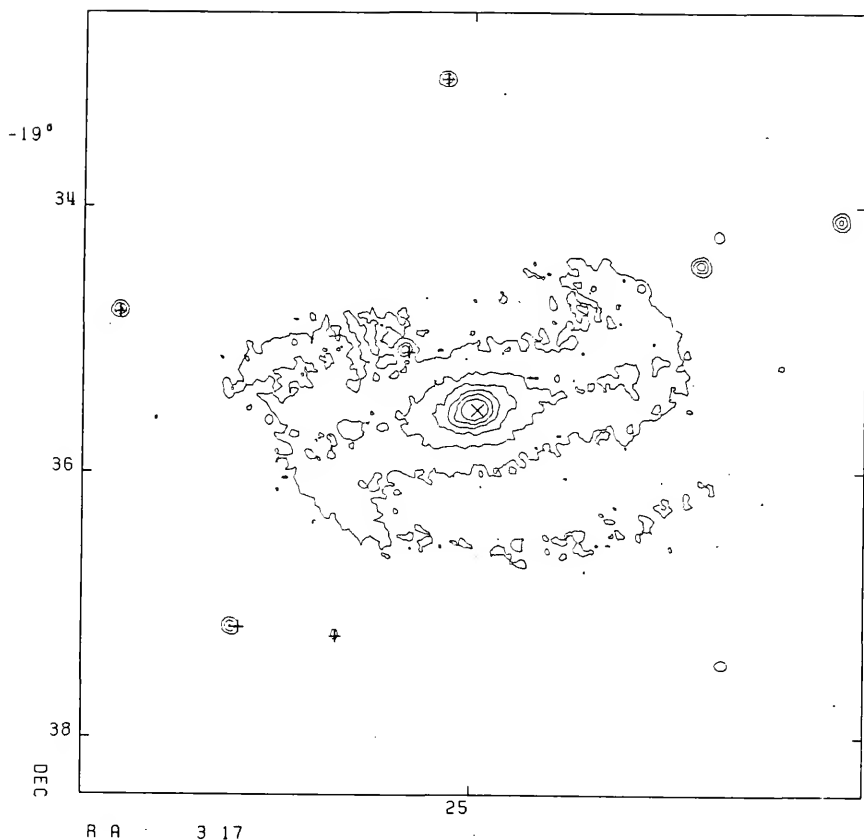


Figure 4-3. Convolved I Passband Image NGC 1300. Contour plot of the convolved image of NGC 1300. Contour levels are arbitrary and fiducial star positions are shown (+).

bulge has a steep rise and a noticeably flat plateau region at the center. These profiles correspond to Freeman type 1 profiles, in that the intensity always lies above the contribution from the disk (Freeman, 1970). This means that

$$I(r) \geq I_0 \exp[-\alpha r] \quad (4-3)$$

for all observable  $r$ .

Elmegreen and Elmegreen (1985) analyzed the disk component of the galaxy as having an exponential form,

$$I(r) = I_0 \exp[-\alpha r] \quad (4-4)$$

where  $\alpha^{-1}$  is an effective scale length and  $I_0$  is a scaling factor. The values quoted in their Table 2 are too large by a factor of 2, thus their scale length for the I passband for NGC 1300 is  $\alpha^{-1} = 6.96 \text{ kpc}$ . At a distance of  $17.1 \text{ Mpc}$  this corresponds to  $\alpha^{-1} = 1.399'$  for NGC 1300.

Estimates for the ellipticity, and hence the inclination, and major-axis position angle were calculated by using a few outer isophotes. These isophotes are far enough from the bar and spiral arm regions so that the assumption can be made that they are unaffected by these components and only have contributions from the disk component. The factor,  $I_0$ , was calculated using an iterative procedure which calculates a model brightness distribution for the disk. By comparing this model with the outer regions of the observations a value for  $I_0$  can be found quickly. This procedure yielded a good fit to the observed outer isophotes using the following parameters:

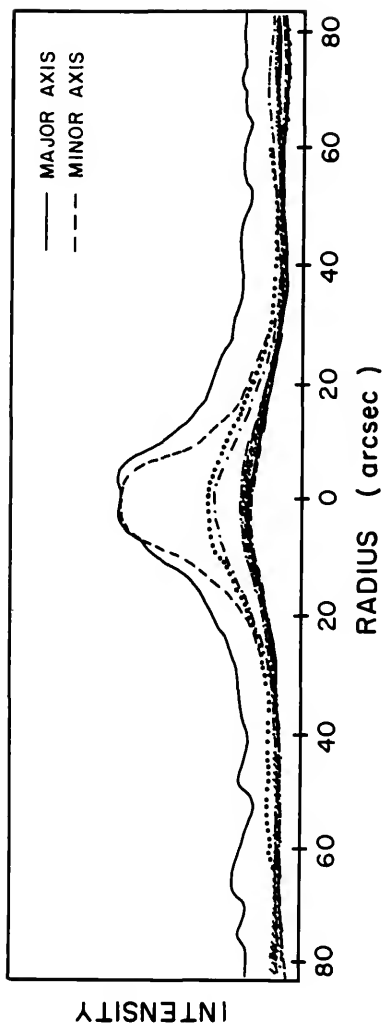


Figure 4-4. Bar Brightness Profiles. Major- and minor-axis profiles for I band image of NGC 1300. Also plotted are cross-sections at intervals of  $r=20''$  along the bar.



1. Axial Ratio  $\beta = 1.546$ , ( $i=50^\circ$ ).
2. Position Angle  $\phi = 101^\circ$ .
3. Length Scale  $\alpha^{-1} = 1.399'$ .
4. Scaling Factor  $I_0 = 150$ , (arbitrary units).

Thus, the form of the disk brightness distribution is

$$I(r) = 150 \exp[-r/1.399] \quad (4-5)$$

where  $r$  is in arcminutes.

Figure 4-5 shows this disk and the observed major-axis profile. As this exponential form for the disk surface brightness gave a good fit to the observations in all but the very inner regions, no other functional form was tried. In the inner region, where the exponential form deviates most significantly from the observations, the exact form of the components is unimportant, as the region of most interest is in the outer bar region. The isophotes in the central bulge region are not used in trying to extract a bar figure from the observations. Using an exponential form for the disk surface brightness rather than some other functional form was a choice of convenience and because this form gave a good fit to the observations. This does not imply that the disk is actually an exponential disk. No attempt was made to calculate a definitive disk type; the objective of this component fitting procedure was just to get an estimate of the bar figure.

The model disk brightness distribution was subtracted from the smoothed image, leaving the bar, spiral arms and bulge components. The spiral arms in this "disk-subtracted"

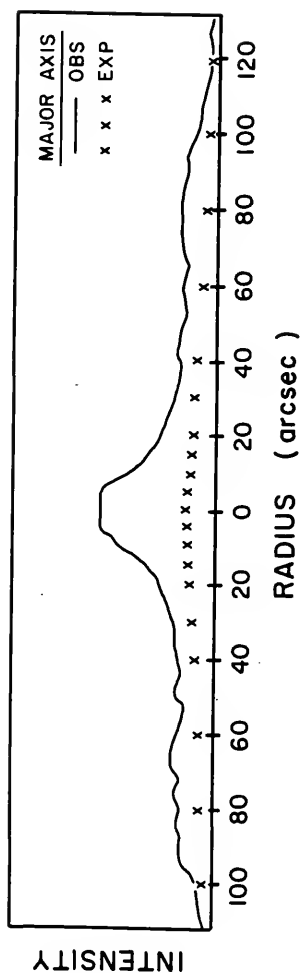


Figure 4-5. Disk Surface Brightness. Exponential disk and observed major-axis profile for I band image of NGC 1300.

image can be traced through almost  $340^\circ$  in azimuth. The next step in isolating the bar contribution is to remove the bulge component.

The removal of the bulge component does not have to be exact. If the assumption is made that the bulge has a limited radial size, and if only the outer isophotes of the bar are used in the modeling procedure, then only a reasonable estimate of the bulge need be removed. As can be seen in Figure 4-5 the central portion of the brightness distribution is rather steep with a broad plateau feature at the center. This is partly due to the photographic plate being saturated at the center (Elmegreen and Elmegreen, 1984). Various functional forms were tried in fitting these inner isophotes. Gaussian functions of the correct width did not have the correct plateau feature at the center; cylindrical functions had the correct plateau feature but not the required wings in the distribution. A functional form represented by a cylinder, convolved with a two-dimensional Gaussian function gave the best fit to both the plateau feature and the wings of the distribution. The forms for the cylinder and the convolving Gaussian are

1. Cylinder:

$$a) I(r) = I_0 \quad r < r_0; \quad I(r) = 0 \quad r > r_0 \quad \text{where } I_0 = 900 \\ \text{(arbitrary units), and } r_0 = 0.1125'.$$

2. Gaussian:

a)  $f(r) = f_0 e^{-r^2/2\sigma^2}$  where  $f_0 = 1$  (arbitrary units), and  $\sigma = 0.225''$  (FWHM).

The resultant bulge is shown in Figure 4-6. The bar major-axis profile after subtraction of the disk and bulge components is shown in Figure 4-7. A contour plot of the resultant brightness distribution is shown in Figure 4-8.

In modeling the brightness distribution of the bar, only isophotes away from the center are used. This is because the true form of the bulge is not known and the procedure used here is only approximate. Two sets of parameters are needed to characterize the bar: a geometrical set consisting of the axial ratio and the position angle of the major-axis of the isophotes; and a major-axis radial brightness distribution.

The geometrical parameters were estimated by comparing model concentric ellipses with the observed isophotes. The parameters used for the geometrical set are

1. Axial ratio  $\beta = 2.93$
2. Position angle  $\phi = 111^\circ$

Two functional forms for the brightness distribution in the bar were used, an exponential of the form

$$I(r) = I_0 \exp[-\alpha/r] \quad (4-6)$$

and a Gaussian of the form

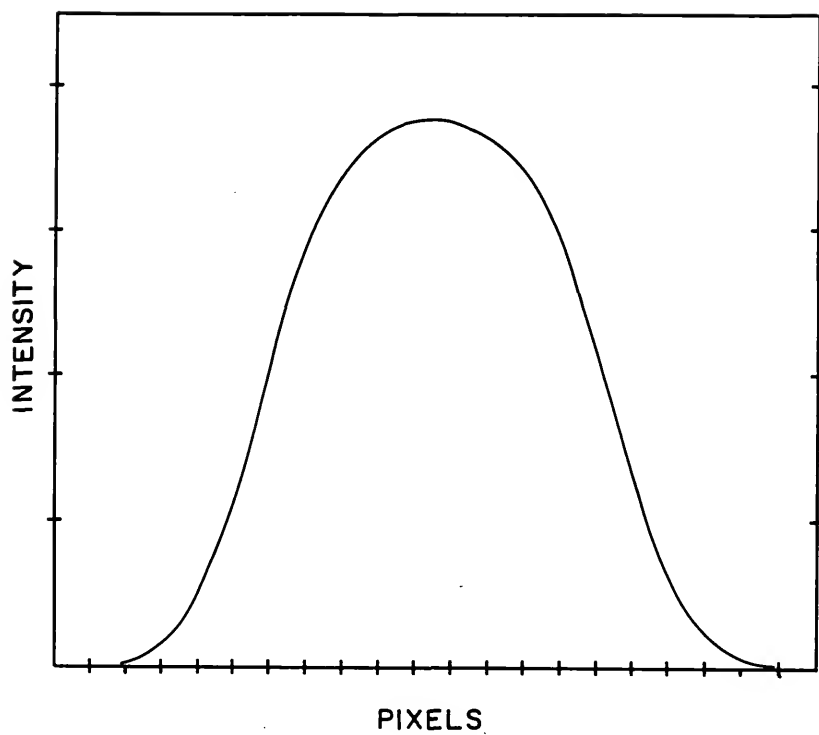


Figure 4-6. Bulge Component Model. Cylindrical function convolved with a Gaussian function used to model the bulge in NGC 1300.

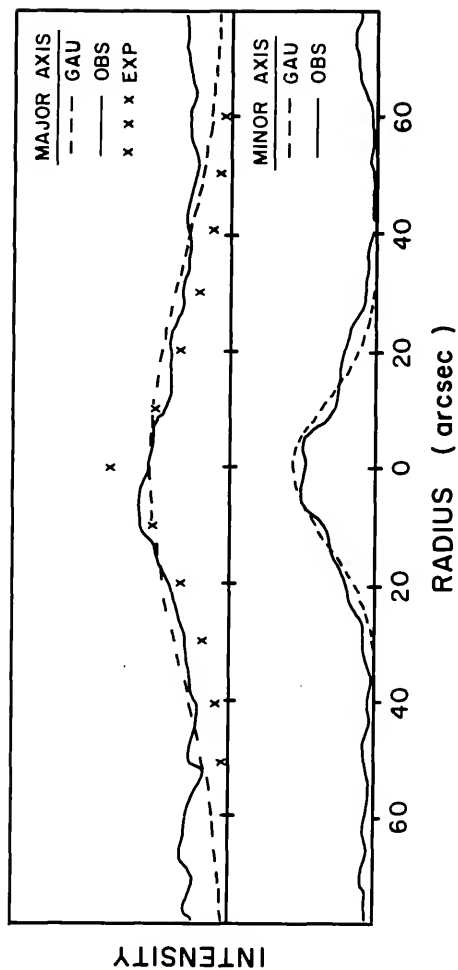


Figure 4-7. Bulge Subtracted Disk Profile. Comparison of model Gaussian and exponential bar major-axis profiles after subtraction of the bulge.

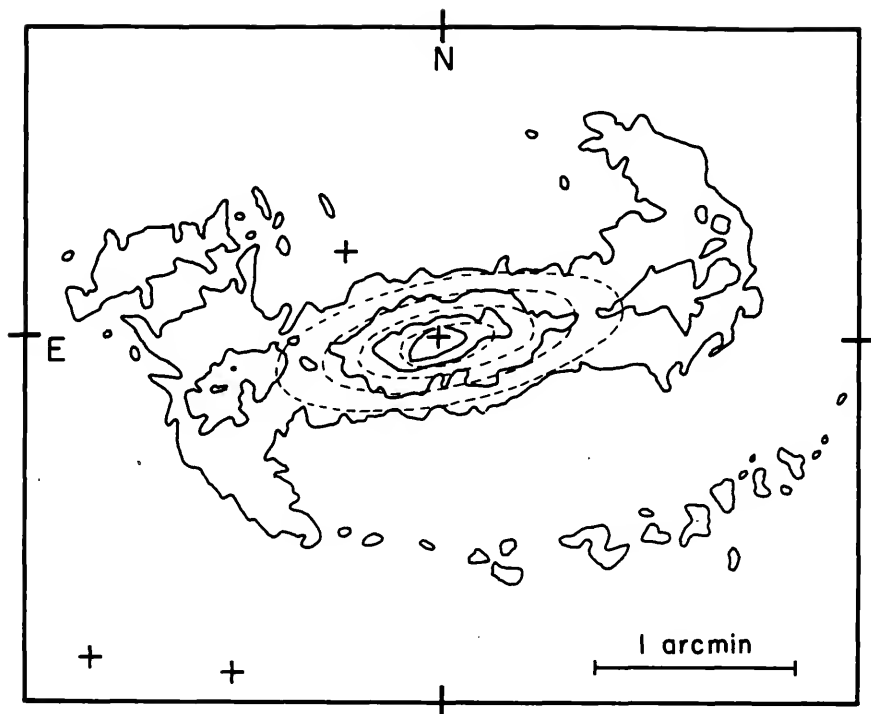


Figure 4-8. Bulge Subtracted Contour Plot. Model brightness distribution contours for NGC 1300. A Gaussian distribution is shown for the bar model. Fiducial star positions and the observed brightness distribution are also marked.

$$I(r) = I_0 e^{-r^2/2\sigma^2} \quad (4-7)$$

In contrast to Baumgart and Peterson (1986), who find that the radial distribution is best fit by an exponential function, the observed profile is significantly better fit by a Gaussian function than by an exponential. Figure 4-7 also compares the "best fit" Gaussian and the "best fit" exponential with the bulge- and disk-corrected profile. Note that at  $r=75''$  the rise in the observed major-axis profile is due to the beginning of the spiral structure. Model deviations from the observed isophotes occur for the outermost levels near the ends of the major-axis. This is due to the onset of spiral structure at the ends of the bar. Some residual effects from the dust lanes are responsible for the deviations near the ends of the major-axis. The observed isophotes are significantly narrower than the model isophotes. The overall fit is, however, good and a Gaussian brightness distribution is used. This "Gaussian bar" is shown in Figure 4-8.

The form of this Gaussian brightness distribution is

$$f(r) = f_0 \exp[-r^2/2\sigma^2] \quad (4-8)$$

where  $f_0=450$  (arbitrary units) and  $\sigma=1.0'$  (FWHM).

As a final check on the quality of the model components, the disk, bulge and bar brightness distributions were added together and compared with the observations. The



isophotes are shown in Figure 4-9; the major-axis and minor-axis profiles in Figure 4-10. The only significant departure of the observations from the model occur at the ends of the bar where the spiral structure begins. The model brightness distribution does not have a spiral arm component, thus discrepancies in the region of the spiral arms are to be expected. This figure indicates that the overall model is a good representation of the observed brightness distribution and is adequate for the calculation of a triaxial ellipsoid for the modeling procedure.

In summary the model components for the I passband are

1. Disk: Exponential

$$I(r) = I_0 \exp[-r/1.399]$$

2. Bulge: Gaussian convolved cylinder

- a) Cylinder

$$I(r)=900 \quad r < 0.1125' \quad I(r)=0 \quad r > 0.1125'$$

- b) Gaussian function

$$f(r) = \exp[-r^2/2(0.225)^2]$$

3. Bar: Gaussian

$$f(r) = 450 \exp[-r^2/2]$$

$$\beta = 2.93, \quad \phi = 111^\circ$$

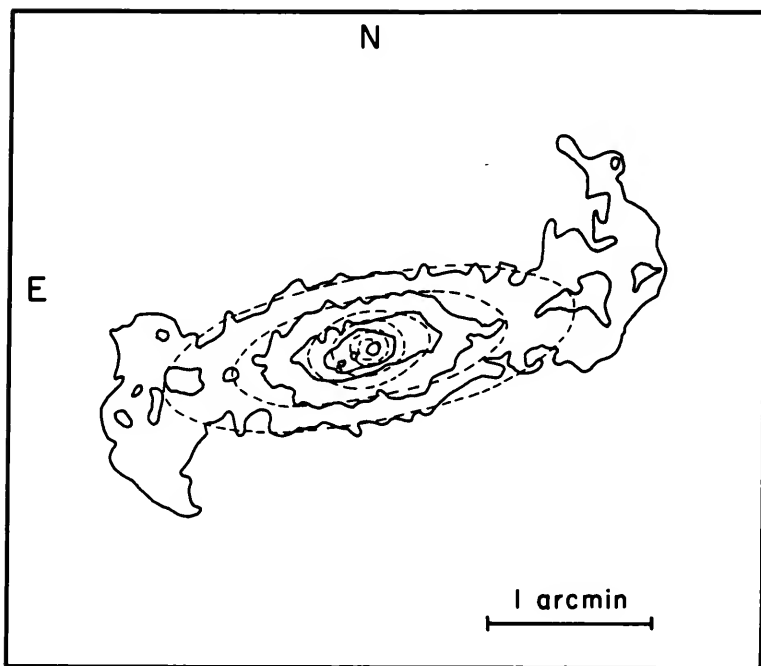


Figure 4-9. I Band Model Isophotes. Model surface brightness distribution in I band for NGC 1300. All components; disk, bar and bulge are added.

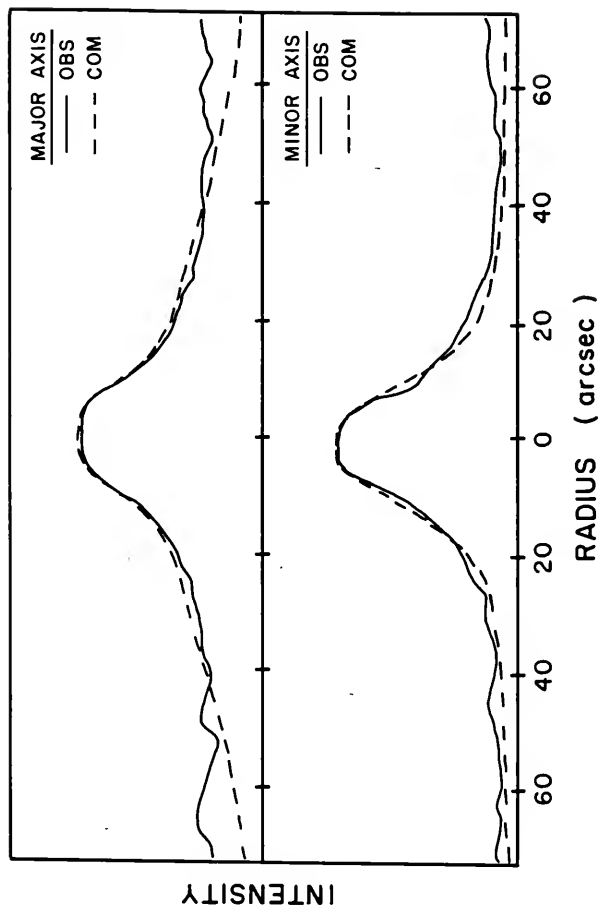


Figure 4-10. I Band Model Profiles. Major- and minor-axis profiles for the resultant I band model for NGC 1300. The observed profiles are shown for comparison.

### Comparisons Between Different Passbands

Surface photometry in the blue passband ( $\lambda=4350\text{\AA}$ ) will be affected significantly by dust obscuration in the bar region. These dust lanes are very evident in the optical photograph of the galaxy. By comparing blue photometry and near infrared photometry some information on this dust obscuration may be obtained. Figure 4-11 is a gray scale representation of the blue image and Figure 4-12 is a contour plot of the smoothed image. The image was smoothed to reduce small scale fluctuations by convolving with a two-dimensional Gaussian function with  $\sigma=0.045''$ , or 2 pixel (FWHM), truncated at the 1% level. Although some fluctuations are still noticeable in Figure 4-12, smoothing with a broader function will degrade the resolution too much. The main features can be identified in Figure 4-12.

The most noticeable features in the blue are the almost circular, bright central bulge region, the arms and the flat bar region. The arms can be traced for about  $180^\circ$  in azimuth and show breaks where they are crossed by dust lanes. Figure 4-13 plots log-intensity as a function of radial distance along the minor-axis for the northern and southern sections separately for both the blue and infrared plates. The two profiles agree well except at  $r=50''$  where the northern profile is fainter than the southern one. This is due to the break in the arms; the northern break being more sharply defined, as can be seen in Figure 1-1. Thus the brightness

NGC 1300 BL 4350A

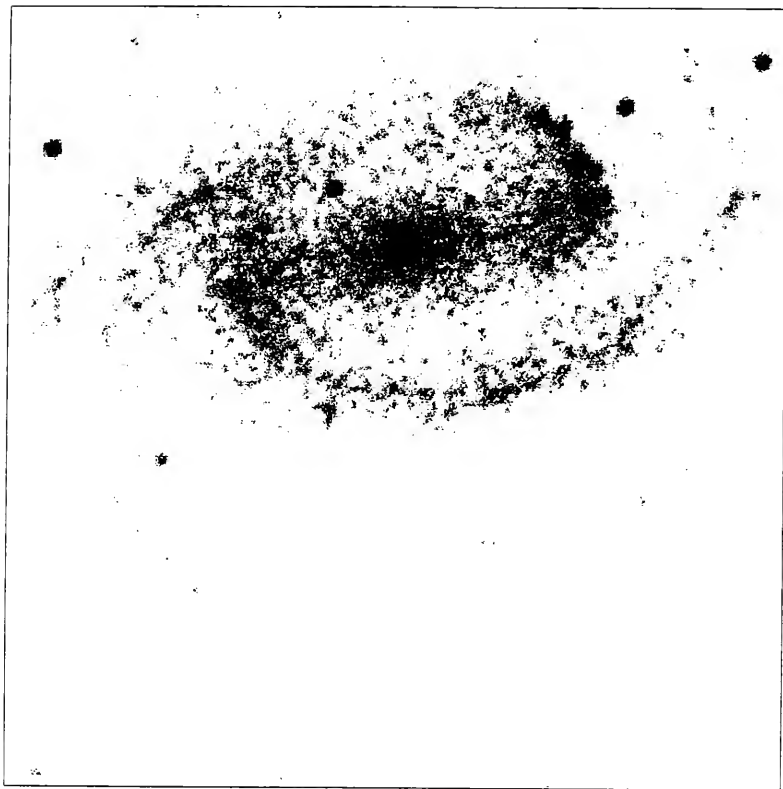


Figure 4-11. Gray Scale of Blue Passband.

## NGC 1300

CONVOLVED

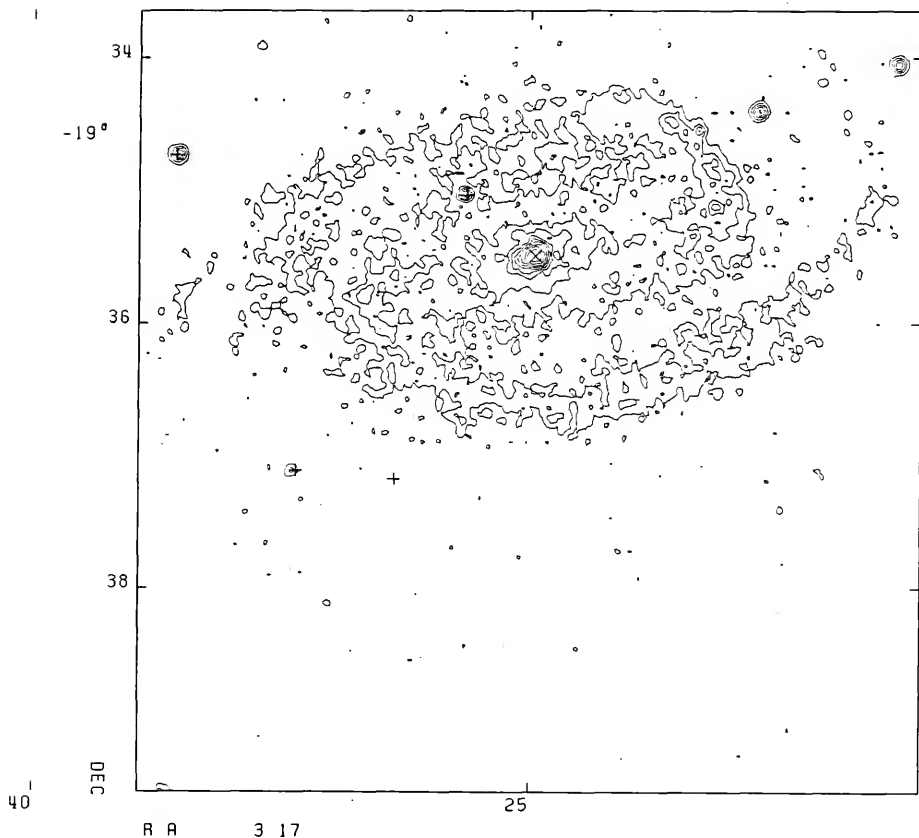


Figure 4-12. Contour Plot Blue Passband. Contour plot of the convolved blue passband image of NGC 1300. Contour levels are arbitrary. Fiducial stars (+) and the center of the galaxy (x) are marked.

drops more significantly in the western arm than in the eastern arm, as shown by these profiles (Figure 4-13). This effect can be seen in both the blue and the near infrared passbands.

These profiles also indicate that in the region between the bar and the eastern arm the brightness drops below that for the corresponding region in the northern section. The effect is more noticeable in the blue than in the I passband. Also hinted at in these profiles is the very steep drop-off in luminosity at large radial distances from the center. Blackman (1983) noticed a similar effect in NGC 7479. The data here do not go deep enough to warrant a detailed analysis but certainly do not rule out the possibility of a steep drop-off in luminosity.

The bulge is very nearly circular, having an apparent axial ratio of 1.15. The rise from the bar region is steep, rising quicker than in the near infrared passband. Figure 4-14 compares the major- and minor-axis profiles for the blue and I passbands. Regions of enhanced brightness are seen at the ends of the bar and the beginning of the spiral arms, indicating vigorous star formation in these regions. The luminosity distribution along the length of the bar is fairly smooth, indicating a lack of star formation. The regions of star formation at the ends of the bar and the beginning of the spiral arms,  $r=80''$  on the major-axis, are bluer than other regions. The region  $r=15''$  to  $50''$  on the

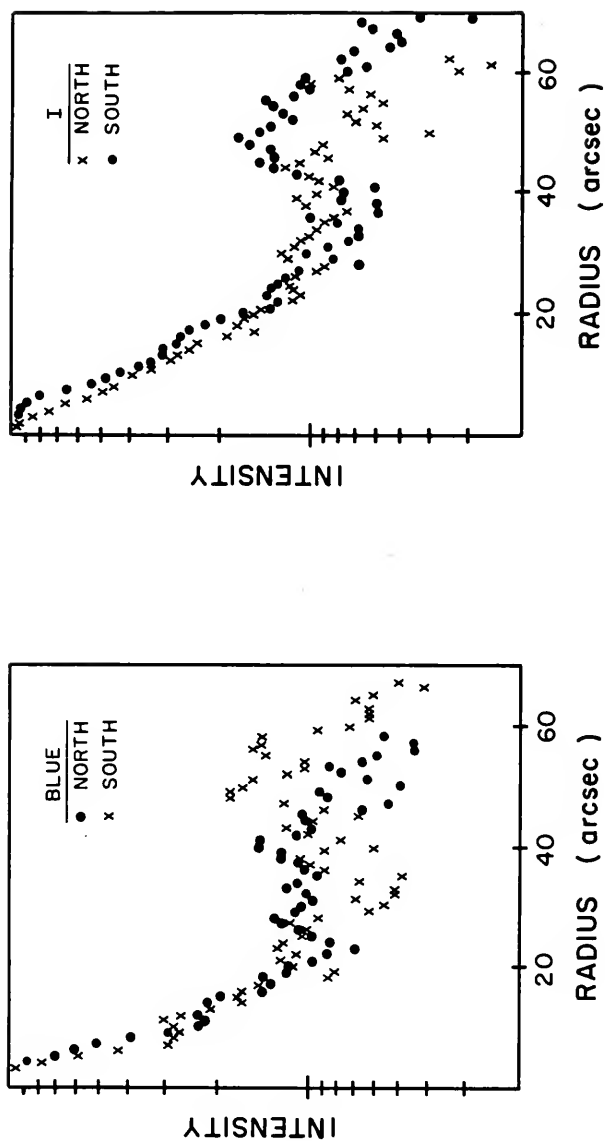


Figure 4-13. Minor-axis Profiles Blue and I Passbands. Log-intensity as a function of radial distance for I and blue passbands. Two halves of the minor-axis are shown for each passband.



major-axis clearly indicates the effects of the dust lanes in that the shapes of the profiles are depressed when compared with the I passband profiles. This justifies the assumption that the I passband should give a better result for the "observed" bar than the blue passband. Comparisons between profiles perpendicular to the bar major-axis at various radial positions along the bar (Figure 4-15) clearly indicate the differing effects of the dust lanes in the different wavelength regions. The profiles at positions  $r=20''$  clearly show the blue profile depressed relative to the I band profile, whereas at the other radial positions, apart from small scale fluctuations, the blue and I profiles are similar.

Photometry of limited spatial extent at  $2.2\mu\text{m}$  shows effects similar to those seen in the blue and I passbands. Figure 4-16 is a contour plot of the data, and Figure 4-17 is a false color image of the galaxy at  $2.2\mu\text{m}$ . The bright central source is clearly visible as are the beginnings of the spiral structure. Some pinching of the isophotes can be seen near the ends of the bar region. The dust obscuration is minimal, as the extinction due to dust at  $2.2\mu\text{m}$  is less than 10% of the associated visible extinction,  $A_K=0.08A_V$ . Although it is small, it has some effect on the isophotes as can be seen in Figure 4-16. The two halves of the major-axis profile are plotted in Figure 4-18 which plots log-flux as a function of radial position from the center. The very bright central source and the beginning of the arms are visible.

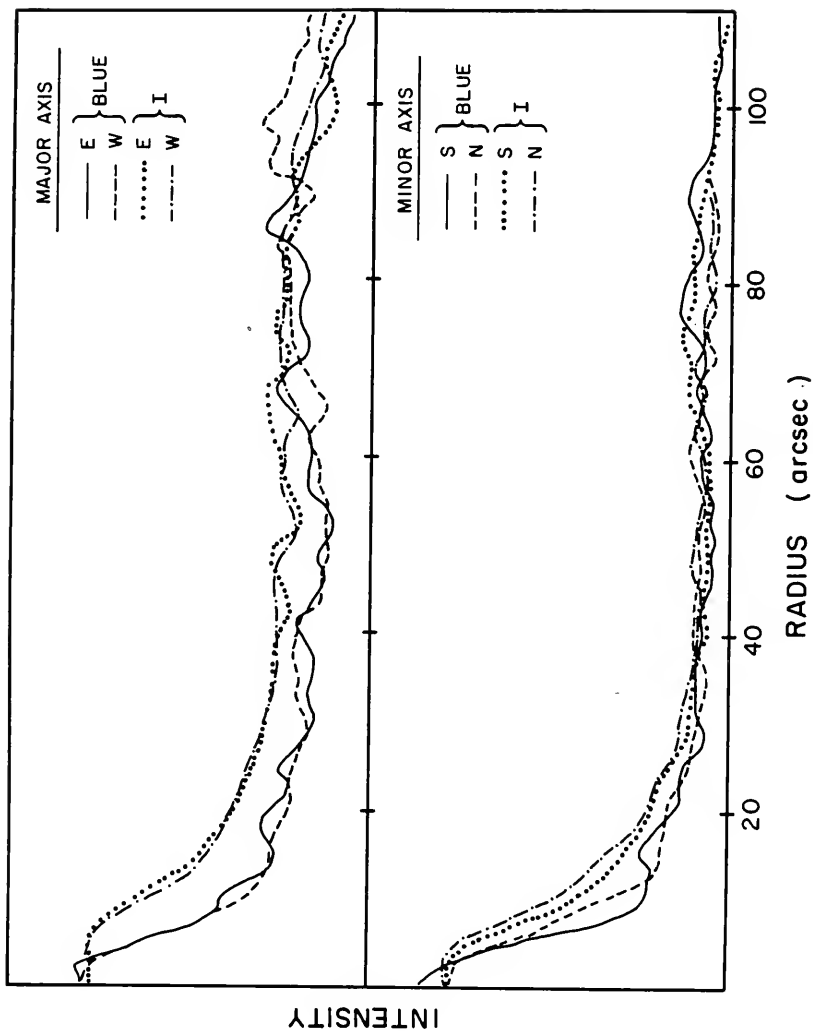


Figure 4-14. Profile Comparison. Major- and minor-axis profiles for I and blue passbands for NGC 1300.

Figure 4-15. Comparison of Blue and I Profiles.  
Comparison of profiles perpendicular to bar major-axis  
for blue and I passbands.

A. West arm.

B. East arm.

Positions indicated are arcseconds along the  
major-axis east or west of the assumed center of the  
galaxy.

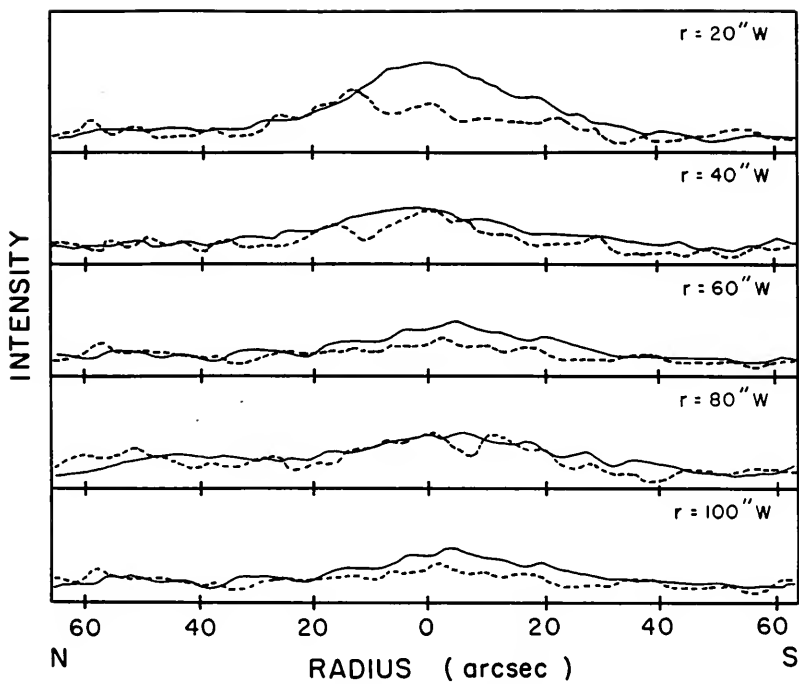


Figure 4-15 cont. (Part A).

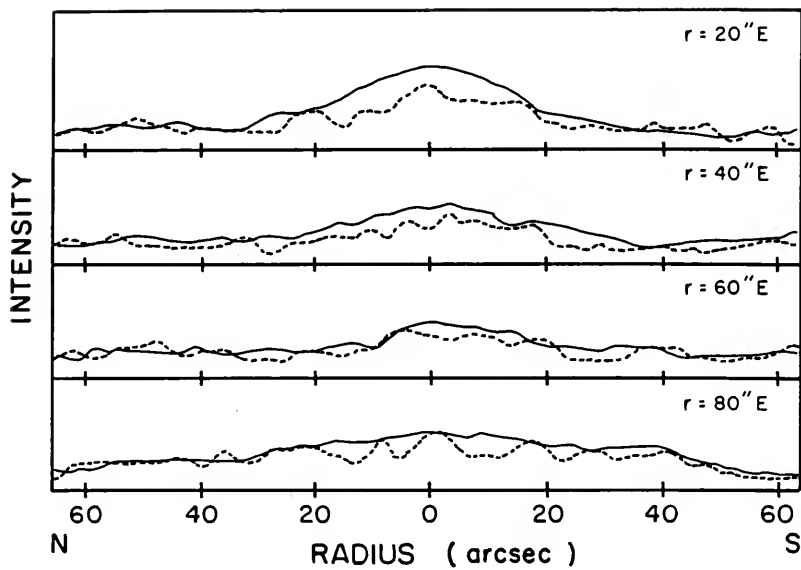


Figure 4-15 cont. (Part B).

Figure 4-19 compares the average radial forms of the major-axes for the three wavelength regions considered here. These profiles are normalized to be approximately equal at the center. The 2.2um profile has the highest peak-flux to average bar-flux ratio of the three passbands. It is interesting to note that the 21cm observations indicate a bright continuum source at the center of the galaxy and little signal in regions immediately surrounding it. It thus, perhaps, suggests that the central source becomes more dominant over its immediate surroundings as the wavelength increases from the I passband to the 21cm observations. The peak-flux to average bar-flux ratio increases as the wavelength increases from 0.825um (I passband) to 2.2um to 21000um (radio). The ratio is approximately 3:15:20 for 0.825:2.2:2100um regions.

### Triaxial Ellipsoid

The surface photometry describes the bar figure in terms of the axial ratio of the isophotes, the two Euler angles and the surface brightness distribution. Using values of  $i=50.2^\circ$ ,  $\phi_{\text{BAR}}=-79^\circ$ ,  $\phi_{\text{LON}}=-85.5^\circ$  and semi-major axis of the bar  $a=77.66''$ , these parameters are  $\beta=2.93$ ,  $\theta=39.8^\circ$ ,  $\psi=6.5^\circ$  and

$$F_S(a_S) = 450 \exp[-a_S^2/2\sigma^2], \quad \sigma = 1.0' \text{ (FWHM)} \quad (4-9)$$

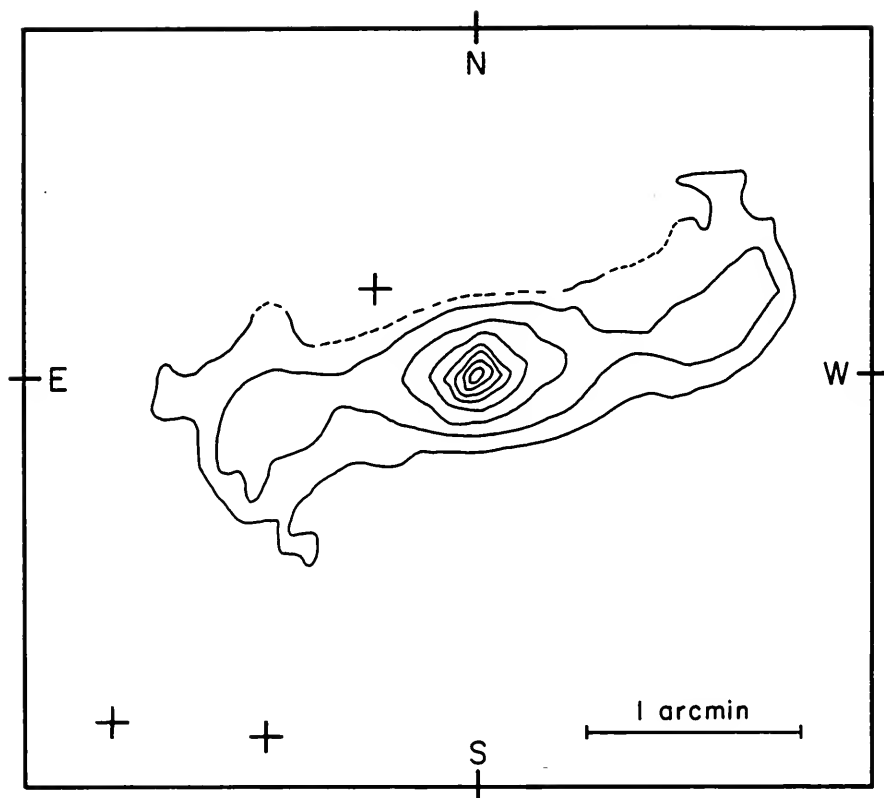
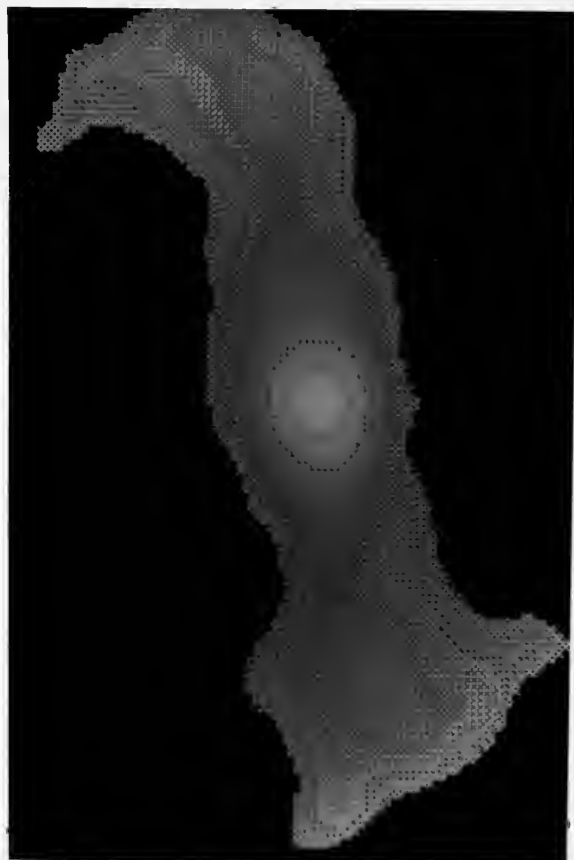


Figure 4-16. Contour Plot 2.2um. Fiducial star positions are marked (+).

Figure 4-17. False Color Plot 2.2 $\mu$ m. Blue represents low flux and yellow represents high flux. North is to the top and east is to the left.





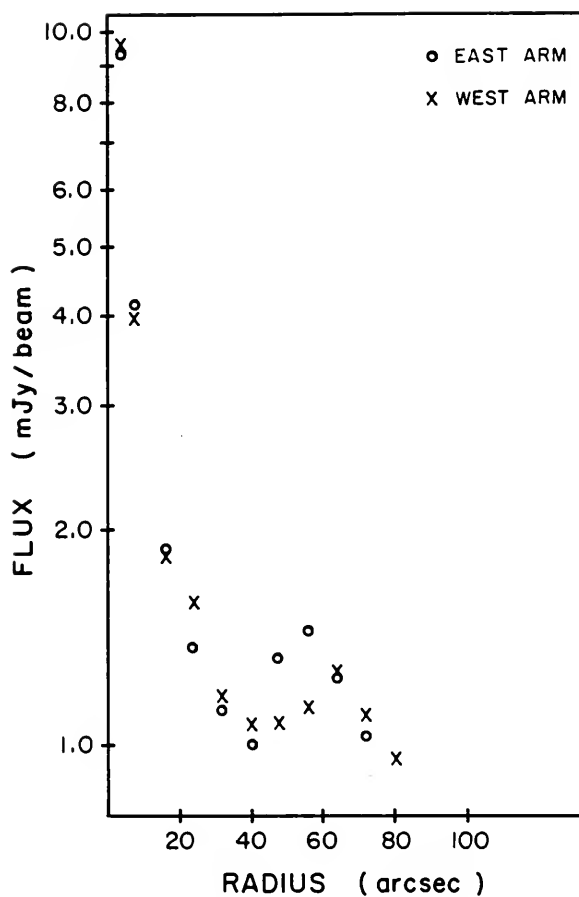


Figure 4-18. Flux Profile 2.2 $\mu$ m. Two halves of the major-axis brightness profile for 2.2 $\mu$ m image of NGC 1300.

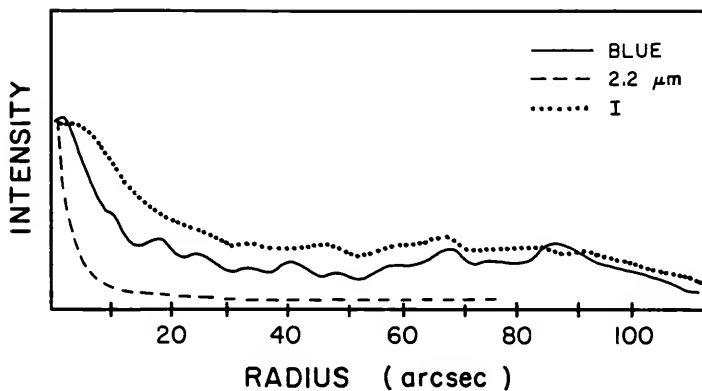


Figure 4-19. Comparison Between Different Wavelengths. Radial forms of major-axis profiles for blue, I and 2.2μm images of NGC 1300.

The maximum value for the third Euler angle and the parameters  $t$  and  $u$ , which describe the families of triaxial ellipsoids, can be calculated from these parameters (Ball, 1984). If the semi-major axis is  $a$  and the other semi-axes are  $b$  and  $c$  where  $c$  is perpendicular to the disk, then (Ball, 1984)  $u=c/a$ ,  $u/t=b/a$ , and

$$\tan \phi_{\max} = \frac{\cos \theta (\sin^2 \psi + \beta^2 \cos^2 \psi)}{(\beta^2 - 1) \sin \psi \cos \psi}. \quad (4-10)$$

Numerically  $\phi_{\max} = 82.55^\circ$ ; the minimum value occurs when  $t$  vanishes, giving  $\phi_{\min} = 80.74^\circ$ .

All possible shapes of triaxial ellipsoids satisfying the observations fall within this narrow range of  $\phi$ . The uncertainty in  $\phi$  arises because, for an inclined triaxial figure with three finite axes, the longest axis of the ellipsoid need not point in the same direction as that of its two-dimensional projection. As the figure becomes more elongated the figure begins to resemble a rod of infinitesimal thickness and the discrepancy between the direction of its longest axis and that of its two-dimensional projection diminishes (Ball, 1984). Following the procedure outlined in Ball (1984) and Hunter et al. (1986), the various figures for the triaxial ellipsoid can be calculated. Table 4-1 shows the quantities of interest in the range allowed by the observations. The ellipsoid is prolate if  $b/c=1$  which corresponds to  $\phi=81.56^\circ$ . As  $b/c$

increases the ellipsoid becomes more flattened in the disk plane,  $b/c > 1$ ; as  $b/c$  decreases the flattening takes place perpendicular to the disk plane,  $b/c < 1$ . The two limits for correspond to the cases when one or the other of the shorter semi-axes vanishes.

Thus, for NGC 1300 the prolate case corresponds to  $a = 77.66''$ ,  $b/c = 1.00$ ,  $a/c = 2.94$  and  $\phi = 81.56^\circ$ .

For  $\phi$  values lower than  $81.56^\circ$  the figure is flattened perpendicular to the disk plane. It is very unlikely that the bar in a real galaxy is flattened perpendicular to the disk plane; these values for  $\phi$  will not be used here.

The volume brightness distribution can be calculated by evaluating equation 4-2 (Stark, 1977; Ball, 1984)

$$F_V(a_V) = \frac{-f^{1/2}}{\pi} \int_{a_V}^0 \left[ \frac{d}{da_S} F_S(a_S) \right] (a_S^2 - a_V^2)^{-1/2} da_S \quad (4-12)$$

Using

$$F_S(a_S) = F_{SO} \exp[-a_S^2/2\sigma^2]$$

and integrating gives (Appendix A)

$$F_V(a_V) = \left( \frac{F_{SO}^2 f}{2\sigma^2 \pi} \right)^{1/2} \exp[-a_V^2/2\sigma^2] \quad (4-13)$$

Under the assumption of constant M/L within the bar region, the volume density distribution is

TABLE 4.1  
Bar Projection Parameters for NGC 1300

$\phi$ ( $^{\circ}$ )	$u^2$	$t^2$	$b/a$	$c/a$
80.74	$1.02 \times 10^{-4}$	$5.27 \times 10^{-5}$	$3.19 \times 10^{-3}$	0.440
81.00	0.0343	0.2011	0.185	0.413
81.56	0.1156	1.0000	0.340	0.340
82.00	0.1860	2.7406	0.431	0.261
82.54	0.2847	327.87	0.534	0.029

$$a = 1.2943''$$

$$\theta = 39.8^{\circ}$$

$$\psi = 6.5^{\circ}$$

$$\rho(r) = \rho_0 \exp[-r^2/2\sigma^2] \quad (4-14)$$

where  $\sigma = 1.0'$  (FWHM).

The triaxial ellipsoid specified by this volume density distribution and these geometrical parameters can now be incorporated into the hydrodynamical models of the galaxy. The photometric data should be quite valuable in reducing the uncertainty associated with the non-uniqueness of the models. The mass distribution of the axisymmetric component has been constrained by the rotation curve from the HI observations and the non-axisymmetric mass distribution has been constrained by the near infrared surface photometry.

## CHAPTER V MODELING

### The Beam Scheme

The hydrodynamical modeling of NGC 1300 and the other galaxies considered in this project was carried out using a two-dimensional, gas-dynamical scheme known as the "beam scheme." This computational method was first introduced by Sanders and Prendergast (1974) and has been used on numerous occasions to model the two-dimensional gas flow in galaxian disks (Huntley, 1977; Peterson and Huntley, 1980; Schempp, 1982; Huntley, Sanders and Roberts, 1978; Sanders and Tubbs, 1980; Ball, 1984, 1986; Hunter et al., 1986). The hydrodynamical properties have been reviewed by Sanders and Prendergast (1974) and various aspects of its applicability to barred spiral galaxies have been discussed in the references given above. Thus only a short overview of its essential features will be given here.

The behaviour of the constituent gas in the galaxy is represented by hydrodynamical equations. If the gas density is given by  $\rho$ , the gas velocity vector by  $\vec{V}$ , the pressure by  $P$  and the kinetic energy density by  $E$ , then neglecting the effects of magnetic fields, the equation of mass continuity for a compressible fluid becomes



$$\frac{\partial}{\partial t} (\rho) + \nabla \cdot (\rho \tilde{V}) = 0 \quad (5-1)$$

the equation of motion

$$\frac{\partial}{\partial t} (\rho \tilde{V}) + \nabla \cdot (\rho \tilde{V}^2 + \tilde{P}) - F = 0 \quad (5-2)$$

and the energy density

$$\frac{\partial}{\partial t} (E) + \nabla \cdot [\tilde{V}(E + \tilde{P})] - Q = 0 \quad (5-3)$$

Here  $Q$  explicitly represents dissipative terms, such as viscosity and heat conduction;  $F$ , the force, consists only of gravitational and viscous terms. Omitting the viscous terms from  $F$  means that  $F$  becomes solely gravitational and is specified by Poisson's equation:

$$F = -\nabla \phi, \quad \nabla^2 \phi = \pi G \rho. \quad (5-4)$$

The essential characteristic of the "beam scheme" is that the velocity distribution is broken into a number of discrete beams with a velocity distribution  $F(u, v, w)$ . The velocity distribution is Maxwellian and for each computational cell has the form

$$F_j(u, v, w) = A_j \exp\left[(-1/2\sigma_j^2)((u-u_j)^2 - v^2 + w^2)\right] \quad (5-5)$$

where  $j$  represents the cell,  $A_j$  is proportional to the mass density in cell  $j$ , and  $\sigma_j$  is the velocity dispersion.

As the two-dimensional form is similar to the one-dimensional form, the one-dimensional form will be used here for illustrative purposes. In one dimension this consists of a central beam and two side beams offset by  $\Delta u$  from the central beam. In each beam all matter moves at a single velocity with the mass density in the beams being  $a_j$  for the central beam and  $b_j$  for the side beams. Sanders and Prendergast (1974) show that a good choice is  $a_j = 4b_j$ , giving  $(\Delta u_j) = 3\sigma_j^2$ .

The mass density,  $\rho_j$ , momentum density,  $p_j$ , and energy density,  $E_j$ , for the three beams are

1. Central beam;

$$\begin{aligned}\rho_j &= 4b_j \\ p_j &= 4b_j \bar{u}_j \\ E_j &= 2b_j \bar{u}_j^2 + 4b_j \sigma_j^2\end{aligned}$$

2. Side beams;

$$\begin{aligned}\rho_j &= b_j \\ p_j &= b_j (\bar{u}_j \pm \sqrt{3} \sigma_j) \\ E_j &= b_j \left( \frac{\bar{u}_j^2}{2} \pm \sqrt{3} \bar{u}_j \sigma_j + 5/2 \sigma_j^2 \right)\end{aligned}\tag{5-6}$$

where  $\bar{u}_j$  is the bulk velocity and  $\sigma_j$  is the velocity dispersion.

The system evolves over a number of timesteps with each beam transporting a proportion of its mass, momentum and energy to a neighbouring cell. The fraction transported is equal to the portion of the cell traversed in each time step. The size of each time step,  $t$ , is computed by using the Courant condition (Roache, 1976):

$$\Delta t < L/u_{\max} \quad (5-7)$$

where  $L$  is the cell size and  $u_{\max}$  is the maximum gas velocity in any cell at the start of each time step.

At the conclusion of each time step the Maxwellian velocity is re-established giving rise to an artificial viscosity,  $\eta$ , where

$$\eta = \rho_j \Delta u_j L. \quad (5-8)$$

This viscosity has been discussed by Sanders and Prendergast (1974), Huntley (1977) and Huntley, Sanders and Roberts (1978) and its justification lies in the fact that a real, physical viscosity must be present in the gas to avoid gas streamlines crossing. Ball (1984) found that the details of the viscosity are unimportant, which is fortunate as there is little information available on the real viscosity in the interstellar medium.

Having given a brief overview of the essential characteristics of the beam scheme, the reasons for its use

in modeling the gas response for the galaxies considered here will be discussed. The beam scheme has demonstrated its effectiveness in modeling gas flows on a galactic scale (Huntley, 1977; Sanders and Tubbs, 1980; Schempp, 1982; Ball, 1984; Hunter et al., 1986) and the results agree with those from other two-dimensional gas codes using the same initial conditions (Sanders, 1977; Berman, Pollard and Hockney, 1979). The numerical stability of the scheme is excellent in all regions where the gas flow is not subsonic (Ball, 1984). The artificial viscosity present in the scheme ensures stability of the flow even in the presence of shocks. Although the beam scheme indicates the presence of shocks in the gas it does not accurately produce their strengths or their positions. Van Albada et al. (1981) find that the density maximum is severely underestimated and is displaced downstream by a significant amount. In the smooth region of the flow only the most general features are represented. Despite these drawbacks the scheme which is second order accurate in time and better than first order accurate in space, has sufficient accuracy and spatial resolution to model the VLA HI observations. The scheme, while clearly resembling standard upwind, finite-difference schemes, also exhibits properties similar to "smooth-particle" codes (Roache, 1976). It thus represents a compromise between the mathematical formality of treating the galaxy as a continuous fluid and the physical complexity of treating it as a collection of diffuse HI clouds.

Before describing the application of the beam scheme to a particular galaxy (NGC 1300), some general properties of its implementation must be noted. These properties describe the initial conditions for the modeling and, once decided upon, remain constant for a particular galaxy. They include the choice of the grid size, the computational frame, the sound speed and the initial start-up conditions.

The grid chosen is a two-dimensional Cartesian grid of  $32 \times 64$  cells. A Cartesian grid is used, as both dimensions of the cells are the same, which gives a numerical viscosity which is nearly constant everywhere in the disk. A polar grid for the computations could lead to confusion between numerical artifacts and real structure. Numerical artifacts could give rise to rings or possibly even spiral features on a polar grid, whereas on a Cartesian grid these artifacts are most unlikely to give forms that could be confused with real structure. The grid size of  $32 \times 64$  is used on the assumption that the forces and gas responses are bisymmetric and that the full  $64 \times 64$  grid can be calculated using only a  $32 \times 64$  computational grid. One of the longer boundaries defines the meridian plane of the galaxy; any matter crossing this boundary re-enters the grid at a point symmetric, with respect to the galaxy center, with that which it has just left. The other boundaries of the grid are transparent and any matter crossing them is permanently lost from the calculations. The gas disk is also constrained to

lie within a radius of 32 grid cells; again, any matter having a radius greater than this is removed from consideration. Thus, there is a gradual loss of gas during the course of a calculation but the amount of gas lost, typically, does not seriously affect the calculations until four or five bar rotations have taken place. Tests showed that if a quasi-static situation was going to develop (steady-state apart from gas diffusion through the boundaries), that it would develop after approximately 1 to 1.5 bar rotations. Thus the gas diffusion will not seriously affect the calculations as long as the timescale is kept to less than about 3 to 4 bar rotation periods.

The gas density is initially constant over the disk and is maintained in a strictly isothermal state. The thermal or turbulent velocity dispersion of the gas is chosen to be 17km/sec although the model calculations are not very sensitive to changes of this value on the order of 10km/sec. This result was shown in Huntley, Sanders and Roberts (1978) and also confirmed by a series of tests during the modeling of NGC 3992. Various models were calculated with velocity dispersions ranging from 7km/sec to 27km/sec with very little discernible difference between the models. Huntley (1980) also found very little difference in the final models when the velocity dispersion was changed by a factor of four.

The gaseous disk initially rotates as a solid body with angular frequency  $\sqrt{2}/2$  that of the galaxian bar that will eventually be established. The gas is in equilibrium initially, but if at any timestep the velocity field is not close to the equilibrium field for the forces then present, severe disruption of the gas flow can result. This necessitates the careful introduction of the perturbing forces.

The perturbing forces are gradually introduced into the system over 100 timesteps. Thus, for each timestep 1% of the initial uniform-rotation force is turned-off and 1% of the perturbing force is turned-on. This allows the gas to adjust quasi-statically to the noncircular perturbing force of the imposed galaxian bar. These first 100 timesteps generally correspond to between 0.4 and 0.8 bar rotations which is long enough so that no severe disruption of the gas flows result. This should eliminate the problems found by Schwarz (1985) in the beam scheme models of Schempp (1982). Schempp used the following turn-on procedure. The gas is initially in uniform circular motion and the bar field is turned-on linearly over one-twentieth of a bar rotation, approximately 10 timesteps. Schwarz found that this very rapid, essentially impulsive, turn-on of the bar force field induces radial motions in the gas. These transient motions have timescales which are long, compared with 0.5 bar rotation periods. Thus some of these transients may still be

present after 0.5 bar rotation periods. Schempp, in his models, turns on the noncircular force field over a period of two bar rotations. However, as the beam scheme continually, although gradually, loses mass through the grid boundaries, two bar rotation periods was considered to be excessively long for the turn-on period. The bar force was thus turned-on in the first 100 timesteps of the calculation. This generally meant between 0.4 and 0.8 bar rotation periods. As the evolution of the model was generally followed for about 3 to 3.5 bar rotations, the gas has ample time to settle into a quasi-static configuration. Numerical experiments were performed in which the noncircular perturbing force was turned-on over 300 timesteps (1.2 to 2.4 bar rotations) and over 50 timesteps (0.2 to 0.4 bar rotations); the response was compared with models in which the perturbing force was turned-on over 100 timesteps. After 600 timesteps, 2.5 to 5 bar rotations, there were essentially no differences between the two situations, thus indicating that turning-on the noncircular force field in the first 100 timesteps is slow enough so that the gas can respond quasi-statically, and that all transients have died away by the time the calculations are stopped, but not too slow as to be computationally excessive. The response from 400 to 600 timesteps can thus be considered to be quasi-static, with the only secular changes being the gradual decrease in mass, the gradual



increase in contrast between the highest and lowest densities present and the gradual increase in the buildup of matter at the center few pixels. This buildup is artificial, a result of the code and has been discussed by Huntley (1977) and Ball (1984); it does not seriously effect the computations.

The choice of the computational frame is not straightforward, as numerical effects alter the gas response in various frames of reference (Huntley, 1980). In the inertial frame the rotation speed of the bar can become large enough so that it sweeps past more than one cell in one timestep. The gas does not have a chance to respond properly to the perturbation, which it sees as being broadened or smeared out. This corresponds to effectively increasing the viscosity in the grid. In a frame rotating with the bar a "corotation zone" exists in which the computed velocities are nearly zero. A non-physical ring of gas forms at this zone as it is easier for the gas to enter this region than it is to leave it. Huntley (1980) and Ball (1984) have discussed these effects in more detail and conclude that a frame intermediate between the inertial frame and the rotating perturbation frame is the best choice for the computational reference frame. However in choosing this intermediate frame care must be taken to avoid having a corotation zone in the computational frame. The intermediate frame chosen is that recommended by Ball (1984). The frame is chosen so that the estimated corotation zone occurs at

approximately five grid cells off the computational grid, at  $r=37$  grid cells. This ensures that all velocities on the computational grid are high enough to avoid numerical artifacts and to minimize the problems of added viscosity and lower effective resolution in the outer parts of the grid.

As mentioned earlier the beam scheme is a multi-parameter scheme; the task of searching through this multi-parameter space for an astronomically plausible solution could be daunting, unless some observational constraints are used to reduce the volume of this space. The constraints used for this task have been discussed in detail in Chapters 2, 3 and 4, but they will be summarized here before the discussion of the modeling results.

The axisymmetric mass distribution is initially constrained by the rotation curve from the HI observations. These observations resulted in the choice of the axisymmetric mass distribution being a Toomre disk of order  $n=1$ . This disk, out to a radius of  $r=3.2'$ , has a mass of  $4.9 \times 10^{10} \text{ Mo}$ . The total HI mass, at an assumed distance of 17.1 Mpc, calculated from the observations is  $2.54 \times 10^9 \text{ Mo}$ ; this gives the ratio  $M_{\text{H}}/M_{\text{T}}=0.052$  and thus, as the gas is a small fraction of the total mass, the self gravity of the gas will be ignored. No halo was added to the basic model initially, although models with halos will also be considered.

The initial non-axisymmetric mass distribution is provided by the triaxial ellipsoid calculated from the near infrared surface photometry. The shape of the ellipsoid, whether it is prolate or flattened, and the central density are free parameters. The form of the density distribution and the length of the major-axis are fixed by the photometry. The non-axisymmetric mass distribution is only useful if the forces arising from it can be calculated.

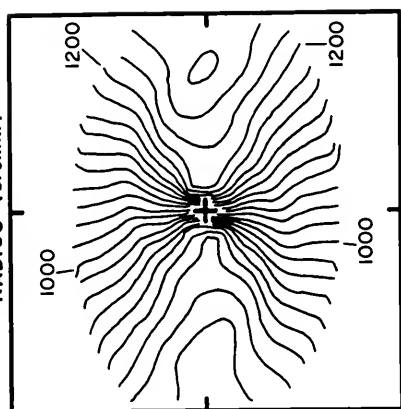
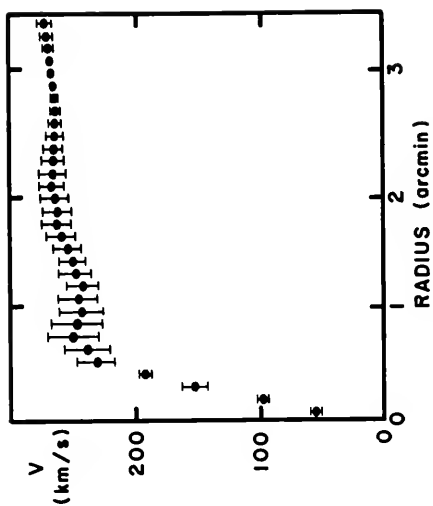
Following the procedure of Hunter et al. (1986), the ellipsoid is divided into 300 concentric homoeoids (ellipsoidal shells). The potentials and hence, the forces, for these homoeoids can be evaluated exactly without resort to elliptic integrals or numerical integration. Thus the triaxial ellipsoids given by the surface photometry can be easily incorporated into the hydrodynamical modeling code. Schempp (1982) in his conclusion states that the prolate spheroids chosen for his models are completely arbitrary and that the Miller and Smith (1979) bars are very restricted. Also Baumgart and Peterson (1986) show that the Miller and Smith (1979) bars are not good fits to the observations. In light of these comments and the success in modeling NGC 3359 (Ball, 1984) and NGC 3992 (Hunter et al., 1986) using this approach should provide good "observational" constraints for the theory and should give more plausible results than either an arbitrary bar figure or the purely theoretical Miller and Smith bar.

The basic modeling philosophy is to start with a gaseous disk and the triaxial ellipsoidal bar. The best model using these components is calculated and gradually various other components such as oval distortions and halos are added. Each time a new component is added, the best model is calculated, matching, as closely as possible, the observed rotation curve, velocity field, and morphological features. As the models are computed in the galaxy plane and have greater resolution than do the observations, each successful model is projected onto the sky plane and convolved with a synthetic beam to give a resolution matching that of the observations. For an elongated disk galaxy, the shape of the angle-averaged rotation curve depends considerably upon the true orientation of the galaxy in space. By varying the location of the bar major-axis relative to the position angle of the line of nodes, the angle-averaged rotation curve can be radically altered. Figure 5-1, taken from Hunter et al. (1986), shows the change in the rotation curve for NGC 3992 when projected at two different values of  $\phi$ , where  $\phi$  is the angle between the bar major-axis and the line of nodes. This shows, very vividly, that the models must be projected into the same orientation as the observed galaxy in order for the results to be meaningful. All the results displayed in the next section are projected and convolved to the same orientation and resolution as the observations and are thus directly comparable with the observations in Chapter 3.

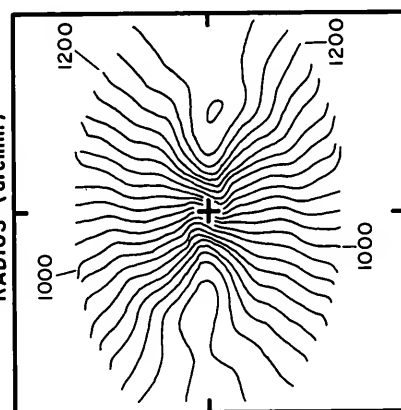
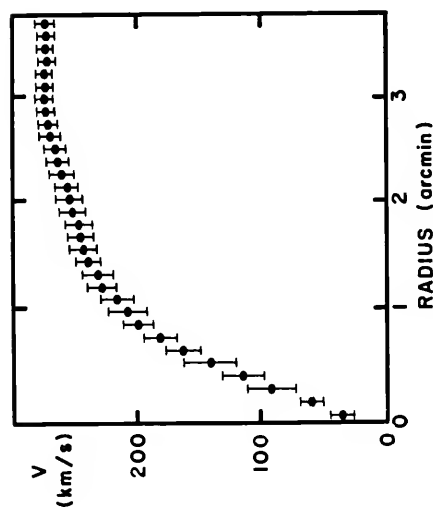
Figure 5-1. Dependence of Rotation Curve on Projection Parameters. This diagram is from Hunter et al. (1986) and shows the curves for two values of  $\phi$ , where  $\phi$  is the angle between the bar major-axis and the line of nodes. The velocity fields for these two cases are also shown.

A.  $\phi = 0^\circ$ .

B.  $\phi = 90^\circ$ .



B



A

### Hydrodynamical Modeling of NGC 1300

In this section the results of calculations for NGC 1300 using the beam scheme are presented. Three basic types of models were constructed. The simplest form was an  $n=1$  Toomre disk and a triaxial ellipsoidal bar. Adding oval distortions of the disk density distribution to this simple model increased the strengths of the gas response to the perturbing potential. These models may also have a halo component added. The halo, being axisymmetric, tends to reduce the effects of the non-axisymmetric components, but by differing amounts in the inner and outer regions. This is due to the manner in which the matter is distributed in the halo. Models which consisted of a disk component and oval distortions of the disk were also calculated.

#### Triaxial Bar Models

Models using the  $n=1$  Toomre disk and the triaxial ellipsoidal mass distribution (inferred from the surface photometry in Chapter 4) were noticeably unsuccessful in reproducing any of the features observed in the HI observations.

Initially, the mass of the bar was 0.10 times the mass of the underlying disk. This value was chosen as the mass-to-luminosity ratio for the bar then approximates the mass-to-luminosity ratio for the disk. The bar figure used was a prolate figure with  $b/a=c/a=0.340$ . The pattern speed of the

perturbing potential, the bar, was then varied in a series of models to find the best gas response. The results were quite uniform. No spiral arm response was evident at all. The density distribution can be characterized as a broad ring of gas located outside the bar zone. Inside the bar zone, the gas forms a bar-like feature with gas-depleted regions on either side. This gaseous bar joins the ring thus forming a figure-of-eight pattern. This type of gas response was seen in all models with only a disk and a triaxial ellipsoid. The only difference between models with differing pattern speeds is the location and radial thickness of the ring feature. As the pattern speed is slowed, the ring feature becomes broader. The radial distance to the center of the ring also increases, being located at approximately the position of corotation. This is expected as it is easier for the gas to fall into this region than it is to move away from the corotation zone. Figure 5-2 shows a typical example of the gas response for models of this type. In this example, corotation occurs at the end of the bar at 6.4kpc. The pattern speed corresponding to this is 19.3km/sec/kpc.

Another departure from the observations occurs in the velocity fields for these models. An example of a typical result is presented in Figure 5-3 which is the velocity field associated with the gas response in Figure 5-2. The overall feature in this velocity field is circular rotation. The departures from circular rotation are not very



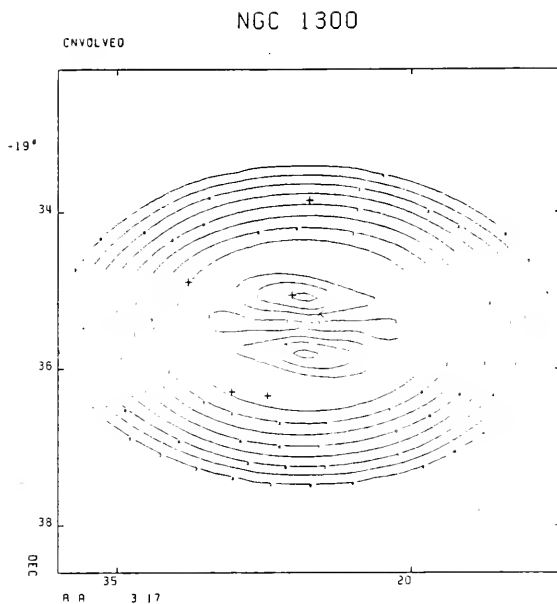
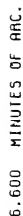


Figure 5-2. Gas Response for Disk and Triaxial. Gas density for a model with a disk and a bar. The contour interval is 0.10 times the peak density. The bar is horizontal.

significant and do not match the kinematic effects seen in the observations. The rotation curve for these models reproduces the observed rotation curve well in the region where reliable velocities can be calculated from the observations. Figure 5-4 is the rotation curve for this model. Once again it should be emphasized that the models were calculated in galactocentric coordinates and then projected to the same inclination as the observed galaxy. The model results were also convolved with a two-dimensional Gaussian function to produce a final resolution comparable with that obtained in the HI observations. Thus the modeling results shown are directly comparable with the HI observations, except that in the models the position angle of the bar is  $-90^{\circ}$  (horizontal) whereas in the observations the position angle of the bar is  $-79^{\circ}$ .

In an attempt to determine when spiral arms would begin to form, the bar mass was raised gradually in a series of models. The pattern speed was kept constant at  $19.3 \text{ km/sec/kpc}$ , placing corotation at the end of the bar. No spiral arm response was seen in the gas until the bar mass was approximately 2.2 times the disk mass. With a bar mass this high, the rotation curve, Figure 5-5, is very obviously dominated by the bar in the inner regions and does not match the observations at all. As this model is very unrealistic, it is unlikely that a real galaxy would have a bar 2.2 times as massive as the disk; it will not be considered any further in this study.



20 km/sec. The bar is horizontal.

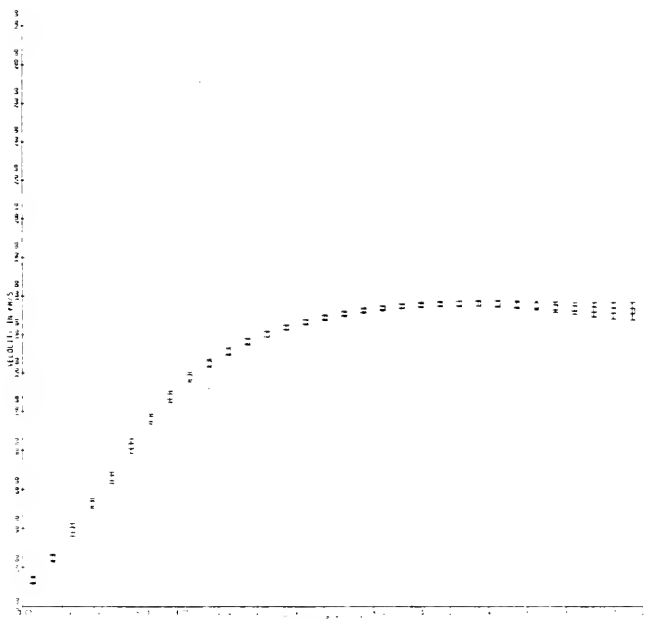


Figure 5-4. Model Rotation Curve. Rotation curve derived from the velocity field of Figure 5-3. The projection parameters are the same as for the observed galaxy. Each grid unit corresponds to 0.1 arcminute. The error bars represent one standard deviation.

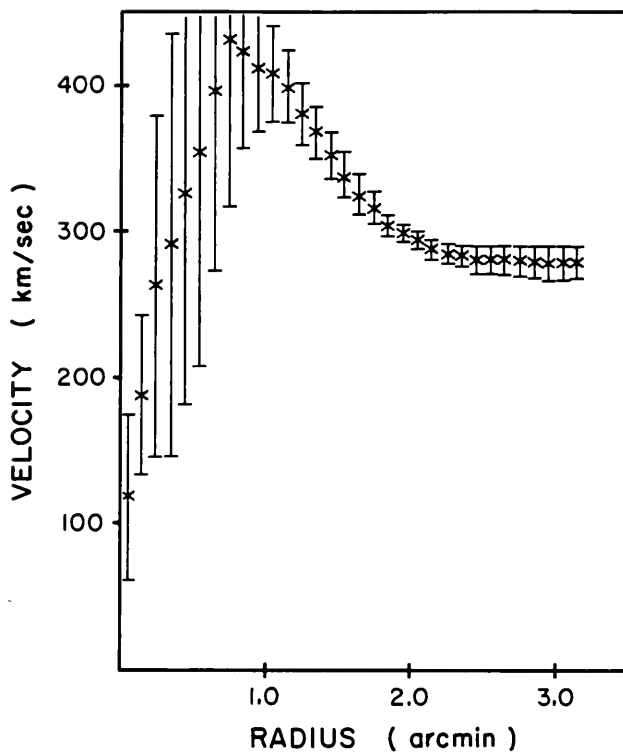


Figure 5-5. Supermassive Bar Rotation Curve.  
The bar mass is 2.2 times the disk mass.

The reason that these models fail to reproduce the observed galaxy is that the forces resulting from the bar mass distribution have a limited radial range. At radial distances greater than the length of the bar, the strengths of the forces, both radial and azimuthal, decrease very rapidly, until near the edges of the galaxy they have essentially no effect on the gas. Thus, it is extremely difficult for spiral arms to form in regions outside the bar, as the gas sees the bar as essentially a point mass. The only way to get spiral features to form in these models is to use a supermassive bar, i.e. increase the strengths of the forcing terms outside the bar region until they are strong enough to evoke some response in the gas.

#### Oval Distortion Models

Following the lack of success using models consisting of a disk component and a triaxial ellipsoidal mass distribution (a bar), models were constructed using a disk and oval distortions of the disk mass distribution. These oval distortions are sometimes considered as "massless bars" as they only involve a redistribution of the disk mass and do not have any mass themselves. Appendix B contains a full discussion and derivation of the forces for oval distortions of an  $n=1$  Toomre disk.

Two forms of these perturbations were considered; the  $\ell=1$  and  $\ell=2$  cases. The forces, radial and azimuthal, for

these cases were calculated using equations B-28 to B-31 (Appendix B). The results using these distortions were quite clear cut. Models using the  $\ell=1$  distortions had spiral arms which were very loosely wound and extended all the way to the edge of the computational grid. This implies that the forces arising from these distortions do not decay rapidly enough as a function of radius. These distortions have essentially all the gas residing in these loosely wound arms and very little in the interarm regions. The arms have the S shape characteristic of oval distortions and have a gaseous bar. This gaseous bar is not observed in NGC 1300.

The parameter,  $\beta$ , in equations B28 to B31, is a length scale characterizing the radial dependence of these mass distortions. A large  $\beta$  implies a large radial extent for the mass distortions and, conversely, a small  $\beta$  means that the mass distortions are more centrally concentrated. However, even for small  $\beta$ , these oval distortions affect essentially the whole computational grid and do not give a gas morphology which resembles the observations. The amplitude of the perturbation, represented by  $\epsilon$ , was varied in attempts to change the gas response. The only effect of lowering  $\epsilon$  was to lower the contrast between arm and interarm regions until the arms essentially disappeared. Changing  $\epsilon$  had very little effect on either the radial extent of the arms or the amount of winding of the arms. Thus, the strengths of the forces do not drop rapidly enough

and  $\ell=1$  perturbations were not considered any further in the modeling procedures.

In the treatment of oval distortions in Huntley (1977) and Appendix B, it is noted that as  $r \rightarrow \infty$ , the forces for the  $\ell=1$  perturbations are  $\propto r^{-3}$ , whereas those for the  $\ell=2$  perturbations are  $\propto r^{-4}$ . Thus, the  $\ell=2$  perturbations have a lesser effect at large  $r$  than do the  $\ell=1$  perturbations and should give arms more closely matched to the observed spiral arms. Figure 5-6 is the gas response for a typical model using a disk and an  $\ell=2$  oval distortion. The arms have a better degree of winding than do the arms for  $\ell=1$  distortions. A gaseous bar region is evident in this model; the beginning of the arms slightly precedes the bar position. In the observations the central region is completely devoid of gas. This model shows depletion only on either side of a gaseous bar. The distortion used here is a large amplitude distortion, but the arms do not have the correct azimuthal extent.

The azimuthal extent of the arms is approximately  $120^\circ$ . In the observations, out to the maximum modeling radius of  $3.2'$  or  $15.9\text{kpc}$  at the adopted distance of  $17.1\text{Mpc}$ , the azimuthal extent of the arms is approximately  $225^\circ$ . The azimuthal extent of the arms for the  $\ell=2$  distortions is decidedly better than that for the  $\ell=1$  distortions, but still does not give an acceptable match to the observations.



The velocity field for this model (Figure 5-7) again shows that the dominant component is circular rotation and as such, fits the observations fairly well in its gross properties. However, the noncircular effects seen in the observations are not matched at all in this model. The model suffers from the defect of having noncircular effects that are much smaller than those in the observations.

Various combinations of  $\Omega_p$ , the pattern speed of the perturbation,  $\beta$ , the length scale of the mass redistribution and  $\epsilon$ , the amplitude of the perturbation were tried. No combination was found that gave an acceptable match to the observations for either the gas response or the velocity field. However, using  $\ell=2$  distortions resulted in models which were more acceptable than those utilizing  $\ell=1$  distortions.

### Composite Models

The third type of models attempted were models using an  $n=1$  Toomre disk, a triaxial bar figure,  $\ell=2$  oval distortions and a halo component. Models were calculated without the halo component, but the results are so similar to those with the halo that no separate discussion of these will be given. The difference between the models with halo components and those without halo components is in the axisymmetric component and the amplitude of the oval distortion needed to generate the same spiral pattern in the two types of models.

MODEL #6A

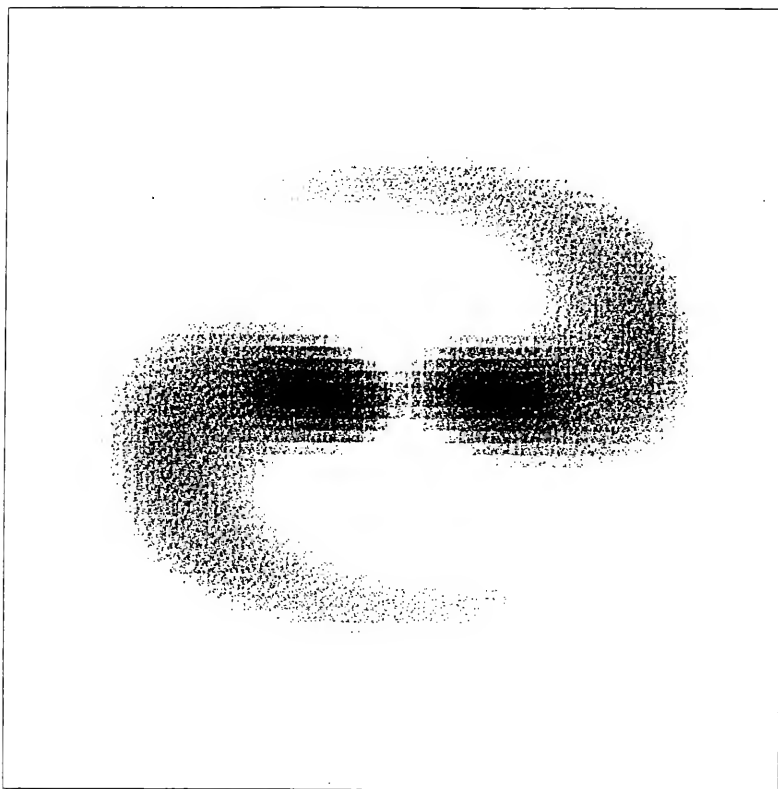


Figure 5-6. Oval Distortion Model Gas Response. Gray scale representation of the gas response for a model with a disk and an  $l=2$  oval distortion.

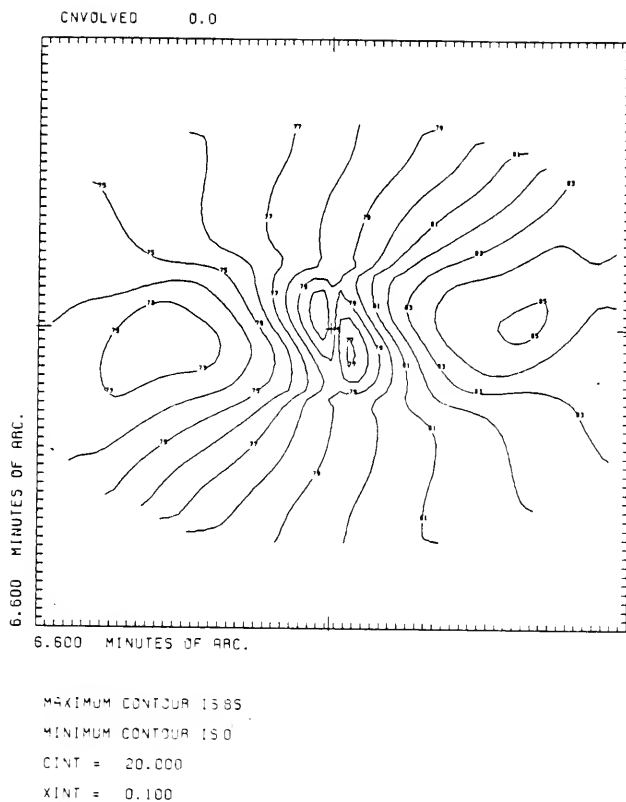


Figure 5-7. Oval Distortion Model Velocity Field. Contours are labeled in units of 20 km/sec. Projection parameters are the same as for the observed galaxy. Pro-

The mass of the disk is higher in models without the halo than in models with the halo. However, the match to the rotation curve is as good in these models as it is in models with a halo. The amplitude of the oval distortion,  $\epsilon$ , is slightly greater in models with a halo than in models without a halo. This indicates that the effects of adding a halo are slightly different from those in models with a higher disk mass. A slightly stronger oval distortion is needed to overcome the effects of the added axisymmetric halo than is needed to overcome the effects of the higher disk mass. As the disk surface density drops-off quicker than the halo core density this means that the oval distortion has to be greater than that for the disk to produce the same forces at large radii from the center. However, apart from these slight differences, the two types of models give very similar results. Only the best model using a disk, a halo, a triaxial bar and an  $\ell=2$  oval distortion will be discussed in detail. This model represents the best model possible using the modeling philosophy outlined at the beginning of this chapter. Some possible improvements and alternative approaches will be discussed later in this chapter.

Figures 5-8 to 5-11 show the results of the hydrodynamical modeling procedure for the best model for NGC 1300. Figure 5-8 is a gray scale representation of the gas response and Figure 5-9 is a contour plot of this response. The associated velocity field is shown in Figure 5-10 and

the angle-averaged rotation curve derived from these velocities is shown in Figure 5-11. Several faults are immediately obvious in these models.

The gas response shows some gas in the bar region (the bar is horizontal in these diagrams), whereas in the observations the bar region is essentially devoid of gas. The spiral arms do not have the azimuthal extent seen in the observations. The model arms have an azimuthal extent of approximately  $145^\circ$  whereas the observed HI arms extend for about  $225^\circ$ . However, the very low contrast extension of the model arms, between  $145^\circ$  and  $180^\circ$  in azimuth, connects with the beginning of the next arm, providing a resemblance of the joining of the arms in the HI observations. The amplitude along the arms in the model falls too rapidly to successfully reproduce the observations. In the observations, the amplitude of the arms remains approximately constant apart from the breaks, through about  $180^\circ$  in azimuth (see Figure 3-4). The spatial positioning of the arms in the models does not coincide with the position of the observed HI arms. The HI arms are more tightly wound, having a pitch angle of approximately  $5^\circ$  in the inner region, than are the model arms. The pitch angle of the model arms is about  $14^\circ$ .

The most immediate difference between the observed velocity field and the model velocity field in Figure 5-10 is that the model velocity field covers the complete grid,

MODEL #4A

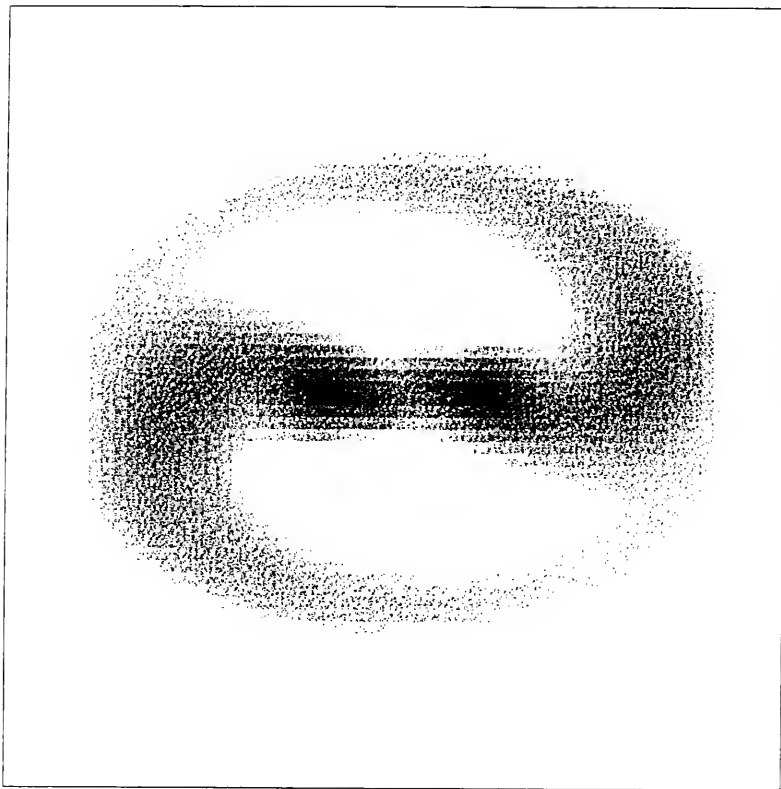


Figure 5-8. Composite Model Gray Scale. Gray scale representation of the gas response for the composite model consisting of a disk, a bar, an  $\ell=2$  oval distortion and a halo. The bar is horizontal.

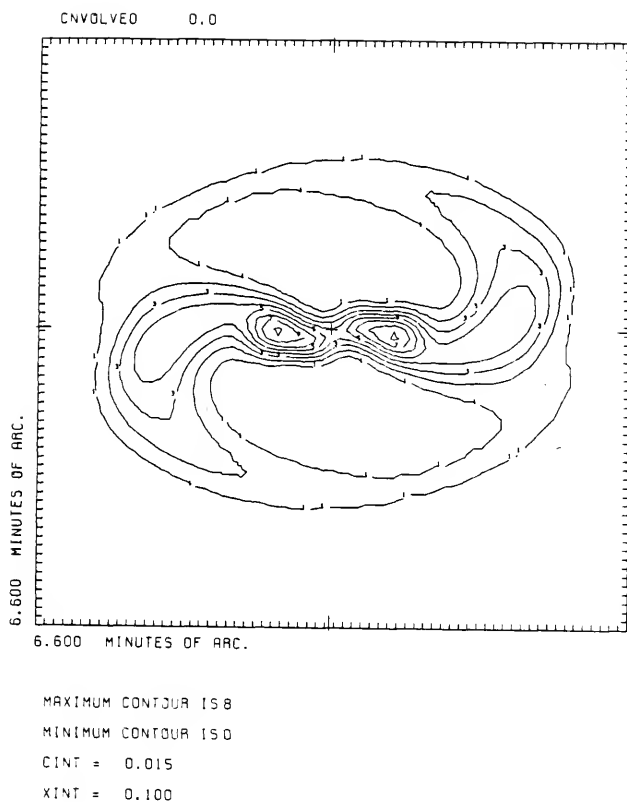
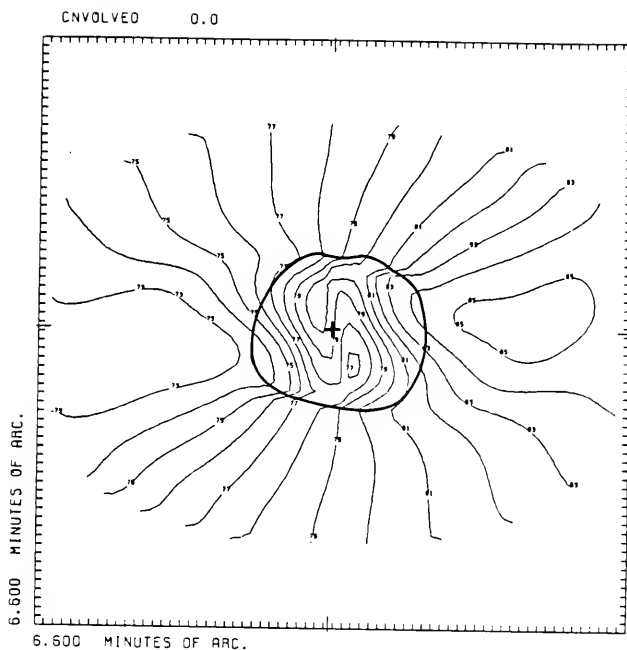


Figure 5-9. Composite Model Contour Plot.  
Contour plot of the gas response in Figure 5-8.  
Contours are plotted at approximately 10% of peak  
density.



MAXIMUM CONTOUR 1585

MINIMUM CONTOUR 150

CINT = 20.000

XINT = 0.100

Figure 5-10. Composite Model Velocity Field. Velocity field for the model in Figure 5-8. Contour levels are numbered in units of 20 km/sec.



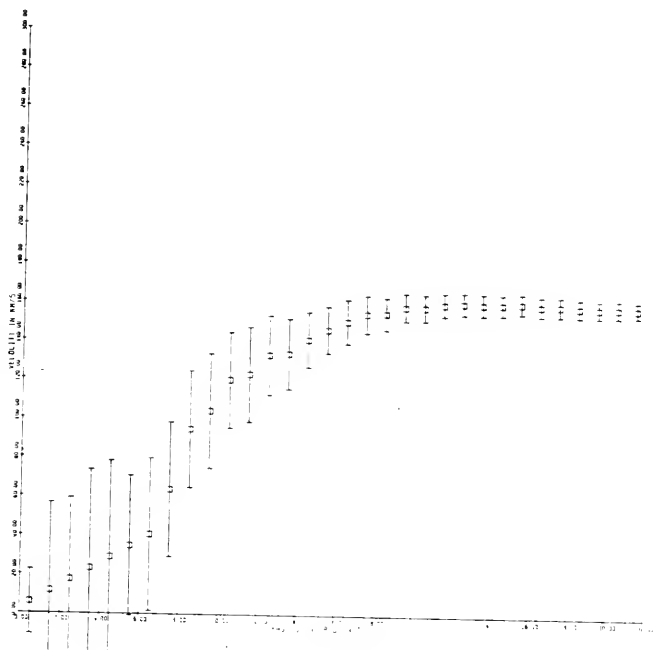


Figure 5-11. Composite Model Rotation Curve. Rotation curve derived from the velocities in Figure 5-10. Each grid unit is 0.1 arcminute. The error bars represent one standard deviation and the projection parameters are the same as for the observations.

whereas the observed HI velocity field covers only the spiral arm regions. Also evident in the model velocities is the skewing of the velocity contours in a direction parallel to the bar, in the center of the galaxy. However, this region has no reliable velocity information in the HI observations. Also shown on Figure 5-10 is the approximate outline of the gas-depleted region in the HI observations. Unfortunately, although optical velocities exist in this region they are confined to a ring about the nucleus at  $r=10''$  and at positions  $r=50''$ . Thus, they do not provide much additional information to elucidate the velocity field. It is thus evident that most of the skewing of the model velocity contours in this region occurs in the "hole" region in the HI observations. Another noticeable discrepancy between the observed and the model velocity fields is the lack of strong noncircular effects in the model. The observations show noncircular effects in all regions of the galaxy, but the strongest noncircular effects in the model occur in the center region. The overall pattern of circular rotation in the galaxy is matched well by the velocities in Figure 5-9, thus indicating that circular motion is dominant in the galaxy, but that noncircular effects are strong.

The rotation curve for this model, Figure 5-11, matches the observed HI rotation curve very well in the region of reliable velocity information,  $r > 1.0'$ . Again, the different strengths of noncircular effects can be seen by comparing the error bars in the model rotation curve with the error

bars in the observed HI rotation curve, Figure 3-15. The error bars represent plus or minus one standard deviation and, in the model, are due entirely to noncircular effects. These effects are much more prominent in the observations than in the model. Very large noncircular effects are present in the inner 1.0' of the model, but these correspond to the region where the velocity contours are highly skewed.

This model is very successful in modeling the rotation law of the galaxy thereby giving a good estimate for the mass of the system. The procedure has demonstrated also that the use of a triaxial figure based on the observations can successfully reproduce some of the observed features. The model almost succeeds in clearing out the center region of the galaxy, although some gas is seen in a bar-like figure. The spiral arms have been modeled, although they do not give an ideal match to the observations. However, in spite of the lack of success in modeling all of the observed features, this model gives valuable insight into the dynamics and kinematics of NGC 1300.

This model has an  $n=1$  Toomre disk with  $C=568.4(\text{km/sec})\text{arcmin}$  and  $b=2.6162'$ . These parameters give a disk mass, out to a radius of 3.2', of  $M_D=5.4 \times 10^{10} M_\odot$ . The halo component added has the form used by Hunter et al. (1986) in modeling NGC 3992, with a core radius of  $r_C=4.9\text{kpc}$ . The mass of the halo is 1.004 times the disk mass, giving  $M_H=5.42 \times 10^{10} M_\odot$ . The mass of the triaxial

ellipsoid is 0.094 times the disk mass,  $M_B = 5.1 \times 10^9 M_\odot$ . This implies that the mass-to-luminosity ratio for the bar is approximately the same as the mass-to-luminosity ratio for the disk, i.e.  $M_B/L_B \approx M_D/L_D$ . The bar figure is a prolate figure with a radius of 1.293' (6.4kpc) and axial ratios for the shorter axes  $b/a=c/a=0.340$ . The mass distribution is a Gaussian distribution with  $\sigma=0.5'$ , 2.5kpc (FWHM). The total system mass is thus  $M_T = 1.13 \times 10^{11} M_\odot$ . This gives a ratio  $M_{HI}/M_T = 0.022$ , and thus gives some justification for not using self-gravity in these models.

The total perturbation consists of a prolate triaxial ellipsoidal figure and an  $\ell=2$  oval distortion of the disk density distribution. The length scale for the oval distortion,  $\beta$ , is 2.9kpc. This parameter does not correspond to anything physical in the galaxy and only characterizes the radial dependence of the distortion. The amplitude of the distortion,  $\epsilon$ , corresponds to a maximum perturbed surface density of ~5% of the unperturbed density. This maximum occurs at  $r=2\text{kpc}$ . At a radius of  $r=10\text{kpc}$  the perturbed density is only 0.01% of the unperturbed density. As there seems to be little observational evidence for an asymmetrical disk, this value for  $\epsilon$  probably represents the upper limit for the amplitude of the oval distortion. The perturbation is rotated with a pattern speed of 19.3km/sec/kpc, thus placing corotation just outside the bar. The bar radius is 6.4kpc and the corotation radius is 6.9kpc.

The values of these parameters represent the combination in the model that gave the best overall match to the observations. The pattern speed, halo mass distribution, bar and oval distortion parameters were all varied in an exhaustive search through parameter space to find the optimal combination.

Varying the relative bar mass resulted in no significant increase in the noncircular effects in the outer regions of the galaxy. However, above a relative bar mass of  $0.18M_D$ , the effects became so strong in the central region that the model no longer bore any resemblance to the observed galaxy. Below a relative mass of  $0.05M_D$ , the gas depleted region began to lose its identity. The bar mass chosen,  $M_B=0.1M_D$ , was thus selected to give  $M_B/L_B=M_D/L_D$ .

Models with flattened bars were constructed to determine the effects of various triaxial figures. The bar was flattened in the galaxy plane (bars flattened perpendicular to the disk plane hardly seem plausible) such that  $b/a > c/a$ . The major-axis of the bar was kept constant for these experiments, but the density in the bar was varied. This gives a total bar mass that was constant for all models constructed. This allowed comparisons to be made between the models. Agreeing with the results found by Hunter et al. (1986), these experiments showed that flattening the bar had little effect on the gas response as long as the radial extent and relative bar mass were kept

constant. Some differences in the details of the velocity fields are evident in the centers of the respective models, but these differences are insignificant. As the results are so similar to the results with a prolate bar, only prolate bar models are discussed.

Various scale lengths and amplitudes for the oval distortion were tried. The amplitude has an upper limit which can be set by considering the surface photometry. An oval distortion produces a dumbbell-shaped density distribution. As no feature of this type is observed in the surface photometry of NGC 1300, this indicates that the perturbed surface density cannot be a significant fraction of the unperturbed surface density. Using this surface photometry constraint, the values for  $\beta$  and  $\epsilon$  can be set. The strongest possible oval distortion is needed, both to provide the spiral arms and to provide noncircular effects in the velocity field.

The effects of changing the halo parameters are to change the shape of the rotation curve and to change the amplitudes of the perturbation terms for a given gas response. The addition of a halo increased the strength of the oval distortion needed to produce spiral arms; changing its mass distribution by changing the core radius, altered the shape of the rotation curve. A total halo mass of approximately a disk mass interior to the disk radius was chosen as being physically reasonable.

As the pattern speed varies, so does the amplitude of the gas response. As the pattern speed is lowered from 19.3km/sec/kpc (corotation at the end of the bar) the gas response decreases and the beginnings of the arms start to precede the bar. Figure 5-12 shows a gray scale representation of this model with a pattern speed of 16.7km/sec/kpc, corotation at 1.5 times the bar radius. This figure should be compared with Figure 5-8 for an illustration of the effect of decreasing the pattern speed. In both these diagrams, the bar is horizontal. Figure 5-12 clearly shows the gas preceding the bar. This effect is undesirable, as it is not seen in the HI observations. If the pattern speed is increased beyond 19.3km/sec/kpc then corotation would lie somewhere inside the end of the bar. In other words, corotation must occur beyond the radius of the bar; otherwise, it is difficult to understand how the bar could be stable (Contopoulos, 1985). The experiments in varying the pattern speed showed that the optimal value of  $\Omega_p$  is about 19.3km/sec/kpc, placing corotation just beyond the end of the bar. This result is in agreement with the conclusion from stellar dynamics.

From the numerous experiments investigating the effects of changing various parameters, the following remarks may be made about the hydrodynamical models of NGC 1300:

1. The gas response is most sensitive to changes in the pattern speed,  $\Omega_p$ .

NGC 1300 MODEL AQ

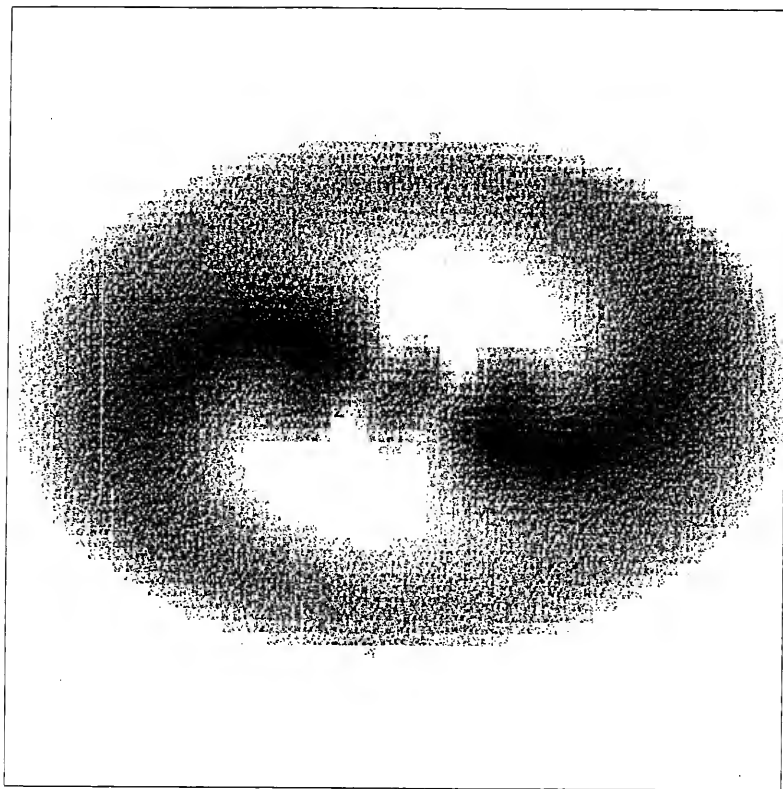


Figure 5-12. Slow Pattern Speed Model Gray Scale. Gray scale representation of the gas response for the composite model with a slower pattern speed than that for the model in Figure 5-8. The bar is horizontal.



2. Having fixed  $\Omega_p$ , the models are not very sensitive to the actual shape of the triaxial figure as long as the radius and relative mass are kept constant. This is in agreement with the conclusions of Sanders and Tubbs (1980).
3. The gas response is not very sensitive to changes in the disk and halo parameters, provided that they are adjusted to produce a distribution of circular velocities that approximate the observed HI rotation curve. However, the actual axisymmetric component can have profound effects on the gas response. Changing the background potential, while still providing a good match to the observed rotation curve for a given perturbation can drastically alter the gas response (Contopoulos et al., 1986).

These conclusions confirm those found by Ball (1984) and Hunter et al. (1986).

The only previously-published dynamical model for NGC 1300 is that of Peterson and Huntley (1980). Their model included the self-gravity of the gas and used a Miller and Smith (1979) bar-figure as their bar perturbation. As with the present models, the Peterson and Huntley (1980) model suffers from shortcomings when compared with the observations. The bar figure they used has no basis in observational data. It is a "nice, convenient" theoretical figure which mimics a bar. The models for NGC 1300

calculated in this study used a bar figure which is based on observations, and thus more closely mimics the actual three-dimensional figure in the galaxy.

The gas response in their models more nearly reproduces the optical object than the HI observations. The model they used has a central bulge component and a gas bar. The pitch angle of the spiral arms is slightly less than in the present models,  $\alpha = 12^\circ$ , compared with  $\alpha = 14^\circ$  for the present models. Both models, therefore, fail to reproduce the position and extent of the arms correctly. The azimuthal extent of the arms in Peterson and Huntley's model is about  $155^\circ$  whereas the extent in the present model is about  $145^\circ$ . Corotation in the self-gravity model is at 8.5kpc or about 1.3 times the bar radius. The present models have a better gas response when the corotation radius is at the end of the bar, 6.9kpc, than when the radius is about 8kpc.

Roberts (1979) notes that dust lanes in the bar region may be manifestations of shock fronts in the gas. In recognition of the two straight dust lanes emerging from the nucleus of NGC 1300 and their turning and following the spiral arms, the best model for NGC 1300 was examined for the presence of shock regions. Such evidence could consist of abrupt changes in amplitude or direction of the velocity vectors from one pixel to the next. Figures 5-13 to 5-15 show these velocity vectors. Figure 5-13 shows the total velocity field. In all these diagrams the bar extent and

position is marked and is rotating in a clockwise direction. The approximate position of one of the arms is also shown. Figure 5-14 is a plot of the velocity vectors in the frame of the perturbation; Figure 5-15 is a plot of the noncircular velocities.

Various features are evident from these diagrams. Very large perturbed velocities exist in the central regions of this model. Gas is flowing into the very center of the galaxy. Gas is flowing away from the "hole" on either side of the bar. The magnitude of the velocities at these points is large. This implies that the creation of the hole occurs rapidly in the evolution of these models. There are abrupt and large changes in direction and amplitude of the velocity vectors in this region, possibly indicating the presence of shock fronts. However, the gas density is so low in this region that, if there are shock fronts, they are not evident in the gas response. Also marked are the approximate positions of the minor-axis Lagrangian points. Some circulation is evident at these positions. Outflow occurs near the end of the bar.

Shock fronts appear to exist on the leading edge of the bar and in the region where the two arms join. These positions are marked on Figures 5-13 and 5-14. The shocks on the leading edge of the bar are evident only in the inner half of the bar, and thus, although they are in approximately the same positions as the observed dust lanes,

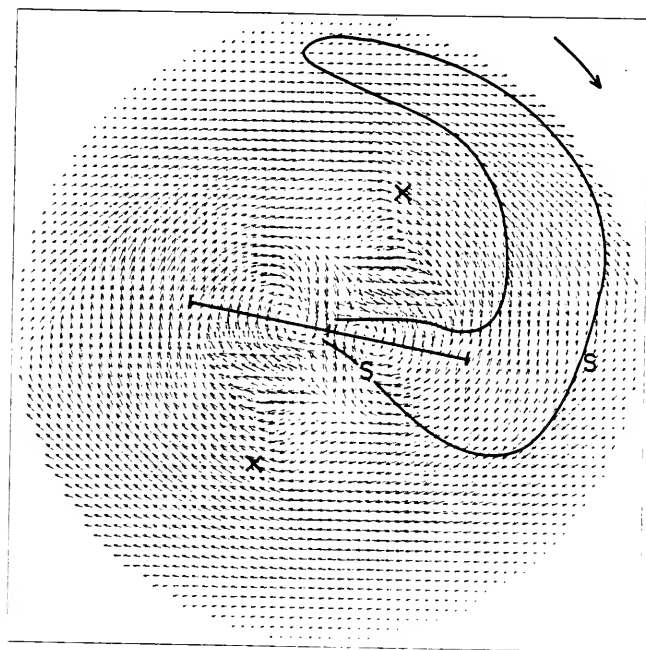


Figure 5-13. Velocity Field Vectors. Velocity field vectors for the model in Figure 5-8. Each arrow is proportional to the size of the velocity and shows the direction of flow for each pixel. The bar rotates clockwise. Maximum velocity is 223 km/sec. The bar position and the approximate position of one of the arms is shown. Shock regions (S) and Lagrangian points (X) are shown.

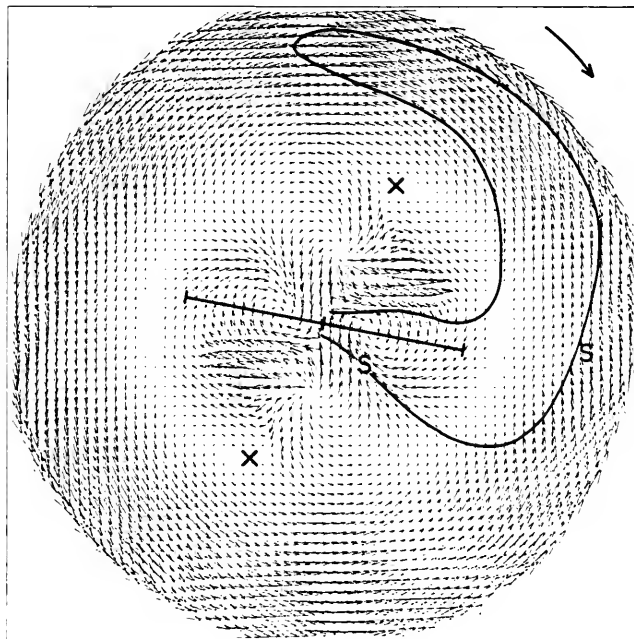


Figure 5-14. Velocity Field in Perturbation Frame. Maximum velocity is 190 km/sec. Symbols are the same as for Figure 5-13.

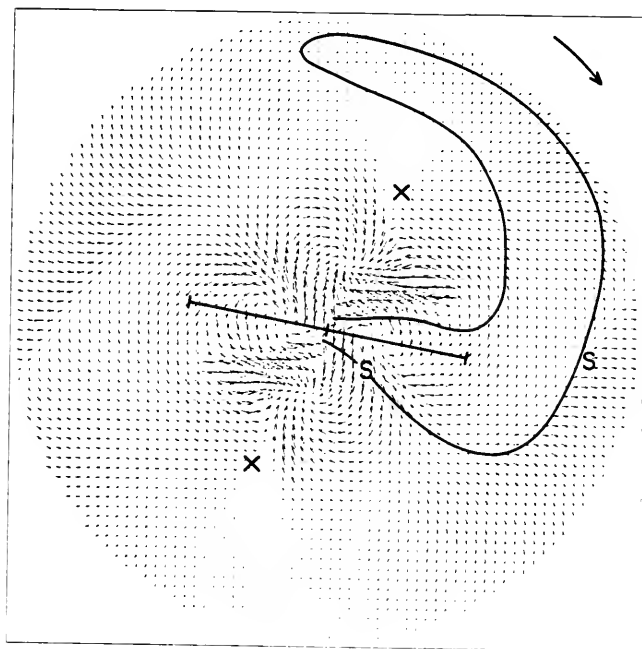


Figure 5-15. Noncircular Velocities. The maximum velocity is 179 km/sec. Symbols are the same as for Figure 5-13.

they do not extend far enough along the bar. The change in velocity across these regions is about 32km/sec giving a Mach number of 1.8 (Mach number is the ratio of velocity change in the shock to sound speed). The shocks in the region where the two arms meet is expected, as fast moving gas meets slower moving gas. The change in velocity across these regions is about 21km/sec giving a Mach number of 1.2. Although the Mach number is not very large, the shock is more evident in the abrupt change in direction of the velocity vectors than in the change in amplitude.

Resonances, especially the Lindblad and the  $\pm 4/1$  resonances, have some important consequences in stellar dynamics (Contopoulos, 1985). Consequently, the positions of these resonances were calculated for the best model for NGC 1300. The positions of these resonances are

Inner Lindblad	----
Inner 4/1	----
Corotation	$6.9 \pm 0.5 \text{ kpc}$
Outer 4/1	$11.2 \pm 0.5 \text{ kpc}$
Outer Lindblad	$14.4 \pm 0.5 \text{ kpc}$

A good opportunity exists in NGC 1300 to supplement the HI rotation curve with the optical rotation curve. The optical values exist in the region where the most unreliable HI data exists. The HI rotation curve in the inner 1.0' is determined by only a few pixels. In this region the optical rotation curve is well determined; it can be used to

calculate the positions of the inner resonances. However, Figure 3-16 shows that the optical rotation curve lies only slightly above the HI rotation curve and consequently, no inner resonances are observed. Thus, although the model does not match the rotation curve very well in the inner 1.0', it does accurately indicate that no inner resonances exist.

NGC 1300 was examined for any peculiarities which may be evident. The breaks in the arms could be manifestations of some of these resonances. The position angles and radii, in the plane of the galaxy, were calculated for these breaks, as were the position angles and radii for the "kinks" in the HI arms. For the east arm these parameters are

Break $\phi = 69.7 \pm 2^\circ$	$R = 8.9 \pm 0.5 \text{ kpc}$
Kink $\phi = 180.0 \pm 2^\circ$	$R = 12.3 \pm 0.5 \text{ kpc}$
Break $\phi = 232.7 \pm 2^\circ$	$R = 16.2 \pm 0.5 \text{ kpc},$

and for the west arm,

Break $\phi = 90.0 \pm 2^\circ$	$R = 11.1 \pm 0.5 \text{ kpc}$
Kink $\phi = 180.0 \pm 2^\circ$	$R = 12.8 \pm 0.5 \text{ kpc}$
Break $\phi = 249.7 \pm 2^\circ$	$R = 21.8 \pm 0.5 \text{ kpc}$

These measurements indicate that the peculiarities seen in the observed gas distribution probably are not due to the 4/1 and Lindblad resonances.



### Bulge Models

In the analysis of the infrared surface photometry the subtraction of a bulge component was an important step. However, none of the models discussed up to this point have included a bulge component. Dr. R. H. Sanders pointed out that adding a bulge component to the models should produce an inner Lindblad resonance, helping the formation of shock fronts. Consequently, a bulge was added to the model containing a halo, a triaxial component, an oval distortion and the Toomre disk. The bulge added closely resembled the bulge fitted to the surface photometry. The mass of this component was estimated from the light contribution of the fitted bulge to the overall bar-bulge luminosity. As the photographic plate is saturated in this region, only a lower limit can be calculated. This lower limit shows that bulge mass should be greater than 10% of the bar mass. A series of models was calculated using various bulge masses between  $0.1M_{\text{BAR}}$  and  $2.0M_{\text{BAR}}$ . The mass distribution in the bulge is a circular Gaussian distribution with  $\sigma = 0.225''$  (FWHM). Models were also calculated in which the pattern speed was varied. As with all previous models, the best gas response occurred when corotation was placed just beyond the end of the bar. The model chosen as the best representation of NGC 1300 is shown in Figures 5-16 to 5-23. This model has the same components as the composite model with the addition of a bulge. The bulge mass is 0.094 times the bar mass. Bulge

masses lower than  $0.85M_{\text{BAR}}$  had essentially no effect, whereas bulge masses greater than  $1.1M_{\text{BAR}}$  caused large humps in the rotation curve. Thus, the total system mass for this model is  $1.2 \times 10^{11} M_{\odot}$ , giving  $M_{\text{HI}}/M = 0.021$ .

The gas response (Figure 5-16) shows a change in the central region and the regions at the ends of the bar. The central region now has a definite bulge component visible in the gas response. In this respect the model now more nearly resembles the optical morphology than the HI. The beginning of the arms now leads the bar by approximately  $12^{\circ}$  in azimuth. These regions now have slightly higher densities than the model shown in Figure 5-9, although the azimuthal extent and pitch angle of the arms has not changed (Figure 5-17). The velocity field shown in Figure 5-18 shows essentially no change in the outer regions of the model. It still shows a lot of twisting of the contours in the central region. However, as can be seen from Figure 5-18, this twisting is confined to the region where no reliable information is available from the HI. The optical velocities from Peterson and Huntley (1980) help only at the very center and at a radius of about  $1.0'$ . The region of no HI velocity information is indicated on this diagram. Figure 5-19 shows the outer regions of this velocity field compared with the observed velocities. As is common with all the models calculated, the model velocity field does not have the required deviations from circular rotation.

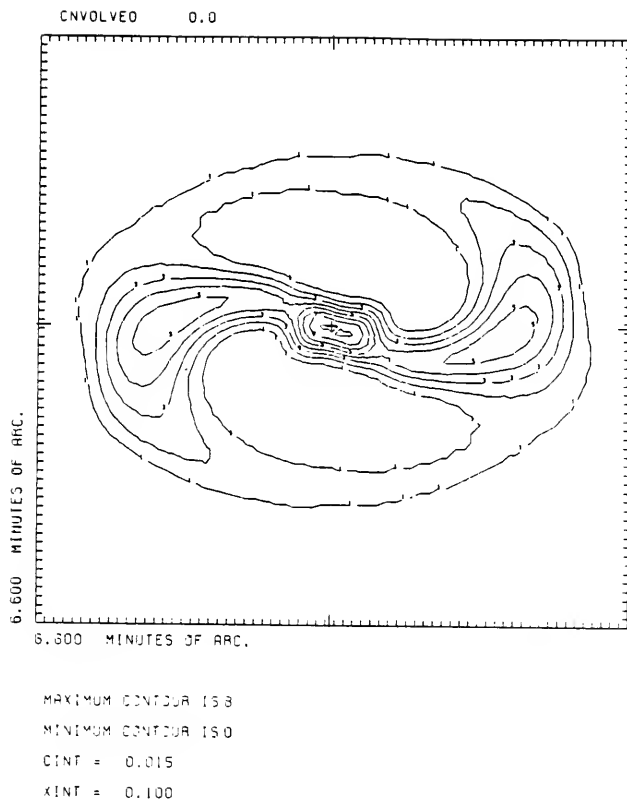


Figure 5-16. Gas Response for Bulge Model. Contours for the gas response for the composite model containing a bulge. Contour interval is 0.1 times peak density. The bar is horizontal.

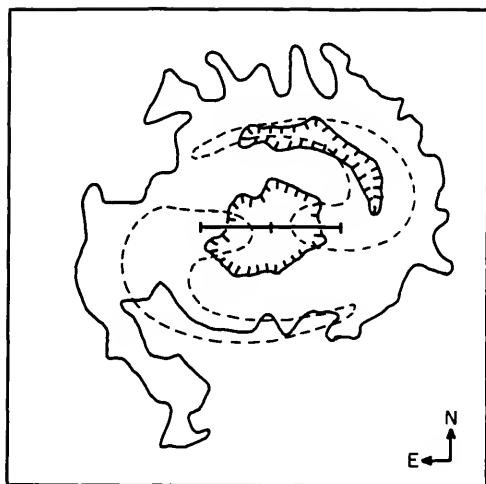


Figure 5-17. Density Compared with Observations. Position of model arms compared with the 20% level of the observed HI distribution. The position and size of the bar is marked.

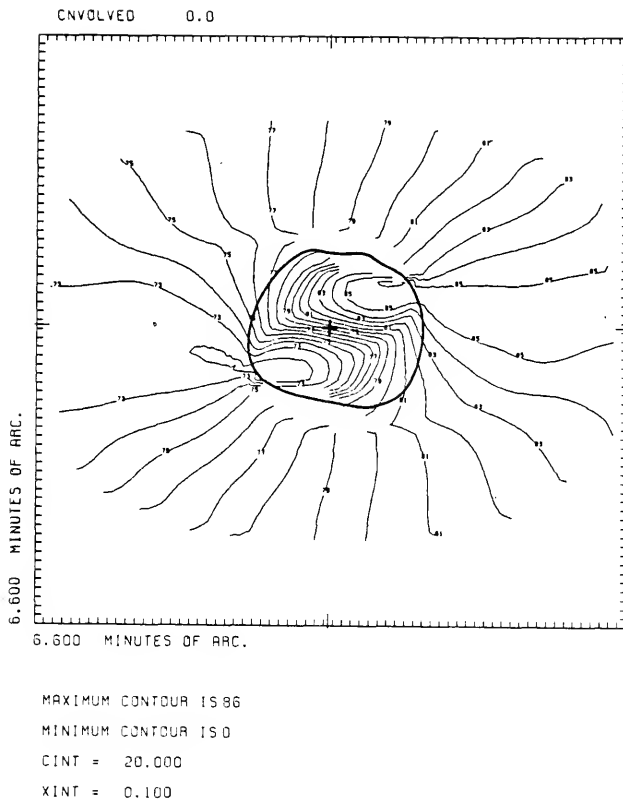


Figure 5-18. Bulge Model Velocity Field. Velocity field for the model shown in Figure 5-16. The approximate outline of the "hole" region in the observations is drawn. Contours are labeled in units of 20 km/sec.

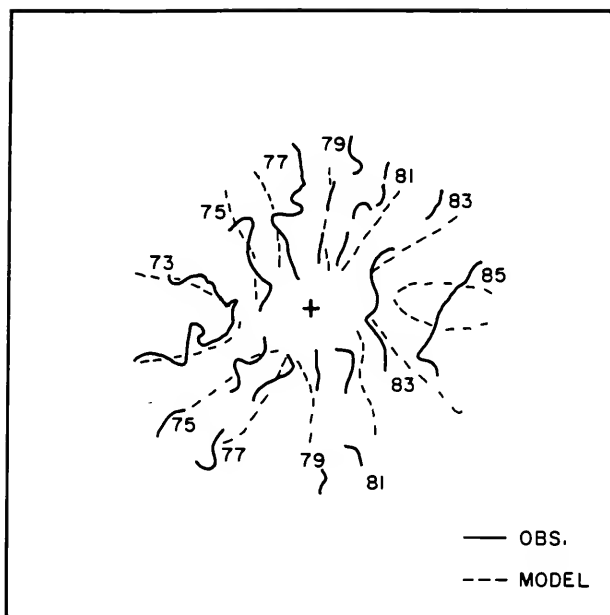


Figure 5-19. Velocity Compared with Observations. Observed velocity contours (—) compared with model velocity contours (---). Contours are labeled in units of 20 km/sec.

The rotation curve from this model fits the observed rotation curve very well, even in the inner 1.0' where the optical velocities define the rotation curve. Figure 5-20 shows the model rotation curve compared with the observational rotation curve. Apart from a hump at  $r=1.2'$  the model rotation curve is a good match to the observations. The radial extent of the bar and bulge are indicated on this figure. The error bars are representative of the errors in the various positions along the observed rotation curve.

The addition of the bulge has substantially increased the shock fronts. These shock fronts are indicated in Figures 5-21 to 5-23 which are the velocity field vectors, the velocity vectors in the perturbation frame and the non circular velocities respectively. The bar and arm positions are also indicated. Bar rotation is clockwise. The positions of these shock fronts are on the trailing edge of the bar. These fronts extend all the way along the bar and show some indication of turning along the arms. The Mach number across these fronts is approximately 7. The position of these shocks is not accurately given by the beam scheme.

The velocity vectors in the perturbation frame (Figure 5-22) show circulation around the minor-axis Lagrangian points very clearly. Figure 5-23 shows the noncircular velocities. The largest noncircular motions occur in the bar and bulge region.

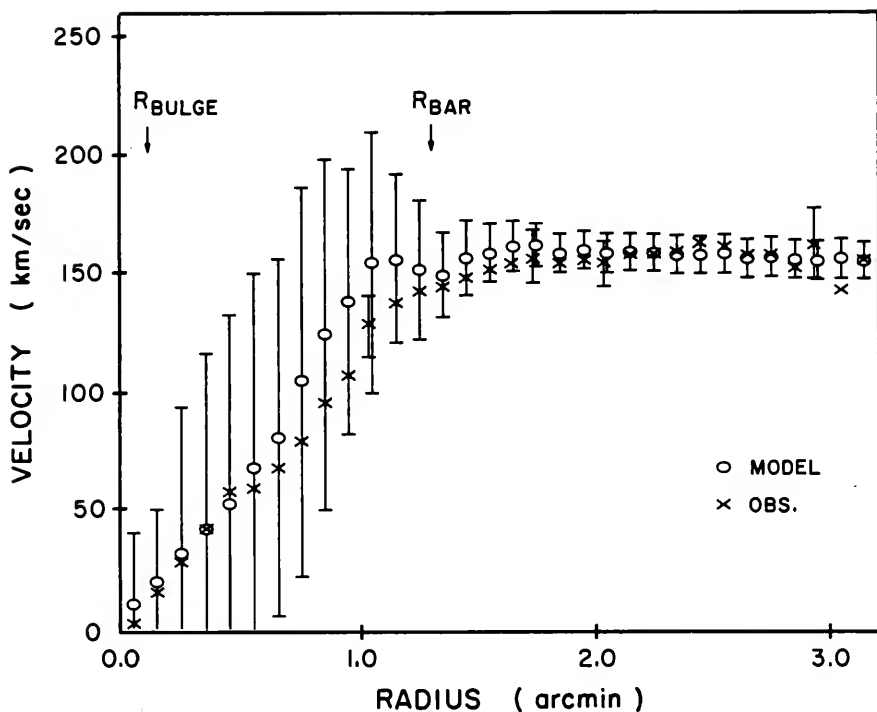


Figure 5-20. Comparison of Rotation Curves. Observed rotation curve compared with the rotation curve for the composite model with a bulge. Representative error bars are shown for the observations. Error bars represent one standard deviation.



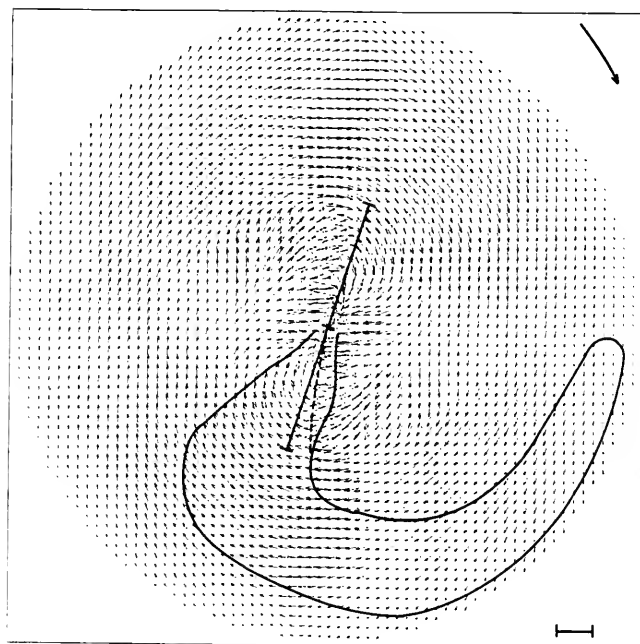


Figure 5-21. Velocity Vectors for Bulge Model. Velocity field vectors for the composite model with a bulge. The bar rotates clockwise. Shock regions are shown (--) as well as the approximate position of the bar and arm. The maximum velocity of 292 km/sec. is shown in the bottom right corner.

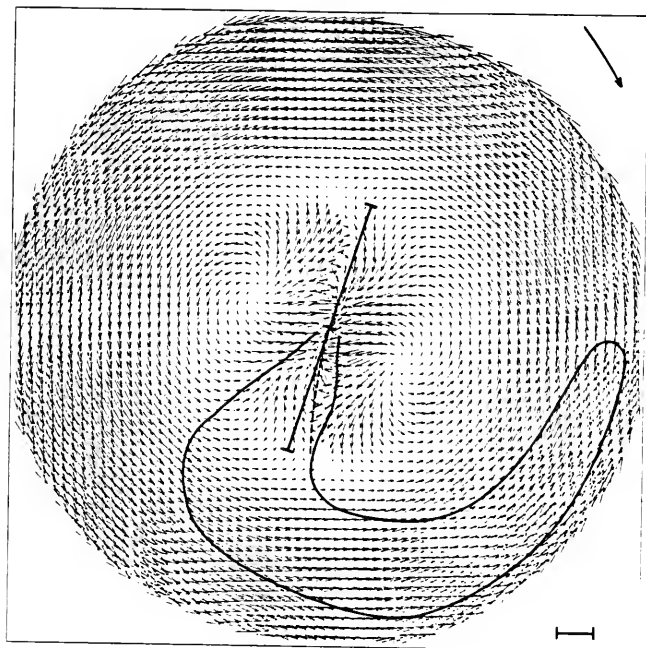


Figure 5-22. Velocity Field in Perturbation Frame. Velocity vectors in the rotating frame of the perturbation. Symbols are the same as for Figure 5-21. Maximum velocity is 315 km/sec.

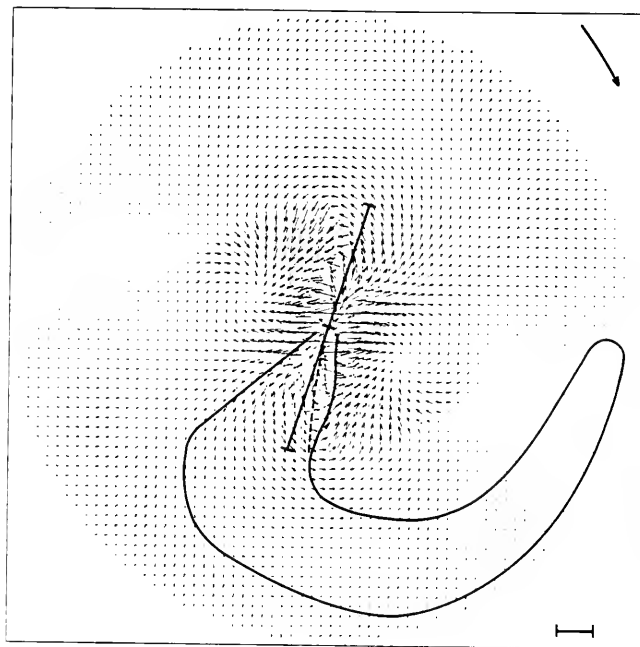


Figure 5-23. Noncircular Velocities. Velocity vectors for composite model with a bulge. Symbols are the same as for Figure 5-21. Maximum velocity is 272 km/sec.

The difficulties with the present modeling philosophy may be reduced by considering other techniques. The inclusion of self-gravity in the models may reduce the spatial discrepancy between the model arms and the observed HI arms by making the model arms more-tightly wound than they are without self-gravity. However, the model of Peterson and Huntley (1980) does not have the arms wound tightly enough, and self-gravity is included in their model. As the inclusion of self-gravity requires a self-consistent bar and disk combination, after considering the results of Peterson and Huntley (1980), no models with self-gravity were calculated. It is also unlikely that the inclusion of self-gravity will solve all the problems of the present models but is certainly worth investigating.

An alternative approach is to use a spiral potential outside the bar. In a series of models Contopoulos et al. (1986) have shown that it is possible to generate arms outside the bar region with a spiral potential. But what is the origin of the spiral potential? Is it provided by the stellar component or through some other mechanism? The near infrared surface photometry indicates that there is some spiral structure evident in the red light distribution. This probably indicates that the older stellar component may provide a spiral potential for the perturbation outside the bar region. The inclusion of a spiral perturbation which mimics the near infrared photometry could solve the problem

with the positioning and strengths of the model arms. However, no models using a spiral perturbation have been calculated, but should be investigated.

## CHAPTER VI

### RESULTS FROM OTHER GALAXIES

The observations and analyses of the barred spiral galaxy NGC 1300 have been described in detail in Chapters 1-4. The hydrodynamical modeling results will be compared with the results from three other barred spiral galaxies, NGC 1073, NGC 3359 and NGC 3992. The analyses of these galaxies have been published elsewhere and only a summary of the main features, both observational and theoretical, will be given here. Full details for each galaxy can be found in the references given in each section.

#### NGC 3359

This galaxy has been studied extensively by Ball (1984, 1986).

#### Observational Results

The neutral hydrogen distribution in NGC 3359 was mapped at the VLA during 1983 using both the C and D arrays (Ball, 1984, 1986). The beam synthesized in these observations was  $18.04'' \times 17.64''$  (FWHM). This angular resolution is somewhat better than previous observations of HI in barred spirals. The observed channel maps were

corrected for continuum emission, CLEANed using the Clark variation of the Hogbom algorithm and integrated using the "window" technique of Bosma (1978), to give the neutral hydrogen distribution and its associated temperature-weighted velocity field (Figures 6-1 and 6-2).

The most striking feature of the gas distribution (Figure 6-1) is its clumpy nature. The initial impression is that NGC 3359 is not an example of a grand design spiral, but the overall, global distribution does indeed follow a grand design spiral pattern traced by a broad ridge of high surface density. These observations are in accordance with Elmegreen and Elmegreen (1985) who classify it as a grand design spiral whose spiral structure is nevertheless patchy. Emphasizing the grand design nature of the spiral structure is the location of Hodge's (1969) HII regions. These regions are strongly correlated in position with the broad ridge of surface density which traces the spiral structure (Ball, 1984, 1986). This broad ridge has a surface density  $> 1.6 \times 10^{21} \text{ cm}^{-2}$  upon which many irregular gas complexes are found.

Away from the arms, the clumpy structure of the HI persists, but the background level of the surface brightness is appreciably lower. Toward the nucleus the HI distribution may be characterized as forming an irregular, slightly-elongated ring with a radius of approximately  $1.0''$ . This could be the HI arms becoming blended by beamsmeearing at

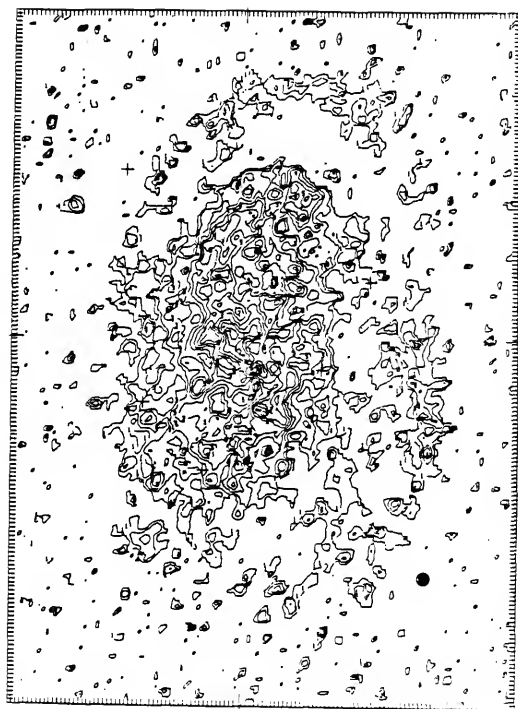


Figure 6-1. HI Distribution NGC 3359.  
Observed gas density for NGC 3359 from Ball (1984).  
North is to the top and east is to the left.



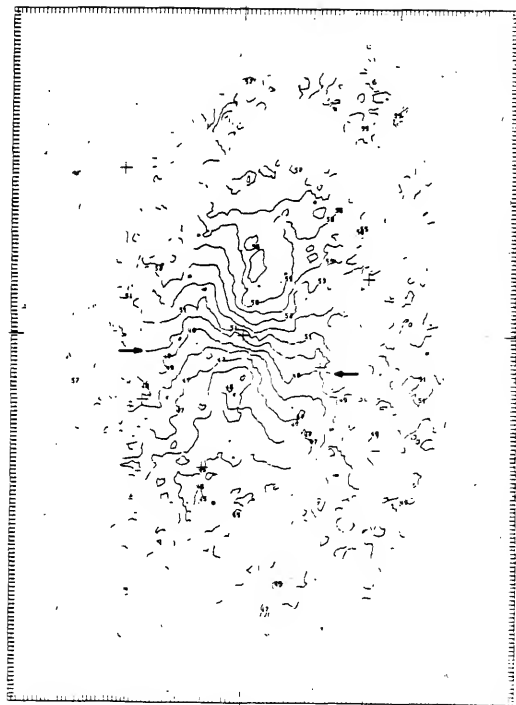


Figure 6-2. Velocity Field NGC 3359. Contours are labeled in units of 20 km/sec. The 1000 km/sec. level is indicated.

small radii. However, this region, interior to the ring, coincides rather closely with the region that would be swept out by the bar rotating about its center. The angle-averaged, deprojected surface density of HI also shows this region to be depleted relative to the rest of the galaxy. This depletion in HI is observed to a greater or lesser extent in all the barred galaxies in this project. Sensitive observations in the CO line would be required to determine whether or not the total gas surface density (HI and  $H_2$ ) is depleted in this region.

The temperature-weighted, mean radial velocity field (Figure 6-2) shows perturbations in the galactic rotation field associated with the spiral structure. The demarcation of the spiral structure is even more prominent in the velocity field than in the density distribution. The effects appear as well-defined, continuous distortions in the velocity contours at positions which coincide with the HI and optical arms. Some skewing of the velocity contours occurs in the region dominated by the bar. The contours are skewed away from the direction perpendicular to the kinematic major-axis; this is indicative of gas flow along the bar (Kalnajs, 1978). "Thus, the underlying dynamics of NGC 3359 are evidently dominated by a broad, bisymmetric, grand design spiral pattern, which strongly perturbs the rotational velocities of the gaseous disk" (Ball, 1986).

The angle-averaged rotation curve derived from these results is presented in Figure 6-3. Several features are evident. First, there is no truncation signature apparent in the rotation curve. Second, the curve, in the inner 1.0', rises steadily, then at the end of the bar flattens abruptly, remaining approximately constant at 130km/sec,  $r=1.2'$  to  $2.5'$ . The curve then begins to rise again, reaching its maximum of 153km/sec at  $r=3.5'$ , then flattens and enters into a long, gradual decline.

Table 6-1 summarizes the observed, integrated properties of the galaxy.

#### Hydrodynamical Models

The results of the hydrodynamical modeling procedure are determined by the masses and mass distributions of the axisymmetric and non-axisymmetric components, the disk and bar respectively, and the angular velocity at which the non-axisymmetric component stirs the gaseous disk. The axisymmetric component was determined largely by the rotation curve. An  $n=0$  Toomre disk was found to provide a good representation for the axisymmetric component as determined by the angle-averaged rotation curve. Two differing approaches were used to determine the non-axisymmetric component. A triaxial ellipsoidal figure, calculated using Stark's (1977) method, and an oval distortion were used.

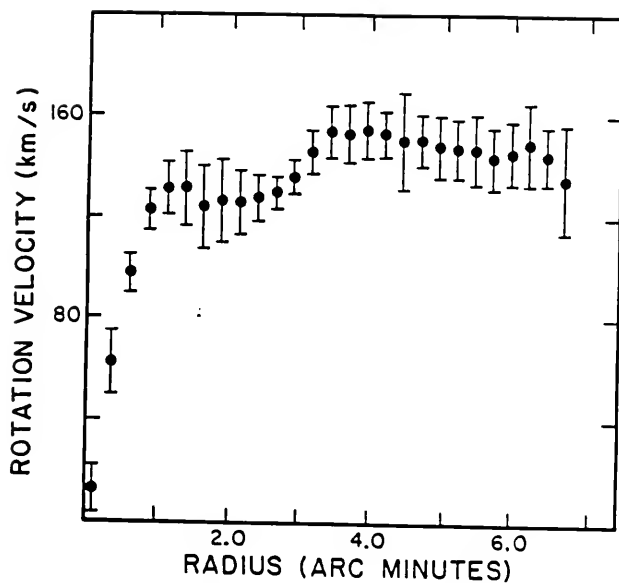


Figure 6-3. Rotation Curve NGC 3359. Observed rotation curve for NGC 3359 from Ball (1984). Error bars represent one standard deviation.

TABLE 6.1

Summary of Integrated Properties of NGC 3359

Parameter	NGC 3359
Synthesized beam (FWHM) (arcsec)	18.04x17.64
Synthesized beam (FWHM) (kpc)	0.96x0.94
Total HI map rms noise ( $10^{19} \text{cm}^{-2}$ )	13.0
Peak HI density ( $10^{21} \text{cm}^{-2}$ )	3.51
Observed systemic velocity (km/sec)	1009.0
Adopted distance (Mpc)	11.0
Diameter of HI disk (arcmin)	8.20
Position angle, line of nodes ( $^{\circ}$ )	-8.0
Inclination angle ( $^{\circ}$ )	51.0
Observed width, Global profile (km/sec)	326
Maximum rotation velocity (km/sec)	153
Radius of maximum velocity (kpc)	11.20
Mass within hydrogen disk, $M$ , ( $10^{10} \text{Mo}$ )	12.0
Atomic hydrogen mass, $M_{\text{HI}}$ ( $10^9 \text{Mo}$ )	5.00
$M_{\text{HI}}/M$	0.042
$M/L_B$ (solar units)	11.1
$M_{\text{HI}}/L_B$ (solar units)	0.46

The results using these parameters were quite clear-cut. Models using the triaxial ellipsoid failed to produce results which were similar to those observed. No combination of pattern speed and bar mass yielded a "good model." The oval distortion, however, worked very well in matching the locations and amplitudes of the velocity distortions in the galaxy. A hybrid model, consisting of an oval distortion and a triaxial ellipsoid, was found to be the best compromise in fitting the density, velocity and luminosity distributions of NGC 3359. The bar has a mass of approximately 3.9% of the disk mass, giving  $M_B/L_B \approx 0.6 M_D/L_D$ ; thus it does not contribute significantly to the non-axisymmetric forces. The pattern speed of the bar-oval distortion combination lies somewhere between 108.5 km/sec/arcmin and 95.0 km/sec/arcmin or, 34.0 km/sec/kpc to 29.8 km/sec/kpc. This places corotation at between 1.05' and 1.2', or between 1.0 and 1.2 times the radius of the bar. The mass of the disk for this model is  $5.9 \times 10^{10}$  Mo; the bar mass is  $2.3 \times 10^9$  Mo, giving a total galaxy mass within 3.75' or 12 kpc of  $6.13 \times 10^{10}$  Mo. No halo was added to these models.

#### NGC 3992

NGC 3992 has been studied observationally by Gottesman et al. (1984) and theoretically by Hunter et al. (1986).

### Observational Results

This galaxy was observed between 1980 and 1983 at the VLA using both the C and D arrays. The beam synthesized in these observations was  $26.1'' \times 20.0''$  (FWHM). These observations were converted to a series of channel maps, corrected for continuum emission, CLEANed and integrated using Bosma's (1981) method to give maps of the neutral hydrogen density distribution and the temperature-weighted, mean radial velocity field (Figures 6-4 and 6-5).

The spiral structure is only weakly visible in the HI distribution, although when only densities greater than 0.5 of the peak gas density are considered, the correlation with the observed spiral structure is more apparent (Figure 1 of Hunter et al., 1986). The contrast between this gas structure and the general background level of the gas is low, indicating that the structure is not strongly defined at the resolution of this survey. Inside the optical ring, or roughly the region dominated by the bar, the HI is deficient. This "hole" can be approximated by an ellipse with a semi-major axis of  $0.95''$ . After referring to  $^{12}\text{CO}$  observations (Gottesman et al., 1984) conclude that "...while it is possible that the  $\text{H}_2$  density is somewhat larger than that of the HI, the total gas content in the center of NGC 3992 appears to be less than in the disk." The depletion of gas in the central region is vividly illustrated by the angle-averaged, deprojected surface

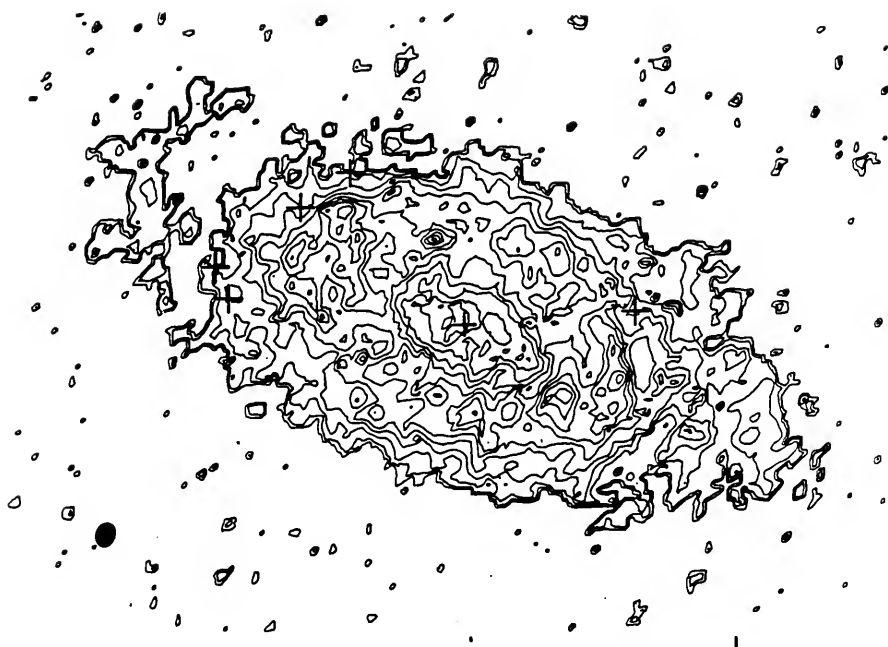


Figure 6-4. HI Distribution NGC 3992. Observed gas distribution for NGC 3992 from Gottesman et al. (1984). The beam is indicated in the bottom left. North is to the top and east is to the left.



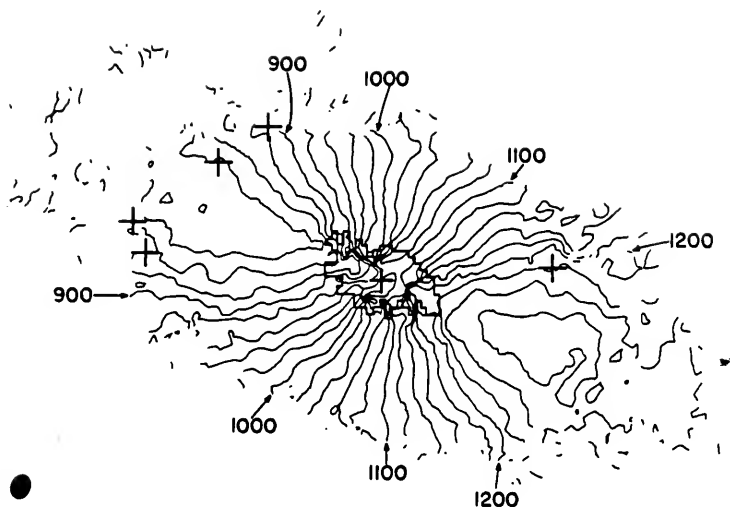


Figure 6-5. Velocity Field NGC 3992. Contours are labeled in km/sec. The extent of the gas depleted region is shown.

density (Figure 4 of Gottesman et al., 1984). This gas depletion in the central region of NGC 3992 is more pronounced than in NGC 3359.

The temperature-weighted, mean radial velocity field is shown in Figure 6-5. Reliable velocities are not shown in the central  $1.0'$ , the hole, due to the low density of the atomic gas in this region. Weak irregularities in the velocity contours are associated with the optical spiral structure. These irregularities are not as strong as those observed in NGC 3359; the velocity field as a whole is dominated by circular rotation. However, there is a discontinuity in the contours as the line of sight crosses the bar. This is explained as gas flowing around strong bars and skewing the velocity contours, but as the gas density is so low in these observations, this interpretation is uncertain.

The angle-averaged rotation curve derived from the velocity field is shown in Figure 6-6. The curve inside  $r=1.0'$  is uncertain due to the gas-depleted "hole," but between  $r=1.0'$  and  $r=3.5'$ , the curve rises slowly, reaching its maximum value of  $V=278\text{km/sec}$  at  $r=3.0'$ . At  $r=3.8'$  there is a very noticeable drop in the rotation curve which then flattens out again to  $V=250\text{km/sec}$ . This sharp drop, seen in both halves of the galaxy has been interpreted as resulting from the truncation of the disk of the galaxy (Gottesman et al., 1984; Hunter et al., 1984).

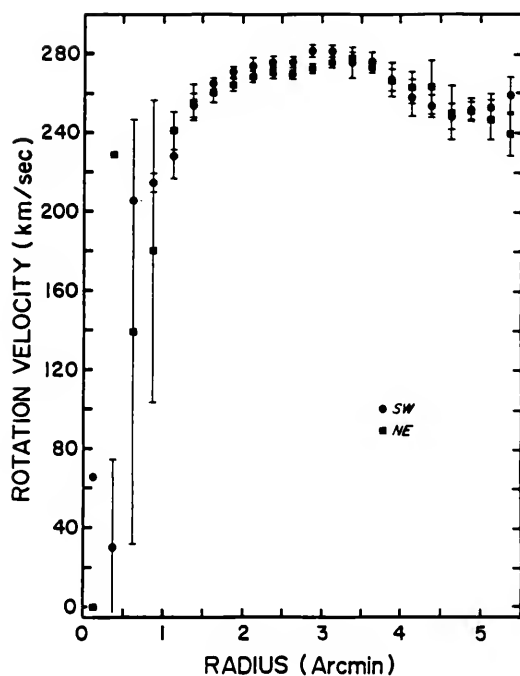


Figure 6-6. Rotation Curve NGC 3992. Observed rotation curve for NGC 3992 from Gottesman et al. (1984). Two halves of the major-axis are shown. Error bars represent one standard deviation.

Table 6-2 summarizes the observed, integrated properties of the galaxy, NGC 3992.

### Hydrodynamical Models

The dynamical components considered by Hunter et al. (1986) in modeling NGC 3992 were

1. An axisymmetric Toomre disk of index  $n=0$ , truncated as indicated by the observations.
2. A spherical halo constrained by the observed kinematics and truncation of the disk.
3. A triaxial stellar bar constrained by near infrared photometry.
4. An oval distortion of the axisymmetric disk.

Combinations of these parameters yielded models which displayed the main features in the observations but also had significant deviations from the observations. Spiral arms, the kinematic offset and the central hole were all partially reproduced. However, the arms are not in the correct position and are more tightly wound in the observations than in the models.

The results from the modeling show that a halo containing roughly one disk mass, interior to the disk radius, must surround the galaxy. A stellar bar and an oval distortion must coexist in order to excite the observed gas response. Neither component by itself satisfactorily reproduces the observations and, although the combination of

TABLE 6.2

Summary of Integrated Properties of NGC 3992

Parameter	NGC 3992
Synthesized beam (FWHM) (arcsec)	26.10x20.00
Synthesized beam (FWHM) (kpc)	1.80x1.38
Total HI map rms noise ( $10^{19} \text{ cm}^{-2}$ )	4.80
Peak HI density ( $10^{21} \text{ cm}^{-2}$ )	1.71
Observed systemic velocity (km/sec)	1045.8
Adopted distance (Mpc)	14.2
Diameter of HI disk (arcmin)	8.40
Position angle, line of nodes ( $^{\circ}$ )	-111.5
Inclination angle ( $^{\circ}$ )	53.4
Observed width, Global profile (km/sec)	598
Maximum rotation velocity (km/sec)	273
Radius of maximum velocity (kpc)	12.80
Mass within hydrogen disk, $M$ , ( $10^{10} \text{ Mo}$ )	22.8
Atomic hydrogen mass, $M_{\text{HI}}$ , ( $10^9 \text{ Mo}$ )	3.80
$M_{\text{HI}}/M$	0.017
$M/L_B$ (solar units)	9.50
$M_{\text{HI}}/L_B$ (solar units)	0.16

triaxial bar and oval distortion only partially reproduces the observations, the combination is better than either component individually. The stellar bar must have a mass of between 18% and 30% of the mass of the truncated disk. Bars less massive than 18% of the disk mass do not exert forces strong enough to sweep out the hole, nor provide the observed velocity contour discontinuities, nor generate the required contrast and extent of the spiral arms. Bars more massive than 30% of the disk mass are ruled out observationally as no central maximum at  $r=1.0'$  is seen in the rotation curve. However, a bar of this mass implies that the mass-to-luminosity ratio for the bar varies between 4 and 7 times that for the disk. Models were completely unsuccessful when the mass of the bar was such as to make  $M_B/L_B \approx M_D/L_D$ . The pattern speed of the non-axisymmetric components is 51.7 km/sec/kpc, placing corotation at just beyond the end of the bar at  $r=4.3$  kpc or 1.02 times the bar radius. The disk mass for this model is  $9.75 \times 10^{10} M_\odot$ , the halo mass is  $9.14 \times 10^{10} M_\odot$  and the triaxial bar mass is  $2.5 \times 10^{10} M_\odot$ , giving a total system mass, out to  $r=14.9$  kpc ( $r=3.6'$ ), of  $2.14 \times 10^{11} M_\odot$ .

#### NGC 1073

This barred spiral galaxy has been observed and modeled by England, Gottesman and Hunter (1986, private communication).

### Observational Results

NGC 1073 was observed in 1983 and 1984 using the VLA C and D arrays. The final resolution achieved was  $20.3'' \times 19.7''$  (FWHM). In contrast with the other galaxies in this survey, the velocity bandwidth used for NGC 1073 is 12.63 km/sec (FWHM); the channel separation is 10.35 km/sec. As with all the galaxies in this project, the channel maps were corrected for continuum emission, CLEANed and integrated to produce maps of the neutral hydrogen distribution and the associated temperature-weighted, mean radial velocity field (Figures 6-7 and 6-8).

In contrast with the optical image, the neutral hydrogen distribution shows little evidence for spiral structure. If only densities greater than 0.5 of the peak observed gas density are considered, a correlation exists between the bright optical regions and these regions of high HI density. Though the majority of these bright optical patches occur near the arms, no clear spiral pattern emerges. At a gas density level of 0.4 of the peak observed gas density the observed gas forms a broad ring, extending from approximately the inside of the optical spiral arms to well outside the arms ( $r=1.0'$  to  $r=2.0'$ ). A gas bar, aligned with the optical bar, becomes evident at a gas density level of 0.3 of the peak observed density (peak observed density is  $1.77 \times 10^{21}$  atoms/cm<sup>2</sup>). On either side of the bar the gas level is below about 0.15 of the peak density. This gas in

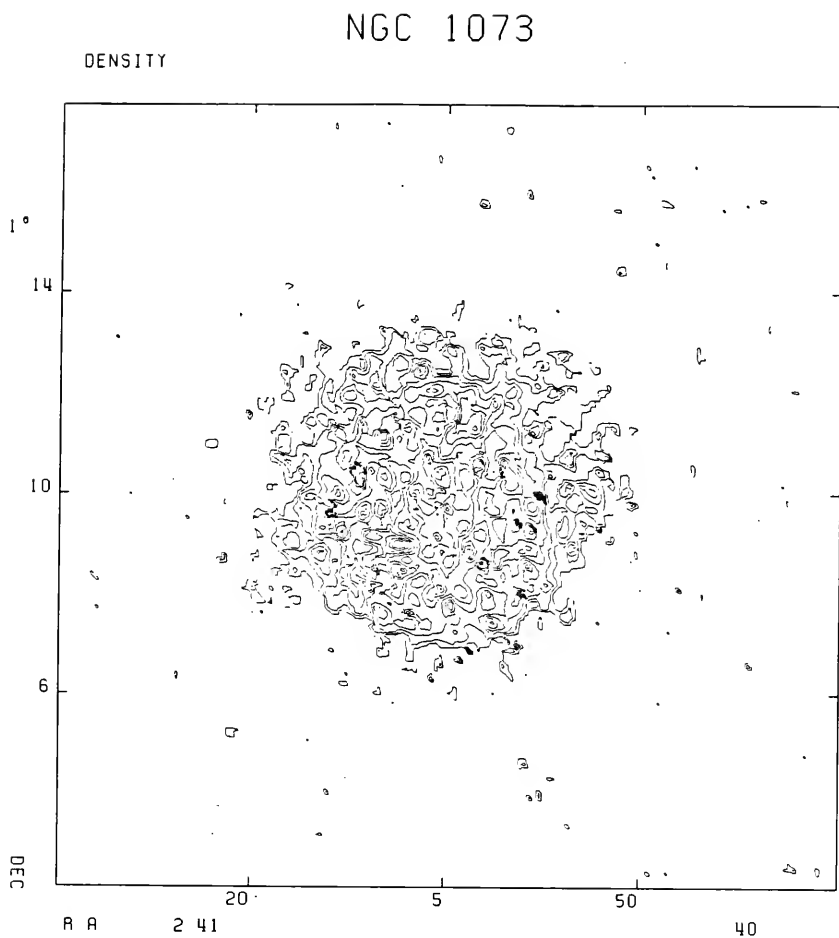


Figure 6-7. HI Distribution NGC 1073. Observed gas density for NGC 1073. North is to the top and east is to the left.



## NGC 1073

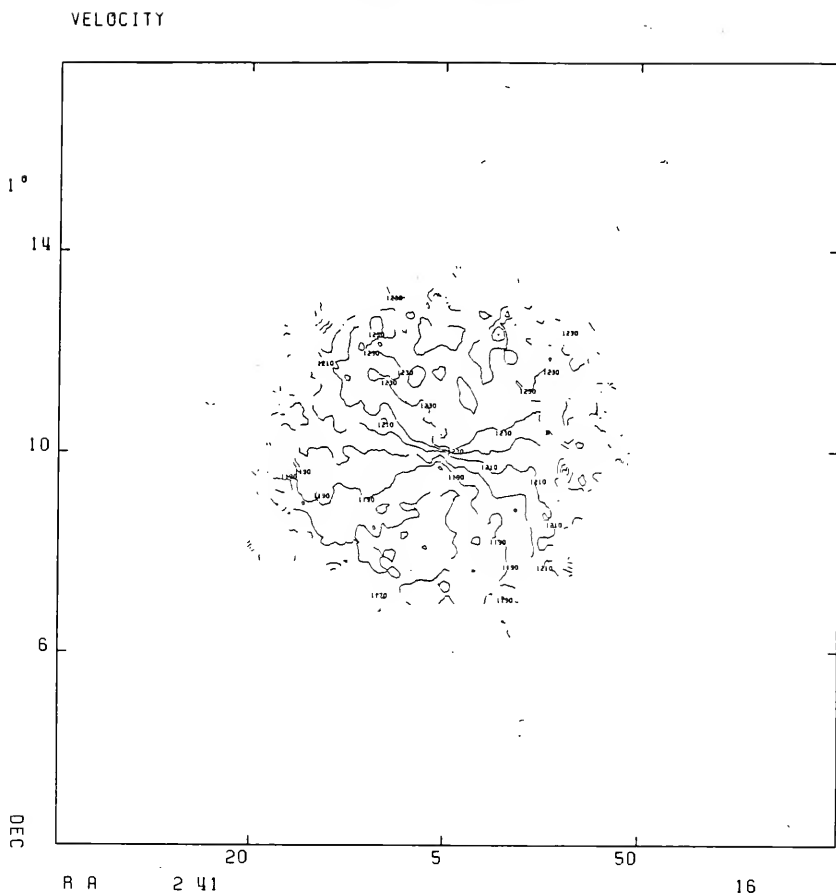


Figure 6-8. Velocity Field NGC 1073. Contours are labeled in km/sec.

the bar region for NGC 1073 is the exception for the galaxies studied for this project. No other barred galaxy used here shows evidence for any gas along the bar. In fact all the other galaxies show gas depletion in a large region surrounding the bar. The general background gas density in the disk is approximately 0.25 to 0.30 of the peak observed gas density.

The temperature-weighted, mean radial velocity field (Figure 6-8) shows that the dominant component in the rotation field is, once again, circular motion. The bar major-axis coincides very closely with the kinematic minor-axis, and the velocity contours are very nearly parallel to the bar. Some irregularities in the velocity contours (departures from circular motion) are evident where the velocity contours cross the peak of the gas ring.

Figure 6-9 shows the angle-averaged rotation curve derived from the velocity field shown in Figure 6-8. The curve rises steeply in the inner region, then flattens out, reaching its maximum of 96km/sec at  $r=1.8'$ . The rising part of the curve is approximately the region occupied by the bar. At  $r=2.5'$ , the rotation curve drops off, exhibiting the features of a truncation signature. The angle-averaged, deprojected surface density indicates that the signal-to-noise ratio in this region is good and that the apparent truncation signature is not solely a result of low hydrogen surface brightness. This apparent truncation signature is

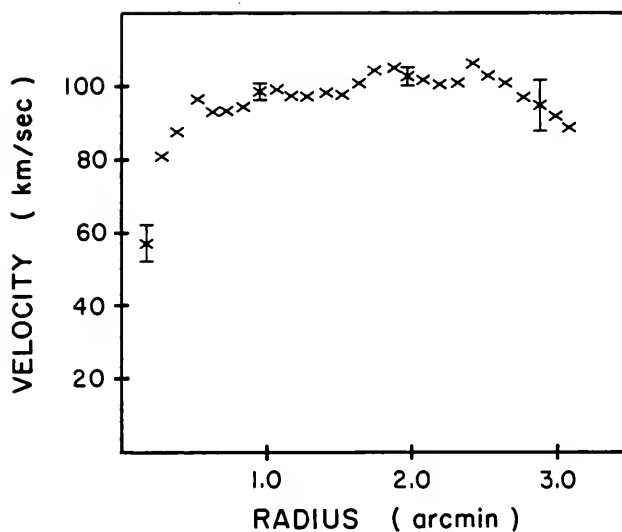


Figure 6-9. Rotation Curve NGC 1073. Representative error bars shown are plus or minus one standard deviation.

evident in the rotation curves calculated using a  $\pm 15^\circ$  wedge around the major-axis for both halves of the galaxy.

Table 6-3 summarizes the observed, integrated properties of NGC 1073.

### Hydrodynamical Models

An  $n=0$  Toomre disk is used to provide the axisymmetric component for the models of NGC 1073. The axisymmetric component is determined from the observed rotation curve. The non-axisymmetric component consists of a triaxial ellipsoidal bar and an oval distortion. The triaxial ellipsoidal figure is calculated using near infrared surface photometry as a constraint. As little evidence for spiral arms exists in the HI, the oval distortion is needed only for providing perturbations in the radial velocity field. A disk and the triaxial figure are sufficient to reproduce the broad ring and the gas bar, but do not provide sufficient perturbations in the velocity contours. The bar has a mass of 7% of the disk mass. A mass larger than this gives a large central peak in the rotation curve; this peak is not observed. This bar mass gives  $M_B/L_B \sim 1.5 M_D/L_D$ .

The oval distortion is very weak and its sole function is to provide perturbations in the radial velocity field. The maximum perturbed surface density (at  $r=0.89'$ ) is 3.6% of the unperturbed density. If the distortion is increased, the ring is broken into spiral arms, which are not observed

TABLE 6.3

Summary of Integrated Properties of NGC 1073

Parameter	NGC 1073
Synthesized beam (FWHM) (arcsec)	20.30x19.70
Synthesized beam (FWHM) (kpc)	1.33x1.30
Total HI map rms noise ( $10^{19}\text{cm}^{-2}$ )	5.30
Peak HI density ( $10^{21}\text{cm}^{-2}$ )	1.77
Observed systemic velocity (km/sec)	1208.9
Adopted distance (Mpc)	13.6
Diameter of HI disk (arcmin)	6.60
Position angle, line of nodes ( $^{\circ}$ )	-15.4
Inclination angle ( $^{\circ}$ )	18.5
Observed width, Global profile (km/sec)	107
Maximum rotation velocity (km/sec)	96
Radius of maximum velocity (kpc)	7.10
Mass within hydrogen disk, $M$ , ( $10^{10}\text{Mo}$ )	3.00
Atomic hydrogen mass, $M_{\text{HI}}$ , ( $10^9\text{Mo}$ )	2.80
$M_{\text{HI}}/M$	0.093
$M/L_B$ (solar units)	3.22
$M_{\text{HI}}/L_B$ (solar units)	0.30

in the HI. The oval distortion also perturbs the gas bar, giving it the characteristic dumbbell shape of oval distortions. This shape may be observed in the HI gas distribution but is at the limit of the resolution and signal-to-noise of the observations, so the evidence is not conclusive. These non-axisymmetric components, the bar and oval distortion, have a pattern speed lying between 28.5km/sec/kpc and 19.3km/sec/kpc, placing corotation at between 1 and 1.2 times the bar radius (bar radius is 2.8kpc). The disk mass for this model is  $3.0 \times 10^{10} \text{ Mo}$ , the triaxial mass is  $2.1 \times 10^9 \text{ Mo}$  giving a total mass for the system of  $3.21 \times 10^{10} \text{ Mo}$ . No halo component is used in modeling NGC 1073.

## CHAPTER VII PROPERTIES OF BARRED SPIRAL GALAXIES

### Observational Comparisons

The neutral hydrogen observations of the four barred spiral galaxies (NGC 1073, NGC 1300, NGC 3359 and NGC 3992) show differences in the morphologies of the galaxies. NGC 1073 shows a complete ring with some high density clumps at positions corresponding to some features in the optical object. NGC 1300, on the other hand, shows almost perfect correlation of the HI features with the optical features. NGC 1300 has arms in the HI, and very little gas in the interarm regions; however, NGC 1073 shows little correlation between the the HI and the optical. NGC 3359 and NGC 3992 lie somewhere between these extremes. NGC 3359 has reasonable correlation between the HI and the optical arms when only the upper levels of the gas are considered. NGC 3992 shows the same effect, but the correlation is not globally as good as in NGC 3359. This is mainly due to resolution effects broadening the HI and causing the arms to be smeared together. However, both NGC 3359 and NGC 3992 have these arm features, in the HI, superimposed on a large broad disk feature. The contrast between the HI arms and the background gas is low for NGC 3992, but slightly higher for

NGC 3359. Neither galaxy has a contrast greater than 1.5:1. Thus, although NGC 1300, NGC 3359 and NGC 3992 all may be classified as grand design spirals in the HI, only NGC 1300 is obviously a grand design system in the HI.

All four galaxies show a depletion of gas in the central region. NGC 1300 and NGC 3992 have a complete "hole" in the gas. Any gas in these regions is below the sensitivity limit of this survey. NGC 1073 has a depleted central region, but uncharacteristically, has a gas bar. The bar gas density is enhanced when compared with the surrounding region, but is still lower than that in the rest of the galaxy. NGC 3359 has the least depleted region of the survey objects. These depleted regions all correspond very closely to the region occupied by the bar of the galaxy, which strongly suggests some interaction between the bar and the gas as being the cause of the gas depletion. The extent of the neutral HI gas is larger than the optical object for all the observed galaxies.

The velocity fields for these four galaxies all show that the dominant component is circular rotation. Superimposed upon this general rotation are deviations from circular motion. NGC 1300 shows the largest amplitude irregularities in its velocities, while NGC 1073 has the smallest amplitude irregularities. However NGC 1300 only has reliable velocities in the arm regions; the gas density is too low in the center and interarm regions to give reliable



velocity information. NGC 1073, on the other hand, has reliable velocity information over the whole region of the observations. NGC 3359 and NGC 3992 lie between the extremes of NGC 1073 and NGC 1300. NGC 3992 does not display many (nor very large) irregularities in the velocity contours, whereas NGC 3359 shows moderately large deviations. In all galaxies these deviations occur at the positions of the spiral arms. NGC 3992 shows a discontinuity in the velocity contours as the line of sight crosses the bar region. This may be due to the gas flowing around a strong bar and skewing the velocity contours, but as there are no reliable velocity data in the bar region, this interpretation is uncertain. NGC 3359 shows skewing of the velocity contours in the bar region but NGC 1073 and NGC 1300 show little evidence for this effect.

Two of the survey galaxies, NGC 3992 and NGC 1073, have evidence for truncation of their disks. The rotation curves exhibit features which have been interpreted by Hunter, Ball and Gottesman (1984) and Gottesman et al. (1984) as being the signatures characterizing a truncation of the disk. The other galaxies in the survey do not exhibit these features. Their rotation curves continue to rise or remain approximately flat; whereas the curves for NGC 1073 and NGC 3992 have the abrupt drops at their truncation radii.

Near infrared surface photometry of all four galaxies shows an object dominated by the bar. In NGC 1073, NGC 3359

and NGC 3992 there is very little evidence for spiral arm structure. NGC 1073 has some low surface brightness evidence for the broken ring feature observed in the optical images. NGC 3359 and NGC 3992 have stumpy protrusions at the end of the bar. These features correspond to the beginning of the spiral arms, but do not extend for more than about 30° in azimuth from the ends of the bar. In contrast to these galaxies NGC 1300 shows significant spiral structure in the near infrared. The spiral arms can be traced through almost 180° in azimuth from the ends of the bar. This indicates that the arms in NGC 1300 have a significantly larger portion of red stars than do the arms in the other galaxies in this survey.

#### Dynamical Properties

The hydrodynamical models calculated for the four barred spiral galaxies considered in this survey have several features in common. The pattern speed for the perturbation is quite fast, placing corotation just outside the end of the bar for all the galaxies. The response of the gas to the imposed perturbation decreases as the pattern speed is lowered. A faster pattern speed would place corotation within the ends of the bar; it would be difficult to imagine how the bar could remain stable (Contopoulos, 1985). The most successful models for the survey galaxies had corotation just outside the bar, the conclusion is that

corotation in barred spiral galaxies occurs just outside the end of the bar. It cannot be inside the bar or too far from the end of the bar. Other studies of gas motions in barred spiral galaxies (Teuben et al., 1986; Sanders and Tubbs, 1980; Schwarz, 1985) have also indicated that corotation is just outside the end of the bar.

This conclusion is reinforced by models for other barred spiral galaxies using stellar and gas dynamics. Teuben and Sanders (1985) used numerical integrations of two-dimensional stellar orbits to study the dynamics of barred spiral galaxies. Their results show that bars can only be constructed from the principal basic parallel family of periodic orbits ( $x_1$  in the notation of Contopoulos, 1983), as all other families have orbit density distributions which are not conducive for the formation of bars. Periodic orbits have been studied by Contopoulos (1970, 1975) and others. These studies have indicated that the simple periodic orbits are ovals which may be elongated either parallel or perpendicular to the bar. Near a resonance both families are present, but far from a resonance only one family is dominant. The three principal resonances in a galaxy with a bar distortion are the inner and outer Lindblad resonances and corotation. Between the inner Lindblad resonances and corotation, the parallel family is dominant. Thus, as the inner Lindblad resonances do not exist, the bar must exist from the center to just

inside corotation. Evidence for the non-existence of the inner Lindblad resonances comes from an examination of the gas density contours in the center of the models. Little evidence is seen for a gas response perpendicular to the imposed perturbation, which would indicate the presence of the inner resonances as the dominant stellar orbits in this case are the ones perpendicular to the imposed perturbation. Teuben et al. (1986) in their study of NGC 1365, and Sanders and Tubbs (1980) in their study of NGC 5383 support the conclusion that the inner Lindblad resonances are deep within the bar.

Both stellar orbit theory (Teuben and Sanders, 1985) and the present study indicate that the bars must tumble in the same sense as galactic rotation implying trailing spiral arms.

The presence of dust lanes in these galaxies is a most conspicuous characteristic of the gas in the region of the bar. Two of the survey galaxy models, NGC 3992 and NGC 1300, were examined for evidence of shocks. As expected evidence for shock regions can be seen in the bar region. The positions of the shock regions in NGC 1300 approximately correspond to the positions of dust lanes seen in the optical image of the galaxy. The shock fronts in the models for NGC 3992 also correspond to the approximate position of the dust patches seen in the optical image. Other gas dynamical calculations have revealed the same phenomenon

(Sanders and Tubbs, 1980; Schwarz, 1985 amongst others). Unfortunately, due to resolution and viscous effects discussed in van Albada and Roberts (1981) and van Albada et al. (1981) only the general position of shocks can be estimated from the models. However, it seems that shock regions should exist in the bar region in barred spiral galaxies, and will most likely be evident in the galaxy as a dust lane. Shock regions may also occur at the end of the bar. At these points, there is gas outflow as seen in the velocity vectors for NGC 3992 and NGC 1300. It is this outflow which results in the shocks in the region where the bar meets the arms. In NGC 1300, in particular, this region has a concentration of HII regions. These HII, star forming regions are the result of these shocks. At the Lagrangian points perpendicular to the bar on the minor-axis, there is stable circulation. Evidence for these points can be seen in the models for NGC 1300 and NGC 3992.

Spiral arms are difficult to produce using triaxial ellipsoids as the only perturbation. The bar figures used in the models for the present survey are unsuccessful in producing spiral arms in the models. This could imply that these bars are generally weak, as their effects are not far-reaching. The lack of a spiral response is due to the lack of a tangential force component in the outer reaches of the disk. Strong bars (bars whose forces have significant effects far from their ends) can begin to produce a spiral

response. The supermassive bar model for NGC 1300 began to show a stubby spiral response at the ends of the bar. The only procedure successful in producing significant spiral response was the addition of some other perturbing component. Oval distortions of the underlying disk were used in this study to provide this extra potential, but other studies have used spiral perturbations (Roberts, Huntley and van Albada, 1979) to provide the extra forcing terms. The addition of these extra forcing terms is very successful in producing a spiral arm response in the gas. Although the bar is incapable of producing spiral arms by itself, it can produce very strong effects in the center of the galaxy. Good examples are the effects in the center of the models for NGC 1300. Thus it seems that even moderate bars can drive large noncircular gas motions, typically 50-150km/sec.

Linear theory predicts that the arms cannot exist beyond the outer Lindblad resonance. However, the models calculated for NGC 1300, NGC 3359 and NGC 3992 all show spiral arms extending beyond the outer Lindblad resonance. This arises from the fact that, as the bar is a strong deviation from axial symmetry, the linear theory is no longer applicable. The use of non-linear theory allows the arms to extend beyond the outer Lindblad resonance, as is evident from the models calculated here. Other computations of the gas response in barred spiral galaxies have shown also that the arms can extend beyond the outer Lindblad

resonance (Sanders and Tubbs, 1980; Schwarz, 1985 and others).

Contopoulos (1985) noted that the  $4/1$  resonances play an important role in stellar dynamics. Two of the galaxies in this study which were examined for effects of these resonances, NGC 1300 and NGC 3992, showed no noticeable effects in the gas response. Thus, it appears that although these resonances may be important in stellar dynamics, their effects may not be as important in gas dynamics.

The existence of halo components surrounding barred spiral galaxies has not been resolved. The models for NGC 1300 and NGC 3992 incorporated a halo component, but the models for NGC 1073 and NGC 3359 did not. The models with halo components did not give significantly better matches to the observations than those without a halo. In the models with halo components, the halo was about as massive as the disk, possibly indicating that, if halos do exist, they do not have masses within the disk radius many times larger than the disk mass.

What about the central "hole" in the gas observed in a number of barred spiral galaxies? The models show a build-up of some gas due to the loss of angular momentum of the gas as a result of interactions with the bar. Some of the gas build-up in the center is due to numerical viscosity effects. However, observationally it appears that there may be a total gas deficiency in the central regions. Further

observations of different gas components and further numerical simulations are required to elucidate this dilemma.



## CHAPTER VIII SUMMARY

The conclusions for this dissertation fall into three categories. The observational results for NGC 1300, the hydrodynamical modeling results for NGC 1300 and the dynamical properties of barred spiral galaxies.

### Neutral Hydrogen Results for NGC 1300

The 21cm observations of NGC 1300 reveal the galaxy to be an excellent example of a grand design spiral system. The HI gas is confined almost exclusively to the spiral arms, with very little interarm gas. These HI arms correlate very well with the positions of the optical arms. In common with a number of other barred spiral galaxies, NGC 1300 shows a large gas-poor region in its center. This is the region occupied by the optical bar. The HI arms can be traced through about  $310^\circ$  in azimuth. The HI gas has a well-defined extent, with a major-axis diameter of  $6.4''$  at a level of  $1.59 \times 10^{21}$  atoms/cm<sup>2</sup>. The mass of gas observed at the VLA was  $2.54 \times 10^9$  Mo.

The velocity field shows reliable data only in the regions that have detectable HI gas. Thus the central portion and interarm regions do not have any velocity

information. The dominant component of the velocity field is circular rotation. Analysis of this velocity field yielded a systemic velocity of 1575.0km/sec, a position angle for the line of nodes of  $-85.5^{\circ}$  and an inclination of  $50.2^{\circ}$  with respect to the plane of the sky.

The rotation curve derived from this velocity field rises, reaching a maximum of 185km/sec at a radial distance of 2.5', then drops slowly out to a distance of about 3.2'. The effects of the noncircular component in the velocity field is evident in the rotation curve. The observational parameters are summarized in Table 8-1.

#### Hydrodynamical Results

The hydrodynamical models for NGC 1300 were partially successful in reproducing the observed features. The models consisted of an  $n=1$  type Toomre disk, a halo component, a triaxial ellipsoidal bar figure, an  $\ell=2$  oval distortion of the disk density distribution and a central bulge.

This model produced spiral arms which did not have the correct pitch angle (the pitch angle was too large). The arms did not have the observed azimuthal extent. However, the circular component of the velocity field and the rotation curve were well-matched by this model. The noncircular velocity amplitudes in the model were not as large as those in the observations. The central gas-depleted region was partially reproduced by the model. It is unlikely

TABLE 8.1  
Summary of Results for NGC 1300

Parameter	NGC 1300
Synthesized beam (FWHM) (arcsec)	20.05x19.53
Position angle of beam ( $^{\circ}$ )	64.5
Channel separation (km/sec)	20.6
Channel rms noise (K)	1.26
Total HI map rms noise ( $10^{19}\text{cm}^{-2}$ )	5.00
Peak HI density ( $10^{21}\text{cm}^{-2}$ )	1.59
Observed systemic velocity (km/sec)	$1575.2 \pm 0.5$
Adopted distance (Mpc) <sup>a</sup>	17.1
Diameter of HI disk (arcmin) <sup>b</sup>	6.40
Peak continuum brightness (K)	12.6
Position angle, line of nodes ( $^{\circ}$ )	$-85.5 \pm 0.5$
Inclination angle ( $^{\circ}$ )	$50.2 \pm 0.8$
Observed width, Global profile (km/sec) <sup>c</sup>	345
Maximum rotation velocity (km/sec)	185
Radius of maximum velocity (arcmin)	2.47
Mass within hydrogen disk, M, ( $10^{10}\text{Mo}$ )	1.20
Atomic hydrogen mass, $M_{\text{HI}}$ , ( $10^9\text{Mo}$ )	2.54
$M_{\text{HI}}/M$	0.021
$M/L_B$ (solar units)	5.02
$M_{\text{HI}}/L_B$ (solar units)	0.11

a De Vaucouleurs and Peters (1981).

b Measured at an observed surface density,  $N_{\text{H}} = 1.59 \times 10^{20} \text{cm}^{-2}$ .

c Full width at 0.2 of peak.

however, that the inclusion of the self-gravity of the gas will reduce these problems.

Models using just a bar and the background disk were totally unsuccessful in reproducing the observed features. Only a combination of all parameters yielded good results. The component parameters for the best model were, a disk ( $M_D = 5.4 \times 10^{11} M_\odot$ ), a triaxial bar ( $M_B = 0.094 M_D$ ), a halo ( $M_H = 1.004 M_D$ ), an  $\ell=2$  oval distortion and a central bulge ( $M_{BUL} = 0.094 M_D$ ). Corotation was placed just outside the end of the bar,  $r_{CR} = 6.9 \text{ kpc}$ . The pattern speed corresponding to this is  $\Omega = 19.3 \text{ km/sec/kpc}$ . Ranges for these parameters were found by inspecting partially successful models. This indicated that for this disk and halo combination  $0.05 M_D < M_B < 0.12 M_D$  and  $0.08 M_D < M_{BUL} < 0.10 M_D$ . The most important resonances occurred at  $r = 11.2 \text{ kpc}$  (outer 4/1) and  $r = 14.5 \text{ kpc}$  (outer Lindblad). The inner Lindblad and inner 4/1 resonances do not exist.

### Dynamical Properties

The dynamical conclusions resulting from the comparison of models for NGC 1073, NGC 1300, NGC 3359 and NGC 3992 are

1. The bar figure must tumble in the same sense as galactic rotation and is a rapidly rotating figure. Corotation must occur just beyond the end of the bar.
2. The inner Lindblad resonances must either not exist or be very close to the center of the galaxy.

3. Bars only are not sufficient to generate the observed spiral arms. Another component, an oval distortion or a spiral perturbation must be added to produce spiral arms.
4. The arms can extend beyond the outer Lindblad resonance. Linear theory restricts the arms to lying inside the outer Lindblad resonance.
5. Shocks are observed along the bar in approximately the same positions as the observed dust lanes. Shock regions are evident at the ends of the bar. These may be observed as HII regions.

Although these models have some shortcomings (they only partially reproduce the observations), they provide an important stepping stone in the construction of self-consistent models for barred spiral galaxies, and should thus be considered as only one of the first steps in the development of a general theory.

Future analyses of barred spiral galaxies should include observations of as many gas components as possible (molecular observations could be very significant). All observed components should be taken into account when modeling these systems. If spiral features are seen in the older stellar population, these should be included in the models.

## APPENDIX A DERIVATION OF VOLUME BRIGHTNESS DISTRIBUTION

In utilizing the infrared surface photometry and the method of Stark (1977) in the hydrodynamical modeling code, a procedure is needed to extract the volume brightness distribution from the surface brightness distribution.

Two functional forms for the surface brightness are considered and the corresponding volume brightness distributions described. The two forms are Gaussian and Exponential. Stark (1977) has shown that the volume brightness distribution,  $F_V(a_V)$ , and the surface brightness distribution,  $F_S(a_S)$ , are related by,

$$F_V(a_V) = \frac{-f^{1/2}}{\pi} \int_{a_V}^{\infty} \left[ \frac{d}{da_S} F_S(a_S) \right] (a_S^2 - a_V^2)^{-1/2} da_S, \quad (A-1)$$

where  $f$  is a constant for a given bar geometry.

### Gaussian Surface Brightness Distribution

If the surface brightness distribution is Gaussian,

$$F_S(a_S) = F_{SO} \exp(-a_S^2/2\sigma^2), \quad (A-2)$$

then the volume brightness distribution can be derived by substituting equation (A-2) into equation (A-1) and integrating.

Thus,

$$\begin{aligned}
 F_V(a_V) &= \frac{-f^{1/2}}{\pi} \int_{a_V}^{\infty} \left[ \frac{d}{da_s} F_{so} \exp(-a_s^2/2\sigma^2) \right] (a_s^2 - a_V^2)^{-1/2} da_s \\
 &= \frac{-f^{1/2}}{\pi} \int_{a_V}^{\infty} \frac{-F_{so} a_s}{\sigma^2} \exp(-a_s^2/2\sigma^2) (a_s^2 - a_V^2)^{-1/2} da_s \\
 &= \frac{F_{so} f^{1/2}}{\pi \sigma} \int_{a_V}^{\infty} a_s \exp(-a_s^2/2\sigma^2) (a_s^2 - a_V^2)^{-1/2} da_s. \quad (A-3)
 \end{aligned}$$

Changing variables, letting  $w = a_s$ , gives,

$$F_V(a_V) = \frac{F_{so} f^{1/2}}{2\sigma^2 \pi} \int_{a_V}^{\infty} \exp(-w^2/2\sigma^2) (w^2 - a_V^2)^{-1/2} dw. \quad (A-4)$$

The integral can be evaluated by using equation 3.382.2 of Gradshteyn and Ryzhik (1980) to give,

$$\begin{aligned}
 F_V(a_V) &= \frac{F_{so} f^{1/2}}{2\sigma^2 \pi} \left[ \left( \frac{1}{2\sigma^2} \right)^{1/2} \exp(-a_V^2/2\sigma^2) \Gamma(1/2) \right] \\
 &= \frac{F_{so} f^{1/2}}{2\sigma^2 \pi} \cdot (2\sigma^2) \exp(-a_V^2/2\sigma^2) \cdot \sqrt{\pi} \\
 &= \left[ \frac{F_{so}^2 f}{2\sigma^2 \pi} \right]^{1/2} \exp(-a_V^2/2\sigma^2). \quad (A-5)
 \end{aligned}$$

Thus,

$$F_V(a_V) = \left( \frac{F_{SO}^2 f}{2\sigma^2 \pi} \right)^{1/2} \exp(-a_V^2 / 2\sigma^2), \quad (A-6)$$

and a Gaussian surface brightness distribution leads to a Gaussian volume brightness distribution.

### Exponential Surface Brightness Distribution

If the surface brightness distribution,  $F_S(a_S)$ , in equation (A-1) has the form,

$$F_S(a_S) = F_{SO} \exp(-\alpha a_S), \quad (A-7)$$

then, the volume brightness distribution,  $F_V(a_V)$ , is,

$$\begin{aligned} F_V(a_V) &= \frac{-f^{1/2}}{\pi} \int_{a_V}^{\infty} \left[ \frac{d}{da_S} F_{SO} \exp(-\alpha a_S) \right] (a_S^2 - a_V^2)^{-1/2} da_S \\ &= \frac{-f^{1/2}}{\pi} \int_{a_V}^{\infty} \left[ F_{SO} \exp(-\alpha a_S) (-\alpha) \right] (a_S^2 - a_V^2)^{-1/2} da_S \\ &= \frac{\alpha F_{SO} f^{1/2}}{\pi} \int_{a_V}^{\infty} \exp(-\alpha a_S) (a_S^2 - a_V^2)^{-1/2} da_S. \end{aligned} \quad (A-8)$$

Using formula 3.387.6 of Gradshteyn and Ryzhik (1980) the integral in equation (A-8) can be evaluated, giving,

$$F_V(a_V) = \frac{\alpha F_{SO} f^{1/2}}{\pi} K_0(\alpha a_V), \quad (A-9)$$



where  $K_0(x)$  is a modified Bessel Function of the second kind of order zero.

Thus, for a Gaussian surface brightness distribution, the volume brightness distribution is also Gaussian,

$$F_V(a_V) = F_O \exp(-a_V^2/2\sigma^2), \quad (A-10)$$

and, for an exponential surface brightness distribution, the volume brightness distribution has the form,

$$F_V(a_V) = F_O K_0(\alpha a_V). \quad (A-11)$$

APPENDIX B  
 OVAL DISTORTIONS FOR n=1 TYPE TOOMRE DISKS

The unperturbed stellar density distribution for the n=1 Toomre disk is of the form, Toomre (1963),

$$\sigma(r) = \frac{C_1}{2\pi G} (a^2 + r^2)^{-3/2}, \quad (B-1)$$

where G is the gravitational constant, and  $C_1$  and a are constants.

Perturbations were added to the stellar density distribution of equation (B-1), resulting in oval distortions of this density distribution. The resultant density distribution has the form,

$$\sigma(r, \theta) = \frac{C_1}{2\pi G} (a^2 + r^2)^{-3/2} [1 + \epsilon(\beta, r) \cos 2\theta], \quad (B-2)$$

where  $\epsilon(\beta, r)$  is the amplitude of the perturbation.

A functional form for  $\epsilon(\beta, r)$  can be obtained from Huntley (1977) and Hunter (1986, private communication). The form for  $\epsilon(\beta, r)$  is,

$$\epsilon(\beta, r) = \frac{\epsilon_1 \beta^\gamma r^2 (a^2 + r^2)^{3/2}}{(\beta^2 + r^2)^{\ell + 3/2}} \quad \begin{array}{l} \gamma = 2(\ell - 1) \\ \ell = 1, 2, \dots \end{array} \quad (B-3)$$

The resulting density distribution is,

$$\sigma(r, \theta) = \frac{C_1^2}{2\pi G} \left[ (a^2 + r^2)^{-3/2} \right] \times \left[ \frac{1 + \epsilon_1 \beta^\gamma r^2 (a^2 + r^2)^{3/2}}{(\beta^2 + r^2)^{1+3/2}} \cos 2\theta \right], \quad (\text{B-4})$$

where  $\epsilon_1$  is a constant and is generally small,

$\beta$  is a length scale for the distortion, and

$\ell$  is the order of the distortion.

Only distortions of order  $\ell=1$  and 2 are considered here.

The potential for this density distribution becomes, Hunter (1986, private communication),

$$\phi(r, \theta, Z=0) = \phi_0 + \phi'(r, \theta, Z=0), \quad (\text{B-5})$$

where  $\phi_0$  is the unperturbed axisymmetric potential.

The form of the perturbed potential  $\phi'(r, \theta, Z=0)$ , for the  $m=2$  (dipole) distortion is, Hunter (1986, private communication),

$$\phi'(r, \theta, 0) = 2\pi G \sum_{m=0}^{\infty} \int_0^{\infty} J_2(kr) \int_0^{\infty} u J_2(ku) \sigma(u, \theta) du dk. \quad (\text{B-6})$$

The perturbed density distribution,  $\sigma'(r, \theta)$ , given by equation (A-4), is,

$$\sigma'(r, \theta) = \frac{C_1^2}{2\pi G} \frac{\epsilon_1 \beta^\gamma r^2 \cos 2\theta}{(\beta^2 + r^2)^{\ell+3/2}}. \quad (\text{B-7})$$

Substituting equation (B-7) into equation (B-6) gives,

$$\phi'(r, \theta, 0) = 2\pi G \int_0^{\infty} J_2(kr) dk$$

$$\int_0^{\infty} \frac{C_1^2}{2\pi G} \frac{\epsilon_1 \beta^\gamma r^2 \cos 2\theta}{(\beta^2 + r^2)^{\ell+3/2}} r J_2(kr) dr, \quad (B-8)$$

or simplifying,

$$\phi'(r, \theta, 0) = C_1^2 \epsilon_1 \beta^\gamma \cos 2\theta \int_0^{\infty} J_2(kr) dk$$

$$\int_0^{\infty} r^3 J_2(kr) (\beta^2 + r^2)^{-\ell-3/2} dr. \quad (B-9)$$

Let the inner integral be  $Q_1$ , i.e.,

$$Q_1 = \int_0^{\infty} \frac{r^3 J_2(kr)}{(\beta^2 + r^2)^{\ell+3/2}} dr. \quad (B-10)$$

This can be evaluated using equations 6.565-4 of Gradshteyn and Ryzhik (1980), hereafter designated GR, giving,

$$Q_1 = \frac{\beta^{1/2-\ell} k^{\ell+3/2}}{2^{\ell+3/2} \Gamma(\ell+5/2)} K_{(1/2-\ell)}(k\beta), \quad (B-11)$$

where  $K_{(1/2-\ell)}(k\beta)$  is a modified Bessel function.

Equation (B-9) becomes,

$$\phi(r, \theta, 0) = \frac{C_1^2 \epsilon_1 \cos 2\theta}{2^{\ell+3/2} \Gamma(\ell+5/2)} \beta^{(\gamma+1/2-\ell)} \times$$

$$\int_0^{\infty} J_2(kr) k^{\ell+3/2} K_{(1/2-\ell)}(k\beta) dk. \quad (B-12)$$

Evaluating the integral,  $Q_2$ , using equation GR 6.576-3, where

$$Q_2 = \int_0^{\infty} J_2(kr) b^{\ell+3/2} K_{(1/2-\ell)}(k\beta) dk, \quad (B-13)$$

gives,

$$Q_2 = \frac{r^{2\Gamma(5/2)} \Gamma(\ell+1)}{2^{-(\ell+1/2)} \beta^{\ell+3/2} \Gamma(3)} F(5/2, \ell+1; 3; -r^2/\beta^2); \quad (B-14)$$

$F(m, n; o; p)$  is Gauss' Hypergeometric function.

Thus,

$$\begin{aligned} \phi'(r, \theta, 0) = & \frac{C_1^2 \epsilon_1 \cos 2\theta}{2} r^2 \beta^{\gamma-4-2\ell} \frac{\Gamma(5/2) \Gamma(\ell+1)}{\Gamma(\ell+5/2) \Gamma(3)} \\ & \times F(5/2, \ell+1; 3; -r^2/\beta^2). \end{aligned} \quad (B-15)$$

Two forms of the oval distortion are considered here; the  $\ell = 1$  and the  $\ell = 2$  forms. As  $\ell$  increases, both the amplitude and radial extent of the perturbation decreases.

#### $\ell = 1$ Perturbations

The perturbed potential,  $\phi'_{\ell=1}(r, \theta, 0)$ , is, from equation (B-15) with  $\ell = 1$ ,

$$\begin{aligned} \phi'_{\ell=1}(r, \theta, 0) = & \frac{C_1^2 \epsilon_1 \cos 2\theta r^2 \beta^{-6}}{2} \frac{\Gamma(5/2) \Gamma(2)}{\Gamma(7/2) \Gamma(3)} \\ F(5/2, 2; 3; -r^2/\beta^2) = & \frac{C_1^2 \epsilon_1 \cos 2\theta}{10} \frac{r^2}{\beta^6} \\ & F(2, 5/2; 3; -r^2/\beta^2). \end{aligned} \quad (B-16)$$

From Huntley (1977), using equations 15.2.18 and 15.1.13 from Abramowitz and Stegun (1964), hereafter AS, the hypergeometric function,  $F(2, 5/2; 3; -r^2/\beta^2)$  can be evaluated,

$$F(2, 4/2; 3; -r^2/\beta^2) = \frac{4\beta^4}{3(\beta^2+r^2)^{3/2}} \left[ \frac{\beta+2(\beta^2+r^2)^{1/2}}{[\beta+(\beta^2+r^2)^{1/2}]^2} \right]. \quad (\text{B-17})$$

Hence, the perturbed potential, for the  $\ell = 1$  perturbation, is,

$$\phi'_{\ell=1}(r, \theta, 0) = \frac{2C_1^2 \epsilon_1 \cos 2\theta}{15(\beta^2+r^2)^{3/2}} \frac{r^2}{\beta^2} \left[ \frac{\beta+2(\beta^2+r^2)^{1/2}}{[\beta+(\beta^2+r^2)^{1/2}]^2} \right]. \quad (\text{B-18})$$

#### $\ell = 2$ Perturbations

The perturbed potential, for the  $\ell = 2$  perturbation,  $\phi'_{\ell=2}(r, \theta, 0)$ , is from equation (B-15),

$$\phi'_{\ell=2}(r, \theta, 0) = \frac{C_1^2 \epsilon_1 \cos 2\theta}{2} \frac{r^2}{\beta^6} \frac{\Gamma(5/2) \Gamma(3)}{\Gamma(9/2) \Gamma(3)}$$

$$F(5/2, 3; 3; -r^2/\beta^2) = \frac{2C_1^2 \epsilon_1 \cos 2\theta}{35} \frac{r^2}{\beta^7}$$

$$F(5/2, 3; 3; -r^2/\beta^2). \quad (\text{B-19})$$

Using AS 15.1.8 to evaluate the hypergeometric function gives,

$$F(5/2, 3; 3; -r^2/\beta^2) = (1+r^2/\beta^2)^{-5/2}. \quad (\text{B-20})$$

Therefore, the perturbed potential, for the  $\ell = 2$  perturbation, is,

$$\begin{aligned}\phi'_{\ell=2}(r, \theta, 0) &= \frac{2C_1^2 \epsilon_1 \cos 2\theta}{35} r^2 [\beta^6 (1+r^2/\beta^2)^{5/2}]^{-1} \\ &= 2C_1^2 \epsilon_1 \cos 2\theta r^2 [\beta (\beta^2)^{5/2} (1+r^2/\beta^2)^{5/2}]^{-1},\end{aligned}$$

or

$$\phi'_{\ell=2}(r, \theta, 0) = \frac{2C_1^2 \epsilon_1 \cos 2\theta}{35} \frac{r^2}{\beta} \frac{1}{(\beta^2 + r^2)^{5/2}}. \quad (\text{B-21})$$

The perturbed potentials for the  $n=1$  Toomre disk differ from those for the  $n=0$  Toomre disks by constant factors. These factors are, for the  $\ell = 1$  case,

$$K_1 = \frac{2}{5\beta^2}, \quad (\text{B-22})$$

and, for the  $\ell = 2$  case,

$$K_2 = \frac{2}{7}. \quad (\text{B-23})$$

Thus,

$$\phi'_{\substack{n=1 \\ \ell=1}}(r, \theta, 0) = \frac{2}{5\beta^2} \phi'_{\substack{n=0 \\ \ell=1}}(r, \theta, 0), \quad (\text{B-24})$$

and,

$$\phi'_{\substack{n=1 \\ \ell=2}}(r, \theta, 0) = \frac{2}{7} \phi'_{\substack{n=0 \\ \ell=2}}(r, \theta, 0). \quad (\text{B-25})$$

The radial and tangential forces corresponding to these perturbed potentials are,

$$F'_{\substack{R \\ \ell}}(r, \theta) = \frac{\partial \phi'_{\ell}(r, \theta)}{\partial r}, \quad (\text{B-26})$$

and,

$$F'_{T \ell}(r, \theta) = \frac{1}{r} \frac{\partial \phi_{\ell}'(r, \theta)}{\partial \theta}. \quad (B-27)$$

Thus, the forces can be calculated easily from the  $n=0$  disk forms, giving,

$$F'_{R \ell=1}(r, \theta) = \frac{2C_1^2 \epsilon_1 \cos 2\theta}{15} \frac{r}{\beta^2} \times \left\{ \frac{3\beta(2\beta^2 - r^2)(\beta^2 + r^2)^{1/2} - r^2(\beta^2 + 4r^2) + 6\beta^4}{(\beta^2 + r^2)^{5/2} (\beta + (\beta^2 + r^2)^{1/2})^3} \right\} \quad (B-28)$$

$$F'_{T \ell=1}(r, \theta) = \frac{-4C_1^2 \epsilon_1 \sin 2\theta}{15(\beta^2 + r^2)^{3/2}} \frac{r}{\beta^2} \left[ \frac{\beta + 2(\beta^2 + r^2)^{1/2}}{[\beta + (\beta^2 + r^2)^{1/2}]^2} \right], \quad (B-29)$$

and,

$$F'_{R \ell=2}(r, \theta) = \frac{2C_1^2 \epsilon_1 \cos 2\theta}{35} \frac{1}{\beta} \left[ \frac{2r\beta^2 - 3r^3}{(\beta^2 + r^2)^{7/2}} \right], \quad (B-30)$$

$$F'_{T \ell=2}(r, \theta) = \frac{-4C_1^2 \epsilon_1 \sin 2\theta}{35} \frac{r}{\beta(\beta^2 + r^2)^{5/2}}. \quad (B-31)$$

The total forces are,

$$F_R(r, \theta) = F_R^O(r, \theta) + F_R'(r, \theta), \quad (B-32)$$

and,

$$F_T(r, \theta) = F_T'(r, \theta), \quad (B-33)$$



where,

$$F_R^O(r, \theta) = \frac{-C_1^2 r}{a(a^2 + r^2)^{3/2}} \quad (\text{B-34})$$

is the axisymmetric force for the  $n=1$  Toomre disk.

The forces from the  $\ell=1$  perturbations effect essentially the whole computational grid, whereas the forces from the  $\ell=2$  perturbations have a lesser effect at large  $r$ . As  $r \rightarrow \infty$  the forces for the  $\ell=1$  perturbations are  $\propto r^{-3}$  and the forces for the  $\ell=2$  perturbations are  $\propto r^{-4}$ .

## BIBLIOGRAPHY

- Abramowitz, M., Stegun, I. A., eds. (1965), Handbook of Mathematical Functions (New York: Dover).
- Allen, C. W., (1973), Astrophysical Quantities, 3rd. ed., (London: Athlone Press).
- Arp, H., Sulentic, J. W., (1979), Ap. J., vol. 229, 496.
- Baars, J. W. M., Genzel, R., Pauliny-Toth, I. I. K., Witzel, A., (1977), Ast. Ap., vol. 61, 99.
- Ball, J. R., (1984), Ph. D. Dissertation, Univ. of Florida.
- Ball, J. R., (1986), In Press.
- Baumgart, C. W., Peterson, C. J., (1986), P. A. S. P., vol. 98, 56.
- Berman, R. H., Pollard, D. J., Hockney, R. W., (1979), Ast. Ap., vol. 78, 133.
- Black, J. H., (1985), in Molecular Astrophysics, eds. G. H. F. Dierksen, W. F. Huebner, P. W. Langhoff (Dordrecht, Holland: D. Reidel).
- Blackman, C. P., (1983), M. N. R. A. S., vol. 202, 379.
- Bosma, A., (1978), Ph. D. Thesis, Univ. of Groningen.
- Bosma, A., (1981), Ast. J., vol. 86, 1791.
- Bottinelli, L., Chamaraux, P., Gougenheim, L., Lauque, R., (1970), Ast. Ap., vol. 6, 453.
- Bracewell, R., (1965), The Fourier Transform and its Applications, (New York: McGraw Hill).
- Burbidge, E. M., Burbidge, G. R., (1975), The Masses of Galaxies, in Galaxies and the Universe, Vol. IX of Stars and Stellar Systems, eds. A. and M. Sandage and J. Kristian, (Chicago: Univ. of Chicago).
- Burkhead, M. S., Burgess, R. D., (1973), Ast. J., vol. 78, 606.

- Casertano, S., (1983), M. N. R. A. S., vol. 203, 735.
- Christiansen, W. N., Hindman, J. V., (1952), Aust. J. Sc. Res. A5, 437.
- Clark, B. G., (1980), Ast. Ap., vol. 89, 377.
- Clark, B. G., (1985), in Synthesis Imaging: Proceedings of the 2nd NRAO-VLA Summer School, ed. R. Perley, (Socorro, New Mexico: NRAO).
- Contopoulos, G., (1970), Ap. J., vol. 160, 113.
- Contopoulos, G., (1975), Ap. J., vol. 201, 566.
- Contopoulos, G., (1983), Ast. Ap., vol. 117, 89.
- Contopoulos, G., (1985), Comments in Astrophysics, XI, 1.
- Contopoulos, G., Hunter, J. H. Jr., Gottesman, S. T., England, M. N., (1986), In Preparation.
- Cornwell, T. J., (1985) in Synthesis Imaging: Proceedings of the 2nd NRAO-VLA Summer School, ed. R. Perley, (Socorro, New Mexico: NRAO).
- D'Addario, L. R., (1985) in Synthesis Imaging: Proceedings of the 2nd NRAO-VLA Summer School, ed. R. Perley, (Socorro, New Mexico: NRAO).
- Dalgano, A., (1985), in Molecular Astrophysics, eds. G. H. F. Dierksen, W. F. Huebner, P. W. Langhoff (Dordrecht, Holland: D. Reidel).
- De Vaucouleurs, G., (1963), Ap. J. Suppl., vol. 8, 31.
- De Vaucouleurs, G., de Vaucouleurs, A., Corwin, H. G. Jr., (1976), Second Reference Catalogue of Bright Galaxies, (Austin: Univ. of Texas).
- De Vaucouleurs, G., Peters, W., L., (1981), Ap. J., vol. 248, 395.
- Elmegreen, D. M., (1981), Ap. J. Suppl., vol. 47, 229.
- Elmegreen, D. M., Elmegreen, B. G., (1984), Ap. J. Suppl., vol. 54, 127.
- Elmegreen, B. G., Elmegreen, D. M., (1985), Ap. J., vol. 288, 438.
- Ewen, H. I., Purcell, E. M., (1951), Nature, vol. 168, 356.

- Fomalont, E. B., Wright, M. C. H., (1974), in Galactic and Extra-Galactic Radio Astronomy, eds. G. L. Verschuur, K. I. Kellerman (New York: Springer Verlag).
- Freeman, K. C., (1970), Ap. J., vol. 160, 811.
- Gallouet, L., Heidmann, N., Dampierre, F., (1973), Ast. Ap. Suppl., vol. 12, 89.
- Gottesman, S. T., Ball, J. R., Hunter, J. H. Jr., Huntley, J. M., (1984), Ap. J., vol. 286, 471.
- Gradshteyn, I. S., Ryzhik, I. M., (1980), Tables of Integrals, Series and Products (New York: Academic Press).
- Hawarden, T. G., Fairclough, J. H., Joseph, R. D., Leggett, S. K., Mountain, C. M., (1985), IRAS Symposium, New Light on Dark Matter, Noordwijk, Holland.
- Hjellming, R. M., Basart, J. P., (1982), An Introduction to the NRAO Very Large Array, ed. R. M. Hjellming (Socorro, New Mexico: NRAO).
- Hodge, P. W., (1969), Ap. J. Suppl., vol. 18, 73.
- Hogbom, J. A., (1974), Ast. Ap. Suppl., vol. 15, 417.
- Hohl, F., (1978), Ast. J., vol. 83, 768.
- Hohl, F., Zang, T. A., (1979), Ast. J., vol. 84, 585.
- Hunter, J. H. Jr., Ball, J. R., Gottesman, S. T., (1984), M. N. R. A. S., vol. 208, 1.
- Hunter, J. H. Jr., Ball, J. R., Huntley, J. M., England, M. N., Gottesman, S. T., (1986) In Press
- Huntley, J. M., (1977), Ph. D. Dissertation, Univ. of Virginia.
- Huntley, J. M., (1980), Ap. J., vol. 238, 524.
- Huntley, J. M., Sanders, R. H., Roberts, W. W., (1978), Ap. J., vol. 221, 521.
- Jackson, P.D., Kellerman, S. A., (1974), Ap. J., vol. 190, 53.
- Kalnajs, A. J., (1978), IAU Symposium No. 77, Structure and Properties of Nearby Galaxies, eds. E. M. Berkhuysen, R. Wielebinski (Dordrecht, Holland: Reidel).
- Kormendy, J., (1979), Ap. J., vol. 227, 714.

- Liebovitch, L. S., (1978), Ph. D. Thesis, Harvard University.
- McKee, C. F., Ostriker, J. P., (1977), *Ap. J.*, vol. 218, 148.
- Mihalas, D., Binney, J., (1981), *Galactic Astronomy*, 2nd. Ed., (San Francisco: Freeman).
- Miller, R. H., (1971), *Ap. Sp. Sc.*, vol. 14, 73.
- Miller, R. H., (1976), *Ap. J.*, vol. 207, 408.
- Miller, R. H., (1978), *Ap. J.*, vol. 223, 122.
- Miller, R. H., Smith, B. F., (1979), *Ap. J.*, vol. 227, 407.
- Miller, R. H., Smith, B. F., (1980), *Ap. J.*, vol. 235, 793.
- Miller, R. H., Smith, B. F., (1981), *Ap. J.*, vol. 244, 33.
- Morris, M., Rickard, L. J., (1982), *Ann. Rev. Ast. and Ap.*, vol. 20, 517.
- Muller, C. A., Oort, J. H., (1951), *Nature*, vol. 168, 356.
- Ondrechen, M. P., van der Hulst, J. M., (1983), *Ap. J.*, vol. 269, L47.
- Ostriker, J. P., Peebles, P. J. E., (1973), *Ap. J.*, vol. 186, 467.
- Peterson, C. J., Huntley, J. M., (1980), *Ap. J.*, vol. 242, 913.
- Reif, K., Mebold, U., Goss, W. M., van Woerden, H., Siegman, B., (1982), *Ast. Ap. Suppl.*, vol. 50, 451.
- Rieke, G. H., Lebofsky, M. J., Thompson, R. I., Low, F. J., Tokunaga, A. T., (1980), *Ap. J.*, vol. 238, 24.
- Roache, P. J., (1976), *Computational Fluid Dynamics*, Rev. Ed. (Albuquerque, New Mexico: Hermosa).
- Roberts, W. W., (1979), *Photometry, Kinematics and Dynamics of Galaxies*, ed. D. S. Evans (Austin: Univ. of Texas).
- Roberts, W. W., Huntley, J. M., van Albada, G. D., (1979), *Ap. J.*, vol. 223, 67.
- Rots, A. H., (1982), *Synthesis Mapping: Proceedings of the NRAO-VLA Workshop* (Charlottesville, Virginia: NRAO).

- Sandage, A., (1961), *The Hubble Atlas of Galaxies*  
(Washington: Carnegie Institute of Washington).
- Sandage, A., Tammann, G., (1975), *Ap. J.*, vol. 196, 313.
- Sanders, R. H., (1977), *Ap. J.*, vol. 217, 916.
- Sanders, R. H., Huntley, J. M., (1976), *Ap. J.*, vol. 209,  
53.
- Sanders, R. H., Prendergast, K. H., (1974), *Ap. J.*, vol.  
188, 489.
- Sanders, R. H., Tubbs, A. D., (1980), *Ap. J.*, vol. 235, 803.
- Schemp, W. V., (1982), *Ap. J.*, vol. 258, 96.
- Schwab, F. R., (1980), *VLA Scientific Memo No. 132.*
- Schwarz, M. P., (1985), *M. N. R. A. S.*, vol. 212, 677.
- Spitzer, L. Jr., (1978), *Physical Processes in the  
Interstellar Medium* (New York: Wiley).
- Sramek, R. A., (1982), *Synthesis Mapping: Proceedings of the  
NRAO-VLA Workshop* (Charlottesville, Virginia: NRAO).
- Sramek, R. A., (1985), in *Synthesis Imaging: Proceedings of  
the 2nd NRAO-VLA Summer School*, ed. R. Perley, (Socorro,  
New Mexico: NRAO).
- Stark, A. A., (1977), *Ap. J.*, vol. 213, 368.
- Swenson, G. W. Jr., Mathur, N. C., (1968), *Proc. IEEE*, vol.  
56, 2114.
- Telesco, C. M., Harper, D. A., (1980), *Ap. J.*, vol. 235,  
392.
- Teuben, P. J., Sanders, R. H., (1985), *M. N. R. A. S.*, vol.  
212, 257.
- Teuben, P. J., Sanders, R. H., Atherton, P. D., van Albada,  
G. D., (1986), *M. N. R. A. S.*, vol. 221, 1.
- Thaddeus, P., (1977), in *Star Formation*, eds. T. de Jong and  
A. Maeder, (IAU).
- Thompson, A. R., (1985), in *Synthesis Imaging: Proceedings  
of the 2nd NRAO-VLA Summer School*, ed. R. Perley,  
(Socorro, New Mexico: NRAO).
- Toomre, A., (1963), *Ap. J.*, vol. 138, 385.

- van Albada, G. D., Roberts, W. W. Jr., (1981), Inst. for Computer Applications in Sc. and Eng., Report No. 81-1.
- van Albada, G. D., van Leer, B., Roberts, W. W., (1981), Inst. for Computer Applications in Sc. and Eng., Report No. 81-24.
- van de Hulst, H. C., (1945), Neder. Tijd. Natuurkunde, vol. 11, 210.
- van Gorkom, J. H., (1982), Synthesis Mapping: Proceedings of the NRAO-VLA Workshop (Charlottesville, Virginia: NRAO).
- Warner, P. J., Wright, M. C. H., Baldwin, J. E., (1973), M. N. R. A. S., vol. 163, 163.
- Young, J. S., (1985), in The Milky Way Galaxy, eds. H. van Woerden, R. J. Allen, W. B. Burton, IAU Symposium No. 106 (Doordrecht, Holland: Reidel).
- Young, J. S., Gallagher, J. G., Hunter, D. A., (1984), Ap. J., vol. 276, 476.

## BIOGRAPHICAL SKETCH

Born on the 17th of December, 1954, in Pretoria, South Africa, Martin Nicholas England attended Springs Boys High School, Springs, South Africa. With his parents, Michael and Maureen England, and his younger brothers, Neil and Paul, he emigrated to New Zealand in 1973.

He received a B. Sc. and a B. Sc. (Hons.) in physics from Victoria University of Wellington, Wellington, New Zealand, and a M. Sc. in astronomy from the University of Canterbury, Christchurch, New Zealand.

Graduate study for the Ph. D. in astronomy was carried out at the University of Florida, Gainesville, Florida. The Ph. D. degree was received in December 1986.

He married Sheila Murphy in 1982 and they have two children, Kathryn and Maureen.



I certify that I have read this study and that in my opinion it conforms to acceptable standards of scholarly presentation and is fully adequate, in scope and quality, as a dissertation for the degree of Doctor of Philosophy.

---

Stephen T. Gottesman, Chairman  
Professor of Astronomy

I certify that I have read this study and that in my opinion it conforms to acceptable standards of scholarly presentation and is fully adequate, in scope and quality, as a dissertation for the degree of Doctor of Philosophy.

---

*James H. Hunter, Jr.*  
James H. Hunter Jr., Cochairman  
Professor of Astronomy

I certify that I have read this study and that in my opinion it conforms to acceptable standards of scholarly presentation and is fully adequate, in scope and quality, as a dissertation for the degree of Doctor of Philosophy.

---

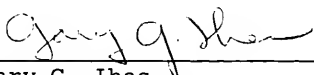
*Thomas D. Carr*  
Thomas D. Carr  
Professor of Astronomy

I certify that I have read this study and that in my opinion it conforms to acceptable standards of scholarly presentation and is fully adequate, in scope and quality, as a dissertation for the degree of Doctor of Philosophy.

---

Haywood C. Smith Jr.  
Associate Professor of Astronomy

I certify that I have read this study and that in my opinion it conforms to acceptable standards of scholarly presentation and is fully adequate, in scope and quality, as a dissertation for the degree of Doctor of Philosophy.

  
\_\_\_\_\_  
Gary G. Ihas  
Professor of Physics

This dissertation was submitted to the Graduate Faculty of the Department of Astronomy in the College of Liberal Arts and Sciences and to the Graduate School and was accepted as partial fulfillment of the requirements for the degree of Doctor of Philosophy.

December 1986

\_\_\_\_\_  
Dean, Graduate School

